

**INVESTIGATION OF THE CONTROLS OF FLUID  
FLOW THROUGH SHALE AND THEIR  
RELATION TO ITS MECHANICAL PROPERTIES**

by

Hamood Said Ali Al-Hajri

Submitted in accordance with the requirements for the degree of  
Doctor of Philosophy

The University of Leeds  
School of Earth and Environment

May 2018



The candidate confirms that the work submitted is his own and that appropriate credit has been given where reference has been made to the work of others.

This copy has been supplied on the understanding that it is copyright material and that no quotation from the thesis may be published without proper acknowledgement.

**(c) 2018 The University of Leeds and Hamood Al-Hajri**

## **Publications**

Lynch, T., Al-Hajri, H. & Fisher, Q. (2017). Experimental investigations into CO<sub>2</sub> injection associated fracture behaviour in shale caprocks. *Energy Procedia*, 114, pp.3210-3218.

## Acknowledgment

At the beginning, I thank Allah for giving me the ability and strength to complete this work.

I would like to express my utmost gratitude and appreciation to my supervisors Prof. Quentin Fisher and Dr. Carlos Grattoni for their endless guidance and continuous support in every step throughout my PhD studies. Their technical and non-technical guidance was valuable and of a great help for me in the planning and development of every piece of this research. Their patience and encouragement provided me with required enthusiasm to complete this work. Special thanks go also to Dr. Samuel Allshorn, Dr. John Martin and Phil Guise for technical support in conducting experimental work in the laboratory. I am particularly grateful for the assistance given by Dr. Tom Lynch and his willingness to give his valuable time.

I am greatly thankful to Dr. Ali Hassanpour who allowed me to use micro-indentation instrument and provided me with all required knowledge. Special thanks go also to Dr. Jabbar Gardy and Mozhdeh Mehrabi who assisted me in performing micro-indentation tests.

I am grateful to the Ministry of Higher education, Oman and Petroleum Development Oman (PDO) for sponsoring me to do PhD. I would like to thank my colleagues in University of Leeds; Samuel Parsons, Omar Khalooq, Ibrahim Al Makrami and Hussain Al-Hashmi for their support. Special thanks also go to my colleagues in PDO, Sultan Al-Amri and Khalfan Al-Bahri.

My deepest love and thanks go to my role models, my father and mother, who were with me and continuously supported me in everything I pursue. They always believed in me and provided me with all the support I need without me asking. May Allah bless them with mercy, health and love. The thanks are also extended to my brothers and sisters for their love and support.

Finally and mostly, much love and appreciation is to my wife who believed in me and left her career for me to peruse my studies. If it was not for her, I would never been able to complete this research. She and our children were the source of inspiration and motivation throughout these years. Unmeasurable appreciation for her patience and thanks to her for being a wife, a friend and a mother.

## Abstract

Understanding mechanisms of fluid flow through shale is very important as these sedimentary rock act as caprock, key source of unconventional hydrocarbon, seal for geological CO<sub>2</sub> storage and radioactive waste disposal sites. Four mechanisms of fluid flow were identified; matrix flow by single or multiphase flow, flow through faults and fractures and flow through preferential pathways induced by high pressure fluid. Knowledge gaps associated with understanding the controls of these mechanisms were identified in this thesis. A series of experimental and simulation work was conducted to fill these knowledge gaps. Shale samples were collected from different location with a wide range of petrophysical, mechanical and mineralogical properties.

Multiphase flow and sealing capacity assessment requires knowledge of threshold pressure of shale, which is challenging using standard methods due to the stress sensitive of shale. Using Mercury Porosimetry Under Confining Stress (MPUCS) instrument, it was proven experimentally that shale would act as effective seal and would not leak by multiphase flow through the undeformed matrix under in situ conditions.

The radioactive waste management industry argues that leakage mainly occurs via flow along pathways formed by high gas pressures (pathway dilation). However, there is no micro mechanical model to describe formation and propagation of these pathways. Pathway dilation in clay-rich sediments was investigated by injecting melted Field's metal into synthetic shale sample. Results suggest that compaction plays a key role in formation and propagation of these pathways.

It is quite important to understand failure mechanics of shale in order to be able to argue the existence of conductive faults and fracture and their capability to re-seal. Anticipation of formation and closure of faults and fractures require knowledge of mechanical properties such as the apparent preconsolidation pressure, which is difficult to obtain for shale. A new simple technique was developed to measure the preconsolidation pressure under hydrostatic condition using MIP instrument. Micro-indentation was proposed to measure elastic properties as it is difficult to obtain core plugs that are sufficient long for tri-axial testing.

Faults and fracture are often argued to be conduits to fluid flow across shale. However, these features could close and re-seal but knowledge of controls for fracture closure is still elusive. Controls of fracture closure in shale were investigated by conducting a series of flow experiments through artificial fracture using a set of different shale samples. It was shown that porosity, clay content and stress state controls fracture closure. It was suggested that fractures in soft shale with high porosity and clay content samples have potential to close and reseal under in situ condition whereas stiff shale will have their fracture open under same conditions. Finite element analysis (FEA) was performed to simulate the same fracture closure experiment, which also provided results that agree with the suggestions made from experimental work.

# Table of Contents

<b>1 Chapter I: Introduction</b> .....	1
1.1 Introduction.....	1
1.2 Mechanisms of fluid flow through shale.....	2
1.2.1 Non-deforming matrix flow (Single and multiphase flow).....	3
1.2.2 Stress-related rock deformation flow (Flow through faults and fractures) .....	4
1.2.3 Fluid pressure-related deformation flow (Pathway dilation) .....	5
1.3 Research goals .....	6
1.3.1 Background .....	6
1.3.2 Summary of research goals .....	10
1.4 Structure of the thesis.....	10
<b>2 Chapter II: Mechanisms of fluid flow through shale and their controls</b> .....	12
1.1 Introduction.....	12
1.2 Single phase flow through shale .....	13
2.1.1 Darcy's Law .....	13
2.1.2 Published data on the permeability of shale.....	14
1.3 Multiphase flow through shale.....	18
2.1.3 Capillary pressure .....	18
2.1.4 Capillary pressure and relative permeability.....	19
1.4 Fault and Fracture related flow .....	21
2.1.5 Formation of faults and fractures .....	21
2.1.5.1 Deformation mechanisms.....	21
2.1.5.2 Brittle tensile and extension fractures .....	26
2.1.5.3 Brittle shear fractures .....	27
2.1.5.4 Ductile deformation .....	30
2.1.6 Fracture closure models and experiments .....	36
1.5 Pathways dilation.....	45
1.6 Summary of key knowledge gaps .....	52
<b>3 Chapter III: Samples characterization</b> .....	53
3.1 Introduction.....	53
3.2 Sample locations .....	53
3.1 Experimental materials and methods .....	55
3.1.1 Mineralogy analysis using X-Ray Diffraction (XRD) .....	55
3.1.2 Total organic content analysis (TOC).....	56



3.1.3	Scanning electron microscope (SEM).....	57
3.1.4	Mercury Intrusion Porosimetry (MIP) .....	59
3.1.5	Mechanical properties .....	60
3.2	Experimental results.....	62
3.2.1	XRD, TOC and SEM microstructural analysis .....	62
3.2.2	Capillary properties and porosity results using MIP .....	66
3.2.3	Multistage triaxial test.....	68
3.3	Discussion.....	71
3.3	Summary .....	75
<b>4</b>	<b>Chapter IV: Investigation of controls of matrix flow within shale in deforming and non-deforming flow regimes .....</b>	<b>76</b>
4.1	Introduction:.....	76
4.2	Sample preparation .....	78
4.2.1	Controls of matrix flow within shale by capillary flow .....	78
4.2.2	Controls of matrix flow within shale by pathway dilation.....	78
4.3	Experimental method .....	80
4.3.1	Controls of matrix flow within shale by capillary flow .....	80
4.3.2	Controls of matrix flow within shale by pathway dilation.....	84
4.4	Experimental results.....	88
4.4.1	Controls of matrix flow within shale by capillary flow .....	88
4.4.2	Controls of matrix flow within shale by pathway dilation.....	96
4.5	Discussion.....	105
4.5.1	Controls of matrix flow within shale by capillary flow .....	105
4.5.1.1	Sealing capacity .....	105
4.5.1.2	Effect of microfractures within the shale matrix.....	107
4.5.2	Controls of matrix flow within shale by pathway dilation.....	108
4.6	Conclusions.....	111
<b>5</b>	<b>Chapter V: Determination of geomechanical properties of shale using micro-indentation and Mercury Intrusion Porosimetry (MIP) .....</b>	<b>113</b>
5.1	Introduction.....	113
5.2	Sample preparation .....	116
5.2.1	Measurement of mechanical properties using micro-indentation .....	116
5.2.2	Estimation of critical effective stress ( $p^*$ ) of shale using MIP technique....	118
5.3	Experimental methods .....	120
5.3.1	Measurement of mechanical properties using micro-indentation .....	120

5.3.2	Estimation of critical effective stress ( $p^*$ ) of shale using MIP technique....	126
5.4	Experimental results.....	127
5.4.1	Measurement of mechanical properties using micro-indentation .....	127
5.4.1.1	Laboratory-dry samples .....	127
5.4.1.2	Acid exposed samples .....	136
5.4.2	Estimation of critical effective stress ( $p^*$ ) of shale using MIP technique....	142
5.5	Discussion .....	149
5.5.1	Measurement of mechanical properties using micro-indentation .....	149
5.5.1.1	Effect of mineral composition.....	149
5.5.1.2	Relationship between Young's modulus, hardness and fracture toughness	152
5.5.1.3	Effect of acid on mechanical properties of shale .....	155
5.5.2	Estimation of critical effective stress ( $p^*$ ) of shale using MIP technique....	156
5.5.2.1	$P^*$ results validation.....	156
5.5.2.2	Effect of mineralogy and permeability on estimating elastic properties of the samples	159
5.6	Conclusions.....	162
<b>6</b>	<b>Chapter VI: Experimental investigation of controls of fracture closure in shale.....</b>	<b>165</b>
6.1	Introduction.....	165
6.2	Sample preparation .....	166
6.3	Experimental method .....	170
6.4	Experimental results.....	174
6.4.1	Fracture closure of the WS sample .....	177
6.4.2	Fracture closure of the ALP sample.....	183
6.4.3	Fracture closure of the AM sample.....	188
6.4.4	Fracture closure of the KC sample.....	193
6.4.5	Fracture closure of the OC sample.....	198
6.4.6	Fracture closure of the D sample .....	203
6.5	Discussion .....	208
6.5.1	Accuracy of the results.....	208
6.5.2	Deformations during fracture closure .....	208
6.5.3	Fracture permeability estimation.....	224
6.5.4	Importance of geomechanical properties in controlling fracture closure.....	226
6.6	Conclusions.....	229

<b>7</b>	<b>Chapter VII: Finite element modelling of fracture closure in shale.....</b>	<b>231</b>
7.1	Introduction.....	231
7.2	Geometry description.....	232
7.3	Material Definition.....	233
7.4	Simulations results .....	236
7.4.1	Fracture closure modelling using elastic material definition .....	236
7.4.2	Fracture closure modelling using SR3 model material definition.....	243
7.4.3	Complete fracture closure simulation .....	251
7.5	Discussion.....	254
7.5.1	Matching SR3 models simulation results with experimental results .....	254
7.5.2	Comparison between elastic simulation and SR3 model simulation .....	256
7.5.3	Estimation of the potential of fracture complete closure during burial.....	259
7.6	Conclusions.....	261
<b>8</b>	<b>Chapter VIII: Conclusion and Future work.....</b>	<b>262</b>
8.1	Conclusions.....	262
8.2	Future work.....	266
9	References .....	267
10	Appendix A .....	284
11	Appendix B .....	287
12	Appendix C .....	291

## List of Figures

<i>Figure 1-1: Summary of Mechanisms of fluid flow through rocks .....</i>	<i>3</i>
<i>Figure 1-2: Picture showing clearly the delamination problem.....</i>	<i>8</i>
<i>Figure 1-3: Typical failure envelope of rock material.....</i>	<i>9</i>
<i>Figure 1-4: Yield envelope in p-q space, black represented the part constructed using experimental data and red box represents the part assumed.....</i>	<i>10</i>
<i>Figure 2-1: Sketch showing parameters of Darcy's equation to calculate permeability of a porous medium.....</i>	<i>13</i>
<i>Figure 2-2: Published data of porosity-depth curves for shales and argillaceous sediments for shale (Mondol et al., 2007). .....</i>	<i>14</i>
<i>Figure 2-3: Void ratio-effective stress relationship of actual data compared to model. Data for clay ranges (a) 25–35%; (b) 35–45%; (c) 45–55%; (d) 55–65% (Yang and Aplin, 2004). .....</i>	<i>15</i>
<i>Figure 2-4 Porosity (thin line), cumulative specific surface area, <math>S_s</math> (dot-dash line) and permeability (thick line) of different mudstones at different effective stresses. Samples used have (a) 36.8% clay content at 6.4 MPa effective stress, (b) 51.8% clay content at 20.5 MPa effective stress and (c) 72.2% clay content at 7.4 MPa effective stress (Yang and Aplin, 1998). .....</i>	<i>16</i>
<i>Figure 2-5 : Permeability data as collected by (Neuzil, 1994). Laboratory-derived permeability vs. porosity data for a variety of natural argillaceous media. Permeability is shown along the lower horizontal scale: the corresponding hydraulic conductivity to water at room temperature is shown along the upper horizontal scale. ....</i>	<i>17</i>
<i>Figure 2-6: Permeability/Porosity relationships for mudrocks from (Yang and Aplin, 2010). The legend shows the range of clay content for each band. The curves correspond to the middle value of clay contents of the band with the same colour. ....</i>	<i>17</i>
<i>Figure 2-7: Typical relative permeability curves for a high permeability rock (Shanley, 2004). .....</i>	<i>20</i>
<i>Figure 2-8: Relative permeability curves for a low permeability rock (Shanley, 2004).....</i>	<i>21</i>
<i>Figure 2-9: Behaviour of rock in stress-strain curve during bi-axial stress application. ....</i>	<i>22</i>
<i>Figure 2-10: Diagram showing typical stress–strain curves obtained during sandstone deformation experiments. Included on the plot are sketches showing the typical form of the deformed samples following the experiments. Curve (i) is typical of rocks that deformed by distributed cataclastic flow. Curve (ii) is typical of rocks deformed at the brittle–ductile transition. Curve (iii) is typical of rock deformed by brittle failure. The diagram is based on (Griggs and Handin, 1960) and taken from (Fisher et al., 2007). .....</i>	<i>23</i>

<i>Figure 2-11: Fractures formation modes.</i> .....	24
<i>Figure 2-12: Types of rock failure. A is a tensile fracture, B is an extension fracture and C&amp;D are shear fractures by formation of shear plane and shear-enhanced compaction respectively (Mandl, 2005).</i> .....	25
<i>Figure 2-13: Stress-strain diagram for each type of failure. Curve A&amp;B correspond to tensile and extension fracture where curve C&amp;D correspond to shear failure either by formation of a shear plane (Curve C) or by shear enhanced compaction (Curve D) (Mandl, 2005).</i> .....	26
<i>Figure 2-14: Extension fracture models (A; Wing crack model, B; Void model, C; Grain contact model and C; Elastic mismatch model) (Mandl, 2005).</i> .....	27
<i>Figure 2-15: Mohr-Coulomb criterion (Fjaer, 2008).</i> .....	28
<i>Figure 2-16: Griffith- Coulomb failure criterion. The left side of the curve represents Griffith failure criterion (red) which describes tensile failure and the right side represents coulomb criterion which describes compression failure.</i> .....	29
<i>Figure 2-17: effect of pore pressure on Mohr circle. Increase of pore pressure decreases pore pressure and moves Mohr circle to the left (blue) and decrease of pore pressure moves the circle to the right and increases its size (red) (Fisher et al., 2013).</i> .....	30
<i>Figure 2-18: A typical yield envelope showing all types of deformations and failure in p, q space (Schutjens et al., 2004).</i> .....	31
<i>Figure 2-19: Yield surface of Cam-Clay and Modified Cam-Clay models.</i> .....	33
<i>Figure 2-20: Plastic potential surface (green) with respect to the yield surface (blue) showing the flow rule as strain components in p-q space of SR3 model (Al Zadjali, 2011).</i> ..	35
<i>Figure 2-21: Change in angle <math>\beta</math> with stress point change to define dilation and compaction (Rockfield, 2014a).</i> .....	36
<i>Figure 2-22: Parameters of fracture closure modelling.</i> .....	37
<i>Figure 2-23: Examples of fracture profiles and their corresponding JRC (Bandis et al., 1983).</i> .....	38
<i>Figure 2-24: Simulation of fracture closure at various; (a) initial average aperture, (b) Young's modulus and (c) fracture surface properties (Duan et al., 2000).</i> .....	39
<i>Figure 2-25: Fracture permeability as function of effective normal stress fitted with an empirical exponential function taken from Gutierrez et al. (2000).</i> .....	40
<i>Figure 2-26: (a) Core sample preparation, (b) permeability reduction as function of confining stress (Cho et al., 2013).</i> .....	41
<i>Figure 2-27: Water permeability variation over time for confining stress values from 1-13 MPa for COX sample (Zhang, 2011).</i> .....	42

<i>Figure 2-28: Water permeability variation over time at different temperatures. Confining and injection pressure were held constant throughout the experiment (Zhang, 2011).</i>	42
<i>Figure 2-29: Strain Vs time for creep process (Fjaer 2008).</i>	43
<i>Figure 2-30: Stress effect on strain vs. time creep process (Fjaer 2008).</i>	43
<i>Figure 2-31: Burgers body model and its response (Goodman, 1980).</i>	44
<i>Figure 2-32: observed increase volumetric strain increase and formation of preferential pathways within a core sample from Bure Underground Research Laboratory (URL) in Paris (Cuss et al., 2014a).</i>	47
<i>Figure 2-33: X-ray computed tomographic (CT) image of a sample sediment containing gas bubbles. Dark grey represents mud and light grey represents sand, black features are gas bubbles (from Boudreau et al., 2005).</i>	48
<i>Figure 2-34: A and B: Plan and cross section of bubble rising in gelatine, C: Path of this bubble as it rises up. This picture is taken from Boudreau et al. (2005).</i>	49
<i>Figure 2-35: Diagram representing development of pipe-type conduit based on available model of diatreme &amp; breccia pipe formation. (e.g. Novikov and Slobodskoy, 1978). This figure is taken from Cartwright et al. (2007).</i>	51
<i>Figure 3-1: The cliff at the beach in Whitby (The map is obtained from google maps).</i>	54
<i>Figure 3-2: The cliff at the beach in Kimmeridge bay (The map is obtained from google maps).</i>	54
<i>Figure 3-3: Rakehead quarry in Accrington (The map is obtained from google maps).</i>	55
<i>Figure 3-4: X-Ray diffraction (XRD) apparatus.</i>	56
<i>Figure 3-5: Typical diffraction pattern of material (PANalytical, 2009).</i>	56
<i>Figure 3-6: Total Organic Carbon (TOC) measurement process.</i>	57
<i>Figure 3-7: Schematic showing different components of SEM instrument (FEI, 2010).</i>	58
<i>Figure 3-8: Mercury Intrusion Porosimetry (MIP) penetrometer assembly.</i>	60
<i>Figure 3-9: Tri-axial test setup and samples prepared for the test.</i>	61
<i>Figure 3-10: Single and multistage triaxial tests (Youn and Tonon, 2010).</i>	61
<i>Figure 3-11: Backscatter scanning electron microscopy (BSEM) images of WS sample.</i>	63
<i>Figure 3-12: Backscatter scanning electron microscopy (BSEM) images of ALP sample.</i>	63
<i>Figure 3-13: Backscatter scanning electron microscopy (BSEM) images of AM sample.</i>	64
<i>Figure 3-14: Backscatter scanning electron microscopy (BSEM) images of KC sample.</i>	64

<i>Figure 3-15: Backscatter scanning electron microscopy (BSEM) images of OC sample. ....</i>	<i>65</i>
<i>Figure 3-16: Backscatter scanning electron microscopy (BSEM) images of D sample. ....</i>	<i>65</i>
<i>Figure 3-17: Mercury cumulative intrusion against mercury pressure for (a) WS, (b) ALP, (c) AM, (d) KC, (e) OC and (f) D samples. ....</i>	<i>67</i>
<i>Figure 3-18: Pore diameter against incremental intrusion for (a) WS, (b) ALP, (c) AM, (d) KC, (e) OC and (f) D samples. ....</i>	<i>68</i>
<i>Figure 3-19: Stages at peak principle stresses in p-q space of (a) WS, (b) KC, (c) OC and (d) D samples. ....</i>	<i>70</i>
<i>Figure 3-20: Ternary plot of mineral composition of shale rocks. The brown envelope encloses the shale-gas and shale-oil resources based on published data from Rickman et al. (2008) and Passey et al. (2010). The black points are the samples used in this research (Figure taken from Valdiviezo-Mijangos and Nicolás-Lopez, 2014). ....</i>	<i>72</i>
<i>Figure 3-21: Correlation between TOC and Young's modulus for Wolfcamp shale (Shukla et al., 2013). ....</i>	<i>72</i>
<i>Figure 3-22: Correlation between uniaxial compressive strength and porosity (Chang et al., 2006). Black points are for the samples tested in this thesis. ....</i>	<i>73</i>
<i>Figure 3-23: Porosity-Young's modulus relationship for shale sample with triaxial test data. ....</i>	<i>74</i>
<i>Figure 3-24: TOC- Young's modulus relationship for shale sample with triaxial test data. ....</i>	<i>74</i>
<i>Figure 4-1: Schematic of compaction assembly (a) before compaction, (b) after compaction. ....</i>	<i>79</i>
<i>Figure 4-2: Photograph of compaction assembly after compaction. ....</i>	<i>80</i>
<i>Figure 4-3: Schematic diagram of MPUCS setup (Guise et al., 2017). ....</i>	<i>82</i>
<i>Figure 4-4: Picture of the MPUCS instrument (Guise et al., 2017). ....</i>	<i>82</i>
<i>Figure 4-5: Figure showing the an example of threshold pressure measurement using the three different methods; <math>P_{th1}</math> using Sutton et al. (2004), <math>P_{th2}</math> using Cranganu and Villa (2005) and <math>P_{th3}</math> using Daniel and Kaldi (2009); the figure is taken from Cranganu and Soleymani (2015). ....</i>	<i>83</i>
<i>Figure 4-6: Schematics of pressure cylinder assembly (a) components of the pressure cylinder, b) full assembly with the sample and compaction assembly. Sizes of some components are exaggerated for the purpose of clarification. ....</i>	<i>84</i>
<i>Figure 4-7: Schematic of Field's metal injection experiment setup. ....</i>	<i>86</i>
<i>Figure 4-8: Photograph of Fields metal injection experiment setup. ....</i>	<i>86</i>

<i>Figure 4-9: ALP-M1 MIP (red) and MPUCS (blue) at 4250 psi net stress ((a) is the mercury saturation vs pressure; (b) is pore diameter vs fractional incremental intrusion) . Red arrow indicates estimate of threshold pressure from MIP. ....</i>	<i>89</i>
<i>Figure 4-10: KC-M1 MIP (red) and MPUCS (blue) at 7000 psi net stress ((a) is the mercury saturation vs pressure; (b) is pore diameter vs fractional incremental intrusion) Red arrow indicates estimate of threshold pressure from MIP. ....</i>	<i>90</i>
<i>Figure 4-11: KC-M1 MIP (red) and MPUCS (blue) at 1000 psi net stress ((a) is the mercury saturation vs pressure; (b) is pore diameter vs fractional incremental intrusion) . Red arrow indicates estimate of threshold pressure from MIP and dashed line indicates the mercury breakthrough recorded. ....</i>	<i>91</i>
<i>Figure 4-12: OC-M1 MIP (red) and MPUCS (blue) at 7000 psi net stress ((a) is the mercury saturation vs pressure; (b) is pore diameter vs fractional incremental intrusion) . Red arrow indicates estimate of threshold pressure from MIP. ....</i>	<i>92</i>
<i>Figure 4-13: OC-M1 MIP (red) and MPUCS (blue) at 1000 psi net stress ((a) is the mercury saturation vs pressure; (b) is pore diameter vs fractional incremental intrusion) . Red arrow indicates estimate of threshold pressure from MIP and dashed line indicates the mercury breakthrough recorded. ....</i>	<i>93</i>
<i>Figure 4-14: : WS-M1 MIP (red) and MPUCS (blue) at 7000 psi net stress ((a) is the mercury saturation vs pressure; (b) is pore diameter vs fractional incremental intrusion) . Red arrow indicates estimate of threshold pressure from MIP. ....</i>	<i>94</i>
<i>Figure 4-15: WS-M1 MIP (red) and MPUCS (blue) at 1000 psi net stress ((a) is the mercury saturation vs pressure; (b) is pore diameter vs fractional incremental intrusion) . Red arrow indicates estimate of threshold pressure from MIP and blue arrow indicates estimate of threshold pressure from MPUCS. Dashed line indicates the mercury breakthrough recorded. ....</i>	<i>95</i>
<i>Figure 4-16: Hydraulic pressure versus time plot to estimate friction. ....</i>	<i>96</i>
<i>Figure 4-17: SY-1 injection pressure vs saturation of the water used to apply injection pressure after removing friction effect. Blue arrow points at the threshold pressure. ....</i>	<i>97</i>
<i>Figure 4-18: 3D Image of SY-1 generated from CT images using ImageJ. The sample is set to be transparent and the metal is shown in white. ....</i>	<i>97</i>
<i>Figure 4-19: SEM images of SY-1 (a) Top segment and (b) bottom segment. ....</i>	<i>98</i>
<i>Figure 4-20: Magnified SEM Images of SY-1(a) Top segment and (b) bottom segment. ....</i>	<i>98</i>
<i>Figure 4-21: Secondary electron microscopy images of fragmented segment of SY-1 (a) Long metal piece (b) Field's metal flowing around the grains. ....</i>	<i>99</i>
<i>Figure 4-22: SY-2 injection pressure vs saturation of the water used to apply injection pressure after removing friction effect. Blue arrow points at the threshold pressure. ....</i>	<i>100</i>



<i>Figure 4-23: 3D image of SY-2 generated from CT images using ImageJ. The sample is set to be transparent and the metal is shown in white. The free hanging dots in the middle of the sample is not metal, they appear when the colour threshold was applied; this is due to low resolution of CT scan used.</i> .....	100
<i>Figure 4-24: SEM images of SY-2 sample.</i> .....	101
<i>Figure 4-25: Magnified SEM Images of SY-2 sample.</i> .....	101
<i>Figure 4-26: Secondary electron microscopy images of fragmented bottom segment of SY-2 (a) Long metal piece (b) Field's metal flowing around the grains.</i> .....	102
<i>Figure 4-27: SY-3 injection pressure vs saturation of the water used to apply injection pressure. Blue arrow points at the threshold pressure.</i> .....	103
<i>Figure 4-28: (a) 3D Image of SY-3 generated from CT images using ImageJ. The sample appeared to be full white because Field's, metal flew in between the aluminium tube and heat shrink of the compaction assembly ;( b) is a slice of CT image set showing Field's metal in the sample.</i> .....	103
<i>Figure 4-29: SEM images of SY-3 sample.</i> .....	104
<i>Figure 4-30: Magnified SEM Images of SY-3 sample.</i> .....	104
<i>Figure 4-31: A zoomed in plot of incremental intrusion fraction against pore diameter for (a) ALP-M1, (b) KC-M1, (c) OC-M1 and (d) WS-M1 samples for both MIP and MPUCS and net stress of 1000 psi except for ALP-M1 sample. Red dashed line is capillary entry pressure using MIP technique and Blue dashed line is capillary entry pressure using MPUCS.</i> .....	108
<i>Figure 4-32: SEM images showing Field's metal flowing around sand grains for samples (a) SY-1, (b) SY-2 and (c) SY-3.</i> .....	109
<i>Figure 4-33: Diagram showing clay particles (orange) and sand grains (grey) (a) before compaction and (b) after compaction. The black arrows shows arching of sand grains ....</i>	110
<i>Figure 5-1: Yield–failure envelope developed by Wong et al. (1997); (b) the elliptical form for the yield–failure envelope proposed by Fisher et al. (2007).</i> .....	115
<i>Figure 5-2: Load path for measuring <math>p^*</math> marked by a red line on the elliptical failure envelope approximated by Fisher et al. (2007).</i> .....	116
<i>Figure 5-3: Samples after mounting them on a flat glass.</i> .....	117
<i>Figure 5-4: Petrothin (a) grinding and (b) polishing machines from Buehler.</i> .....	117
<i>Figure 5-5: Gradual surface polishing steps.</i> .....	117
<i>Figure 5-6: Cubic samples sealing application using Araldite 2011.</i> .....	119
<i>Figure 5-7: Teflon mould and sample after sealing placement</i> .....	119
<i>Figure 5-8: Instron5599 Universal testing machine.</i> .....	120

<i>Figure 5-9: Indentation process in a rock sample.</i> .....	121
<i>Figure 5-10: Sample with indentations impressions on the polished surface. The space between indentations was at least 3mm.</i> .....	121
<i>Figure 5-11: Schematic of load-displacement curve illustrating the indentation program used.</i> .....	122
<i>Figure 5-12: Schematic showing load-displacement data with the important parameters obtained from the plot (Figure taken from Oliver and Pharr (1992)).</i> .....	122
<i>Figure 5-13: schematic showing (a) impression of Vickers indenter with a diagonal <math>d_c</math> indicated with a red arrow and (b) the response of the material during loading and unloading with the parameters required to estimate mechanical properties (Figure taken from Oliver and Pharr (1992)).</i> .....	123
<i>Figure 5-14: Vickers indenter impressions with cracks generated at the corners. The red arrow indicates the crack length, <math>c</math>, used in fracture toughness calculations and <math>a</math> is half of the diagonal length (blue arrow).</i> .....	125
<i>Figure 5-15: Mercury Intrusion Porosimetry (MIP) assembly for (a) mechanical deformation and (b) pore throat characterization.</i> .....	127
<i>Figure 5-16: Load-displacement curves for the successful indentation made on WS sample.</i> .....	128
<i>Figure 5-17: SEM images of the impression made by indents number 2 (left) and 4 (right) taken from WS sample.</i> .....	129
<i>Figure 5-18: Load-displacement curves for the successful indentation made on ALP sample.</i> .....	129
<i>Figure 5-19: SEM images of the impression made by indents number 1-3 (left) and 2-1 (right) taken from ALP sample.</i> .....	129
<i>Figure 5-20: Load-displacement curves for the successful indentation made on AM sample.</i> .....	130
<i>Figure 5-21: SEM images of the impression made by indents number 1 (left) and 5 (right) taken from AM sample.</i> .....	130
<i>Figure 5-22: Load-displacement curves for the successful indentation made on KC sample.</i> .....	130
<i>Figure 5-23: SEM images of the impression made by indents number 3 (left) and 12 (right) taken from KC sample.</i> .....	131
<i>Figure 5-24: Load-displacement curves for the successful indentation made on OC sample.</i> .....	131
<i>Figure 5-25: SEM images of the impression made by indents number 4 (left) and 6 (right) taken from OC sample.</i> .....	131

<i>Figure 5-26: Load-displacement curves for the successful indentation made on D sample.</i>	132
<i>Figure 5-27: SEM images of the impression made by indents number 4 (left) and 12 (right) taken from D sample.</i>	132
<i>Figure 5-28: Load-displacement curves for the successful indentation made on acid exposed WS sample.</i>	137
<i>Figure 5-29: SEM images of the impression made by indents number 2 (left) and 5 (right) taken from acid exposed WS sample.</i>	138
<i>Figure 5-30: Load-displacement curves for the successful indentation made on acid exposed ALP sample.</i>	138
<i>Figure 5-31: SEM images of the impression made by indents number 3 (left) and 4 (right) taken from acid exposed ALP sample.</i>	138
<i>Figure 5-32: Load-displacement curves for the successful indentation made on acid exposed AM sample.</i>	139
<i>Figure 5-33: SEM images of the impression made by indents number 3 (left) and 9 (right) taken from acid exposed AM sample.</i>	139
<i>Figure 5-34: Load-displacement curves for the successful indentation made on acid exposed OC sample.</i>	139
<i>Figure 5-35: SEM images of the impression made by indents number 3 (left) and 12 (right) taken from acid exposed OC sample.</i>	140
<i>Figure 5-36: Load-displacement curves for the successful indentation made on acid exposed D sample.</i>	140
<i>Figure 5-37: SEM images of the impression made by indents number 2-150 (left) and 1-200 (right) taken from acid exposed D sample.</i>	140
<i>Figure 5-38: Volumetric strain at each pressure step for unsealed WS shale rock sample. Data is obtained from MIP test results.</i>	143
<i>Figure 5-39: Volumetric strain at each pressure step for sealed WS shale rock sample. Volumetric strain plotted is for rock and sample together. Data is obtained from MIP test results.</i>	144
<i>Figure 5-40: Volumetric strain at each pressure step for unsealed ALP shale rock sample. Data is obtained from MIP test results.</i>	144
<i>Figure 5-41: Volumetric strain at each pressure step for sealed ALP shale rock sample. Volumetric strain plotted is for rock and sample together. Data is obtained from MIP test results.</i>	145
<i>Figure 5-42: Volumetric strain at each pressure step for unsealed AM shale rock sample. Data is obtained from MIP test results.</i>	145

<i>Figure 5-43: Volumetric strain at each pressure step for sealed AM shale rock sample. Volumetric strain plotted is for rock and sample together. Data is obtained from MIP test results.</i>	146
<i>Figure 5-44: Volumetric strain at each pressure step for unsealed KC shale rock sample. Data is obtained from MIP test results.</i>	146
<i>Figure 5-45: Volumetric strain at each pressure step for sealed KC shale rock sample. Volumetric strain plotted is for rock and sample together. Data is obtained from MIP test results.</i>	147
<i>Figure 5-46: Volumetric strain at each pressure step for unsealed OC shale rock sample. Data is obtained from MIP test results.</i>	147
<i>Figure 5-47: Volumetric strain at each pressure step for sealed OC shale rock sample. Volumetric strain plotted is for rock and sample together. Data is obtained from MIP test results.</i>	148
<i>Figure 5-48: Volumetric strain at each pressure step for unsealed D shale rock sample. Data is obtained from MIP test results.</i>	148
<i>Figure 5-49: Volumetric strain at each pressure step for sealed D shale rock sample. Volumetric strain plotted is for rock and sample together. Data is obtained from MIP test results.</i>	149
<i>Figure 5-50: Young's modulus obtained by nanoindentation versus clay content different shale samples. points encircled in red are outliers. There is an inverse relation between the two paramters but has weak correlation coefficient (Shukla et al.,2013).</i>	150
<i>Figure 5-51: Young's modulus obtained by nanoindentation versus TOC for different shale samples. points encircled in red are outliers. Overall, there is an inverse porpotionality between the two paramters and data is less scattered at higher TOC values (Shukla et al.,2013).</i>	150
<i>Figure 5-52: Young's modulus obtained by nanoindentation versus (quartz+carbonate) for different shale samples. points encircled in red are outliers. There is a direct proportionality between the two paramters(Shukla et al.,2013).</i>	150
<i>Figure 5-53: Young's modulus obtained by microindentation for all samples versus total weight % of clay content. The red arrow indicates the effect of TOC and black arrow indicate the effect of total weight content of quartz &amp; carbonates minerals.</i>	152
<i>Figure 5-54: Estimated Young's modulus using triaxial test against micro-indentation. The dashed black represents 1:1 relationship.</i>	153
<i>Figure 5-55: Relationship between Young's modulus and hardness obtained by micro-indentation technique. This data is for lab dry samples.</i>	153
<i>Figure 5-56: Relationship between Young's modulus and hardness from different authors. Data obtained from Kumar et al. (2012), Corapcioglu (2014) and Shukla et al.(2013).</i>	154

<i>Figure 5-57: Young’s modulus against fracture toughness for shale rocks. Data obtained from Chandler et al. (2016) and Liu (2015).</i> .....	154
<i>Figure 5-58: Relationship between Young’s modulus and hardness from different authors including lab-dry samples and acid-exposed samples results. Data obtained from Kumar et al. (2012), Corapcioglu (2014) and Shukla et al.(2013).</i> .....	155
<i>Figure 5-59: Bar chart describing reduction in Young’s modulus due to acid exposure for a period of one month.</i> .....	156
<i>Figure 5-60: Effect of porosity on preconsolidation pressure of rocks.</i> .....	156
<i>Figure 5-61: Log–log plot of <math>p^*</math> against the product of grain radius and porosity developed by Fisher et al. (2007). Included is the regression line through the data (black). The grey line and equation represent the minimum boundary to the data and were used to calculate <math>p^*</math> values in the simulations presented. Data are from Wong et al. (1997).</i> .....	157
<i>Figure 5-62: Summary of all shale rocks <math>p^*</math> estimated for sealed and unsealed samples.</i> .158	
<i>Figure 5-63: Porosity versus <math>p^*</math> relationship showing a decreasing trend of <math>p^*</math> with increasing porosity.</i> .....	158
<i>Figure 5-64: porosity versus measured <math>p^*</math> (in log-space) for chalk (Blue). Red data points are measure <math>p^*</math> for shale.</i> .....	159
<i>Figure 5-65: Permeability/Porosity relationships for mudrocks (from Yang and Aplin 2010). The red box represent porosity and the corresponding permeability range for the samples used in this test.</i> .....	160
<i>Figure 5-66: Comparison of bulk modulus calculated using Young’s modulus obtained using microindentation technique against bulk modulus obtained from MIP data. Poisson’s ratio is assumed to 0.25 for all samples.</i> .....	161
<i>Figure 5-67: Bulk modulus, calculated using microindentation technique against bulk modulus estimated using MIP data. The blue line represents 1:1 relationship.</i> .....	161
<i>Figure 5-68: Comparison of bulk modulus calculated using <math>E</math> &amp; <math>\nu</math> obtained using triaxial test against bulk modulus obtained from MIP data. There is no triaxial data for ALP and AM samples.</i> .....	162
<i>Figure 5-69: Bulk modulus, calculated using triaxial test results against bulk modulus estimated using MIP data. The blue line represent 1:1 relationship.</i> .....	162
<i>Figure 6-1: Front and side view of sample with proppant pack.</i> .....	165
<i>Figure 6-2: Sample under preparation with ground fracture walls.</i> .....	166
<i>Figure 6-3: Diagram showing visual estimation of sphericity and roundness of proppant (Horiba, 2012).</i> .....	167
<i>Figure 6-4: Proppant embedment test sample.</i> .....	168

<i>Figure 6-5: Experimental setup of fracture closure experiment.</i>	171
<i>Figure 6-6: Picture of the setup used in fracture closure experiment.</i>	171
<i>Figure 6-7: Diagram showing fluid flow directions during conductivity measurement.</i>	172
<i>Figure 6-8: CT images of glass sample taken at 1/3 and 2/3 of the length of the sample. These images for glass sample taken at 500 psi confining pressure.</i>	176
<i>Figure 6-9: Void spaces (blue surfaces) that acts as conduits to fluid flow in glass sample at 500 psi confining pressure. This picture is generated by Avizo.</i>	176
<i>Figure 6-10: Fracture conductivity reduction with time for WS sample at (a) 1000 psi, (b) 2000 psi, (c) 3000 psi and (d) 4000 psi. Fracture conductivity in (c) and (d) is in log-scale.</i>	179
<i>Figure 6-11: Void spaces (blue surfaces) that acts as conduits to fluid flow in WS sample at (a) 1000 psi and (b) 4000 psi. CT images of sample at 1/3 and 2/3 of the length of the sample for (c)1000 psi and (d) 4000 psi confining pressure stages.</i>	181
<i>Figure 6-12: Normalized fracture conductivity of WS sample (in log scale) vs. time for all confining pressure steps.</i>	182
<i>Figure 6-13: WS sample fracture walls after performing the experiment showing impressions of the proppant embedment into fracture wall.</i>	182
<i>Figure 6-14: Fracture conductivity reduction with time for ALP sample at (a) 1000 psi, (b) 2000 psi, (c) 3000 psi and (d) 4000 psi. Fracture conductivity in (d) is in log-scale.</i>	184
<i>Figure 6-15: Void spaces (blue surfaces) that acts as conduits to fluid flow in ALP sample at (a) 1000 psi and (b) 4000 psi. CT images of sample at 1/3 and 2/3 of the length of the sample for (c)1000 psi and (d) 4000 psi confining pressure stages.</i>	186
<i>Figure 6-16: Normalized fracture conductivity of the ALP sample (in log scale) vs. time for all confining pressure steps.</i>	187
<i>Figure 6-17: ALP sample fracture walls after performing the experiment showing impressions of the proppant embedment into fracture wall.</i>	187
<i>Figure 6-18: Fracture conductivity reduction with time for the AM sample at (a) 1000 psi, (b) 2000 psi, (c) 3000 psi and (d) 4000 psi.</i>	189
<i>Figure 6-19: Void spaces (blue surfaces) that acts as conduits to fluid flow in AM sample at (a) 1000 psi and (b) 4000 psi. CT images of sample at 1/3 and 2/3 of the length of the sample for (c)1000 psi and (d) 4000 psi confining pressure stages.</i>	191
<i>Figure 6-20: Normalized fracture conductivity of the AM sample (in log scale) vs. time for all confining pressure steps.</i>	192
<i>Figure 6-21: ALP sample fracture walls after performing the experiment showing impressions of the proppant embedment into fracture wall.</i>	192

<i>Figure 6-22: Fracture conductivity reduction with time for the KC sample at (a) 1000 psi, (b) 2000 psi, (c) 3000 psi and (d) 4000 psi.</i> .....	194
<i>Figure 6-23: Void spaces (blue surfaces) that acts as conduits to fluid flow in KC sample at (a) 1000 psi and (b) 4000 psi. CT images of sample at 1/3 and 2/3 of the length of the sample for (c)1000 psi and (d) 4000 psi confining pressure stages.</i> .....	196
<i>Figure 6-24: Normalized fracture conductivity of the KC sample vs. time for all confining pressure steps.</i> .....	197
<i>Figure 6-25: KC sample fracture walls after performing the experiment showing impressions of the proppant embedment into fracture wall.</i> .....	197
<i>Figure 6-26: Fracture conductivity reduction with time for OC sample at (a) 1000 psi, (b) 2000 psi, (c) 3000 psi and (d) 4000 psi.</i> .....	199
<i>Figure 6-27: Void spaces (blue surfaces) that acts as conduits to fluid flow in OC sample at (a) 1000 psi and (b) 4000 psi. CT images of sample at 1/3 and 2/3 of the length of the sample for (c)1000 psi and (d) 4000 psi confining pressure stages..</i> .....	201
<i>Figure 6-28: Normalized fracture conductivity of OC sample vs. time for all confining pressure steps.</i> .....	202
<i>Figure 6-29: OC sample fracture walls after performing the experiment showing impressions of the proppant embedment into fracture wall.</i> .....	202
<i>Figure 6-30: Fracture conductivity reduction with time for the D sample at (a) 1000 psi, (b) 2000 psi, (c) 3000 psi and (d) 4000 psi.</i> .....	204
<i>Figure 6-31: Void spaces (blue surfaces) that acts as conduits to fluid flow in D sample at (a) 1000 psi and (b) 4000 psi. CT images of sample at 1/3 and 2/3 of the length of the sample for (c)1000 psi and (d) 4000 psi confining pressure stages.</i> .....	206
<i>Figure 6-32: Normalized fracture conductivity of the D sample vs. time for all confining pressure steps.</i> .....	207
<i>Figure 6-33: D sample fracture walls after performing the experiment showing impressions of the proppant embedment into fracture wall.</i> .....	207
<i>Figure 6-34 : Diagram showing the resolution of CT images in the scanning direction.</i> ...	208
<i>Figure 6-35: Diagram showing (a) forces associated with fracture closure and (b) parameters used to determining contact area between sample and proppant.</i> .....	209
<i>Figure 6-36: Failure envelope of (a) WS, (b) KC, (c) OC and (c) D samples with stress state (blue point) for all four confining pressure stages. Green points at which plastic deformation ends and elastic deformation begins.</i> .....	210
<i>Figure 6-37: Failure envelope of (a) WS, (b) KC, (c) OC and (c) D samples with stress state (blue point) for all four confining pressure stages. Preconsolidation pressure was reduced by 50% for all samples.</i> .....	213

<i>Figure 6-38: Failure envelope of (a) WS, (b) KC, (c) OC and (c) D samples with stress state (blue point) for all four confining pressure stages. Preconsolidation pressure was reduced by 75% for all samples.</i>	213
<i>Figure 6-39: Fracture closure experimental results compared with fracture closure model suggested by (Duan et al., 2000) for (a) WS, (b) ALP, (c) AM, (d) KC, (e) OC and (f) D samples.</i>	215
<i>Figure 6-40: Plot of Burger body creep model for various Young's modulus. Red arrow indicates the direction of increasing Young's modulus.</i>	217
<i>Figure 6-41: Fracture conductivity and fracture aperture relationship using experimental data.</i>	217
<i>Figure 6-42: Creep model results against experimental plastic deformation data for WS sample at (a) 1000 psi, (b) 2000 psi, (c) 3000 psi and (d) 4000 psi confining pressure.</i>	219
<i>Figure 6-43: Creep model results against experimental plastic deformation data for KC sample at (a) 1000 psi, (b) 2000 psi, (c) 3000 psi and (d) 4000 psi confining pressure.</i>	219
<i>Figure 6-44: Creep model results against experimental plastic deformation data for OC sample at (a) 1000 psi, (b) 2000 psi, (c) 3000 psi and (d) 4000 psi confining pressure.</i>	220
<i>Figure 6-45: Creep model results against experimental plastic deformation data for D sample at (a) 1000 psi, (b) 2000 psi, (c) 3000 psi and (d) 4000 psi confining pressure.</i>	220
<i>Figure 6-46: Normalized fracture conductivity at different confining pressure stages for Niobrara and Vaca Muerta samples (Iriarte, 2017; Hejazy, 2016) compared to samples tested in this thesis.</i>	222
<i>Figure 6-47: Normalized fracture conductivity at different confining pressure stages for different shale rocks (Alramahi and Sundberg, 2012) compared to samples tested in this thesis.</i>	223
<i>Figure 6-48: Normalized fracture conductivity at different confining pressure stages for different shale rocks (Cho et al., 2013) compared to samples tested in this thesis.</i>	223
<i>Figure 6-49: Diagram explaining cubic law.</i>	224
<i>Figure 6-50: Correlation between normalized fracture conductivity with normalized fracture permeability of proppant packed fracture.</i>	226
<i>Figure 6-51: Correlation between measured proppant embedment at 5000 psi and static Young's Modulus measured from triaxial compression tests on vertical samples (Alramahi and Sundberg, 2012).</i>	227
<i>Figure 6-52: Relationship between (a) Clay plus kerogen content and Young's modulus; (b) Clay content and porosity for different shale samples (Sone and Zoback, 2013). The black points represent the samples used in this research.</i>	228



<i>Figure 6-53: Correlation between Young's modulus and porosity after converting uniaxial compressive strength data presented by Chang et al. (2006) to Young's modulus values. Black points are for the samples tested in this thesis.</i>	228
<i>Figure 7-1: Exaggerated geometry of proppant fracture closure in (a) 2D (b) 3D.</i>	232
<i>Figure 7-2: ELFEN 2D geometry of proppant fracture closure. The black arrows indicates the direction of the face loading applied.</i>	233
<i>Figure 7-3: SR3 model failure envelope for (a) WS sample (b) OC sample (c) KC sample (d) D sample.</i>	235
<i>Figure 7-4: Model geometry with unstructured mesh applied to it.</i>	236
<i>Figure 7-5: Complete fracture closure ELFEN model.</i>	252
<i>Figure 7-6: Elastic complete closure pressure vs. Young's modulus.</i>	253
<i>Figure 7-7: Young's modulus against closure pressure for both elastic simulation and SR3 model simulation.</i>	254
<i>Figure 7-8: fracture closure obtained by experiments and simulations at different elastic modulus against confining pressure for samples (a) WS, (b) KC, (c) OC and (d) D. The error bars represents CT images resolution error.</i>	255
<i>Figure 7-9: Fracture conductivity against fracture aperture for samples (a) WS, (b) KC, (c) OC and (d) D. Data is for experimental results and simulation results at different Young's modulus.</i>	256
<i>Figure 7-10: Comparison between fracture closure simulation results for both elastic and SR3 model simulations for WS sample. The results are at <math>\sigma_c=158</math> MPa for E value of 12.9 GPa</i>	257
<i>Figure 7-11: Comparison between fracture closure simulation results for both elastic and SR3 model simulations for KC sample. The results are at <math>\sigma_c=315</math> MPa for E values of 12.3 GPa and 18.4 GPa.</i>	257
<i>Figure 7-12: Comparison between fracture closure simulation results for both elastic and SR3 model simulations for OC sample. The results are at <math>\sigma_c=340</math> MPa for E values of 13.3 GPa and 20.1 GPa.</i>	258
<i>Figure 7-13: Comparison between fracture closure simulation results for both elastic and SR3 model simulations for D sample. The results are at <math>\sigma_c=328</math> MPa for E values of 26.5 GPa and 39.8 GPa.</i>	258
<i>Figure 7-14: Generated complete fracture closure pressure against depth using porosity-depth curve provided by (Mondol et al., 2005). Data was divided into three porosity ranges; 1.6 % -3.2 %, 3.2% -7.5% and 7.5% -84%.</i>	260

## List of Tables

<i>Table 3-1: Summary of XRD data for each sample.</i> .....	62
<i>Table 3-2: Total organic content (TOC) weight percentage for all samples measured by LECO.</i> .....	62
<i>Table 3-3: Porosity and threshold pressure estimated using MIP technique.</i> .....	66
<i>Table 3-4 : Peak principle stresses before failure and corresponding effective and deviatoric stress of D sample.</i> .....	69
<i>Table 3-5: Peak principle stresses before failure and corresponding effective and deviatoric stress of OC sample.</i> .....	69
<i>Table 3-6: Peak principle stresses before failure and corresponding effective and deviatoric stress of KC sample.</i> .....	69
<i>Table 3-7: Peak principle stresses before failure and corresponding effective and deviatoric stress of WS sample.</i> .....	69
<i>Table 3-8: Summary of mechanical properties of all samples.</i> .....	70
<i>Table 3-9: Summary of samples properties</i> .....	74
<i>Table 4-1 : Summary of the samples used for MPUCS.</i> .....	78
<i>Table 4-2: Samples minerals by percentage weight.</i> .....	78
<i>Table 4-3 : Summary of net stresses used to test the samples.</i> .....	81
<i>Table 4-4: Summary of the results of MPUCS against MIP.* ALP-M1 was test at a net stress of 4,250 psi.</i> .....	96
<i>Table 4-5: Interfacial tension and contact angle for all fluid systems assuming shale is strongly water-wet (Chilingarian et al., 1996).</i> .....	105
<i>Table 4-6: Summary of the results of MPUCS against MIP.* ALP-M1 was test at a net stress of 4,250 psi.</i> .....	106
<i>Table 4-7: Field's metal entry pressure and their corresponding pore diameter for all samples.</i> .....	109
<i>Table 5-1: Summary of famous fracture toughness equations (Moradkhani, 2013).</i> .....	126
<i>Table 5-2: Indentation loads determined for each shale rock.</i> .....	128
<i>Table 5-3 : Summary of parameters obtained from indentation data and the calculated properties using these parameters. This table is for WS and ALP samples.</i> .....	133

<i>Table 5-4: Summary of parameters obtained from indentation data and the calculated properties using these parameters. This table is for AM and KC samples. ....</i>	<i>134</i>
<i>Table 5-5: Summary of parameters obtained from indentation data and the calculated properties using these parameters. This table is for OC and D samples. ....</i>	<i>135</i>
<i>Table 5-6: Summary of mechanical properties estimated using micro-indentation technique for lab-dry samples. ....</i>	<i>136</i>
<i>Table 5-7: Indentation loads determined for all acid exposed shale samples. ....</i>	<i>136</i>
<i>Table 5-8: Summary of mechanical properties estimated using micro-indentation technique for acid exposed samples. ....</i>	<i>137</i>
<i>Table 5-9: Summary of parameters obtained from indentation data and the calculated properties using these parameters. This table is for acid exposed WS, ALP and AM samples. ....</i>	<i>141</i>
<i>Table 5-10: Summary of parameters obtained from indentation data and the calculated properties using these parameters. This table is for acid exposed OC and D samples. ....</i>	<i>142</i>
<i>Table 5-11: Total weight percentage of clay, TOC and quartz &amp; carbonates minerals for all samples. ....</i>	<i>151</i>
<i>Table 6-1: observation noticed after flushing water through the sample for each bonding material tested. ....</i>	<i>169</i>
<i>Table 6-2: Fracture closure samples description. ....</i>	<i>169</i>
<i>Table 6-3: Results of Fancher and Lewis (1933). ....</i>	<i>173</i>
<i>Table 6-4: Properties of the glass sample used to determine initial fracture parameters... </i>	<i>175</i>
<i>Table 6-5: Flow rate steps and their corresponding differential pressures together with fracture conductivity for glass sample at 500 psi confining pressure. ....</i>	<i>175</i>
<i>Table 6-6: Avizo results for glass sample at 500 psi. ....</i>	<i>177</i>
<i>Table 6-7: Initial fracture parameters of WS sample. ....</i>	<i>177</i>
<i>Table 6-8: Results of fracture conductivity test at the end of each confining pressure stage for WS sample. The average conductivity reported is the average at the plateau of the curves shown in Figure 6-10. ....</i>	<i>180</i>
<i>Table 6-9: Avizo results for WS sample for all confining pressure stages. ....</i>	<i>181</i>
<i>Table 6-10: Initial fracture parameters of the ALP sample. ....</i>	<i>183</i>
<i>Table 6-11: Results of fracture conductivity test at the end of each confining pressure stage for the ALP sample. The average conductivity reported is the average at the plateau of the curves shown in Figure 6-14. ....</i>	<i>185</i>

<i>Table 6-12: Avizo results for ALP sample for all confining pressure stages.</i>	186
<i>Table 6-13: Initial fracture parameters of AM sample.</i>	188
<i>Table 6-14: Results of fracture conductivity test at the end of each confining pressure stage for AM sample. The average conductivity reported is the average at the plateau of the curves shown in Figure 6-18.</i>	190
<i>Table 6-15: Avizo results for the AM sample for all confining pressure stage.</i>	191
<i>Table 6-16: Initial fracture parameters of KC sample.</i>	193
<i>Table 6-17: Results of fracture conductivity test at the end of each confining pressure stage for KC sample. The average conductivity reported is the average at the plateau of the curves shown in Figure 6-22.</i>	195
<i>Table 6-18: Avizo results for the KC sample for all confining pressure stages.</i>	196
<i>Table 6-19: Initial fracture parameters of the OC sample.</i>	198
<i>Table 6-20: Results of fracture conductivity test at the end of each confining pressure stage for OC sample. The average conductivity reported is the average at the plateau of the curves shown in Figure 6-26.</i>	200
<i>Table 6-21: Avizo results for the OC sample for all confining pressure stages.</i>	201
<i>Table 6-22: Initial fracture parameters of D sample.</i>	203
<i>Table 6-23: Results of fracture conductivity test at the end of each confining pressure stage for the D sample. The average conductivity reported is the average at the plateau of the curves shown in Figure 6-30.</i>	205
<i>Table 6-24: Avizo results for the D sample for all confining pressure stages.</i>	206
<i>Table 6-25: Principal stresses calculated using stress calculated at the proppant-sample interface. Deviatoric and effective stresses are also estimated using calculated principal stresses.</i>	211
<i>Table 6-26: Plastic threshold stress state and plastic proppant embedment depth associated with it for all four samples.</i>	212
<i>Table 6-27: Plastic threshold stress state and plastic proppant embedment depth associated with it for all four samples at a reduced preconsolidation pressure by 50%.</i>	212
<i>Table 6-28: Plastic threshold stress state and plastic proppant embedment depth associated with it for all four samples at a reduced preconsolidation pressure by 75%.</i>	214
<i>Table 6-29: Summary of parameters for all samples used in (Duan et al., 2000) to estimate fracture closure.</i>	215
<i>Table 6-30: Parameters of the Burger body creep model used to fit experimental data at 1000 psi confining pressure.</i>	218

<i>Table 6-31: Fracture permeability calculated using fracture conductivity at each stage for all samples. Fracture aperture calculated using cubic law, <math>h</math>, is also presented table. ....</i>	225
<i>Table 7-1: Inputs required to define a SR3 failure envelope based on a given tri-axial data. ....</i>	234
<i>Table 7-2: Summary of SR3 model parameters for each samples. ....</i>	234
<i>Table 7-3: Elastic properties of samples used in elastic simulations. ....</i>	236
<i>Table 7-4: Fracture closure elastic simulation results of WS sample from 1000 psi to 4000 psi. ....</i>	237
<i>Table 7-5: Fracture closure elastic simulation results of KC sample from 1000 psi to 4000 psi. ....</i>	238
<i>Table 7-6: Fracture closure elastic simulation results of OC sample from 1000 psi to 4000 psi. ....</i>	239
<i>Table 7-7: Fracture closure elastic simulation results of D sample from 1000 psi to 4000 psi. ....</i>	240
<i>Table 7-8: Fracture closure simulation results of WS sample from 1000 psi to 10,000 psi. Material definition was done based on the elastic properties with varying Young's modulus. ....</i>	241
<i>Table 7-9: Fracture closure simulation results of KC sample from 1000 psi to 10,000 psi. Material definition was done based on the elastic properties with varying Young's modulus. ....</i>	241
<i>Table 7-10: Fracture closure simulation results of OC sample from 1000 psi to 10,000 psi. Material definition was done based on the elastic properties with varying Young's modulus. ....</i>	242
<i>Table 7-11: Fracture closure simulation results of D sample from 1000 psi to 10,000 psi. Material definition was done based on the elastic properties with varying Young's modulus. ....</i>	242
<i>Table 7-12: Fracture closure simulation results of WS sample from 1000 psi to 4000 psi. Material definition was done based on the SR3 parameters obtained earlier. ....</i>	244
<i>Table 7-13: Fracture closure simulation results of WS sample from 1000 psi to 10,000 psi. Material definition was done based on the SR3 parameters obtained earlier with varying <math>\sigma_c</math> and <math>E</math>. ....</i>	245
<i>Table 7-14: Fracture closure simulation results of KC sample from 1000 psi to 4000 psi. Material definition was done based on the SR3 parameters obtained earlier. ....</i>	246
<i>Table 7-15: Fracture closure simulation results of KC sample from 1000 psi to 10,000 psi. Material definition was done based on the SR3 parameters obtained earlier with varying <math>\sigma_c</math> and <math>E</math>. ....</i>	247

<i>Table 7-16: Fracture closure simulation results of OC sample from 1000 psi to 4000 psi. Material definition was done based on the SR3 parameters obtained earlier. ....</i>	<i>248</i>
<i>Table 7-17: Fracture closure simulation results of OC sample from 1000 psi to 10,000 psi. Material definition was done based on the SR3 parameters obtained earlier with varying <math>\sigma_c</math> and E. ....</i>	<i>249</i>
<i>Table 7-18: Fracture closure simulation results of D sample from 1000 psi to 4000 psi. Material definition was done based on the SR3 parameters obtained earlier.....</i>	<i>250</i>
<i>Table 7-19: Fracture closure simulation results of D sample from 1000 psi to 10,000 psi. Material definition was done based on the SR3 parameters obtained earlier with varying <math>\sigma_c</math> and E. ....</i>	<i>251</i>
<i>Table 7-20: Confining pressures at which fracture closes completely found by elastic simulations. ....</i>	<i>252</i>
<i>Table 7-21: Confining pressures at complete fracture closure found by SR3 simulations. .</i>	<i>253</i>

## List of Nomenclature

$p$	Mean effective stress.
$q$	Deviatoric stress.
$p_t$	Tensile strength.
$\sigma_c$	Apparent pre-consolidation pressure.
$p^*$	Critical effective stress.
$Q$	Volumetric flow rate.
$A$	Flow area perpendicular to flow.
$\mu$	Fluid viscosity.
$dL$	Flow path length.
$dP$	Hydraulic potential.
$P_c$	Capillary pressure.
$\sigma$	Interfacial tension.
$r$	Pore throat radius.
$\theta$	Contact between the fluids and rock surface.
$P_b$	Pressure differential due to buoyancy forces.
$\rho_h$	Density of the petroleum.
$\rho_w$	Density of aqueous phase.
$g$	Acceleration due to gravity.
$H$	Vertical height of the petroleum column.
$P_{th}$	Threshold pressure.
$H_{min}$	Minimum petroleum column height for flow to occur.
$Q_w$	Flow rate of the wetting phase.
$Q_{nw}$	Flow rate of the non-wetting phase.
$k_{rw}$	Relative permeability of the wetting phase.
$k_{rnw}$	Relative permeability of the non-wetting phase.
$S_{wc}$	Irreducible water saturation.
$S_{gc}$	Residual oil saturation.
MIP	Mercury intrusion Porosimetry.
DBT	Ductile-brittle transition.
$\sigma_v$	Vertical stress.
$\sigma_h$	Horizontal stress.
$C$	Uniaxial strength of the material.
$\tau$	Shear stress.
$\sigma'$	Normal stress.
$\mu_f$	Coefficient of friction.
$S_o$	Cohesion.
$\varphi$	Angle between normal stress axis and the linear function.
$\sigma_1$	First principal stress.
$\sigma_2$	Second principal stress.
$\sigma_3$	Third principal stress.
$\beta_M$	Shear plane angle.
$T$	Uniaxial tensile strength.
$p_p$	Pore pressure.
CC	Cam-Clay model.

MCC	Modified Cam-Clay model.
SR3	Soft Rock 3 model.
CSL	Critical state line.
$M$	Slope of the critical state line.
$\beta$	Material constants that define the shape of the yield surface.
$n$	Material constants that define the shape of the yield surface.
$g(\theta, p)$	Correction function for the yield function in the deviatoric plane.
$N^\pi$	Material constant.
$\beta^\pi$	Material constant.
$\beta_0^\pi$	Material constant.
$\beta_1^\pi$	Material constant.
$p_c^0$	Initial pre-consolidation pressure.
$\mathbb{P}$	Deviatoric stress tensor.
$J_3$	Third deviatoric stress invariant.
CTC	Compressive triaxial test.
RTE	Reduced triaxial extension.
$\Psi$	Plastic potential function.
$\Delta \mathcal{E}^p$	flow rule.
$\psi$	Dilation angle.
$\delta \varepsilon_{q^p}$	Incremental shear plastic strain.
$\delta \varepsilon_{v^p}$	Incremental volumetric plastic strain.
$\beta^d$	Angle between the strain incremental vector and $p$ -axis.
$p_{to}$	Initial tensile intercept.
$v$	Specific volume.
$\sigma_n$	Normal stress.
$\sigma_o$	Initial normal stress.
$\delta$	Fracture closure.
$\delta_m$	Maximum fracture closure.
$a$	Constant.
$b$	Constant.
$K_{in}$	Initial normal stiffness.
$K_n$	Normal stiffness.
$E$	Young's modulus.
$\nu$	Poisson ratio.
$\bar{\delta}$	Initial average fracture aperture.
$\zeta$	A ratio which reflects surface topography.
$A_r$	Contact area.
COX	Callovo-Oxfordian argillite.
OPA	Opalinus clay.
$G$	Shear moduli.
$K$	Bulk modulus.
$\eta_1, \eta_2$	Viscosity parameters.
$t$	Time.
$k$	Permeability.
$s$	Combined standard variation of peak highest.
$r_c$	Radius of curvature.
$e$	Fracture aperture.



$\phi_0, \phi$	Unloaded and loaded porosity of the buffer.
$P_s$	Swelling pressure.
$P_0$	Atmospheric pressure.
$P_g$	Gas pressure.
$c_r$	Rock compressibility.
$K, K'$	Intrinsic permeability and final dilated permeability.
XRD	X-Ray Diffraction.
TOC	Total organic content.
WS	Whitby mudstone.
KC	Kimmeridge clay.
AM	Accrington mudstone.
$\lambda$	X-ray's wave length.
$d$	Distance between parallel planes of atoms.
$\theta_d$	$\frac{1}{2}$ of the diffraction angle.
$p_{oc}$	Percentage of carbon.
$m_i$	Initial weight.
$m_f$	Weight change after acid treatment.
SEM	Scanning electron microscope.
$V_{pore}$	Sample pore volume.
$V_{total}$	Total mercury volume pumped
$V_{pent}$	Volume of the penetrometer.
$V_{sample}$	Bulk volume of the sample
MPUCS	Mercury porosimeter under confining stress.
$P_{CM}$	Threshold pressures for air-mercury system.
$P_{CR}$	Threshold pressures at reservoir condition.
$D_{\sigma H}$	Depth corresponding to a horizontal stress.
OCR	Overconsolidation ratio.
$H_h$	Hardness.
$P_{max}$	Maximum load applied by the indenter.
$a_c$	Contact area between the indenter and the sample.
$d_c$	Average diagonal length of the impression made by the indenter.
$H_V$	Vickers hardness.
$E_{eff}$	Effective Young's modulus
$A_p$	Projected contact area.
$\beta_i$	Constant which depends on the type of indenter.
$h_c$	Displacement of the indenter recovered when the load is released.
$\epsilon$	Dimensionless constant that depends on the shape of the indenter.
$\nu_i$	Poisson's ratio of the indenter.
$E_i$	Young's modulus of the indenter.
$K_{IC}$	Fracture toughness.
$V$	Change in sample volume.
$V_o$	Initial sample volume.
$Hg_{inc}$	Cumulative mercury intrusion recorded by MIP equipment.
$R$	Grain size.
$W_f$	Proppant pack thickness (fracture aperture).
$W$	Width of the fracture wall.
$C_f$	Hydraulic conductivity of the fracture.

$\rho$	Density.
$D_p$	Particle's diameter.
$v_f$	Velocity of the fluid.
$A_s$	Initial void surface area.
$A_F$	Fracture wall area.
$V_s$	Initial voids volume.
$F$	Force applied on the proppant by the sample.
$F_R$	Reaction force generated by the proppant.
$\sigma_p$	maximum stress at the proppant.
$S_p$	Area of the spherical cap of a single proppant particle in contact with fracture wall.
$N_p$	Number of proppant.
$\sigma_{conf}$	Confining pressure.
$R_p$	Radius of the proppant particle.
$d_p$	Depth of the embedment.
$h$	Fracture aperture.
UCS	Unconfined compressive strength.
CCS	Fracture complete closure stress.

# 1 Chapter I: Introduction

## 1.1 Introduction

Shale comprises around 75% of sedimentary rocks and have a significant impact on fluid flow on a range of scales (Jones and Wang, 1981). Over geological time-scales, shale may act as a barrier to fluid flow allowing overpressures to develop and petroleum to become trapped (Grunau, 1987; Ingram and Urai, 1999). On a shorter time-scale, shale is relied upon to contain radioactive waste and prevent the leakage of CO<sub>2</sub> from geological storage sites (Pusch, 1979; Bachu, 2008). On the other hand, a huge amount of oil and gas is now produced from shale in the USA. The matrix permeability of shale is so low that it is often argued that fluid flow through shale occurs via faults and fractures (Hubbert and Willis, 1957; Palciauskas and Domenico, 1980). Although in many cases, evidence for the presence of shale-hosted fractures or dilational faults within the subsurface remains elusive. Rock mechanics tests can be used to assess the likely stress and pore pressure conditions that result in the development of faults and fractures within shale. However, a massive amount of uncertainty remains regarding the conditions that lead to dilatant fracturing as well as the controls on the closure (self-sealing) of faults and fractures once formed (Cho et al., 2013; Gutierrez et al., 2000). These knowledge gaps create a major uncertainty in a number of safety critical and economically important situations. Examples include:-

- Prediction of the distribution of petroleum and the magnitude of overpressures within the subsurface.
- Assessment of the integrity of radioactive waste disposal sites in long term.
- Prediction of production rates from shale gas resource plays remains difficult to predict.

In this work, multidisciplinary research was conducted aiming to improve the understanding of fluid flow through shale. In particular, it concentrates on investigating the validity of suggested mechanisms of fluid flow through shale and identify their controls. In addition, a geomechanical analysis has been undertaken to understand the link between rock mechanical properties and fluid flow through shale. Key research goals are to:-

- Review evidence from the subsurface (e.g. pore fluid pressures, hydrocarbon distributions, gas production rates from shale rocks etc.) to identify possible mechanisms of fluid flow through shale.
- Conduct laboratory experiments to identify dominant fluid flow mechanisms and their key controls on a range of shale rocks.
- Conduct a series laboratory analysis to understand mechanical properties of shale and how fluids used in wellsite operations such as acid could affect the mechanical properties of shale and hence affect fluid flow through them.
- Conduct Finite Element-based geomechanical modelling of fracture closure based on data obtained from laboratory experiments.

Sample collection and preparation was one of the major challenges faced in this project. Shale rock samples used in the research project were carefully selected to ensure diversity in mineralogy together with geomechanical and petrophysical properties. Laboratory experiments have been developed and conducted to achieve research goals and objectives. All experiment are conducted in Wolfson multiphase laboratory at University of Leeds. Finite element modelling (FEM) was performed using a geomechanical FEM code, ELFEN, developed by Rockfield.

## **1.2 Mechanisms of fluid flow through shale**

Shales act as a seal for over 50% of the world's largest petroleum fields (Grunau, 1987). This shale provided necessary seal and does not allow fluid to flow across it. The possible mechanisms of fluid flow through rocks are related to three main flow regimes;

- Non-deforming matrix flow, where fluid flows through rock without causing deformation to the matrix. Fluid flow is driven by the hydraulic potential or gravity.
- Fluid pressure-related deformation flow, where fluid pressure induces damage to the rock and forms flow pathways.
- Stress-related rock deformation flow, where rock fails to the impact of stress and pore pressure resulting in the formation of faults and fractures. Fractures always have higher permeability than their protolith but faults can act as

barriers or conduits depending on the rheology of the rock and the stress/pore pressure conditions.

All mechanisms of fluid flow through rocks and related flow regimes are summarised in Figure 1-1.

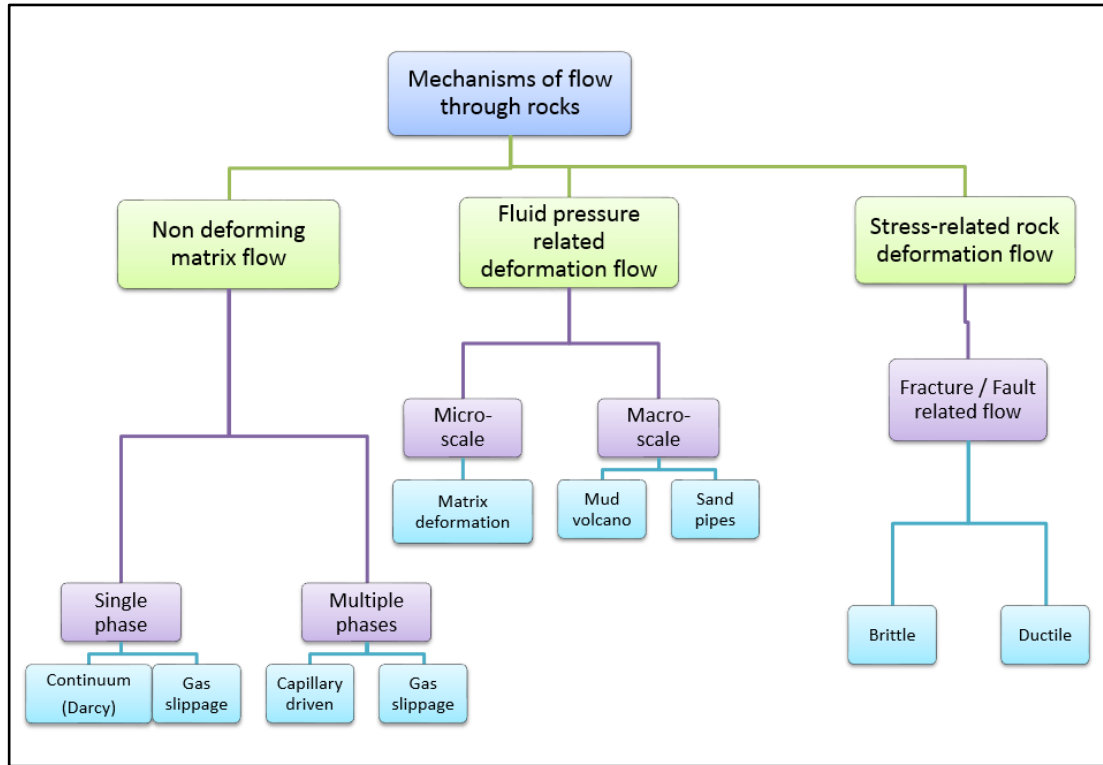


Figure 1-1: Summary of Mechanisms of fluid flow through rocks

### 1.2.1 Non-deforming matrix flow (Single and multiphase flow)

It has been argued that shale caprock leak by two main mechanisms; matrix flow or via faults and fractures (Schowalter, 1979; Watts, 1987; Aplin and Larter, 2005; Teige et al., 2005). Matrix flow can occur in two forms; single phase flow where only one phase is flowing in that media (primarily water in sedimentary rocks) and multiphase flow where more than one phase (water, oil and/or gas) exist in the same media. Single phase flow is characterized by permeability, which is a measure the ability of the rock to transmit fluid through this porous system.

If porous media is initially saturated by brine, then a non-wetting phase such as oil or gas can only enter the pore space if its pressure is higher than that of the non-wetting phase by a value known as the capillary entry pressure. According to the Young-Laplace equation (Young, 1805; Laplace, 1806), capillary entry pressure is

inversely proportional to the pore throat size. It is also related to wettability, which is characterized by contact angle between fluid and the rock and interfacial tension; the latter is basically the force that hold the fluid together in presence of other immiscible fluids.

Wettability is defined as a preference of a certain fluid (in reservoir case; oil, water) to spread on or preferentially cover and wet a solid surface (which in our case is reservoir rock) in presence of other immiscible fluids, which in petroleum systems case are oil, water and gas. It is characterized by the contact angle formed between the drop of fluid and solid rock surface. Petroleum reservoirs caprock are generally considered water-wet but some authors argue that they are oil-wet or have mixed wettability.

Shale rocks have relatively small pore throats which makes their capillary entry pressure very high and not easy to overcome. For flow of petroleum to occur across a water-wet caprock, its phase pressure has to be higher than the phase pressure of the brine by an amount, known as threshold pressure,  $P_{th}$ , to overcome capillary forces (Katz and Thompson, 1986, 1987). This pressure is supplied by the buoyance force exerted by the petroleum column below the caprock. The petroleum column has to be significantly high to exert a pressure higher than capillary entry pressure of the caprock. Fisher et al. (2013) and Dawson et al. (2003) argued, based on the results of Mercury Intrusion Porosimetry (MIP), that shale can provide a capillary seal for a gas column of 0.07-1.4 km and an oil column of 0.165 to 3.6 km (assuming water density 1.1g/cc, gas density 0.2 g/cc and oil 0.7 g/cc). However, MIP results could underestimate capillary pressure due to damage (in a form of microfractures) which will have an impact on petrophysical properties of shale (Holland et al., 2006). Subjecting the sample to confining stress will cause a reduction pore throats (particularly the ones related to microfractures) and hence increase in capillary entry pressure.

### **1.2.2 Stress-related rock deformation flow (Flow through faults and fractures)**

The second mechanism of leakage across petroleum reservoir seals is via conductive faults and fractures. Flow through fractures is subjected to the fact that fracture should remain open to act as a conduit to fluid flow. Gutierrez et al. (2000)

investigated stress-related fracture permeability for a demineralized cemented fracture in shale sample and concluded that fracture never closes completely even when it is stressed above its compressive strength. However, it was suggested that leakage through fracture depends on the behaviour of shale when it is subjected to stress (Ingram and Urai, 1999; Nygård et al., 2006; Fisher et al., 2007). Shale either behaves brittle and forms dilatational faults or behaves ductile where the samples accommodate large strains and lead to closure. Creep, which is a long-term plastic deformation mechanism, of fracture walls also contributes to their closure (Bock et al., 2010). The only way for a closed fracture in shale to open and allow fluid flow is when horizontal stress is reduced. Horizontal stress can be reduced by increasing pore pressure (e.g. Salz, 1977; Whitehead et al., 1987; Teufel et al., 1991; Hettema et al., 2000). Once pore pressure is reduced and horizontal stress increases, fractures tend to self-seal until the sufficient horizontal stress is retained and hence leakage starts again. These are mechanisms of mechanical closure where fractures could also close chemically by precipitation of materials, which is commonly seen in shale rocks (Fisher et al., 2013).

There are many examples in the industry of fracture opening and re-sealing. For example, the North Sea (offshore UK and Norway) has many reservoirs that are capped by shale. Many of these traps were filled to spill but others are dry, which might be a consequence of leakage (Teige and Hermanrud, 2004). However, some fields are filled with petroleum up to their structural spill point despite the caprock having seismic chimneys (e.g. Vik et al., 1998) or hydrocarbon shown within the caprock (e.g. Leith and Fallick., 1997), which is considered a strong evidence of leakage. In addition, many dry or underfilled traps in the same area remain overpressured (particularly Haltenbanken area), which could be an indication that faults or fractures in the caprock had leaked and then re-sealed (Fisher et al., 2013). It is worth mentioning that effective stress on these fractures has to be high enough to force the faults and fractures to close. However, overpressure could reduce effective stress and prevent closure of fractures and hence allow petroleum to leak (Fisher and Kendall, 2008).

### **1.2.3 Fluid pressure-related deformation flow (Pathway dilation)**

It is interesting to note that models for the movement of non-wetting phases through shale vary between industries. In particular, the petroleum industry tends to

argue that non-wetting fluids flow as a result of overcoming capillary forces or due to the presence of faults and fractures (Ingram and Urai, 1999). On the other hand, the radioactive waste disposal industry argue that leakage could occur by matrix deformations induced by pore pressure (Horseman et al., 1999). It is argued that failure induced by pore pressure is by formation of preferential pathways in clay-rich argillaceous formations such as shale rocks (Horseman et al., 1999; Cuss et al., 2014b; Rozhko, 2016; Harrington et al., 2017). This phenomenon is known as “pathway dilation” and this term is widely used in radioactive waste disposal industry.

Formation of dilatational preferential pathways is observed clearly in large scale (e.g. mud volcanos) but still not well understood in micro-scale (Milkov, 2000; Cartwright et al., 2007; Kirkham, 2015). However, theory of pathway dilation in micro-scale is not well developed and all observations and analysis of this phenomenon are done qualitatively using seismic data or pore pressure observations (Horseman, 1999; Cartwright et al., 2007; Cuss et al., 2014a). Further investigation has to be done to identify whether this process could occur at the micro-scale in shale formations.

## **1.3 Research goals**

### **1.3.1 Background**

The aim of this research project is to investigate all possible mechanisms of flowing a non-wetting fluid through shale and identify the controls of each mechanism. Starting with capillary leakage, threshold pressure is normally measured according to standard industrial practise using MIP. MIP is considered as unstressed test because sample is stressed by the mercury until mercury starts to invade the sample (Guise et al., 2017). Rocks are subjected to stress at in situ condition which could be higher than the pressure of mercury before entry in MIP. Tight rocks (e.g. shale rocks) petrophysical properties are normally stress sensitive and measuring them under unstressed condition is questionable (Brace et al., 1968; Guise et al., 2017). Further investigation of the impact of stress on capillary properties is needed to better understand the sealing capacity of shale rocks.

Theory of fracture opening is well-developed and there are models to predict and understand fracture opening available in the literature. However, there are no



theory or model to describe and understand fracture closure. Knowledge of fracture closure in shale is important and will lead to better assessment of caprock integrity and self-sealing. In addition, understanding fracture closure will help estimating hydrocarbon production in tight formation as it will help in understating whether the proppant pack will keep the fracture initiated by hydraulic fracturing open or not. Fracture closure is controlled by three main variables; effective stress, geomechanical properties and fracture morphology (Duan et al., 2000). It is important to highlight that it is difficult to predict fracture morphology in the subsurface. In this research, fracture morphology will be fixed to study the effect of the stress and geomechanical properties.

Geomechanical properties are very important in studying fracture closure in shale. Shales often have a high clay content, which make them soft and have low Young's modulus (Kumar et al., 2012; Shukla et al., 2013). Materials with low Young's modulus are capable to accommodate large strains before they start to undergo plastic deformation. It is important to have a good reliable estimate of geomechanical properties of shale to be able to judge their contribution toward fracture closure.

Measuring Young's modulus, Poisson's ratio and other geomechanical properties has been always a challenge in shale due to anisotropy (Jones and Wang, 1981). In addition, it is difficult to drill core plugs for the mechanical tests due to the laminated nature of shale (Figure 1-2). While retrieving cores from the subsurface, cores tend to get damaged due to the rapid trip speeds particularly if the shale contains gas as it will expand before it can escape due to the low permeability. In this research project, the micro-indentation technique is used to determine Young's modulus and compared against tri-axial test data to investigate its applicability to shale rocks. Effect of some of the fracture fluids on Young's modulus will be investigated as well to find its effect on fracture closure.



*Figure 1-2: Picture showing clearly the delamination problem.*

It is important to highlight that before studying fracture closure on shale, it is very important to understand how they form in the first place. Every rock material has a specific failure envelope that defines its strength and its ability to withstand stress. A typical elastoplastic failure envelope is shown in Figure 1-3 where horizontal axis is the mean effective stress ( $p$ ) and vertical axis is the deviatoric stress ( $q$ ). Depending on the stress state, any deformations with a stress state inside the failure envelope will be elastic and recoverable after removing the stress. On the other hand, any deformations outside the failure envelope will be plastic and unrecoverable even if the stress is removed. The failure envelope consists of two important segments denoted with blue and red colours in Figure 1-3. The blue left segment where rocks experience brittle failure and form discrete slip planes fracture. The red right segment where rocks undergo a ductile failure by shear enhanced compaction. The failure envelope has two intersections with  $p$ -axis,  $p_t$  which is tensile strength of rock and  $\sigma_c$  which is the apparent pre-consolidation pressure of the rock.

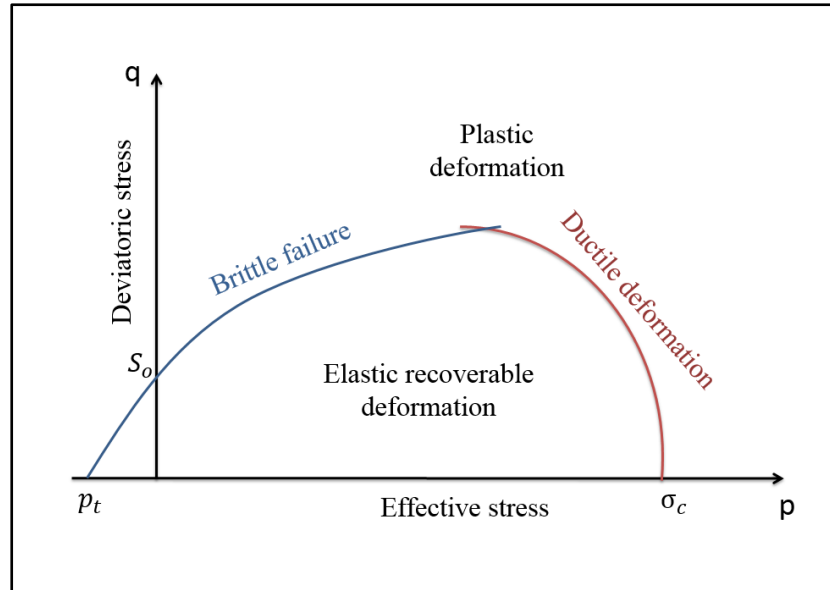


Figure 1-3: Typical failure envelope of rock material.

A good estimation of the failure envelope is always important to be able to predict how a rock will deform under a range of stress conditions. The apparent pre-consolidation pressure ( $\sigma_c$ ) is a very important material property required to construct elastoplastic failure envelopes. However, only a few measurements of the undrained apparent pre-consolidation pressure for shale have been published in the literature (e.g. Petley (1999); Gutierrez et al., 2008). Pre-consolidation pressure ( $\sigma_c$ ) measurement of shale under drained condition takes a long time especially for tight materials such as shale rocks due to their low permeability (Belmokhtar et al., 2018). Generally, during the construction of yield envelopes, pre-consolidation pressure ( $\sigma_c$ ) is assumed because multistage tri-axial compression test can only provide data to the peak point in the  $p$ - $q$  diagram (Figure 1-4). This is because the rock starts to undergo ductile failure beyond the peak point, which cannot be anticipated. Incorrect assumption of this parameter could lead to overestimation or underestimation of rock strength as it is shown in Figure 1-4. In this research, a new simple technique will be introduced to estimate  $\sigma_c$  at hydrostatic condition. The estimated  $\sigma_c$  at hydrostatic condition is known as critical effective stress ( $p^*$ ).

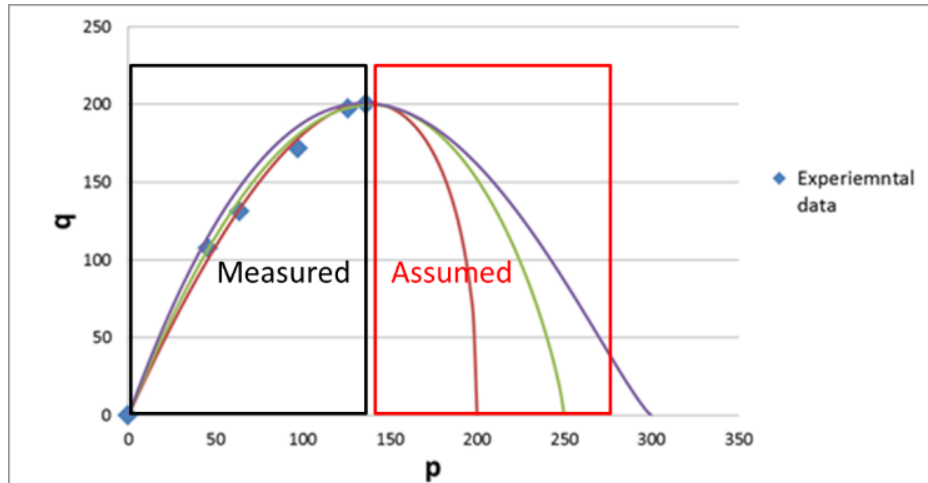


Figure 1-4: Yield envelope in  $p$ - $q$  space, black represented the part constructed using experimental data and red box represents the part assumed.

### 1.3.2 Summary of research goals

Research goals were set to fill the knowledge gaps presented earlier. Research goals can be summarized as:

- Develop a method to measure or estimate threshold pressure of shale under stress to be able to estimate sealing capacity of shale at in situ conditions.
- Investigate the applicability of Micro-indentation as an alternative method to standard tri-axial test for measuring elastic properties of shale.
- Develop a method to measure or estimate preconsolidation pressure of shale to have a better estimate of its strength.
- Investigate experimentally the controls of fracture closure in shale and use the results to simulate the process using FEA techniques.
- Develop a method to investigate the possibility of pathway dilation in shale and how these paths form and propagate in a microscale.

## 1.4 Structure of the thesis

This thesis is consisted of seven further chapters. Potential mechanisms for fluid flow through shale are presented and discussed in **Chapter 2**. Methods used in this thesis to analyse shale samples are described in **Chapter 3**; this chapter also includes a summary of characterization results for each sample. It was important at the beginning to identify the main mechanism of fluid flow through this low permeability rock. The first set of experiments was to investigate the possibility of matrix flow and

deformation flow (pathway dilation) by injecting non-wetting or slightly wetting fluid through shale samples under stress; methods developed and results are presented in **Chapter 4**.

Flow through fractures or dilational faults is a potential mechanism of fluid flow through caprock and requires knowledge of how they form to predict their occurrence. Understanding formation of faults and fractures in any rock requires knowledge of failure envelopes, which are still poorly understood for shale. The apparent pre-consolidation pressure ( $\sigma_c$ ) is one of the basic parameter required to estimate failure envelopes but unfortunately is still elusive. A new simple method to estimate critical effective stress ( $p^*$ ), which is  $\sigma_c$  at hydrostatic condition, is developed and applied in **Chapter 5** to improve understanding of failure envelopes of this particular type of rock. In addition, application of micro-indentation to measure mechanical properties of shale and how some of the fluids used in wellsite's operations impact these properties is also presented in this chapter.

**Chapter 6** will discuss the methodology of studying flow through fractures concentrating on controls of fracture closure and the ability of self-seal in shale when is subjected to stress. Experiments were conducted on several shale sample in the aim of studying the ability of these rocks to self-seal even when fractures are present. In **Chapter 7**, fracture closure was modelled using the finite element method to match experimental results and further study this phenomena. Outcome of this thesis will be discussed and concluded in **Chapter 8**.

## 2 Chapter II: Mechanisms of fluid flow through shale and their controls

### 1.1 Introduction

The theory of fluid flow through rocks is well developed in the literature and authors have identified a range of different mechanisms. Each mechanism is governed by certain conditions and controls. As it was shown in **Chapter 1**, mechanisms of fluid flow through shale are divided into three main regimes; non-deforming matrix flow, pore pressure-related flow involving deformation of the matrix ('pathway dilation') and fault and fracture related flow. All three flow regimes were discussed in details in this chapter.

Non-deforming matrix flow through shale could exist whether the fluid flowing is a single phase fluid or multiphase fluid. Single phase flow in a continuum is characterized by Darcy's Law (Darcy, 1856). A key parameter that controls single phase flow according to Darcy's Law is permeability, which is a measure of the ability of the rock to transmit fluid. However, when two immiscible fluids exist, flow through rock is then controlled by capillary pressure. Once flow is started, relative permeability is a key factor that controls multiphase fluid flow in a continuum. Published data of permeability of shale, capillary pressures and relative permeability are reviewed in details later in this chapter.

Formation of fault and fractures is controlled by the effective stress experienced by the rock as well as its strength. Fractures and faults will initiate and propagate when the effective stress is high enough to cause failure. However, knowledge of geomechanical properties and elastoplastic modelling is essential to be able to anticipate failure. Once fractures are formed, they could remain open and allow fluid flow or re-seal depending on the effective stress across the fracture and the properties of the rock. Effective stress could change by burial, production of hydrocarbon from petroleum reservoirs or tectonic forces. Knowledge of controls of fracture closure is important to be able assess the condition of fractures (open/closed) in deep geological structures. The theory of fracture formation and published data on fracture closure are discussed in details later in this chapter.

The last mechanism to be discussed is pathway dilation, which exists across a wide range of length-scales. It can be observed at the large-scale in structures such as mud volcanos and magma intrusions but still not proven in a small-scale such as caprock and radioactive waste repositories. Pathway dilation will occur when gas pressure reaches a pressure called dilation threshold and will continue until gas pressure reduces below the dilation threshold (Navarro, 2009; Tawara et al., 2014). The formation of preferential pathways is believed to increase intrinsic permeability of the seal when gas pressure exceeds a certain gas breakthrough pressure (Tawara et al., 2014). This pressure is normally lower than capillary threshold pressure. All publications about evidence of pathway dilation are discussed later in this chapter.

## 1.2 Single phase flow through shale

### 2.1.1 Darcy's Law

Darcy (1856) developed a law for single phase fluid flow through porous media (Figure 2-1). The law is valid for laminar flow at steady-state conditions. Darcy's single phase fluid flow can be calculated using the following equation:

$$Q = \frac{-kA}{\mu} \frac{dP}{dL} \quad (2-1)$$

where:  $Q$  is the volumetric flow rate ( $\text{cm}^3/\text{s}$ ),  $A$  is the flow area perpendicular to flow ( $\text{cm}^2$ ),  $k$  is the permeability (Darcy),  $\mu$  is the fluid viscosity (Pa.s),  $dL$  is the flow path length (cm) and  $dP$  is difference in hydraulic potential (atm.). The "-" sign indicates that flow direction is from high pressure to low pressure.

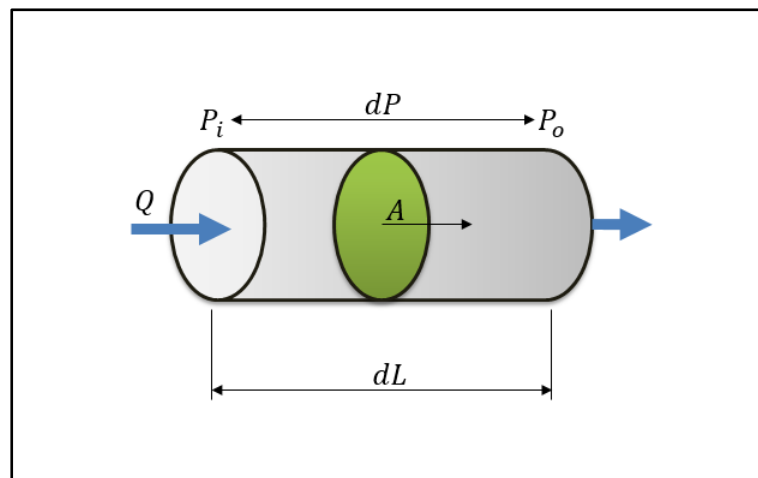


Figure 2-1: Sketch showing parameters of Darcy's equation to calculate permeability of a porous medium

### 2.1.2 Published data on the permeability of shale

The porosity of shale reduces with increasing burial depth due to mechanical and chemical compaction. Mondol et al. (2007) gathered published data of porosity-depth curves for shales and argillaceous sediments and compared them against experimental compaction data on synthetic samples with different kaolinite/smectite ratios (Figure 2-2). Yang and Aplin (2004) also have modelled the void ratio of shale rocks/mudrocks as a function of effective stress, and found that the clay content (defined by percentage of particles less than 2  $\mu\text{m}$  in size) was an important parameter. It was found that porosity of shale at a specific effective stress increases with increasing clay content as it is shown in Figure 2-3.

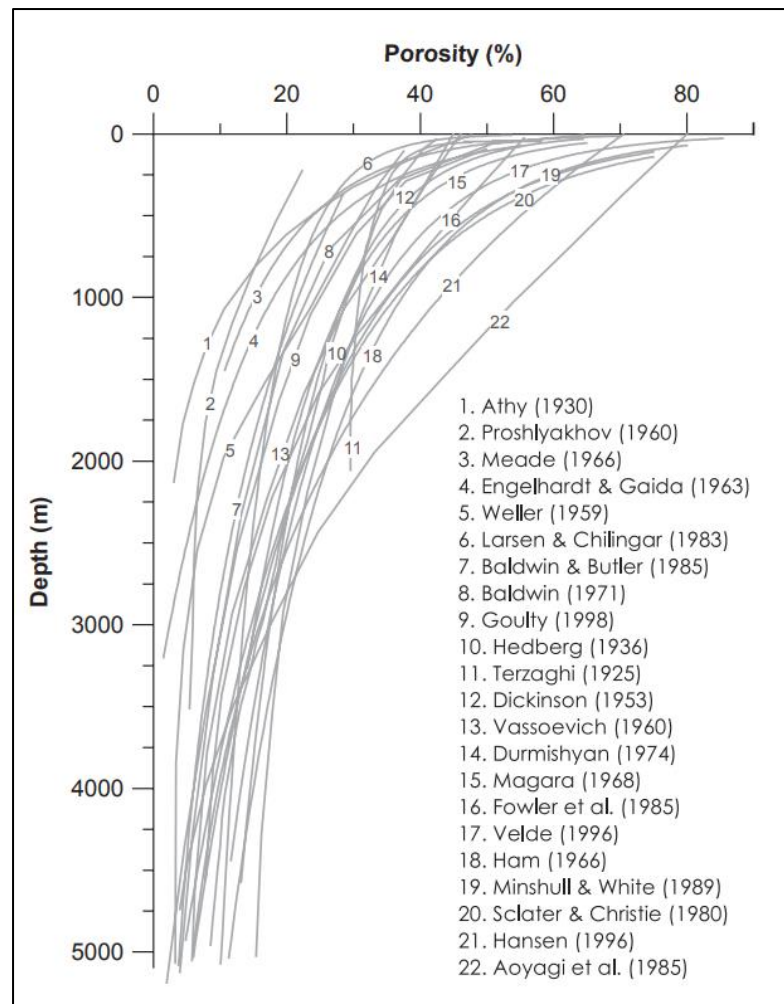


Figure 2-2: Published data of porosity-depth curves for shales and argillaceous sediments for shale (Mondol et al., 2007).



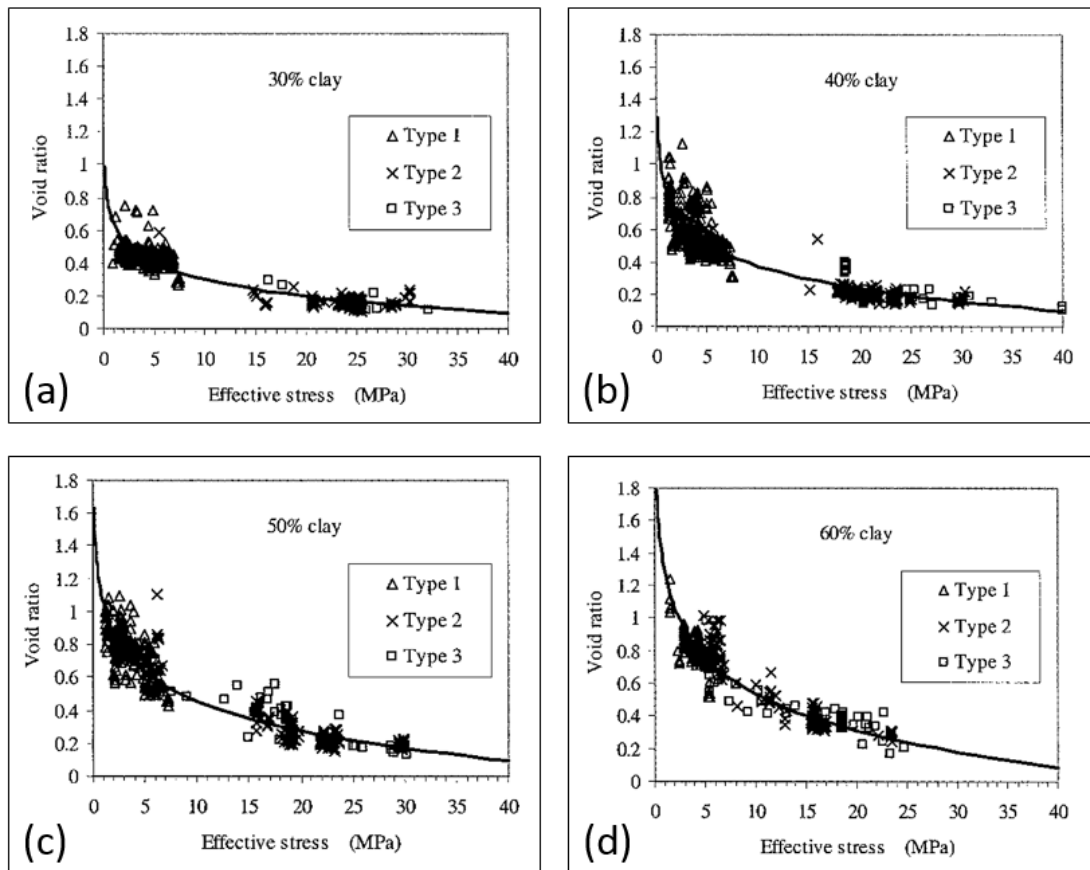


Figure 2-3: Void ratio–effective stress relationship of actual data compared to model. Data for clay ranges (a) 25–35%; (b) 35–45%; (c) 45–55%; (d) 55–65% (Yang and Aplin, 2004).

Although less clear, as variation of permeability is large (Figure 2-5), permeability is also a function of clay content (Figure 2-6), with lower permeabilities with increasing clay content (Neuzil, 1994; Yang and Aplin, 2010). Yang and Aplin (1998) derived an empirical relationship based on real data and found that rocks with more clay tend to have smaller pore sizes and lower permeability (Figure 2-4). A more theoretical description for compaction behaviour is given by Revil et al. (2002), again the clay content affects the pore size distribution and hence permeability. Actual measurements confirm the dependency of permeability on pore size distribution and clay content, and regressions relating these parameters have been published (Yang and Aplin, 2010).

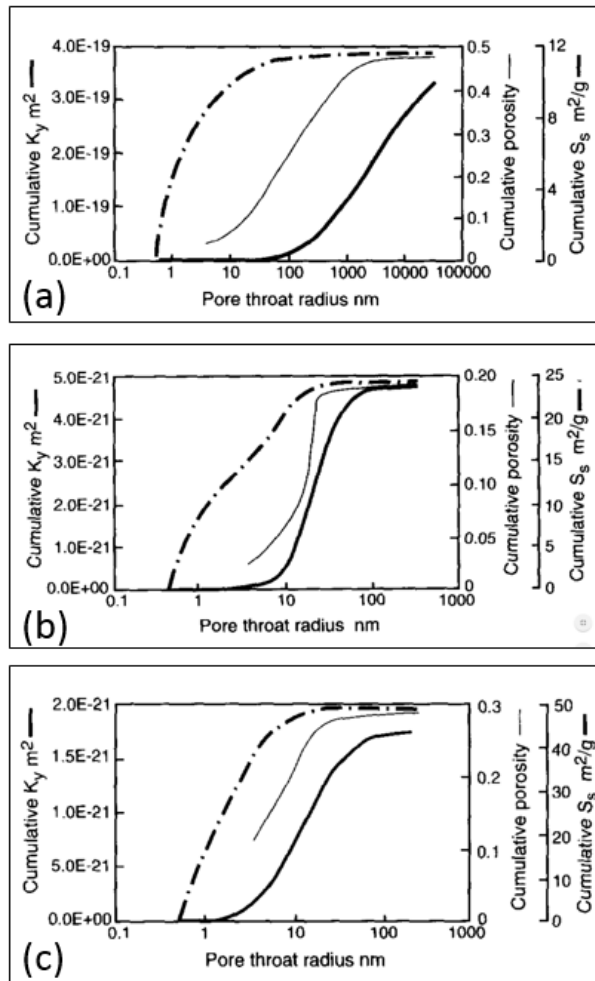


Figure 2-4 Porosity (thin line), cumulative specific surface area,  $S_s$  (dot-dash line) and permeability (thick line) of different mudstones at different effective stresses. Samples used have (a) 36.8% clay content at 6.4 MPa effective stress, (b) 51.8% clay content at 20.5 MPa effective stress and (c) 72.2% clay content at 7.4 MPa effective stress (Yang and Aplin, 1998).

The relationships between porosity, permeability and stress described above are no longer valid when diagenesis plays a role. Chemical diagenesis becomes important and governs compaction process with increasing depth and temperature (Kalani et al, 2015; Ramm, 1992; Ramm, 1994; Giles, 1997). Diagenesis can result in porosity decrease, which will consequently reduce permeability. Reducing permeability will reduce water expulsion rate, which may lead to overpressure generation. Chemical diagenesis involves dissolution of material at grain contacts “pressure solution” and its re-precipitation on grain surfaces adjacent to free pore space (e.g. Heald, 1956; Thompson, 1959). Illitization, which is the reaction of clay minerals (e.g. conversion of smectite to illite) is the most important and well documented chemical diagenetic

process that could occur in shale (Boles and Franks, 1979; Freed and Peacor, 1989; Nadeau et al., 2002; Thyberg et al., 2010; Kalani et al., 2015.).

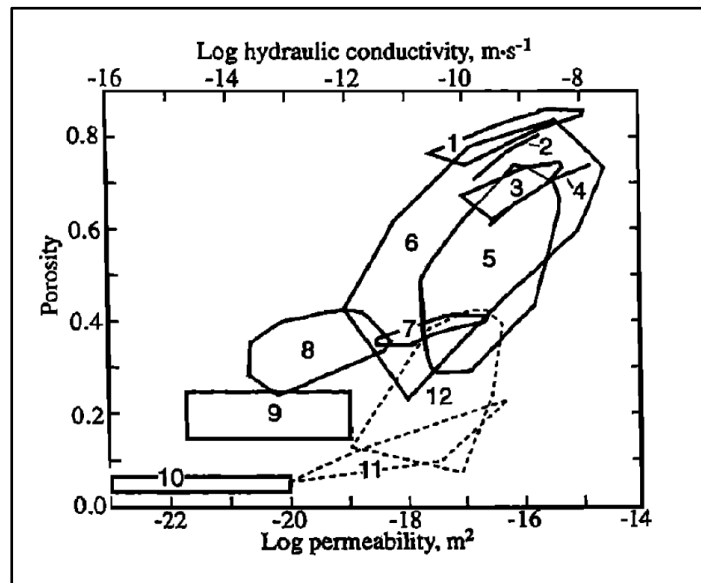


Figure 2-5 : Permeability data as collected by (Neuzil, 1994). Laboratory-derived permeability vs. porosity data for a variety of natural argillaceous media. Permeability is shown along the lower horizontal scale: the corresponding hydraulic conductivity to water a room temperature is shown along the upper horizontal scale.

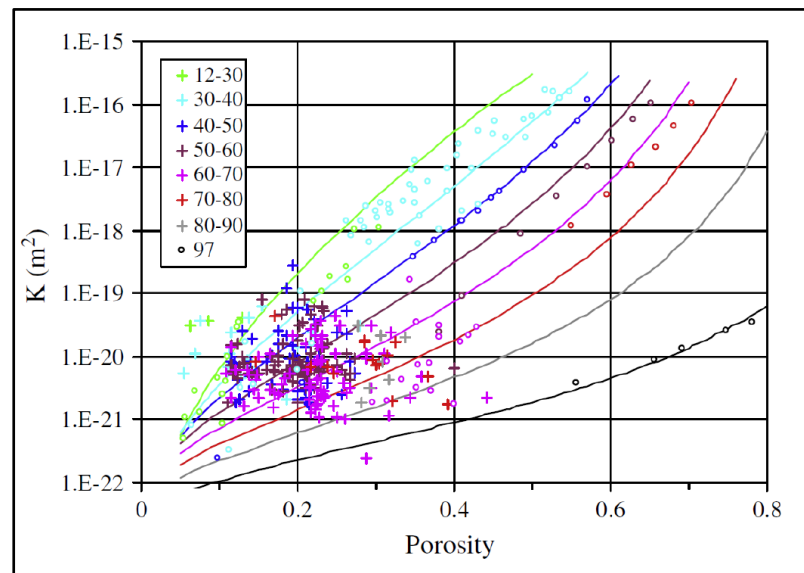


Figure 2-6: Permeability/Porosity relationships for mudrocks from (Yang and Aplin, 2010). The legend shows the range of clay content for each band. The curves correspond to the middle value of clay contents of the band with the same colour.

## 1.3 Multiphase flow through shale

### 2.1.3 Capillary pressure

In all petroleum systems, the multiphase flow regime is active. This flow regime is controlled by the pressures generated when two immiscible fluids are present within the porous medium. This pressure is known as capillary pressure,  $P_c$ , which is defined as the phase pressure difference between the non-wetting (oil/gas) and the wetting phase (brine) required for the non-wetting phase to pass through a pore throat. Young (1805) and Laplace (1806) derived a relation between capillary pressure and pore throat by relating them to fluid properties. The Young-Laplace equation is given by:

$$P_c = \frac{2\sigma \cos \theta}{r} \quad (2-2)$$

where:  $P_c$  is in dynes/cm<sup>2</sup>;  $\sigma$  is the interfacial tension (dynes/cm) between the two phases;  $r$  is pore throat radius ( $\mu\text{m}$ ) and  $\theta$  is the contact between the fluids and rock surface. The Young-Laplace equation was derived using the assumption that the capillary is a single tube with constant radius,  $r$  (Washburn, 1921). However, a porous rock will have a whole range of pore radii represented by a pore-size distribution. To account for the effect of pore size variation within a porous media, Katz and Thompson (1986, 1987) introduced threshold pressure,  $P_{th}$ , which is the pressure required to form a continuous network of non-wetting fluid through a porous medium.

The two fluid properties included in the Young-Laplace equation are physically a measure of wettability and interfacial tension. Interfacial tension is temperature sensitive and it decreases for both oil and water with increasing temperature (Hough et al., 1951). For oil-water system, interfacial tension ranges between 5-35 dynes/cm while for gas system it ranges between 20-70 dynes/cm. However, it is worth mentioning that interfacial tension of gas is pressure sensitive and is around 70 dynes/cm at room pressure but 30 dynes/cm at reservoir conditions (Jennings, 1967; Hough et al., 1951).

Wettability is characterized by contact angle, which is the angle formed by a drop of fluid and rock surface measured through the wetting phase. A strongly water-wet rock will have a contact angle of 0° where a strongly oil-wet rock contact angle could reach 180° (Berg, 1975). Shale is normally assumed to be water-wet (Hubbert,

1953). This is because it has not been in contact with hydrocarbons so that its wettability has not been altered. However, some authors argue that shale can be oil-wet or have mixed wettability (Aplin and Larter, 2005; Hermanrud, 2005; Teige and Hermanrud, 2005; Borysenko et al., 2009). The assumption of oil-wet shale will imply that oil could flow through shale without overcoming a capillary entry pressure (Fisher et al., 2013).

#### 2.1.4 Capillary pressure and relative permeability

The phase pressure required for fluid to overcome capillary pressure in a multiphase flow system is mainly generated by buoyancy. In a petroleum system, hydrocarbons are always less dense than brine, which means that hydrocarbons will have a buoyancy force exerted by the fluid column in the reservoir. The pressure due to buoyancy can be calculated using the Bernoulli equation (Berg, 1975):

$$P_b = gH(\rho_w - \rho_h) \quad (2-3)$$

where  $P_b$  is pressure differential due to buoyancy forces,  $\rho_h$  is density of the petroleum,  $\rho_w$  density of aqueous phase,  $g$  the acceleration due to gravity and  $H$  the vertical height of the petroleum column. Gravity and unit conversion to field units are approximated in a conversion factor of 0.433 which makes the equation to be:

$$P_b = 0.433H(\rho_w - \rho_h) \quad (2-4)$$

where: densities are in  $g/cm^3$ , and  $H$  in feet (Schowalter, 1979; Watts, 1987).

Considering a water-wet porous media, the threshold pressure, buoyancy force,  $P_b$ , should be higher than the threshold pressure,  $P_{th}$ , for fluid flow to occur. In other words, the petroleum column should be sufficiently high to exert enough fluid pressure to overcome threshold pressure. The minimum petroleum column height for flow to occur,  $H_{min}$ , can be calculated by setting  $P_b = P_{th}$  in equation (2-4), which yields:

$$H_{min} = \frac{P_{th}}{0.433(\rho_w - \rho_h)} \quad (2-5)$$

A shale caprock will only act as a seal when the buoyancy pressure exerted by the petroleum column is less than its threshold pressure,  $P_{th,s}$ . Provided that differential pressure is high to allow flow, flow rates can be calculated using a multiphase adaptation of Darcy's Law (Muskat, 1937; Abaci et al., 1992):

$$Q_w = \frac{-k_{rnw}k_{rw}A}{\mu} \frac{dP}{dL} \quad (2-6)$$

$$Q_{nw} = \frac{-kk_{rnw}A}{\mu} \frac{dP}{dL} \quad (2-7)$$

where:  $Q_w$  and  $Q_{nw}$  are the flow rates for the wetting and non-wetting phases respectively, and  $k_{rw}$  and  $k_{rnw}$  are the relative permeability of the wetting phase and non-wetting phase respectively. Relative permeability is the ratio between phase permeability and absolute permeability. Figure 2-7 shows a plot of relative permeability of each phase versus water saturation. There are limits in water saturation at which one phase will stop flowing, known as irreducible water saturation,  $S_{wc}$ , and residual oil saturation,  $S_{gc}$ , respectively (Figure 2-7).

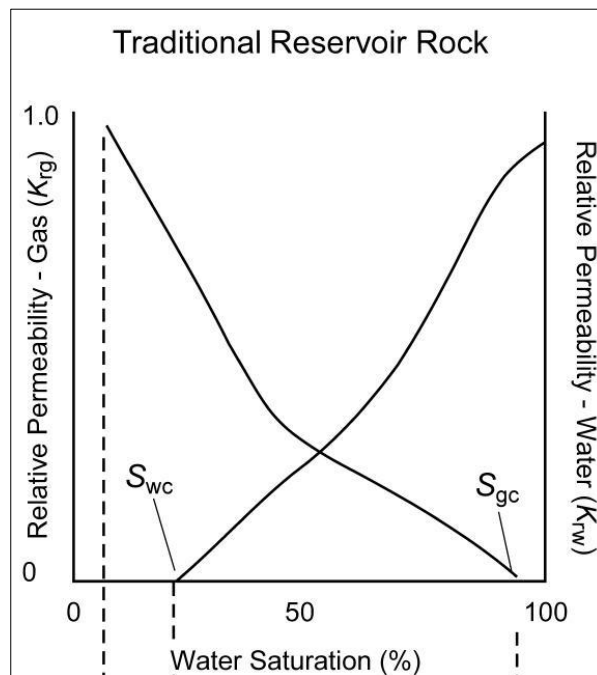


Figure 2-7: Typical relative permeability curves for a high permeability rock (Shanley, 2004).

Shanley (2004) introduced a theory of permeability jail and suggested that in low permeability porous media such as shale, relative permeability behaves differently than high permeability media. In particular, there are water saturation cut-off limits where both phases (wetting and non-wetting) are no longer mobile and relative permeability is zero; a rock with phase saturations between these limits is said to be in a “permeability jail” because neither phase can flow (Figure 2-8). This suggests that at these water saturations, low permeability rocks could act as a total barrier to flow making overpressures more likely to develop. However, this theory is not proven and relative permeability values could be very low in the ‘permeability jail’ region and not necessarily zero.

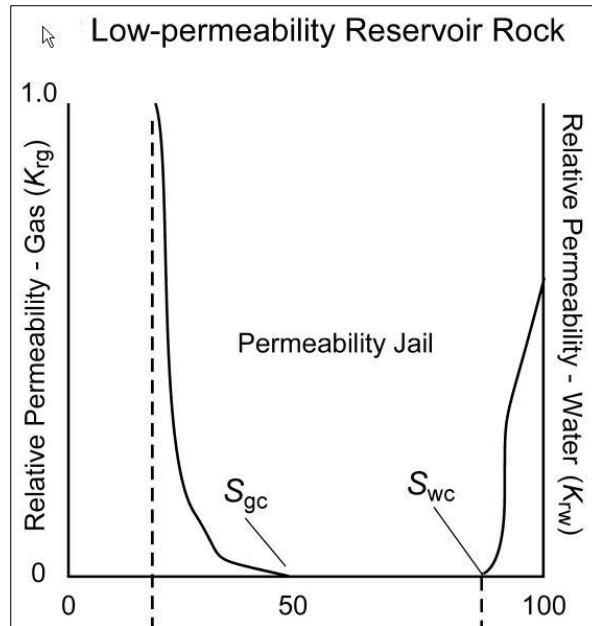


Figure 2-8: Relative permeability curves for a low permeability rock (Shanley, 2004).

## 1.4 Fault and Fracture related flow

### 2.1.5 Formation of faults and fractures

#### 2.1.5.1 Deformation mechanisms

Many experiments have been conducted to study the behaviour of rocks under compressive stress (e.g. Brace, 1964; Brady, 1969a; Brady, 1969b). Rocks will initially deform elastically when loaded, with any deformation of the structure recoverable during unloading. However, under sufficient loading, a rock will reach a yield point beyond which plastic deformation will occur. Plastic deformation is irreversible, so the rocks never return to their initial condition even after unloading (Figure 2-9). In this section, different mechanisms of plastic deformation will be described along with a discussion of the models which have been developed to describe plastic deformation in the literature.

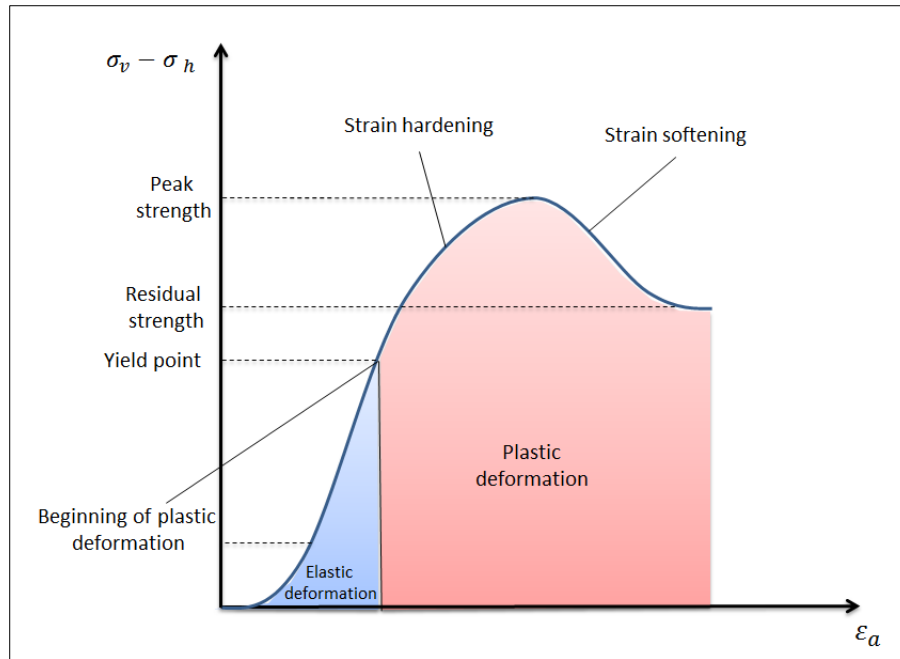
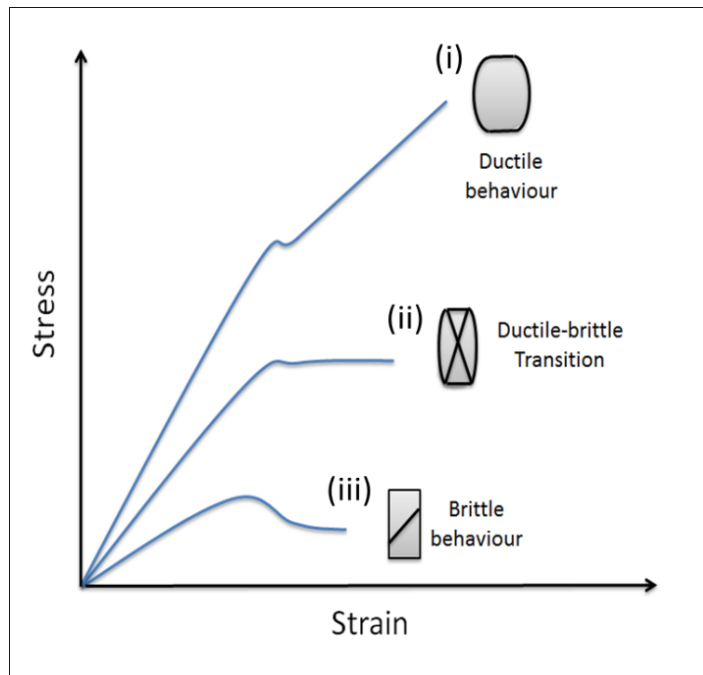


Figure 2-9: Behaviour of rock in stress-strain curve during bi-axial stress application.

Plastic deformations can be brittle or ductile depending on the properties of rock and the stress conditions (Nygård et al., 2006). Rock fails in a brittle manner when it is at low effective stress. The failure mode changes into ductile failure with increasing confining pressure. The brittle failure results in strain localization and formation of discrete slip planes. The stress drop following yield indicates that this is a strain softening process (Fisher et al., 2007). In ductile deformation, no discrete slip planes are developed and most of the strain is accommodated within the sample. A transitional regime exists between brittle and ductile failure called the Ductile-Brittle Transition (DBT) in which deformation occurs in multiple slip planes (Fisher et al., 2007). The three behaviours are summarized in Figure 2-10.





*Figure 2-10: Diagram showing typical stress–strain curves obtained during sandstone deformation experiments. Included on the plot are sketches showing the typical form of the deformed samples following the experiments. Curve (i) is typical of rocks that deformed by distributed cataclastic flow. Curve (ii) is typical of rocks deformed at the brittle–ductile transition. Curve (iii) is typical of rock deformed by brittle failure. The diagram is based on (Griggs and Handin, 1960) and taken from (Fisher et al., 2007).*

Faults and fractures exist in all geological layers at different scales depending on the burial history and circumstances. These are classified according to their mechanism of formation into three different modes; mode I (opening), mode II (sliding) and mode III (tearing) (Mandl, 2005). These modes can occur either separately or in combination of two or more modes. Mode I is considered a fracture whereas other modes are closer to being faults rather than fractures. All three modes are shown and described in Figure 2-11. In terms of definition, the two phenomena are quite different but they share the same literal meaning of discontinuities in rocks. Faults can be defined as a shear fracture or fracture zone along which there has been a visible shear displacement, from a few mms to a few kilometres in scale (Bock et al., 2010). Fractures can be generally described as planes of separation in a solid material with no shear offset (Bock et al., 2010). In other words, it is division of rocks into separate pieces mainly caused by stress exceeding the rock strength or other behaviours related to the elastoplastic behaviour of rocks.

Mode I, described as opening mode, occurs when a tensile stress is applied perpendicular to the plane of the crack. The closest example to describe this mode is a hydraulic fracture. The sliding mode (mode II) occurs when a shear stress is applied parallel to the plane of the crack and perpendicular to crack face forcing the two segments to slide on each other. Finally, mode III occurs when shear stress is applied perpendicular to the crack plane and parallel to the face of the crack.

Fractures can be classified based on the mechanical process causing the fractures as follows (Figure 2-12) (Mandl, 2005):

- 1- Tension Fracture: Brittle fracture in a tensile stress field with minor effective principle stress  $\sigma_v < 0$  which rarely occurs naturally.
- 2- Extension Fracture: Brittle fracture in a compressive stress field with major effective principle stress  $\sigma_v \gg 0$ . This type of fracture is very common and only occurs at relatively small effective stress  $\sigma_h = 0$ .
- 3- Shear Fracture: Brittle or ductile fracture characterized by either the formation of a discrete shear plane or by compaction respectively. Discrete shear planes are often developed after the formation of numerous extension fractures.

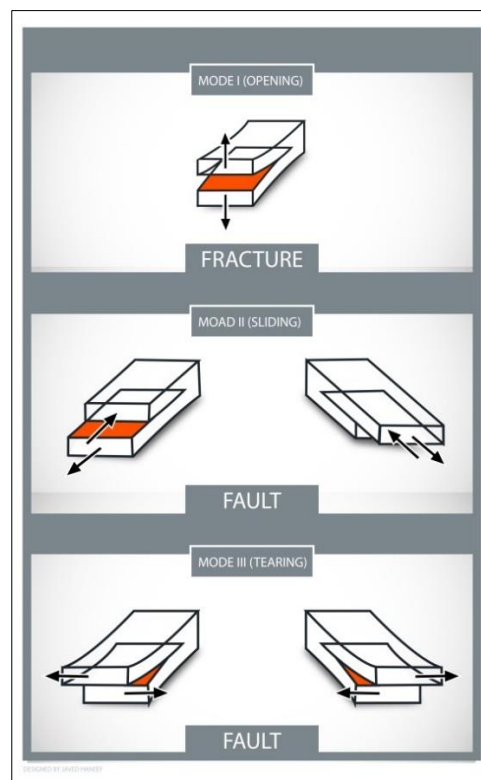


Figure 2-11: Fractures formation modes.

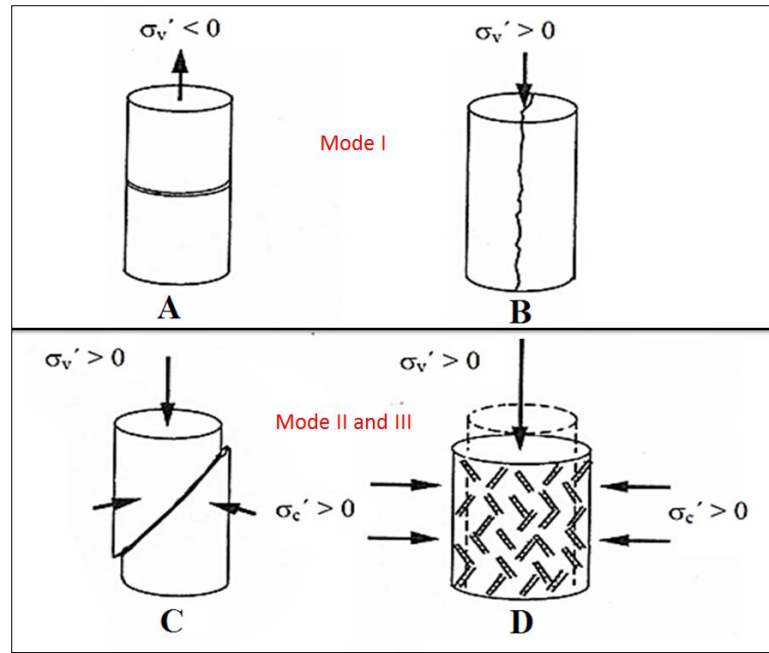


Figure 2-12: Types of rock failure. A is a tensile fracture, B is an extension fracture and C&D are shear fractures by formation of shear plane and shear-enhanced compaction respectively (Mandl, 2005).

A stress-strain diagram of each fracture type is shown in Figure 2-13. Figure 2-13-A corresponds to tensile and extension fractures (Figure 2-13 A&B) under uniaxial tension and uniaxial compression respectively. This behaviour is a linear elastic behaviour where the sample fails immediately after the elastic limit. In this case, the stress value at failure is considered the uniaxial tensile or compressive strength of the sample. Most natural rocks do not exhibit linear elastic behaviour when subjected to stress. Samples usually undergo inelastic deformations after the yield point before reaching the peak stress where failure occurs.

Figure 2-13-C shows typical behaviour of a sample under lateral and axial compressive stress, which is associated with a brittle shear failure. The sample undergoes strain softening after the peak stress, sample load –carrying capacity reduces due to formation of shear fractures. If lateral and axial compressive stress increases, the sample will experience strain hardening only and strain softening will be suppressed (Figure 2-13-D) after the yield point. Samples will experience distortion and grain rearrangement due to failure by shear enhanced compaction, which is a macroscopically ductile type of behaviour but at the grain-scale it often involves brittle processes.

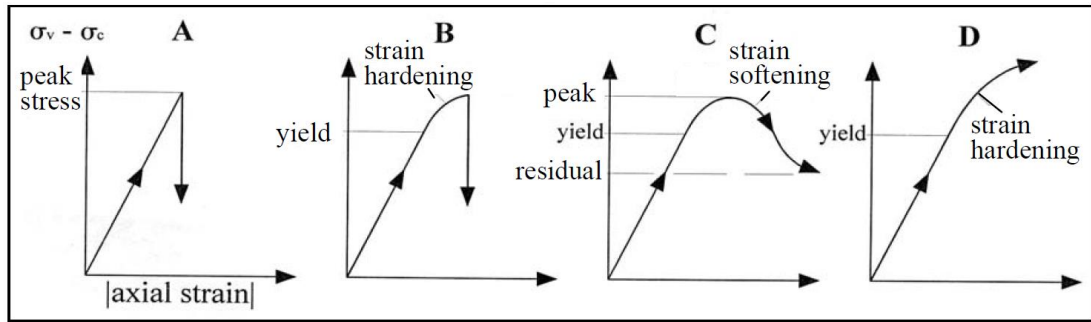


Figure 2-13: Stress-strain diagram for each type of failure. Curve A&B correspond to tensile and extension fracture where curve C&D correspond to shear failure either by formation of a shear plane (Curve C) or by shear enhanced compaction (Curve D) (Mandl, 2005).

### 2.1.5.2 Brittle tensile and extension fractures

Extension and tensile fractures are brittle type of fractures formed in compressive or tensile stress field with high effective stress ( $\sigma_v \gg 0$ ) (Bock et al., 2010). It forms parallel or perpendicular to the maximum principal stress  $\sigma_v$  depending whether it is compressive or tensile stress field. Extension and tensile fractures form when the major effective stress reaches a critical value of:

$$\sigma_v \rightarrow -C \quad (2-8)$$

where:  $C$  is the uniaxial strength of the material.

Extension and tensile fractures initiate due to micro-scale tensile stress induced by the stress applied. According to the mechanism of tensile stress induction, formation of extension fractures can be described using four models, as illustrated in Figure 2-14 (Mandl, 2005) :

1. Wing crack model.
2. Void model.
3. Grain contact model.
4. Elastic mismatch model.

These models are discussed in details in **Appendix B**.

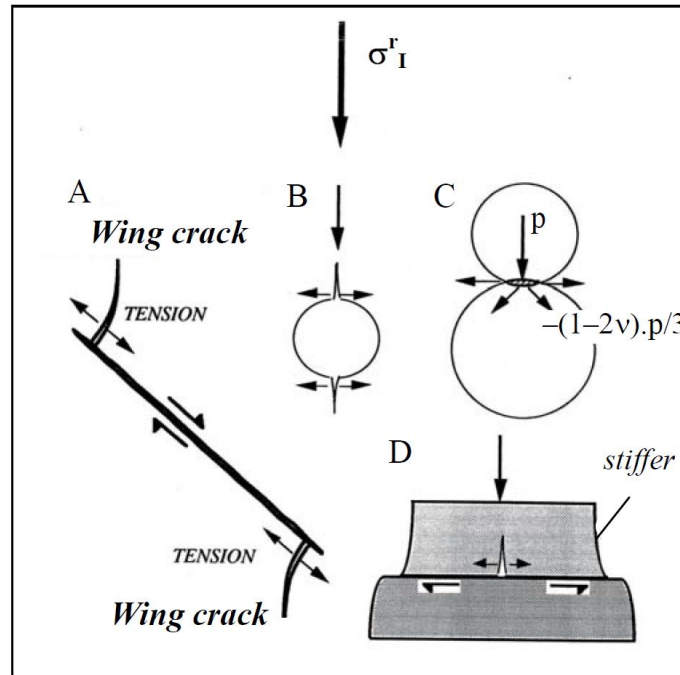


Figure 2-14: Extension fracture models (A; Wing crack model, B; Void model, C; Grain contact model and C; Elastic mismatch model) (Mandl, 2005).

### 2.1.5.3 Brittle shear fractures

Shear failure in the brittle regime has been modeled by several different authors. The most well-known of which is the Mohr-Coulomb criterion. The Mohr-Coulomb criterion is based on the assumption of a linear function (Failure envelope) (Fjaer, 2008):

$$|\tau| = S_o + \mu_f \sigma' \quad (2-9)$$

where:  $\tau$ ,  $\sigma'$  are shear and normal stresses at the failure plane respectively,  $\mu_f$  is the coefficient of friction and  $S_o$  is cohesion.

The coefficient of friction is the slope of the linear function and can be defined using the angle between normal stress axis and the linear function ( $\varphi$ ) above as:

$$\tan \varphi = \mu_f \quad (2-10)$$

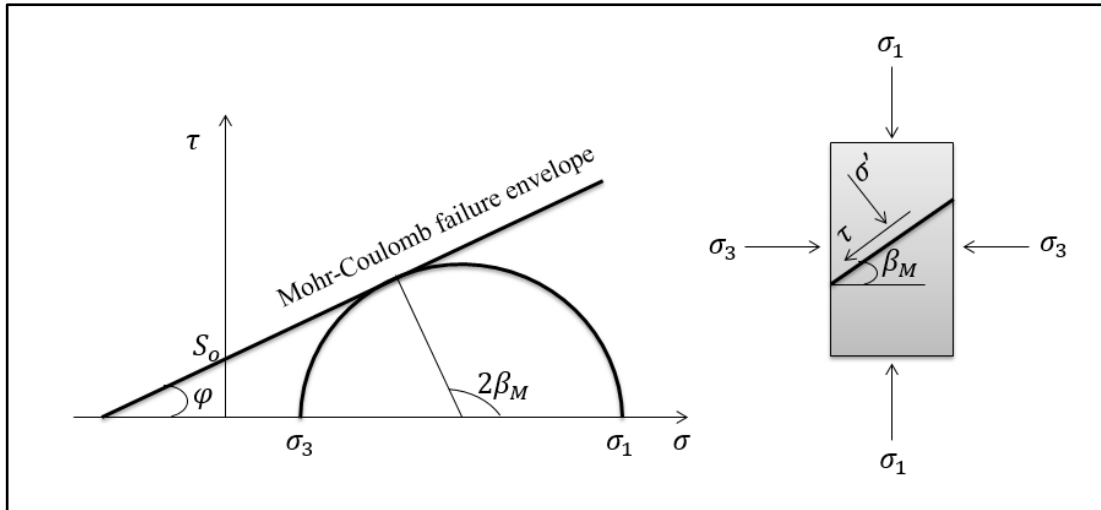


Figure 2-15: Mohr-Coulomb criterion (Fjaer, 2008).

The Mohr-Coulomb criterion suggests that failure occurs at the stress state where the Mohr-circle touches the linear envelope (Figure 2-15). Thus the normal and shear stresses at the failure plane can be calculated using the following equations:

$$\sigma' = \frac{1}{2}(\sigma_1 + \sigma_3) + \frac{1}{2}(\sigma_1 - \sigma_3) \cos 2\beta_M \quad (2-11)$$

$$|\tau| = \frac{1}{2}(\sigma_1 - \sigma_3) \sin 2\beta_M \quad (2-12)$$

$$\varphi + \frac{\pi}{2} = 2\beta_M \quad (2-13)$$

where:  $\sigma_1, \sigma_3$  are the principle stresses and  $\beta_M$  is the shear plane angle.

To accommodate extension fractures in failure criterion, Griffith(1921) proposed a failure criterion based on his elliptical crack model described earlier. The proposed criterion proposed has a parabolic shape and is given by the equation (Fjaer, 2008) :

$$\tau^2 = 4T(\sigma + T) \quad (2-14)$$

where  $T$  is the uniaxial tensile strength.

Griffith criterion provides a good description of failure envelope at low confining pressure but due to its parabolic nature, it does not provide a good fit at higher confining stress. On the other hand, Mohr-Coulomb failure envelope works well at high confining stress, which led to a proposal of modified failure criterion (Brace,1960; McClintock and Walsh,1962) shown in Figure 2-16. This modification is known as Griffith-Coulomb criterion where the right part of the curve is described

by Griffith criterion and the left part of the curve is described by Mohr-Coulomb criterion. The intersection with the shear axis ( $\tau$ -axis) is given by:

$$S_0 = 2T \quad (2-15)$$

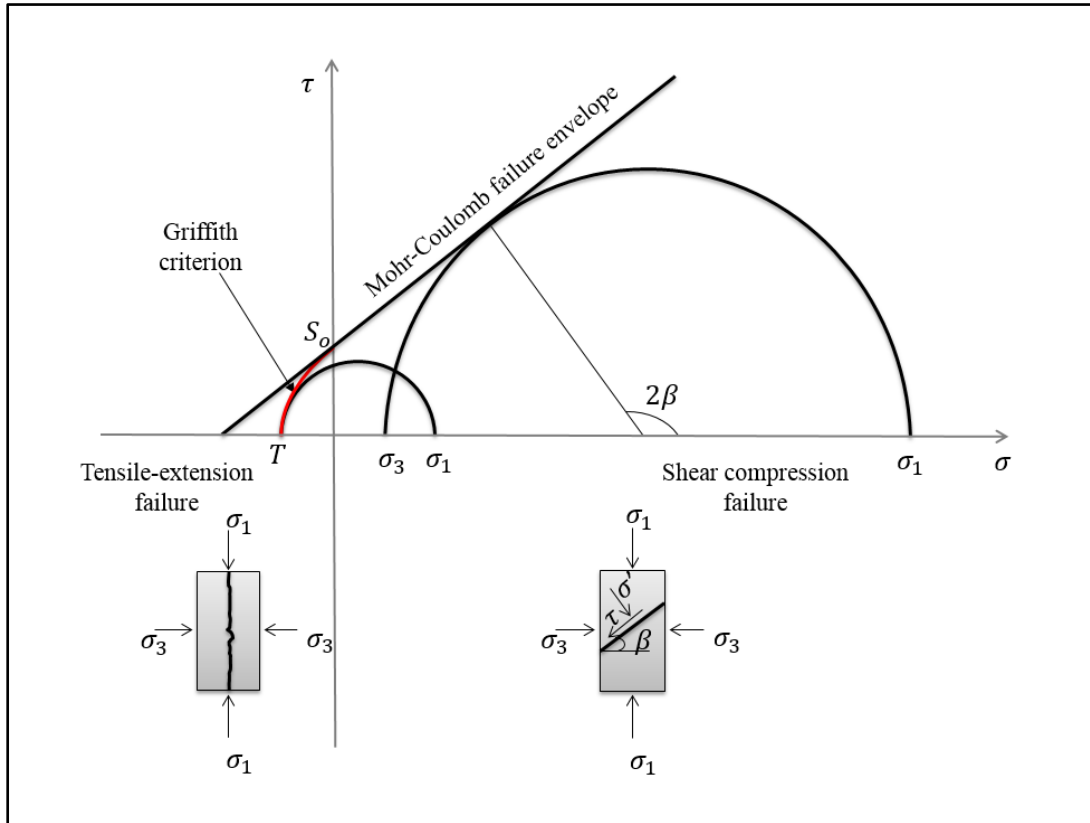
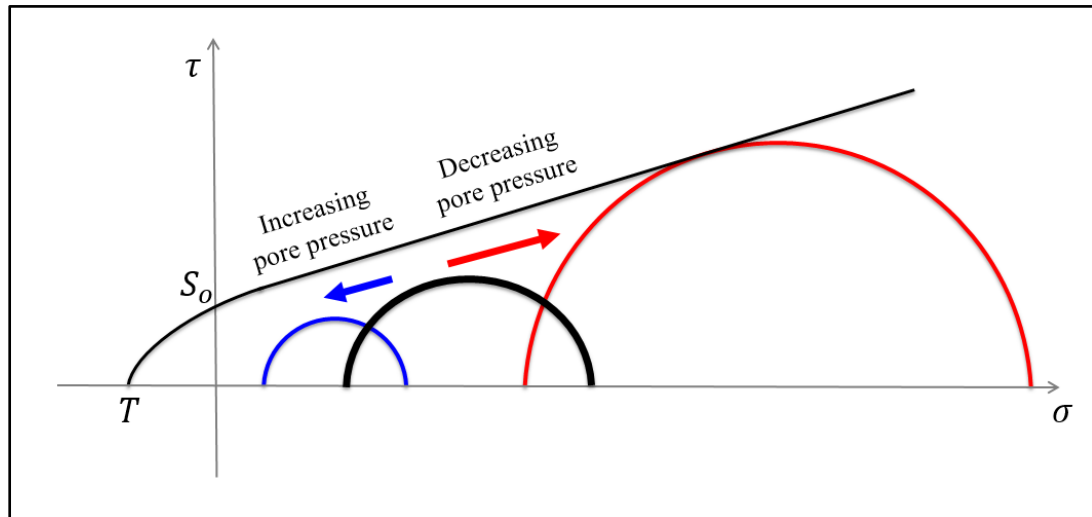


Figure 2-16: Griffith- Coulomb failure criterion. The left side of the curve represents Griffith failure criterion (red) which describes tensile failure and the right side represents coulomb criterion which describes compression failure.

It has been argued that fractures may form by natural hydraulic fracturing due to high pore pressure and form conduits for fluid flow across seals subjected to overpressure (e.g. Hubbert, 1953; Hubbert and Rubey, 1959; Hubbert and Willis, 1957). Pore pressure has to be high enough to overcome horizontal stress and tensile strength of the caprock to induce fracture. However, interpretation of recent measurements of stress evolution in depleting traps (e.g. Salz,1977; Whitehead et al.,1987; Teufel et al.,1991; Hettema et al.,2000) suggest that the increase of pore pressure increases horizontal stress. Hillis (2001) defined this process as horizontal stress-pore pressure coupling. This increase of horizontal stress will have an effect on failure modeling particularly the position and size of Mohr circle as it is shown in Figure 2-17. Increasing pore decreases the size of Mohr circle and moves to the left and

increases the chance of tensile failure . On the other hand, decreasing pore pressure moves the circle to the right and increases its size, which leads to shear compressive failure.



*Figure 2-17: effect of pore pressure on Mohr circle. Increase of pore pressure decreases pore pressure and moves Mohr circle to the left (blue) and decrease of pore pressure moves the circle to the right and increases its size (red) (Fisher et al., 2013).*

The Mohr-Coulomb criterion is widely used because of its simplicity but it does not provide a good fit to experimental data. This is due to the linearity assumption, as well as not satisfying the peak strength theory of rocks (Brady and Brown, 2005).

#### **2.1.5.4 Ductile deformation**

For an intact rock with a given porosity, rock fails in a ductile manner by shear enhanced compaction or porosity collapse when hydrostatic stress is raised. It refers to the fact that there will be irreversible deformation (plastic deformation) characterized by loss of porosity due to pore collapse as confining pressure and/or shear stress increase above the limits (Wong et al., 1997). Shear enhanced compaction or porosity collapse are considered to be part of mechanical compaction processes. Mechanical compaction is usually considered rearrangement of grains and the crushing of soft lithoclasts (Berner, 1980). Mechanical compaction occurs as a result of increase in effective stress whether by burial or hydrocarbon production. As it was discussed earlier, it leads to a dramatic reduction in pore volume and it is referred to



as porosity collapse (Smith et al., 1988). One famous case of mechanical compaction is the compaction of Ekofisk chalk reservoir in the North Sea (Japsen et al., 2011).

To model ductile deformation, a failure envelope is plotted in  $p$ - $q$  space as it was shown earlier. Taking the assumption of the second and third principle stresses to be equal ( $\sigma_2 = \sigma_3$ ),  $p$  and  $q$  will be:

$$p = \frac{1}{3}(\sigma_1 + \sigma_2 + \sigma_3) - p_p = \frac{1}{3}(\sigma_1 + 2\sigma_3) - p_p \quad (2-16)$$

$$q = \sqrt{\frac{1}{2}[(\sigma_1 - \sigma_2)^2 + (\sigma_2 - \sigma_3)^2 + (\sigma_1 - \sigma_3)^2]} = (\sigma_1 - \sigma_3) \quad (2-17)$$

where:  $\sigma_1, \sigma_2, \sigma_3$  are the principle stresses and  $p_p$  is the pore pressure.

The ductile-brittle transition zone (DBT), which was discussed earlier exists between the two curves in which rocks fail by formation of multiple slip planes (Figure 2-18). Deformations at the DBT can either lead to the formation of flow conduits or barriers (Fisher et al., 2007).

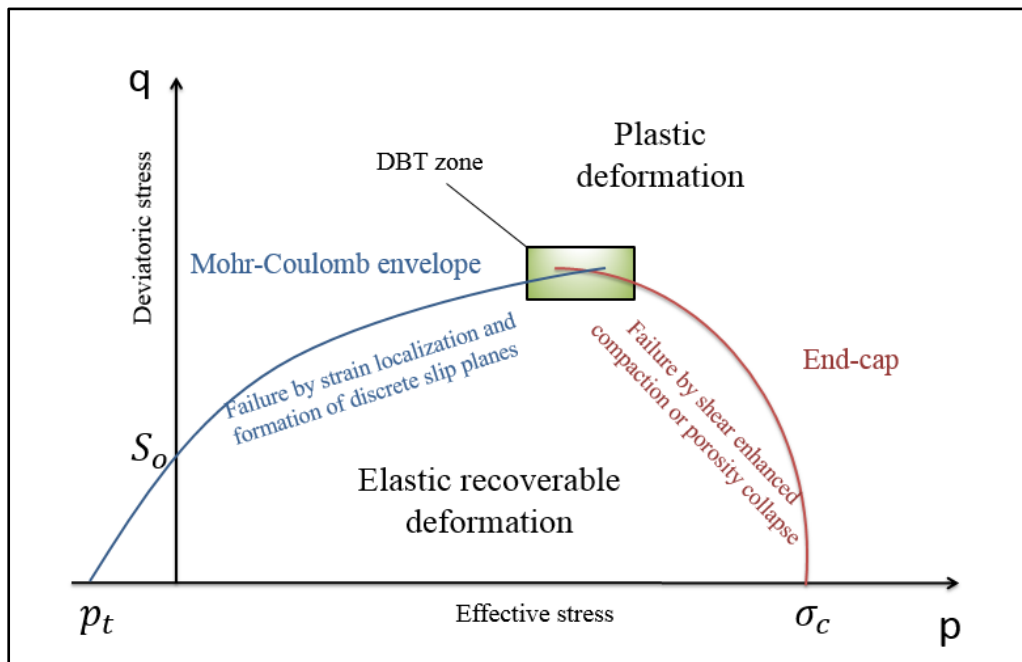


Figure 2-18: A typical yield envelope showing all types of deformations and failure in  $p, q$  space (Schutjens et al., 2004).

Failure envelopes of multi-shear failure (brittle and ductile) for rock are derived from a soil mechanics theory, known as “Critical state theory”. The most commonly used critical state models are the Cam-Clay (CC) (Roscoe et al., 1958), Modified Cam-Clay (MCC) (Roscoe and Burland, 1968) and Soft Rock 3 models

(Crook et al., 2006). Critical state concept was developed from plastic soil mechanics theory to describe mechanical behaviour of soils and rocks. The critical state refers to a failure state at which stressed rock elements can experience unlimited distortion without any change in stress or volume (Wood, 1990). It is the state at which rock failure starts to change from brittle to ductile. The critical state in  $p$ - $q$  space is represented by a straight line passing through the origin and intersection of the yield surface at a critical stress point. The intersection of the yield surface and critical stress line (CSL) correspond to the maximum value of  $q$  (Figure 2-19). It is also important to highlight that the critical stress point is the maximum point that can be reached by a tri-axial test as further stressing will result in unlimited distortion to the rock elements. Further discussion on evolution of the CSL with burial is available in **Appendix C**.

The Cam-Clay (CC) (Roscoe et al., 1958) and Modified Cam-Clay (MCC) (Roscoe and Burland, 1968) models were some of the first plastic constitutive models for describing the mechanical behaviour of soil. These models are based on critical state theory and assume an isotropic material and are based on experimental evidence obtained from tri-axial tests on remoulded soil samples of clay that were isotropically consolidated (Karmakar et al., 2004). The CC and MCC model yield surfaces are presented below respectively:

$$q + Mp \ln\left(\frac{p}{p_c}\right) = 0 \quad (2-18)$$

$$\frac{q^2}{p^2} + M^2 \left(1 - \frac{p_c}{p}\right) = 0 \quad (2-19)$$

where:  $q$  is the deviatoric stress,  $p$  is the mean effective stress,  $p_c$  is the pre-consolidation pressure and  $M$  is the slope of the critical state line.

It can be clearly seen from the above equations and Figure 2-19, that the CC yield surface is plotted as a logarithmic curve because the elastic shear strain is zero and the soil dissipates the applied energy by undergoing plastic shear strains while MCC is plotted as an ellipse because it assumes that the dissipation of energy is due to both the elastic and plastic shear (Karmakar et al., 2004).

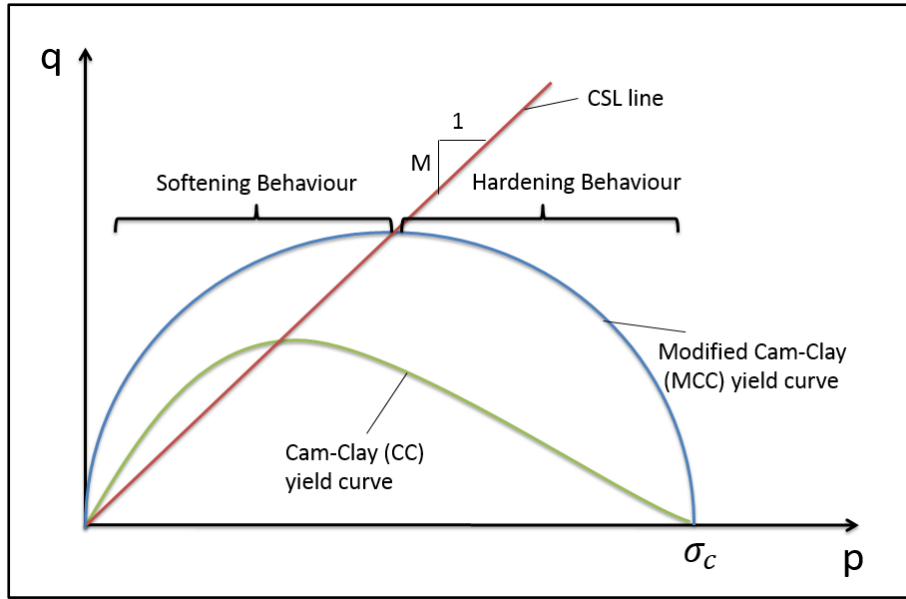


Figure 2-19: Yield surface of Cam-Clay and Modified Cam-Clay models.

The Soft Rock 3 (SR3) model was used in modelling shale samples in this thesis. The SR3 model is flexible and allows additional features such as anisotropy, rate dependence and creep to be added easily to the material characterization (Crook et al., 2006). In addition, the SR3 model is able to reproduce the experimentally observed response in confined tri-axial tests at large strains for a wide range of initial stress conditions. The SR3 yield surface function is defined as (Crook et al., 2006):

$$\Phi(\sigma, \varepsilon_v^p) = g(\theta, p) q + (p - p_t) \tan \beta \left( \frac{p - p_c}{p_t - p_c} \right)^{1/n} \quad (2-20)$$

where:  $\beta$  and  $n$  are material constants that define the shape of the yield surface,  $g(\theta, p)$  is a correction function for the yield function in the deviatoric plane and  $p_t$  is the tensile intercept with the mean effective stress. This function has an influence on the shape of the yield surface. Several expressions of this function were proposed by Van Eekelen (1980). As a general term:

$$g(\theta, p) = \left[ \frac{1}{1 - \beta^\pi(p)} \left( 1 + \beta^\pi(p) \frac{r^3}{q^3} \right) \right]^{N^\pi} \quad (2-21)$$

where:  $N^\pi$  is a material constant and  $\beta^\pi$  is defined similarly by Desai and Salami (1987) as:

$$\beta^\pi(p) = \beta_o^\pi \exp \left( \beta_1^\pi p \frac{p_c^o}{p_c} \right) \quad (2-22)$$

where:  $\beta_0^\pi$  and  $\beta_1^\pi$  are material constants,  $p_c^0$  is the initial pre-consolidation pressure and

$$r^3 = \frac{9}{2} \mathbb{P} : \mathbb{P} : \mathbb{P} = \frac{22}{7} J_3' \quad (2-23)$$

where:  $\mathbb{P}$  is the deviatoric stress tensor and  $J_3'$  is the third deviatoric stress invariant.

The correction function  $g(\theta, p)$  provides a calibration of strength for different experimental tests such as compressive triaxial test (CTC) and reduced triaxial extension (RTE) such that :

$$\text{CTC} \quad g(\theta, p) = 1 \quad (2-24)$$

$$\text{RTE} \quad g(\theta, p) = \left[ \frac{(1+\beta^\pi)}{(1-\beta^\pi)} \right]^{N^\pi} \quad (2-25)$$

Because  $\beta^\pi$  depends on the effective mean stress, it has a big influence on a transition of yield surface from a rounded-triangular shape at low mean stress to a circular shape at high mean stress. Van Eekelen (1980) showed that values of  $N^\pi=0.25$  and  $0 \leq \beta^\pi \leq 0.756$  provide a good fit for sand.

The magnitude and direction of incremental plastic deformation flow is defined and controlled by the flow rule as (Crook et al., 2006):

$$\Delta \varepsilon^p = \Delta \lambda \frac{\partial \Psi}{\partial \sigma} \quad (2-26)$$

where:  $\Psi$  is the plastic potential function, which is a scalar quantity. The SR3 model assumes that the shape of the plastic potential function is the same as the yield surface and expressed as:

$$\Psi(\sigma, \varepsilon_v^p) = g(\theta, p) q + (p - p_t) \tan \psi \left( \frac{p - p_c}{p_t - p_c} \right)^{1/n} \quad (2-27)$$

where:  $\psi$  is the dilation angle. Figure 2-20 shows the plastic potential function with respect to the SR3 yield surface. The flow rule is also presented in the same figure as strain components.

Each point on the plastic potential surface can be defined by the ratio between incremental shear plastic strain ( $\delta \varepsilon_{q^p}$ ) and incremental volumetric plastic strain ( $\delta \varepsilon_{v^p}$ ) and hence defines whether the elements are dilating or compacting (Figure 2-21). In addition, the same ratio can be used to define the angle between the strain incremental vector and  $p$ -axis ( $\beta^d$ ) as:

$$\beta^d = \tan^{-1} \left[ \frac{\delta \varepsilon_q^p}{\delta \varepsilon_v^p} \right] \quad (2-28)$$

And since the flow rule is

$$\delta \varepsilon_q^p = \delta \lambda \frac{\partial \Psi}{\partial q} \quad (2-29)$$

$$\text{And } \delta \varepsilon_v^p = \delta \lambda \frac{\partial \Psi}{\partial p} \quad (2-30)$$

Then

$$\beta^d = \tan^{-1} \left[ \frac{\partial \Psi}{\partial q} / \frac{\partial \Psi}{\partial p} \right] \quad (2-31)$$

Where

$$\frac{\partial \Psi}{\partial q} = 1 \quad (2-32)$$

$$\text{And } \frac{\partial \Psi}{\partial p} = \tan \psi \left[ 1 + \frac{p-p_t}{n(p-p_c)} \right] \left( \frac{p-p_c}{p_t-p_c} \right)^{1/n} \quad (2-33)$$

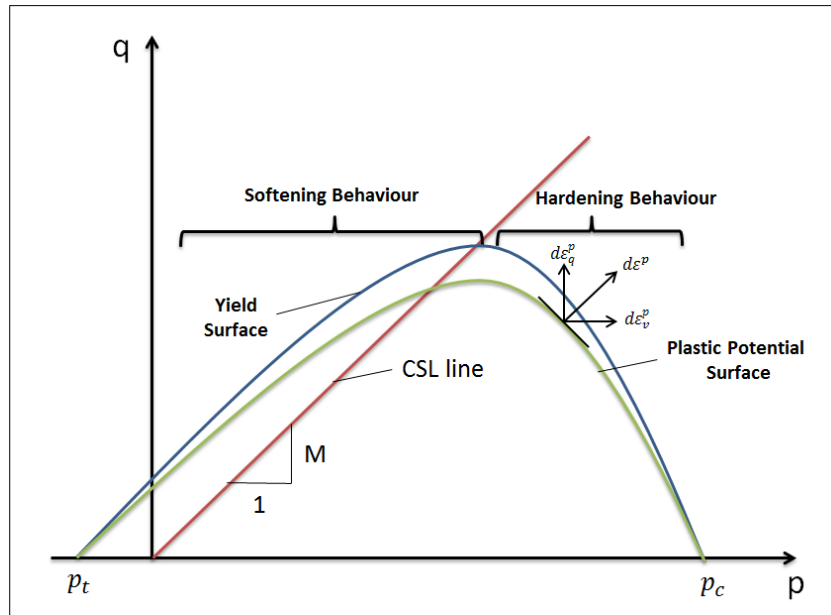


Figure 2-20: Plastic potential surface (green) with respect to the yield surface (blue) showing the flow rule as strain components in  $p$ - $q$  space of SR3 model (Al Zadjali, 2011).

The evolution of yield surfaces is defined by a relationship between pre-consolidation pressure ( $p_c$ ), tensile intercept ( $p_t$ ) and volumetric plastic strain ( $\varepsilon_v^p$ ). This relationship is known as hardening and softening laws and the most commonly used is the piecewise linear function obtained from Cam-Clay hardening constants using the expression:

$$p_c = p_{c0} \exp \left[ \frac{v \varepsilon_v^p}{\lambda - \kappa} \right] \quad (2-34)$$

$$p_t = p_{t0} \exp \left[ \frac{v (\varepsilon_v^p)_{max}}{\lambda - \kappa} \right] \quad (2-35)$$

where:  $p_{c0}$  and  $p_{t0}$  are initial pre-consolidation pressure and initial tensile intercept respectively and  $v$  is the specific volume.

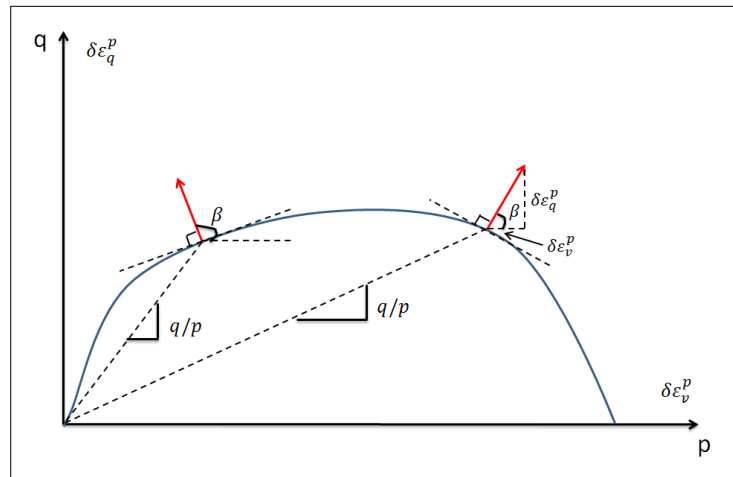


Figure 2-21: Change in angle  $\beta$  with stress point change to define dilation and compaction (Rockfield, 2014a).

### 2.1.6 Fracture closure models and experiments

Fractures have a direct effect on fluid flow through rocks as they become the least resistance flow path. Fractures can close by three main mechanisms, mineral precipitation (cementation), elastic deformation and ductile deformation with creep (Goodman, 1974; Bandis et al., 1983; Horseman et al., 2006; Gale et al., 2007). This thesis will focus on mechanical fracture closure (long term/short term).

Many attempts have been made to model and investigate fracture closure (e.g. Bandis et al., 1983; Goodman, 1974; Duan et al., 2000; Gutierrez et al., 2000; Cho et al., 2013; Babadagli et al., 2015). There are three main factors controlling fracture permeability; normal effective stress, fracture roughness and geomechanical properties of the rock. Babadagli et al. (2015) studied the effect of fracture roughness on single and multiphase flow through fractures. It was shown experimentally that increasing fracture roughness and normal effective stress significantly increase fracture closure in rocks (Cho et al., 2013; Babadagli et al., 2015). Hence, it is important to characterise surface roughness and take it into account when studying this subject.

The most famous short-term fracture closure model was proposed by Goodman (1974), which was based on series of experiments with cylindrical samples. Goodman (1974) obtained the following empirical relationship between normal stress on fracture and closure:

$$\frac{\sigma_n - \sigma_o}{\sigma_o} = \left( \frac{\delta}{\delta_m - \delta} \right)^t \quad (2-36)$$

where:  $\sigma_n$  and  $\sigma_o$  are normal stress and initial normal stress without loading respectively,  $\delta$  and  $\delta_m$  are closure behaviour and maximum closure behaviour and  $t$  is a constant. This relationship is hyperbolic and assumes that fracture closure depends only on initial stress conditions and maximum closure behaviour (Figure 2-22).

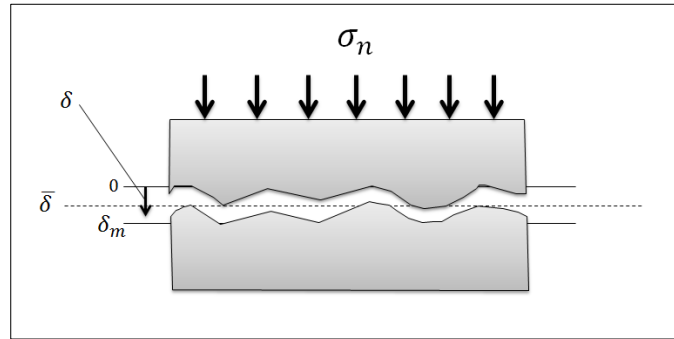


Figure 2-22: Parameters of fracture closure modelling.

Bandis et al. (1983) reviewed Goodman's (1974) fracture closure model and introduced a new parameter called normal stiffness, which controls fracture closure. The fracture closure model proposed was:

$$\sigma_n = \frac{\delta}{a - b\delta} \quad (2-37)$$

where:  $a$  and  $b$  are constants.

Bandis et al. (1983) suggested that fracture closure depends on fracture stiffness, which varies with stress. The two constants ( $a$ ,  $b$ ) are not arbitrary constants, but they are related to the maximum closure ( $\delta_m$ ) and initial normal stiffness of the rock ( $K_{in}$ ) through the following equations:

$$\delta_m = \frac{a}{b} \quad (2-38)$$

$$K_{in} = \frac{1}{a} \quad (2-39)$$

And normal stiffness ( $K_n$ ) variation with stress is found using the following equation:

$$K_n = K_{in} \left( 1 - \frac{\sigma_n}{\delta_m K_{in} + \sigma_n} \right)^{-2} \quad (2-40)$$

Bandis et al. (1983) introduced fracture surface roughness characterization using series of direct shear tests on rock samples. A unique joint roughness coefficient (JRC) was assigned to all resulted joint wall profiles. Fracture roughness profile and their corresponding JRC can be found in Figure 2-23. More profiles and other details can be found in **Appendix A**.

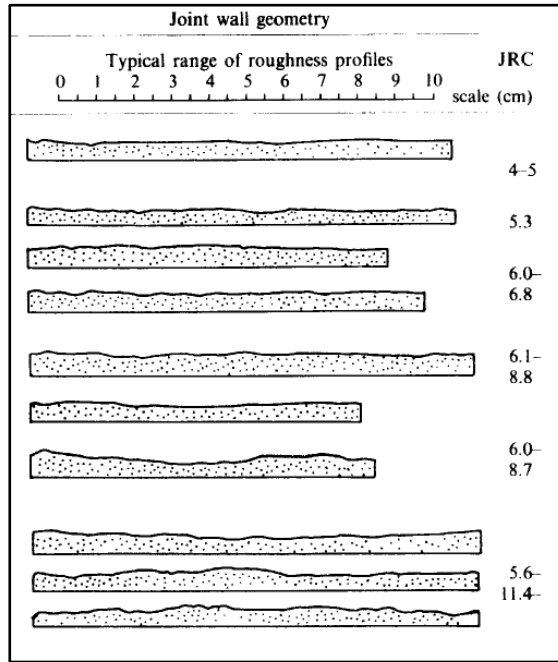


Figure 2-23: Examples of fracture profiles and their corresponding JRC (Bandis et al., 1983).

To some extent, Goodman's (1974) and Bandis et al. (1983) fracture closure models agree with fracture closure behaviour but they do not consider the link between geomechanical properties and fracture closure (Duan et al., 2000). Duan et al. (2000) proposed an empirical model for fracture closure based on simulation results that takes into account material properties and fracture surface properties. The model proposed is:

$$\sigma_n = \zeta \frac{E}{(1-\nu^2)} \left( \frac{\delta}{\bar{\delta}} \right)^2 \quad (2-41)$$

where:  $\zeta$  is a ratio which reflects surface topography,  $E$  is Young's modulus,  $\nu$  is Poisson ratio and  $\bar{\delta}$  is initial average fracture aperture. Contact area ( $A_r$ ) was derived using Hertzian contact theory and found to be:



$$A_r = \frac{2(1-\nu^2)}{\zeta} \xi \frac{\sigma_n}{E} \quad (2-42)$$

where:  $\xi$  is another ratio, which reflects surface topography. The two constants ( $\xi$ ,  $\zeta$ ) do not only correct fracture surface properties, but they also correct errors in material properties. Duan (2000) suggested that ( $\zeta$ ) has the order of ( $10^{-2}$ ) and ( $\xi$ ) between 1-1.5.

Duan et al. (2000) simulated the sensitivity of fracture closure to Young's modulus, initial average aperture and surface topography. It can be clearly seen from the below simulation results shown in Figure 2-24 that fracture closure is very sensitive to Young's modulus and initial fracture aperture and less sensitive to fracture surface properties.

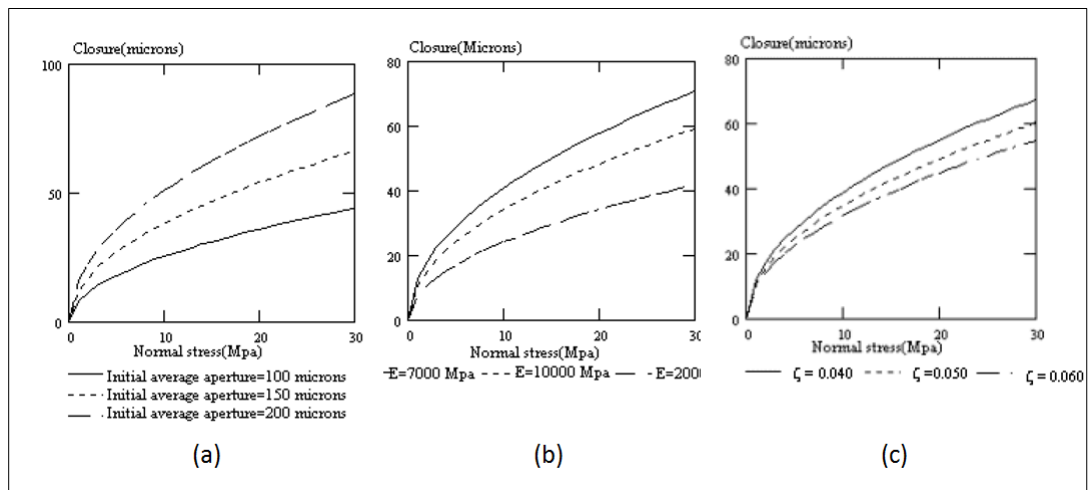


Figure 2-24: Simulation of fracture closure at various; (a) initial average aperture, (b) Young's modulus and (c) fracture surface properties (Duan et al., 2000).

The above relationship assumes linear elastic behaviour where shale behaves in a non-linear and elastoplastic manner (Brown and Scholz, 1986; Van Dam et al., 2000). Although the knowledge of fracture geometry and permeability are very important, there is still very little data available in the literature for softer naturally fractured shaley material in terms of hydraulic properties as function of increasing contact stress across the fracture (Gutierrez et al., 2000).

Gutierrez et al. (2000) studied stress-dependent permeability of a demineralised fracture in shale. A calcite cemented fracture was dissolved using acid (18.5% HCL solution) and placed in a stiff biaxial loading cell. Two types of loads were applied, shear and normal stresses, one at a time while measuring permeability.

Permeability was measured using a steady-state liquid permeameter. Gutierrez et al. (2000) concluded that increasing contact normal stress across the fracture reduced fracture permeability following an exponential law (Figure 2-25). However, loading the sample to twice as much as the intact rock unconfined compressive strength did not completely close the fracture. Gutierrez et al. (2000) experiment duration was obviously short compared to nature where other mechanisms such as mineral precipitation and creep may contribute in fracture closure process.

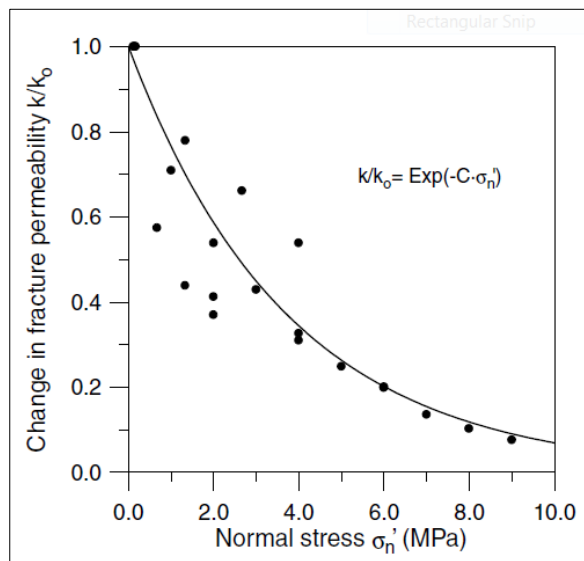


Figure 2-25: Fracture permeability as function of effective normal stress fitted with an empirical exponential function taken from Gutierrez et al. (2000).

Permeability of natural fractures could experience a reduction of more than 80% in shale as it was shown experimentally by some authors (Gutierrez et al., 2000; Cho et al., 2013). Cho et al. (2013) performed fracture closure experiments on shale cores obtained from Bakken formation collected from Williston basin of North Dakota. Cores were cut in the middle with a saw in the aim of imitating natural fractures in shale formation as it shown in Figure 2-26. Cutting all the samples with same saw and method did not solve the roughness problem and yet samples had slight difference in roughness. However, permeability still reduced by about 50% in all samples (Figure 2-26).

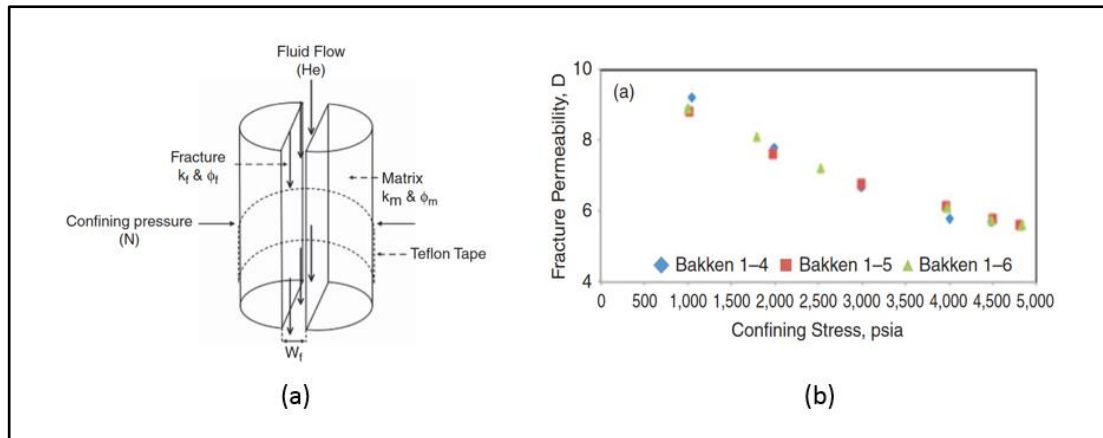


Figure 2-26: (a) Core sample preparation, (b) permeability reduction as function of confining stress (Cho et al., 2013).

It has been argued that faults and fractures could close and self-seal in clay-rich seals (Bock et al., 2010; Zhang, 2011; Fisher et al., 2013). A clear evidence for self-sealing would be the overpressure generated in structures below an extensively faulted top seal (Fisher et al., 2013). Fracture closure experiments were conducted on two clay-rich samples with artificial fractures obtained from radioactive waste disposal research labs to investigate their capability to self-seal (Zhang, 2011). The samples used are; Callovo-Oxfordian argillite (COX) from France and Opalinus clay (OPA) from Switzerland. These compacted claystone are used as a seal to prevent leakage of radioactive waste to the environment. Figure 2-27 presented permeability result of COX sample obtained by follow water through the fracture. This sample was tested up to 13 MPa confining stress for a period of 200 days. The sample experienced a large reduction of permeability throughout the time and reached a minimum permeability of  $2 \text{ E-}19 \text{ m}^2$ , which is similar to the matrix permeability ( $10^{-20}$  to  $10^{-21} \text{ m}^2$ ). The results show clear effect of time and at each confining pressure, permeability took quite a while to stabilize to a final value. Zhang (2011) also studied the effect on temperature on fracture closure of claystone samples. The test was done under confining pressure of 2 MPa and injection pressure of 1 MPa for a range of temperatures between 20-90 °C. The results for both samples show no dependency on temperature during the both heating and cooling stages as it is shown in Figure 2-28. However, fracture closure dependency on time was very clear in both samples and permeability started to stabilize after 300 days.

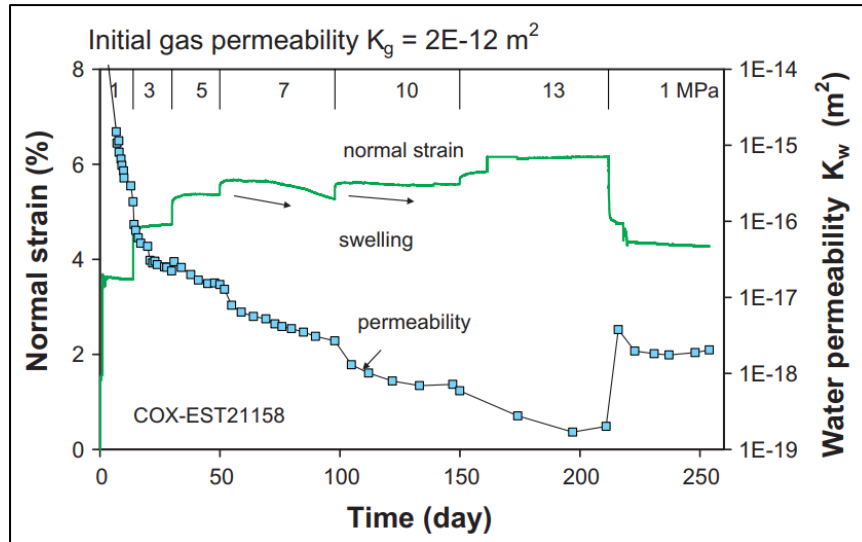


Figure 2-27: Water permeability variation over time for confining stress values from 1-13 MPa for COX sample (Zhang, 2011).

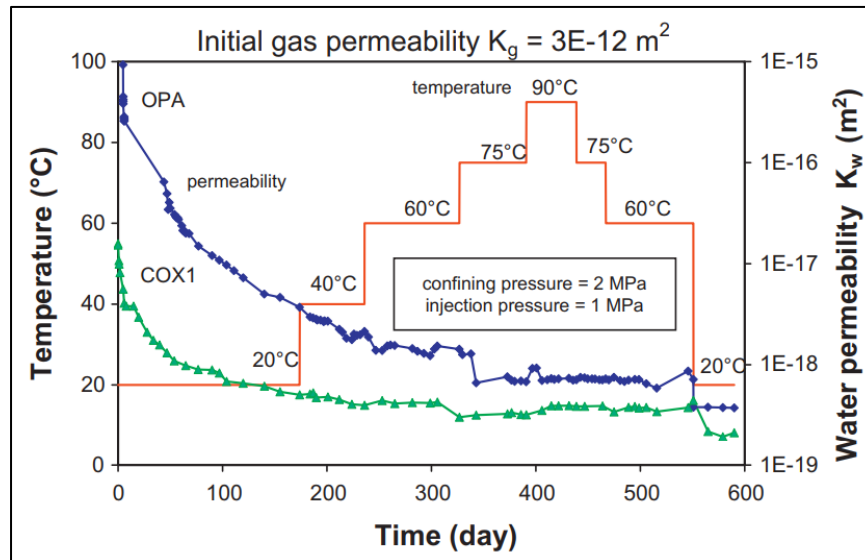


Figure 2-28: Water permeability variation over time at different temperatures. Confining and injection pressure were held constant throughout the experiment (Zhang, 2011).

Time-dependent deformations are known as “Creep”, which are plastic deformations that may occur under constant stresses lower than the strength of the rock (Fjaer, 2008). Creep is related to visco-elastic and visco-plastic behaviours of the solids, which makes it possible to occur in either dry or saturated rocks. Creep is divided into three main stages; transient or primary stage, steady-state stage and accelerated creep stage (Figure 2-29). Primary stage is the stage where deformations decrease significantly with time until it reaches a stage at which deformations are minimal. Deformations are elastic at this stage and will be recovered when stress is

removed. The second stage is the steady-state stage where no significant deformation occurs for a wide span of time. At this stage, some permanent irrecoverable deformations will take place even if the stress in the rock is released. Finally, the last stage is called the accelerating stage where deformations increase rapidly with time which will certainly lead to failure.

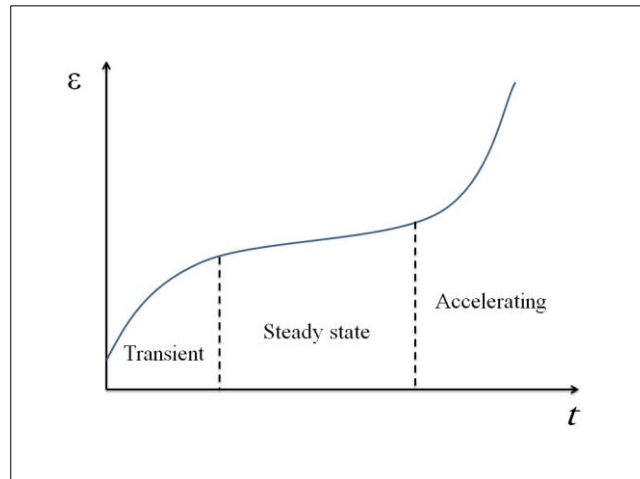


Figure 2-29: Strain Vs time for creep process (Fjaer 2008).

Creep is sensitive to the constant stress applied as it is shown in Figure 2-30. At high stress, creep becomes rapid and changes from transient to accelerating stage directly without passing through a steady-state stage. Rocks experience the same creep stages explained above at moderate stress while at low stress accelerating stage is eliminated and creep remain at steady-state stage. The rate of creep is largely controlled by temperature and may vary from minutes to years. An increase of temperature will accelerate creep process (Shibata et al., 2007).

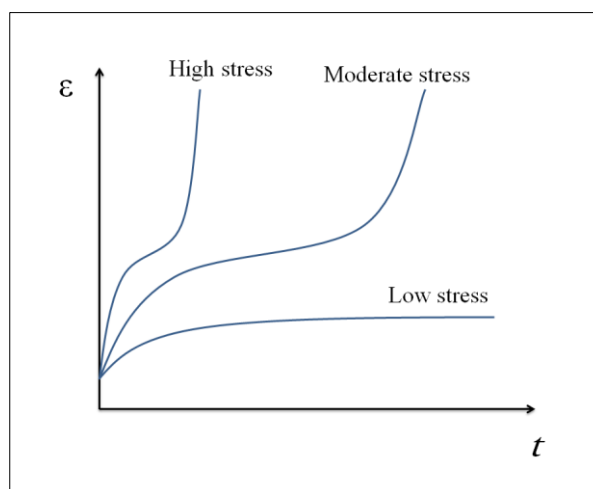


Figure 2-30: Stress effect on strain vs. time creep process (Fjaer 2008).

A whole range of micro-mechanisms are considered responsible for creep such as diffusion, pressure dissolution and dislocation glide of minerals (Bock et al., 2010). There are several visco-elastic models describing creep behaviour using exponential and power functions (Goodman, 1980). The creep data is forced to fit these models which are composed of different combinations of spring (elastic) and dashpot (plastic) systems. All these models describe creep behaviour in transient and steady state stages and not the accelerating stage. The most commonly used creep model for sedimentary rocks is Burgers body model, which takes into account the initial instantaneous shear strain followed by an exponential decrease, which will have a constant rate with increasing time as it is shown in Figure 2-31. The Burger body model for uniaxial creep is giving by:

$$\varepsilon_1(t) = \frac{2\sigma_1}{9K} + \frac{\sigma_1}{3G_2} + \frac{\sigma_1}{3G_1} - \frac{\sigma_1}{3G_1} e^{-\left(\frac{G_1 t}{\eta_1}\right)} + \frac{\sigma_1}{3\eta_2} t \quad (2-43)$$

where:  $\varepsilon_1$  is the strain  $\sigma_1$  is the maximum principle stress,  $G_1$  and  $G_2$  are shear moduli,  $\eta_1$  and  $\eta_2$  are viscosity parameters,  $t$  is time and  $K$  is bulk modulus such that:

$$K = E/3(1 - 2\nu) \quad (2-44)$$

The four parameters  $G_1$ ,  $G_2$ ,  $\eta_1$  and  $\eta_2$  can be calculated using creep data.

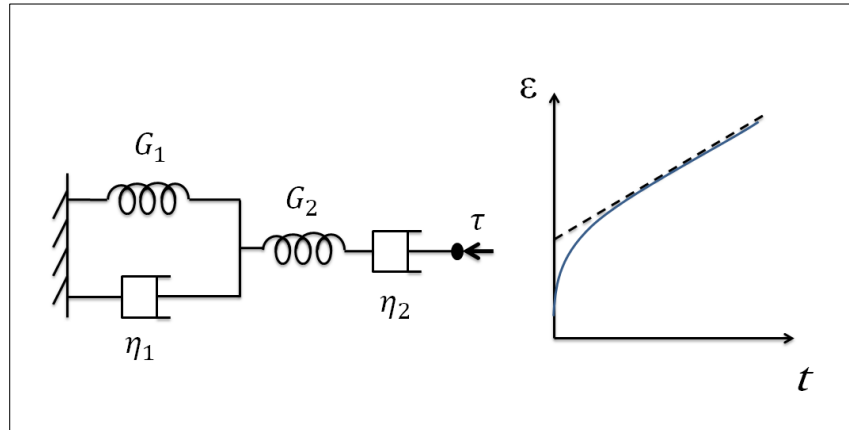


Figure 2-31: Burgers body model and its response (Goodman, 1980).

Burgers equation can be expressed in another form as (Bock et al., 2010):

$$\varepsilon_1(t) = \varepsilon_e + \varepsilon_f \left[ 1 - e^{-\left(\frac{t}{T_1}\right)} \right] + \left[ \frac{\Delta\varepsilon_1}{\Delta t} \right] t \quad (2-45)$$

where the first term represents the instantaneous elastic creep ( $\varepsilon_1$ ), the second term is the primary or transient creep and the third term is the steady-state creep.

Ostensen (1983) modelled fracture permeability using asperity model that a Gaussian distribution as a base. Fracture surface roughness, geomechanical properties and stress were taken into account while deriving this model. The permeability model is:

$$k = \frac{0.76 L s^3}{12} \left[ \ln \frac{2.48 E \left(\frac{s}{r_c}\right)^{1/2}}{3\pi^{1.5}(1-\nu^2)\sigma} \right] \quad (2-46)$$

where:  $k$  is fracture permeability,  $L$  is fracture length per unit area,  $E$  is elastic modulus,  $s$  is the combined standard variation of peak highest,  $r_c$  is the radius of curvature,  $\nu$  is Poisson's ratio and  $\sigma$  is the stress. Fracture aperture is directly proportional to fracture permeability using parallel-plate law (Snow, 1965):

$$k = e^2/12 \quad (2-47)$$

where:  $e$  is the fracture aperture in (m) and  $k$  is in ( $m^2$ ), which is around (1.01E 12 Darcy).

## 1.5 Pathways dilation

Pathway dilation is the name first given to the process of formation, propagation and dilation of preferential pathways formed by a high pressured gas in clay based barriers in porous media (Horseman et al., 1999; Cuss et al., 2014b; Rozhko, 2016; Harrington et al., 2017). It was firstly introduced as a mechanism of fluid flow to explain results from gas migration experiments in a sample from bentonite buffers used in nuclear waste disposal sites (Horseman et al., 1999). Highly compacted clay/sand mixture buffers are commonly used in radioactive waste industries. Cuss et al. (2014b) did a large scale gas injection test on bentonite engineered system. It was observed that gas flux experienced a large reduction when gas pressure was held constant. The suggestion made was that this behaviour is due to slow time-dependent expansion of gas pathways (Cuss et al., 2014b). As the gas pressure increases, cracks expand slowly resulting larger pathways network. If the pressure is reduced, expansion will stop and pathways will start to close gradually with reducing pressure. In classical multiphase flow concepts, gas flow should be proportional to hydraulic potential and flow should continue flowing in the clay when pressure was held constant. However, it was observed when gas pressure was held constant, gas flux reduced dramatically

(Cuss et al., 2014b). These pathways are difficult to explain by non-deformation or fracture flow models (Cuss et al., 2014b; Rozhko, 2016). The mechanisms of formation and propagation of these preferential pathways are still uncertain (Harrington et al., 2017). Horseman et al. (1999) suggested that these pathways may have formed by tensile (or extension) failure of the clay based bentonite.

Buffers exhibit low permeability to gas in unsaturated state and high gas entry pressure in the saturated state providing a reliable self-sealing due to swelling of clay minerals (Rothfuchs et al., 2007). Gas permeability of these buffers is higher than the host rock to allow gas ventilation through the seal. These buffers may also deform and develop preferential pathways as they are exposed to high overpressure, which will increase of intrinsic permeability (Tawara et al., 2014). Tawara et al. (2014) developed a simple model for pathway dilation relating permeability to porosity. Porosity was proposed using a linear relationship between pressure applied on pores and porosity. The model is:

$$\phi = \phi_0(1 + c_r(P_s - P_0) + ac_r(P_g + P_s)) \quad (2-48)$$

$$K = bK' \left(\frac{\phi}{\phi_0}\right)^c \quad (2-49)$$

When  $P_g > P_w + P$

Where:  $\phi_0$ ,  $\phi$  are porosity of buffer when no load considered and with load respectively,  $P_s$  is swelling pressure,  $P_0$  is atmospheric pressure,  $P_g$  is gas pressure,  $c_r$  is rock compressibility,  $K$ ,  $K'$  are intrinsic permeability and final dilated permeability respectively and  $a$ ,  $b$ ,  $c$  are constants that have to be calibrated.

Existence and formation of preferential pathways was observed while injecting gas under in situ conditions in a core sample from Bure Underground Research Laboratory (URL) in Paris (Cuss et al., 2014a). An increase in sample volume was recorded during gas injection by the strain gauges glued around the sample (Figure 2-32). This observation was used as an evidence for the formation of preferential pathways. However, there was still no micromechanical description of formation of these pathways.



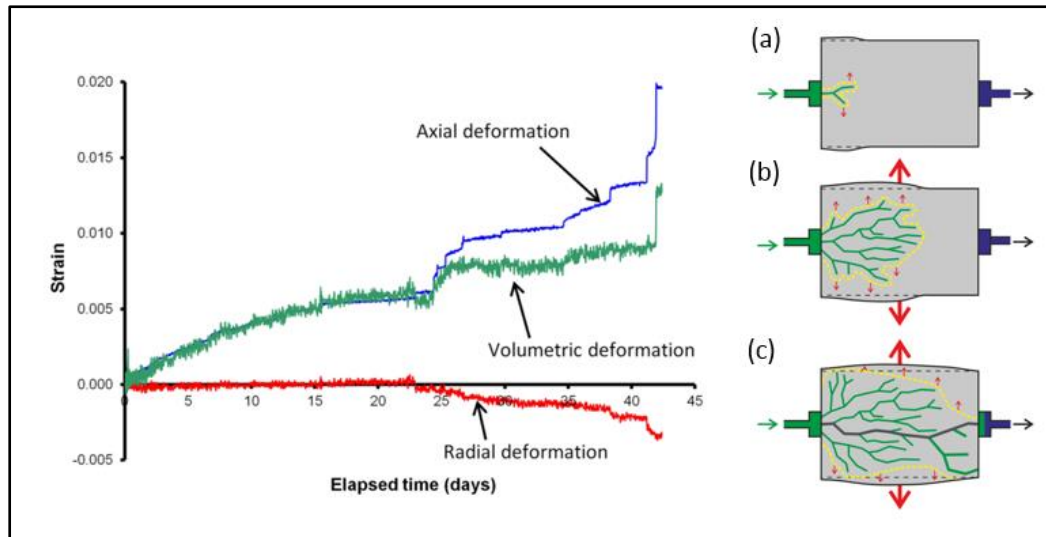
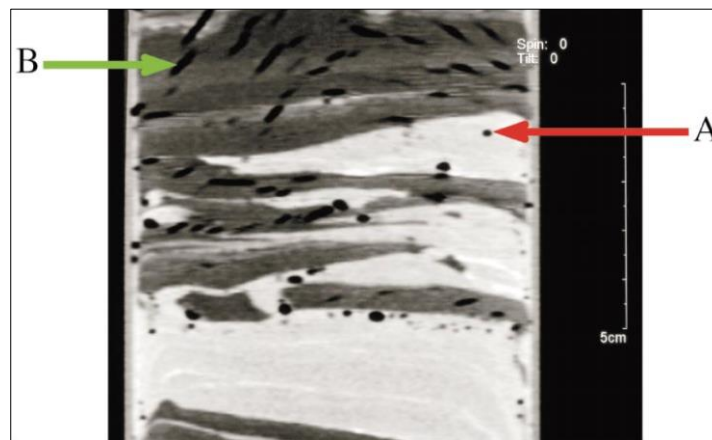


Figure 2-32: observed increase volumetric strain increase and formation of preferential pathways within a core sample from Bure Underground Research Laboratory (URL) in Paris (Cuss et al., 2014a).

There are other mechanisms of seal bypass that might be categorized as pathway dilation processes, bubble movement and formation of pipes. Bubble movement is process in which gas bubbles move by buoyance effect in a medium (in our case muddy sediment) generating stress that could cause failure (Boudreau et al., 2005). Gas bubbles are formed within sediments by natural internal production of gas depending on the organic composition of the medium i.e. methanogenesis. However, the mechanics of bubble formation are still not widely understood (Boudreau et al., 2005). Gas bubbles in soft muddy sediments can either behave fluidly or plastically in response to stress. Boudreau et al. (2005) showed that muddy sediments behave as a fracturing elastic solid where fracture channels are created. Fractures can grow either vertical or sub-lateral following surfaces with least stress intensity factor.

Boudreau et al. (2005) conducted high resolution CT scans of different muddy sediments. Figure 2-33 shows an image of a carbonate-rich fine sand and mud sample from Bridgewater Bay. The light grey layers in the image (Figure 2-33) represent fine sand and the dark grey represent mud layers. The low density bodies which have circular and elliptical shapes in 2D, spherical and oblate spheroidal in 3D respectively, represent gas bubbles formed by natural internal production of methane. The bubbles in sand layers and far from mud-sand boundary have spherical shape while the oblate spheroidal shapes dominate in the mud layers. Boudreau et al. (2005) argues that the spherical shapes refers to bubbles behaving like a fluid or an elastic-plastic solid in

response to stress created by bubbles and oblate spheroidal to mud acting like an elastic solid that fails by fracturing .



*Figure 2-33: X-ray computed tomographic (CT) image of a sample sediment containing gas bubbles. Dark grey represents mud and light grey represents sand, black features are gas bubbles (from Boudreau et al., 2005).*

Bubble growth was induced in gelatine to observe the growth in a transparent medium because it is still difficult to visualize bubble growth in soft sediments using CT scan images (Johnson et al., 2002). Bubbles grow by fracturing in gelatine regardless of it being an elastic soft solid with low Young's modulus (Johnson et al., 2002). Although gelatine is more elastic than muddy sediments, it is close to Cole Harbour sediment which is one of the investigated sediment by Boudreau et al. (2005), thus it makes growing by fracturing behaviour in gelatine very close to the behaviour in soft sediments. Figure 2-34 shows bubble rise in gelatine with a clear fracture path in column high of 35 cm. Bubbles took approximately 3 minutes to rise to the top from the injection port at the bottom.

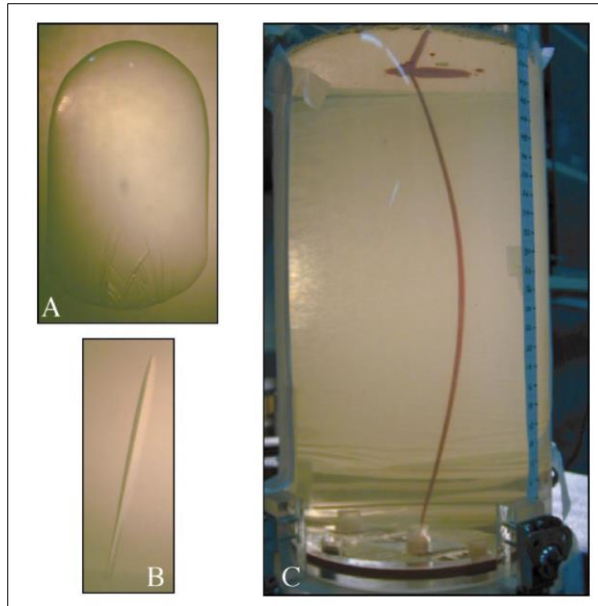


Figure 2-34: A and B: Plan and cross section of bubble rising in gelatine, C: Path of this bubble as it rises up. This picture is taken from Boudreau et al. (2005).

Top seal can also be bypassed through features called pipes. The knowledge of pipes is very limited and not well documented as they only have been described recently using 3D Seismic technology (Løseth et al., 2001; Berndt et al., 2003). Pipes are defined seismically as columnar zones of disturbed reflection that might be associated with amplitude anomalies that are stacked sub-vertically (Cartwright et al., 2007). Pipes are commonly seen in the crest region though some were documented in flat-laying units with circular and sub-circular shapes in plan from. The structure of pipes is poorly understood. Cartwright et al. (2007) described the structure of pipes to appear in two forms, either zones of minor folding and faulting or stacked pockmarks craters that are likely to be gas accumulation that caused unresolved deformations. Intense small scale fracturing (microfractures) is likely to occur at the pipe that leads to permeability enhancement and leakage through the formation (Løseth et al., 2001; Løseth et al., 2003).

Pipes can be classified into four types (Cartwright et al., 2007):

1. Dissolution pipes: This type is formed by dissolution of rock units that leads to instability of overburden resulting a collapse and hence formation of microfractures. High permeabilities are expected to be at the time of the pipe formation which reduces by fracture closure either by cementation or confining stress (Aydin, 2000).

2. Hydrothermal pipes: It is associated with high flux of hydrothermal fluid that leads to hydraulic fracturing. In addition, high flux of hydrothermal fluids enlarges the pipe overtime and leads to rock abrasion and collapse (Barrington and Kerr, 1961) which are associated with the formation of complex multiphase vein networks (Newhouse, 1942). Those pipes act like fluid-flow conduits for millions of years (Barrington and Kerr, 1961), which makes this type of pipe responsible for seal integrity and leakage.
3. Blowout pipes: Blowout pipes formation is poorly understood due to limited number of examples available. They tend to form above gas reservoirs, on structural crests and along up-dip margins of aquifer. In seismic data, their structure appears to be stacked pockmarks which support the argument that those pipes represent discrete blowout events (Løseth et al., 2001). High dynamic flux through the pipe leads to a combination of hydraulic fracturing under elevated pore-fluid pressures and stopping or fluid-driven erosion and collapse. These processes are responsible for the formation of larger pockmarks and hence permeability increase. Cartwright et al. (2007) suggested that blowout pipes are the first stage of the development of conduits for mud volcanoes because they have similar theoretical conditions (Karakin et al., 2001) and seismic expressions.
4. Seepage pipes: Seepage pipes are quite similar to blowout pipes in terms of where they form. The main difference between them is the type of host rock. Blowout pipes in fine-grained sealing (shales) whereas seepage pipe mainly in sand is silt-dominated sequences. The higher permeability of host rock allows vertical seepage to occur and hence provides a vent to prevent overpressure and fracturing of the host rock.

Figure 2-35 represents pipe-type conduits development based on existing models of diatreme formation and breccia pipe formation (Cartwright et al., 2007). This represents the conduits formed by hydrothermal and blowout pipes which involves pathway dilation process. Initially, caprock fails by hydraulic fracturing due to overpressure and then fractures propagate vertically and sub vertically under the same effect. Once fractures propagate to the top, leakage starts and continues due to widening of the conduits by the mechanisms described earlier.

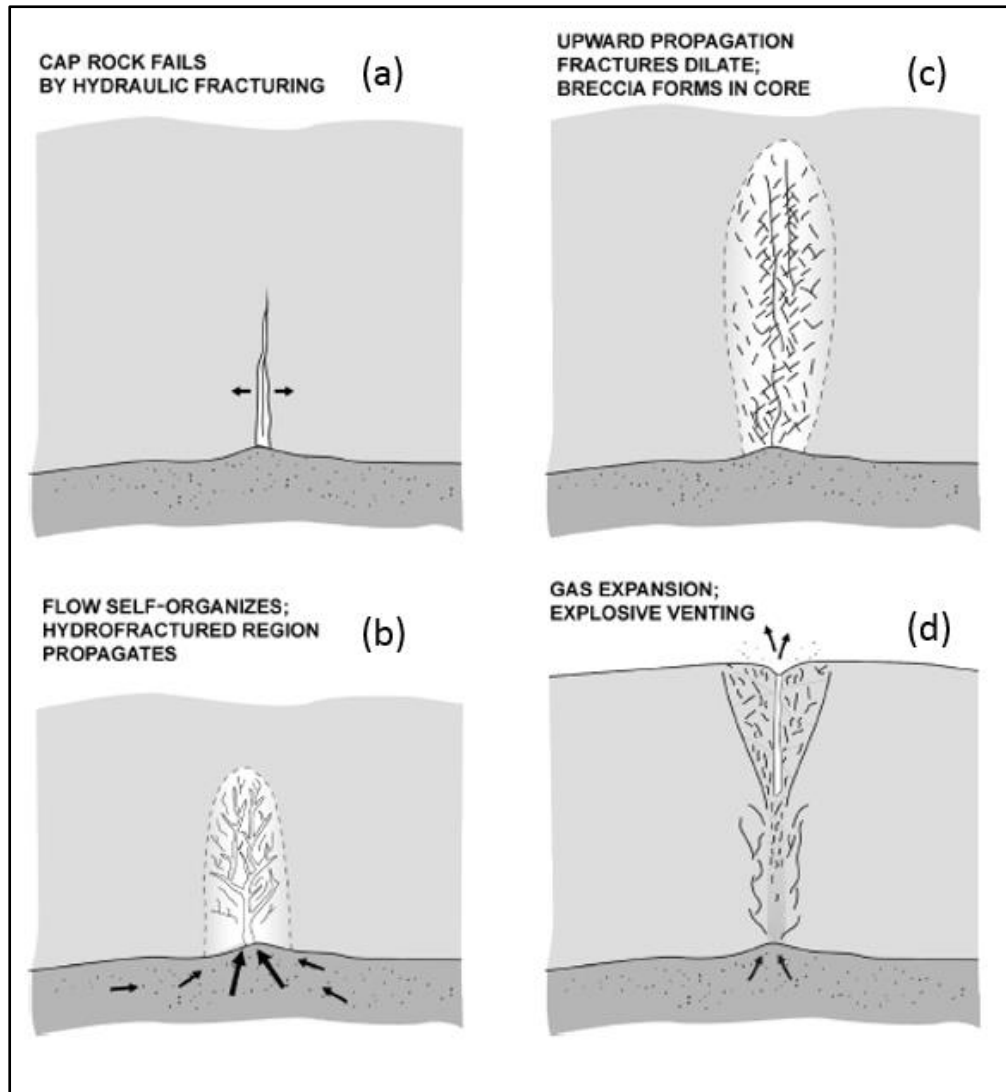


Figure 2-35: Diagram representing development of pipe-type conduit based on available model of diatreme & breccia pipe formation. (e.g. Novikov and Slobodskoy, 1978). This figure is taken from Cartwright et al. (2007).

All the mechanisms of pathway dilation described earlier have no solid microstructural models to describe their formation and propagation. All the analysis was done based on observations of the behaviour of the rock. The evidence presented for the existence of pathways dilation in geological waste disposal were based on pressure and strain measurements. There was no description of the nature of these pathways and how they propagate through the buffer. The same thing applies bubble growth and formation of pipes in soft sediments where evidences provided were based on visual observations and seismic analysis.

## 1.6 Summary of key knowledge gaps

The key knowledge gaps identified from the literature can be summarized as follows:

- Multiphase flow is driven by capillary pressure and threshold pressure of shale estimated using standard industrial techniques in the lab could be underestimated due to stress sensitivity of shale (Brace et al., 1968; Guise et al., 2017). Thus, sealing capacity of shale could be much higher at in situ conditions compared to the one estimated in the lab.
- Fractures and faults in shale could act as conduit to fluid flow and allow petroleum to leak. Flow through fracture is controlled by three main parameters; normal effective stress across fracture walls, fracture wall morphology and mechanical properties of the rock. There are evidences from the industry that these fractures could actually close and re-seal again (Fisher et al., 2013). Some authors even argue that fractures in shale remain open even if the normal effective stress exceeds its uniaxial compressive strength (Gutierrez et al., 2000). However, the knowledge of the exact controls and conditions at which these fractures close is still vague.
- Anticipating of fractures formation and determination of rock failure type are done using elastoplastic failure models, which requires knowledge of geomechanical properties of the rock. Many shales are weakly laminated, which makes coring samples for mechanical testing is quite challenging. In addition, shale rocks are tight and tend to have very low permeability, which makes other mechanical tests (i.e. compaction) very difficult particularly in a drained condition.
- Pathway dilation is claimed to be a mechanism of leakage through shale by radioactive waste management industry (Horseman et al., 1999; Cuss et al., 2014b; Rozhko, 2016; Harrington et al., 2017). However, their claim is based on observations and no micro-mechanical model of how they form and propagate was presented. Evidences of pathway dilation such as bubble movement and formation of pipes presented by other authors from geology were also based on observations and no micromechanical model was presented (Boudreau et al., 2005; Cartwright et al., 2007).

## **3 Chapter III: Samples characterization**

### **3.1 Introduction**

The basic properties of samples used in this research were characterized to help in the interpretation and modelling of the flow and fracture closure experiments. Sample properties are generally divided into three categories:

- Mineral composition.
- Petrophysical properties.
- Geomechanical properties.

Mineral composition was analysed using X-Ray Diffraction (XRD) to understand the exact samples' mineral composition by weight. The XRD does not measure the organic matter content of the sample. So the total organic carbon (TOC) was measured later using LECO combustion analysis method. The XRD results were then compared against microstructural analysis to understand the distribution of minerals across the sample.

Mercury intrusion porosimetry (MIP) instrument was used to characterize pore structures and capable of providing an estimate of pore size distribution, capillary pressures and porosity. Geomechanical properties (elastic and plastic) were measured using a multistage triaxial test. The triaxial test provides a measure of elastic properties (Young's modulus and Poisson's ratio) and plastic properties (peak stresses at different confining pressures). The results of all the tests are summarized and discussed at the end of this chapter.

### **3.2 Sample locations**

A total of six shale samples were collected from different locations. Four samples were collected from outcrops from cliffs and quarries and the other two were from cores obtained from drilling sites. Whitby mudstone (WS) and Kimmeridge clay (KC) samples were collected from cliffs in Sandsend-Whitby and Kimmeridge Bay respectively. Sandsend is located in the eastern coast of the United Kingdom (Figure 3-1). The Whitby mudstone deposited during the Toarcian stage in the Lower Jurassic age could act as a source to petroleum in the North Sea. WS samples were collected from just below the sea level at low tide to eliminate the effect of weathering on rock properties. The samples were preserved in the laboratory in brine because the

WS samples contain laminations, which tend to get very weak when they are dry. Coring from these samples was a challenge due to the delamination issue. The KC sample was collected from Kimmeridge Bay, which is located in the southern west coast of the United Kingdom (Figure 3-2). The KC formation plays as a major source rock for number of petroleum reservoirs in the North Sea. The KC sample is a claystone deposited during the Late Jurassic age. The KC samples were collected from the base of the cliff and then covered by plastic wrap to preserve the sample from weathering.



Figure 3-1: The cliff at the beach in Whitby (The map is obtained from google maps).



Figure 3-2: The cliff at the beach in Kimmeridge bay (The map is obtained from google maps).

The third sample was collected from a quarry in Accrington, known as “Rakehead Quarry”. Rakehead Quarry is located in central UK in Lancashire as it is shown in the map in Figure 3-3. The shale sample collected is a mudstone deposited during Westphalian age; it is locally known as the “Accrington Mudstone Formation”.



The Accrington Mudstone (AM) samples collected were carefully wrapped and stored in a dry area as these samples are sensitive to water.



Figure 3-3: Rakehead quarry in Accrington (The map is obtained from google maps).

The ALP sample was obtained from top seal of an oil reservoir in North America; its exact location is confidential. The remaining two samples are OC and D samples were the most stiff shale samples in the set. The location information of these samples are confidential and cannot be disclosed in this thesis.

### 3.1 Experimental materials and methods

#### 3.1.1 Mineralogy analysis using X-Ray Diffraction (XRD)

The XRD technique is widely used to determine mineralogy of materials due to its simplicity and accuracy. The apparatus consists of X-ray tube that generates X-rays, which are focused on to the sample placed on a sample plate and an X-ray detector, which detects the diffracted X-rays from the samples (Figure 3-4). This concept was firstly introduced by Bragg (1913) who derived an equation that relates X-ray wave length, signal intensity and diffraction angle to the spacing of atomic layers within minerals. This equation is known as Bragg's law:

$$\lambda = 2 d \sin \theta_d \quad (3-1)$$

where  $\lambda$  is the X-ray's wave length,  $d$  is the distance between parallel planes of atoms and  $\theta_d$  is  $\frac{1}{2}$  of the diffraction angle. In this apparatus, the wave length is always fixed to reduce the number of variables while X-rays source and detector are allowed to rotate in a circular path to be able to detect any diffraction angle. Each individual mineral has characteristic spacing and that these can be used to assess the minerals present. Reflected signal intensity together with diffraction angle forms a diffraction

pattern that is unique for every substance. A typical diffraction pattern of a substance is shown in Figure 3-5.

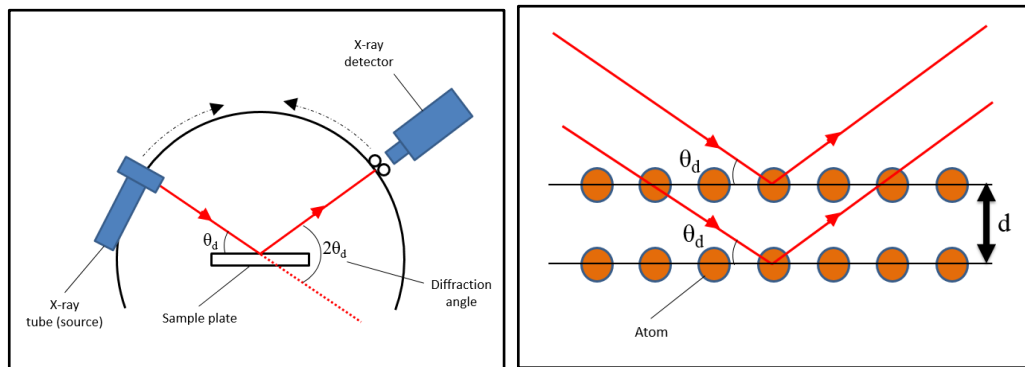


Figure 3-4: X-Ray diffraction (XRD) apparatus.

Samples are normally ground down to powder of a size 0.002 mm to 0.005 mm. The powder is then spread in a holder and put inside the instrument. The instrument can automatically detect minerals based on the diffraction patterns.

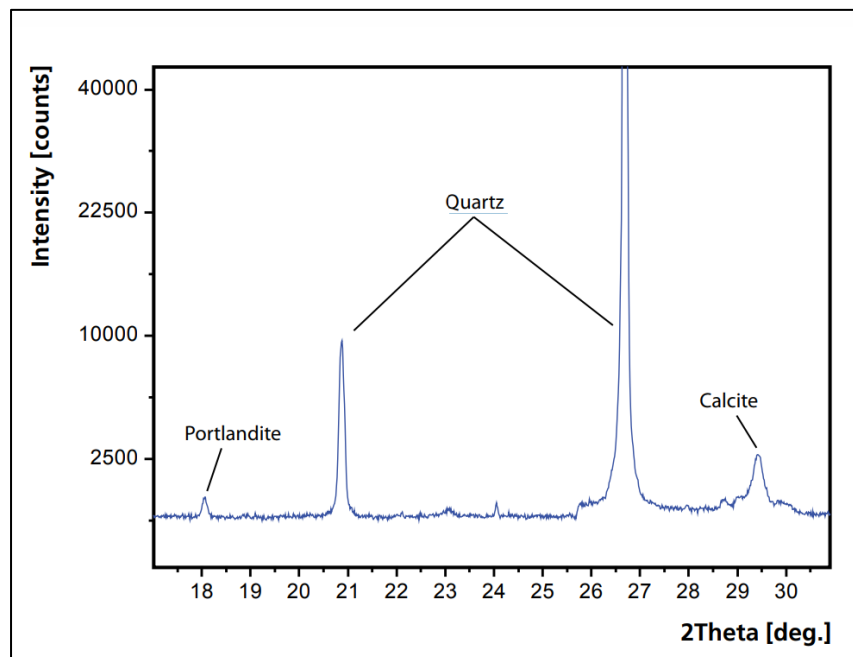


Figure 3-5: Typical diffraction pattern of material (PANalytical, 2009).

### 3.1.2 Total organic content analysis (TOC)

Total Organic Content (TOC) was measured for all samples following standard operating procedure for measuring TOC using LECO adopted by the geochemistry laboratory at the University of Leeds. First, the samples are ground to powder and sieved to a size less than 125  $\mu\text{m}$  (as per laboratory recommendations). The required

amount is about 1 g and initial weight has to be measured accurately to be used as a reference,  $m_i$ . The samples then are treated with acid (10% HCL) for 24 hours to dissolve carbonate minerals. The samples are then rinsed with deionised water to remove acid and oven dried. After they get dry completely, the weights of samples are recorded to calculate weight change after acid treatment,  $m_f$ . The percentage of carbon in the samples are then measured using carbon/sulphur analyser from LECO. The LECO analyser is basically a combustion furnace that burns the remaining organic carbon in the samples in excess oxygen environment to force it to react and form CO<sub>2</sub> gas. The produced gas, CO<sub>2</sub>, is detected using infrared cells and recorded for each sample. Figure 3-6 represents the process of TOC measurement. The percentage of carbon,  $p_{oc}$ , obtained from LECO is then used to calculate TOC using the following equation:

$$TOC = p_{oc} \left( \frac{m_f}{m_i} \right) \quad (3-2)$$

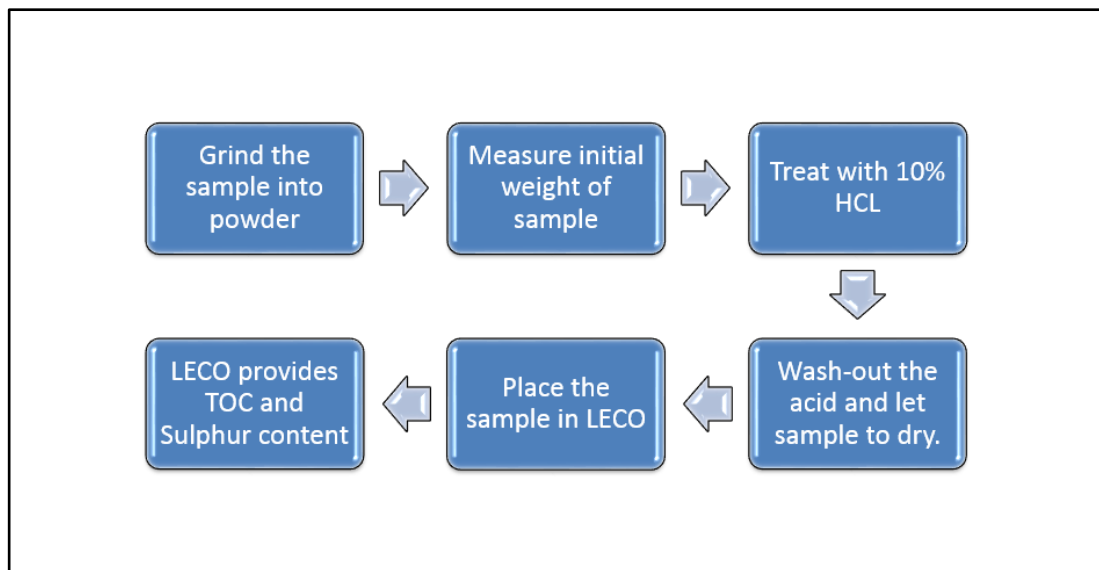


Figure 3-6: Total Organic Carbon (TOC) measurement process.

### 3.1.3 Scanning electron microscope (SEM)

Scanning electron microscope (SEM) is used to produce the images of surfaces by focusing a beam of electrons on that surface (FEI, 2010). As the electrons beam hits the surface, it generates four types of signals; secondary electrons, backscatter electrons, X-rays and light. The secondary electron signals are captured by a detector and processed to provide information about surface topography in an image format.

The representation of image will be in gray-scale with dense material in bright white and light material in dark colour. Figure 3-7 shows the main components of SEM instrument.

Backscatter Scanning Electron Microscopy (BSEM) technique was used to obtain microstructural information. The backscatter signals are captured using a detector and give information about the atomic number of the material. The brightness of BSEM images is directly proportional to the mean atomic number of the mineral/phase being imaged, so it is particularly useful for determining the distribution of minerals and porosity (Erdman and Bell, 2015). The SEM used was Quanta FEG 650 provided from Field Electron Ion Company (FEI). Around 2cm square and 0.5 cm thick blocks were prepared for BSEM analysis using standard preparation procedures. First, the sample was cut into blocks and impregnated with a low viscosity resin. The blocks were then ground carefully until the area of interest is exposed. The sample was then polished with successively decreasing sized diamond paste, finishing with a polish using 0.25  $\mu\text{m}$  diamond. Finally, the sample was coated with a 5 nm layer of carbon, ready for examination using the SEM.

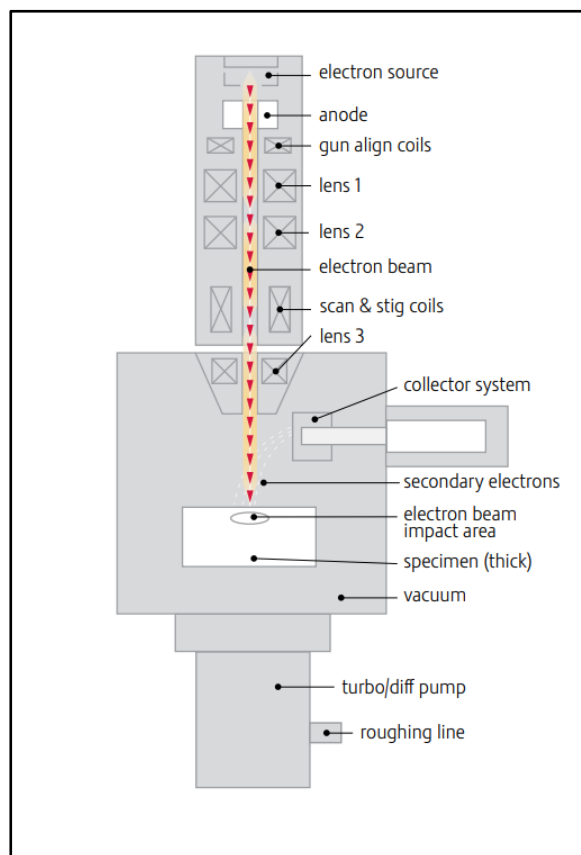


Figure 3-7: Schematic showing different components of SEM instrument (FEI, 2010).

### 3.1.4 Mercury Intrusion Porosimetry (MIP)

Mercury Intrusion Porosimetry (MIP) is a technique widely used to measure capillary entry pressure, threshold pressure and pore size distribution. The measurements conducted during this study were made using a Micromeritics Autopore IV 9520 system. MIP works on the principal that mercury is non-wetting, so it required a pressure to enter pore throats. The machine is capable of applying mercury injection pressure of up to 60,000 psi. Pressure at which the mercury starts entering the pores is the capillary entry pressure. Pore sizes are calculated using mercury pressure by Young-Laplace's equation (equation (2-2)).

The setup of the MIP consists of the following (Figure 3-8):

- Capillary tube
- Sealed sample cap (penetrometer)
- Cap
- Electrical Contact

The working principle of MIP is simple because it has one input variable (pressure) and one output variable (volume). External pressure is applied to force mercury into the glass penetrometer. Pressure is applied in steps automatically using pre-set pressure steps defined by the user before performing the test. The instrument measures mercury flow rate continuously throughout the test and gives in order to increase pressure whenever the mercury flow rate goes to a minimum pre-set value (in this case 0.001 cm<sup>3</sup>/min). The other end of the penetrometer is sealed using a cap with an electrical port to measure capacitance. Capacitors are used to detect change in mercury volume at the penetrometer. However, it is important to mention that the samples have to be cleaned properly and completely dry before performing the test to ensure that all the pores are empty. Presence of liquid molecules in pores will effect volume measurement, which will introduce a bias in the resulted measurement.

The MIP technique could be used to estimate effective porosity of a sample. The machine calculates the total volume pumped into the glass cup throughout the test. The difference between total mercury volume pumped and summation of penetrometer and sample bulk volume will yield the sample pore volume. The equation is:

$$V_{pore} = V_{total} - (V_{pent} - V_{sample}) \quad (3-3)$$

where  $V_{pore}$  is sample pore volume,  $V_{total}$  is the total mercury volume pumped,  $V_{pent}$  is the volume of the penetrometer and  $V_{sample}$  is bulk volume of the sample. However, It is important to correct the total mercury pumped volume to accommodate compressibility of the sample.

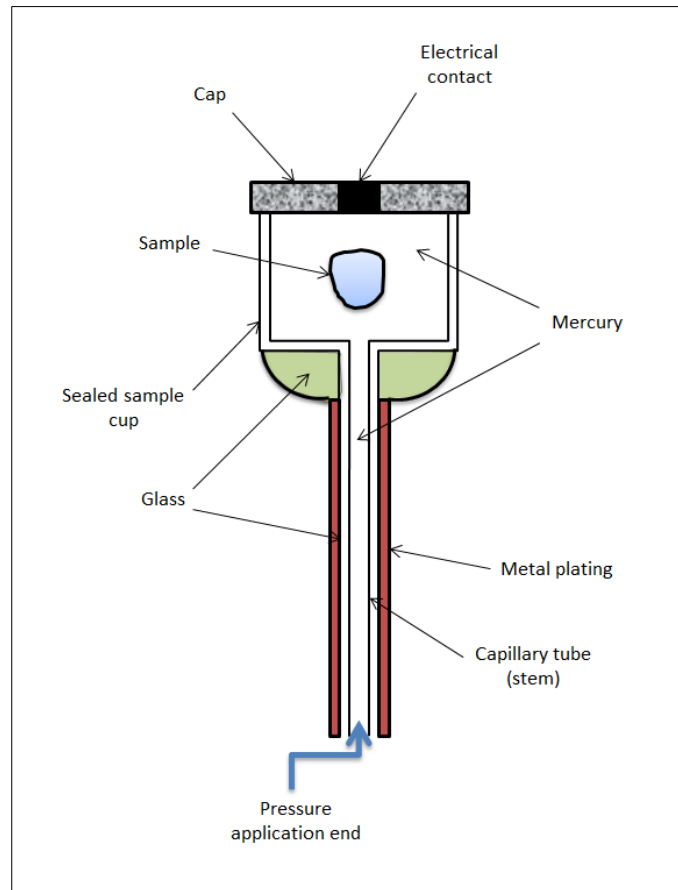


Figure 3-8: Mercury Intrusion Porosimetry (MIP) penetrometer assembly.

### 3.1.5 Mechanical properties

The triaxial test is one of the most common methods used to measure mechanical properties of rock materials. It is undertaken under various triaxial stresses and the results are used to calculate parameters such as elastic properties and the failure envelopes. The samples were prepared according to ISRM (1983) with two sets of strain gauges glued in two different sides of the sample as is shown in Figure 3-9. The setup of the experiment is shown in Figure 3-9 is based on ISRM (1983) testing procedure. After placing the sample in the cell, a pre-defined hydrostatic confining stress is applied to the sample using hydraulic oil in the cell through the rubber sleeve. An axial stress is then applied to the sample using the hydraulic rig until it fails. The stresses and strain gauges deformations are recorded using an online computer.

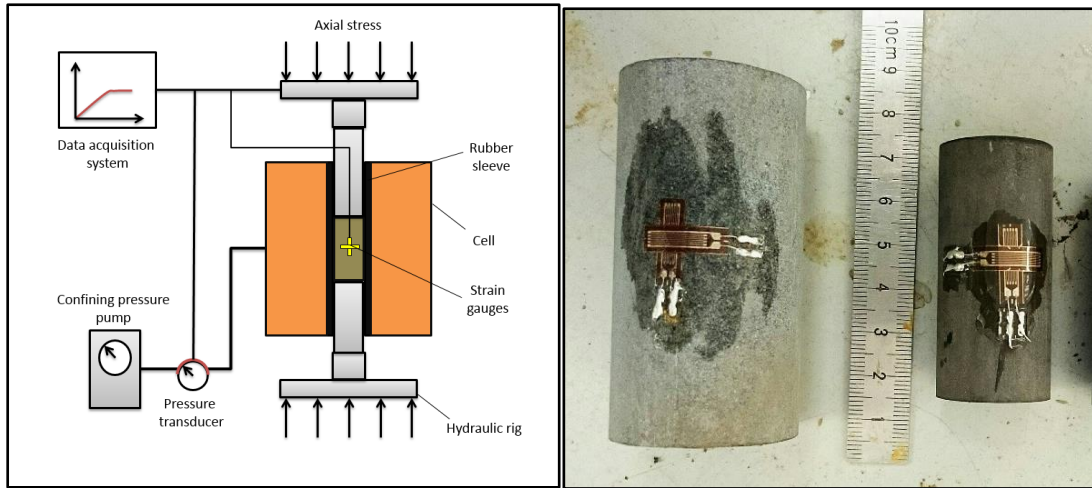


Figure 3-9: Tri-axial test setup and samples prepared for the test.

Initially, the test used to be performed in a single-stage where the sample is stressed until it fails. As this is a destructive test, each sample will provide only one point in the failure envelope as it shown in Figure 3-10. Three points at least are required to estimate failure envelope, which is sometimes challenging when few samples are available (Youn and Tonon, 2010). Kovari and Tisa (1975) proposed a multi-stage tri-axial test by increasing confining pressure to the next desired stress just before failure to shift the stress state to right of the failure envelope as it is shown in Figure 3-10. This process can be repeated several times to get several points of the failure envelope using just one sample. Multi-stage mechanical properties was proven to be relatively close to single-stage results for shale rocks (Kim and Ko, 1979).

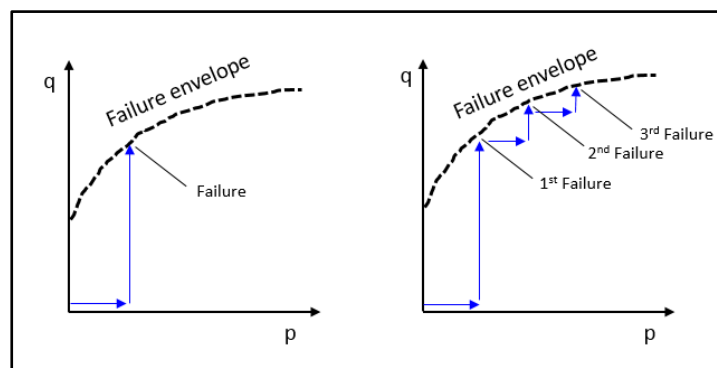


Figure 3-10: Single and multistage triaxial tests (Youn and Tonon, 2010).

Shale is known for being difficult to core due to weak bond between clays and its sensitivity to water. Thus, drilling a core that is long enough for a triaxial test becomes challenging and impossible in some of the cases. Due to this problem, performing triaxial test on some of the shale samples is impossible.

## 3.2 Experimental results

### 3.2.1 XRD, TOC and SEM microstructural analysis

The XRD test was performed for all six samples using the technique explained earlier. The results are summarized in Table 3-1. TOC was measured as well using LECO and the results are also tabulated in Table 3-2.

Sample name	Mass percentage (%)										Total
	Quartz	Albite	Micro-cline	Calcite	Dolomite	Mica	Illite-smectite	Kaolinite	Chlorite	Pyrite	
WS	18.1	3.6	0	7.3	1.4	8.6	35.2	18.1	0	7.5	99.7
ALP	18.3	7.1	3	1.9	3.5	15.1	24.6	7.9	5.4	13.6	100.4
AM	34.2	11.7	0	0	0	19.6	11.6	8.9	14.5	0	100.6
OC	35.9	2.3	0	19.2	3.6	8	21.7	2.7	3	3.7	100.2
KC	14.5	1.7	0	10.8	35.5	5	23.9	3.7	0	3.7	98.9
D	46.4	10.9	0	0	0	19.6	6	8.7	9	0	100.6

Table 3-1: Summary of XRD data for each sample.

Sample	TOC (%)
WS	3.36
ALP	6.53
AM	0.72
KC	6.70
OC	3.38
D	0.52

Table 3-2: Total organic content (TOC) weight percentage for all samples measured by LECO.

The BSEM images of the WS sample are shown in Figure 3-11. The sample is composed of a mixture of clay minerals (illite-smectite and kaolin), quartz as well as traces of mica, dolomite, calcite and pyrite. The detrital quartz is very fine grained with a size of  $<10 \mu\text{m}$ . The pyrite is composed of framboids with a size of  $>2 \mu\text{m}$  indicating that the sediment was deposited in sub-oxic conditions (Fisher and Wignall, 2001).



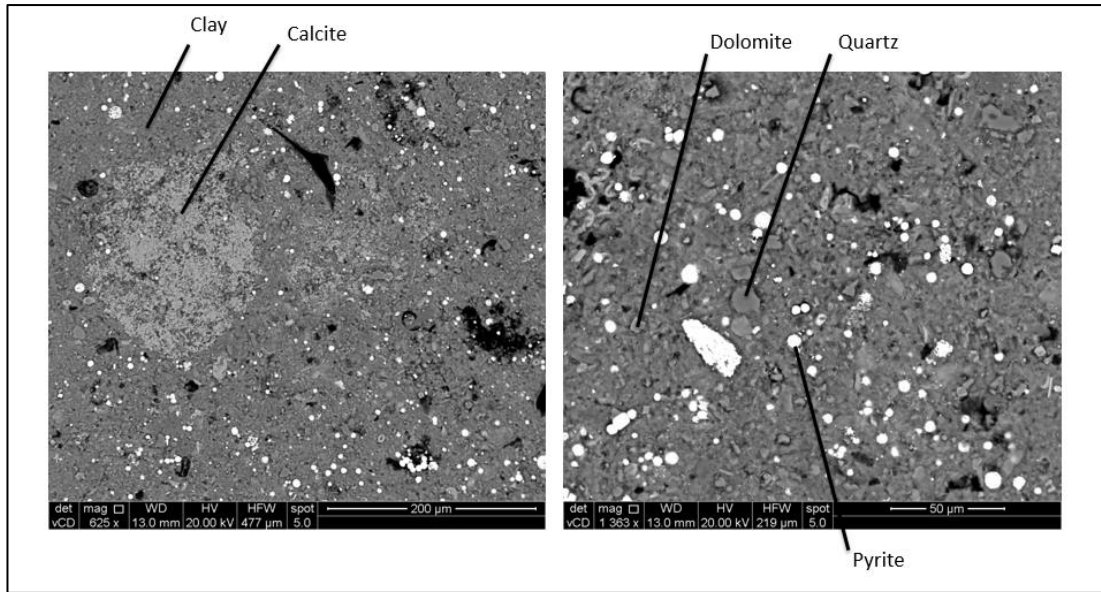


Figure 3-11: Backscatter scanning electron microscopy (BSEM) images of WS sample.

The ALP sample is also clay-rich (Figure 3-12). It has less clay than the WS sample with a clear evidence of relatively higher pyrite content scattered throughout the sample. Most of the clay minerals present are illite-smectite. There is a small amount of carbonate minerals present within the sample but slightly less than the ones present in the WS sample. The quartz average grain size is relatively large in the ALP sample (i.e. up to 50μm diameter) compared to the one observed in the WS sample.

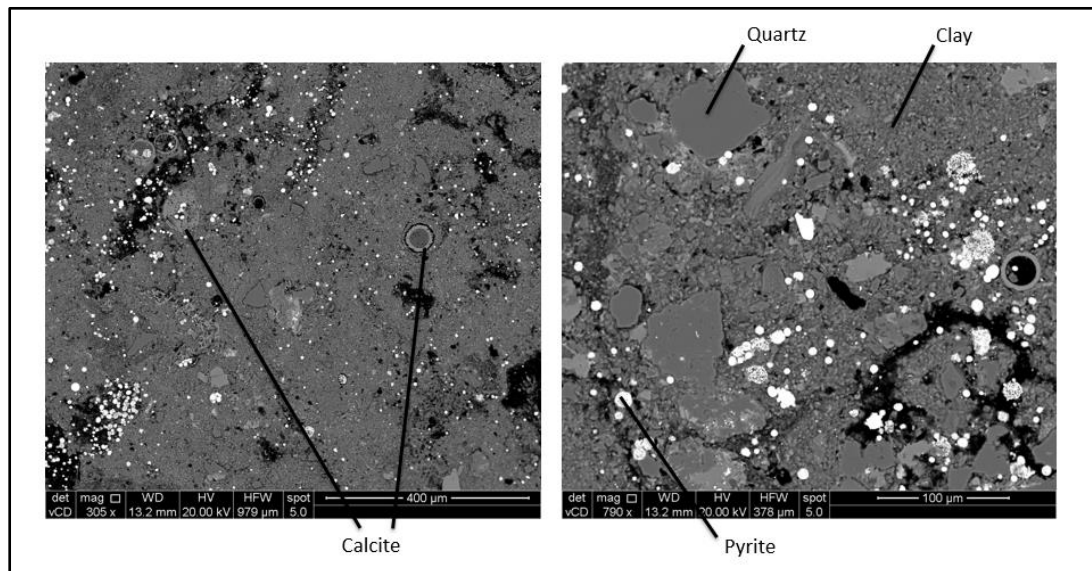


Figure 3-12: Backscatter scanning electron microscopy (BSEM) images of ALP sample.

The AM sample has a similar total clay quartz content (Figure 3-13) to the ALP sample. This sample has a mixture of clay minerals; chlorite, illite-smectite, kaolinite

and mica which can be seen in Figure 3-13. This sample has no pyrite or carbonate minerals noticed within the sample. The AM sample has relatively small average quartz grain size as it can be seen in Figure 3-13.

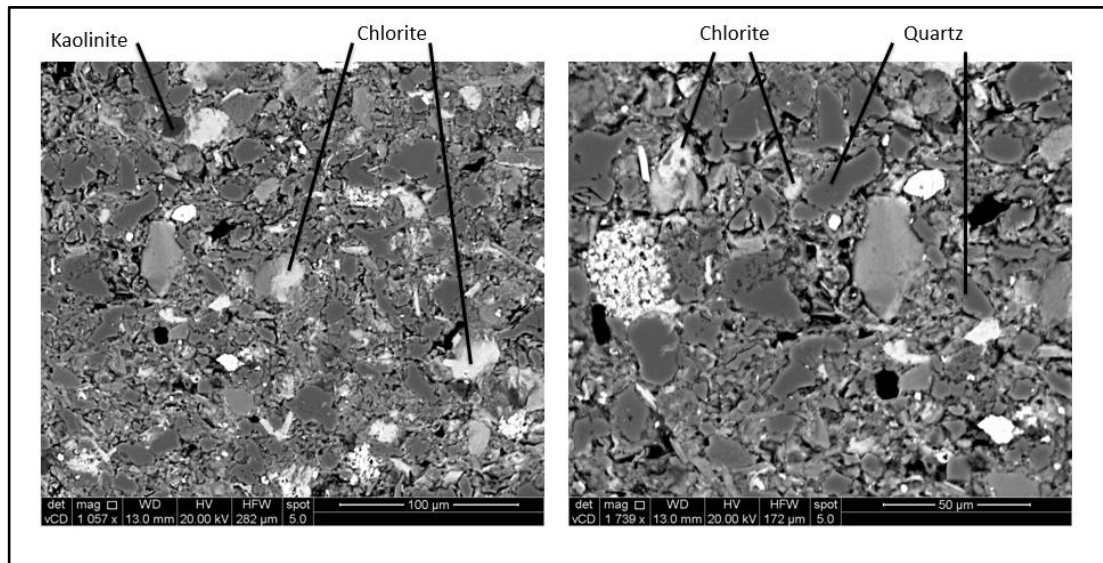


Figure 3-13: Backscatter scanning electron microscopy (BSEM) images of AM sample.

The KC sample has quite a different mineralogy than the other samples. It is carbonate-rich dominated by dolomite with relatively small amount of quartz, clay and pyrite present between the dolomite rhombuses (Figure 3-14). The quartz grains are very small surrounded by clay minerals dominated by illite-smectite. Pyrite is also present with relatively small amounts scattered within the rock.

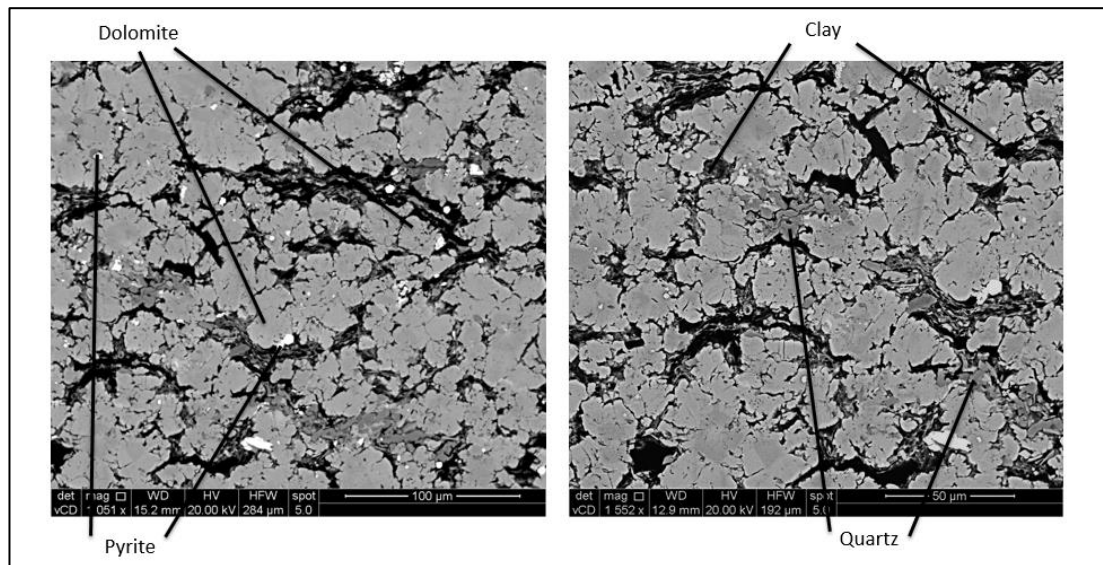


Figure 3-14: Backscatter scanning electron microscopy (BSEM) images of KC sample.

The OC sample has relatively moderate quartz content with relatively low clay content and moderate carbonate content (Figure 3-15). The quartz average grain size is relatively fine (10  $\mu\text{m}$ ) and most of the clay minerals present are illite-smectite. This sample has relatively small amount of pyrite scattered across the sample.

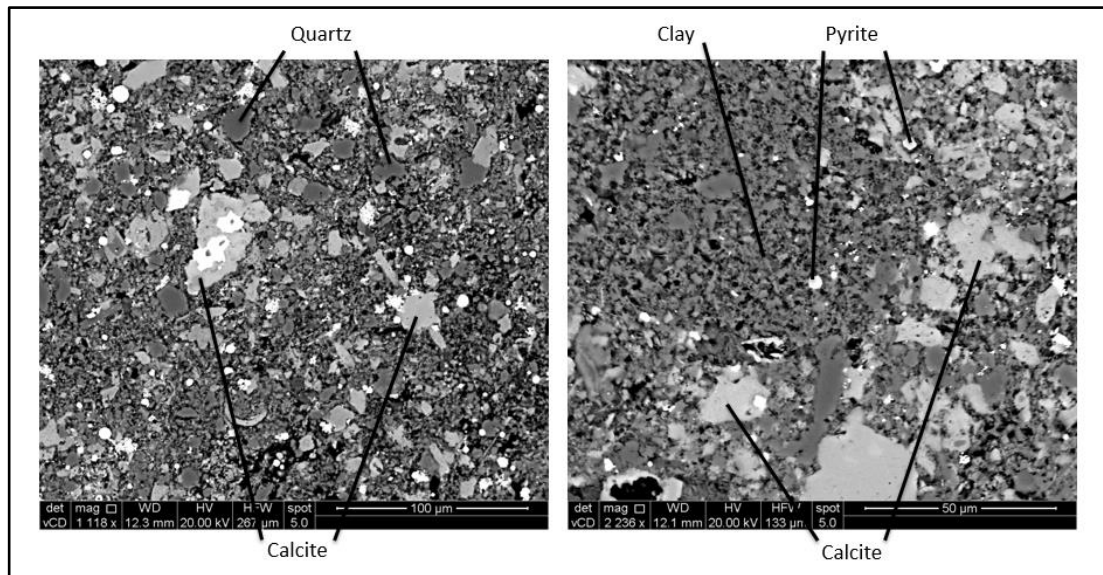


Figure 3-15: Backscatter scanning electron microscopy (BSEM) images of OC sample.

The D sample is quartz-rich with a moderate clay content; it contains relatively coarse grained detrital quartz grains ( $\sim 100 \mu\text{m}$ ) as shown in Figure 3-16. A variety of clay minerals are present (illite, smectite, chlorite and kaolinite). There was no pyrite or carbonate minerals observed in this sample.

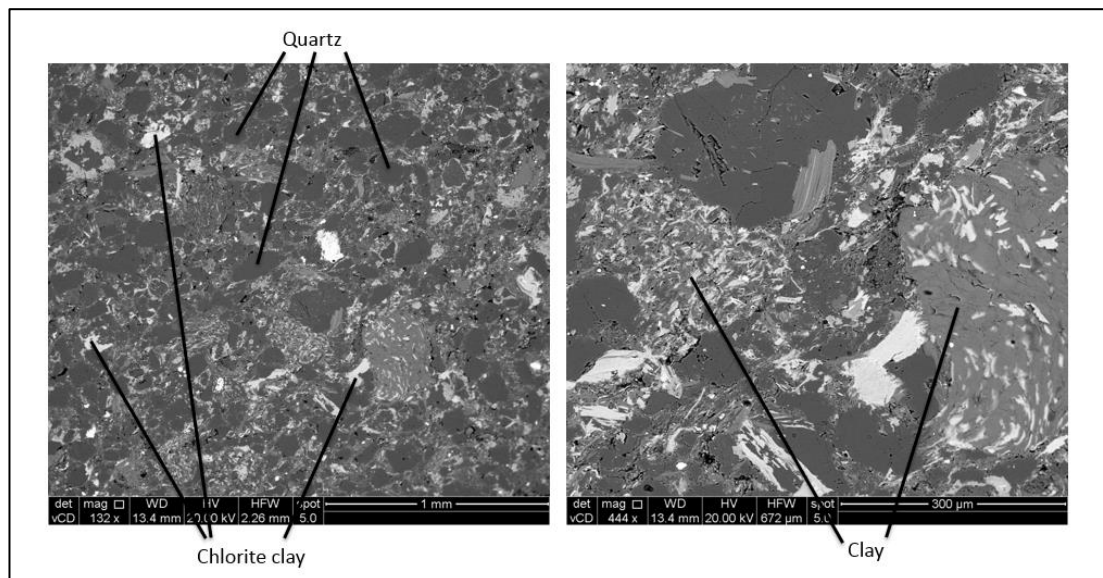


Figure 3-16: Backscatter scanning electron microscopy (BSEM) images of D sample.

### 3.2.2 Capillary properties and porosity results using MIP

All samples were tested using the MIP instrument to a maximum pressure of 60,000 psi. The measured mercury volume against mercury pressure was recorded and plotted in Figure 3-17. The pore size corresponding to each mercury step was calculated and used to generate pore size distribution. The pore size distribution in a form of pore diameter against incremental intrusion relationship for all sample are shown in Figure 3-18

The threshold pressure was estimated graphically using the method proposed by Daniel and Kaldi (2009). The threshold pressures together with the porosity estimated at the end of the experiment are shown in Table 3-3

Sample	Effective porosity (%)	Threshold pressure (psi)
WS	8.06	13,000
ALP	5.04	11,000
AM	3.01	18,000
KC	2.35	20,000
OC	1.71	20,000
D	0.35	400

*Table 3-3: Porosity and threshold pressure estimated using MIP technique.*

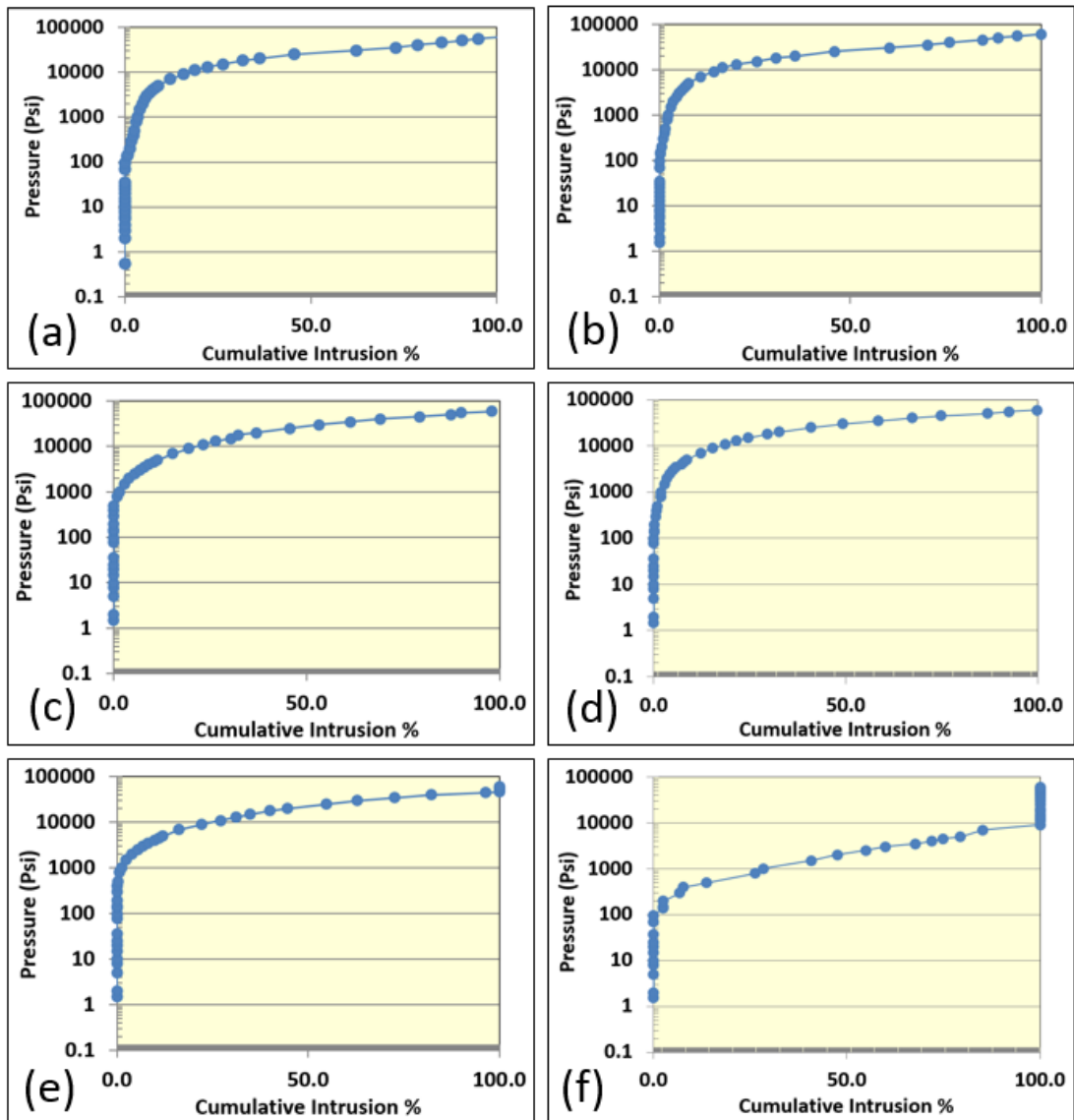


Figure 3-17: Mercury cumulative intrusion against mercury pressure for (a) WS, (b) ALP, (c) AM, (d) KC, (e) OC and (f) D samples.

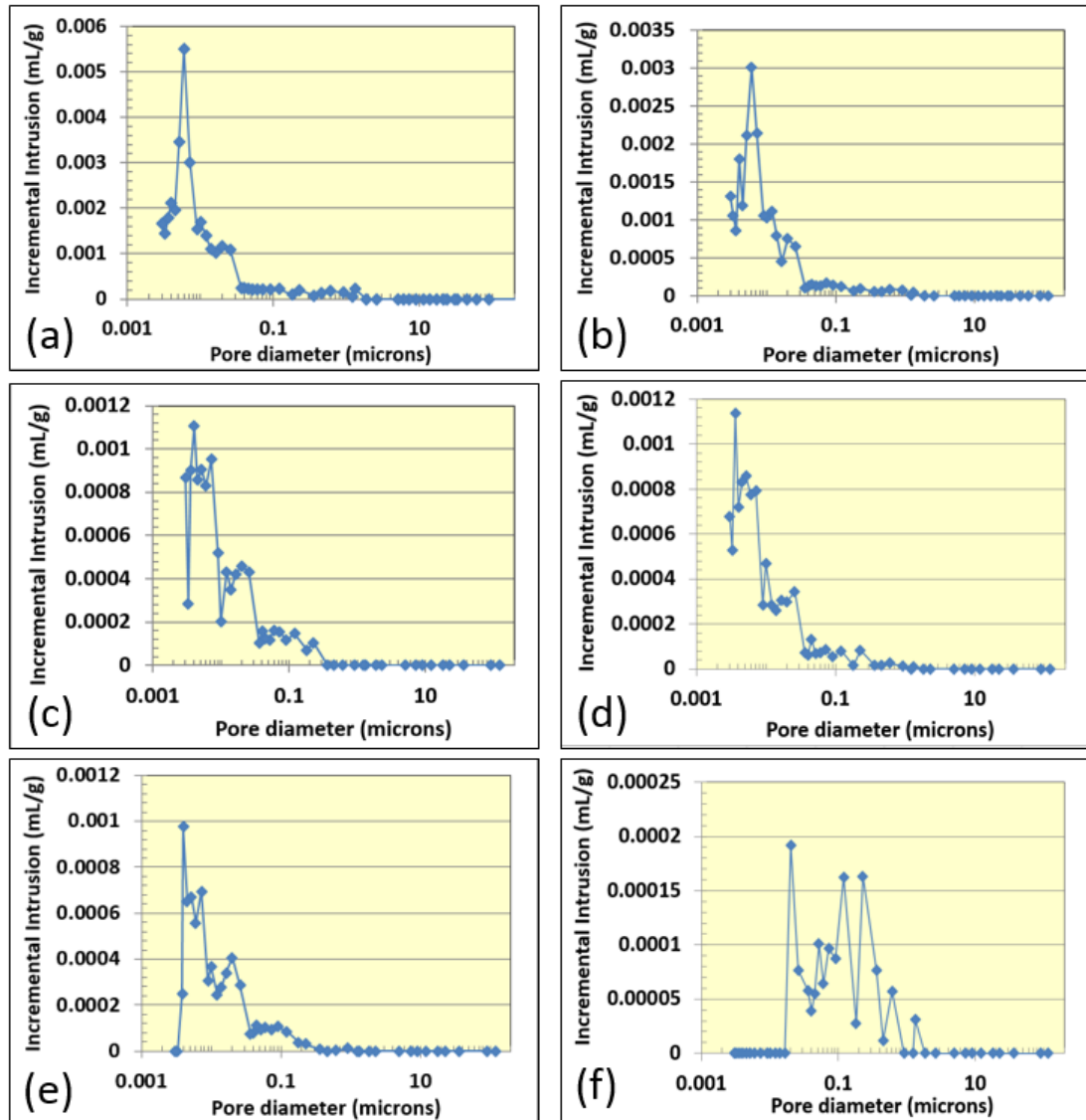


Figure 3-18: Pore diameter against incremental intrusion for (a) WS, (b) ALP, (c) AM, (d) KC, (e) OC and (f) D samples.

### 3.2.3 Multistage triaxial test

Mechanical multistage triaxial test was performed for four samples only; WS, KC, OC and D. It was difficult to drill a long enough core for the other two sample due to weak bonding between laminae. D sample is the stiffest sample in this sample set and was tested for 6 stages before failure. The peak principal stresses and the corresponding effective and deviatoric stresses are presented in Table 3-4. OC sample was only able to be tested for 3 stages before complete brittle failure (Table 3-5). KC and WS were tested for 5 stages before failure and the results are presented in Table 3-6 and Table 3-7 respectively.

$\sigma_1$ (MPa)	$\sigma_3$ (MPa)	$p$ (MPa)	$q$ (MPa)
125.6	3.0	43.9	122.6
175.0	10.0	65.0	165.0
234.4	20.0	91.5	214.4
319.7	40.0	133.2	279.7
356.6	50.0	152.2	306.6
393.1	60.0	171.0	333.1

Table 3-4 : Peak principle stresses before failure and corresponding effective and deviatoric stress of D sample.

$\sigma_1$ (MPa)	$\sigma_3$ (MPa)	$p$ (MPa)	$q$ (MPa)
122.3	3.0	42.8	119.3
138.8	6.0	50.3	132.8
155.5	10.0	58.5	145.5

Table 3-5: Peak principle stresses before failure and corresponding effective and deviatoric stress of OC sample.

$\sigma_1$ (MPa)	$\sigma_3$ (MPa)	$p$ (MPa)	$q$ (MPa)
183.8	10	67.9	173.8
220.8	20	86.9	200.8
254.6	30	104.9	224.6
282.1	50	127.4	232.1
308.3	68	148.1	240.3

Table 3-6: Peak principle stresses before failure and corresponding effective and deviatoric stress of KC sample.

$\sigma_1$ (MPa)	$\sigma_3$ (MPa)	$p$ (MPa)	$q$ (MPa)
45.1	3.0	24.1	21.1
53.6	6.0	29.8	23.8
67.6	10.0	38.8	28.8
95.4	20.0	57.7	37.7
115.4	30.0	72.7	42.7

Table 3-7: Peak principle stresses before failure and corresponding effective and deviatoric stress of WS sample.

The stresses and strains recorded are used to calculate Young's modulus and Poisson's ratio of the samples. Unconfined compressive strength (UCS), cohesion and friction angle are estimated using the principle peak stresses before failure. All properties estimated using triaxial data for all samples are summarized in Table 3-8. The peak principle stresses are then used to calculate effective and deviatoric stress at every stage. These stresses (shown in Figure 3-19) are part of the failure envelope of the sample.

Sample	E (GPa)	$\nu$	UCS (MPa)	Cohesion (MPa)	Friction angle
WS	12.89	0.102	36.5	10.6	29.8°
KC	24.50	0.299	101.4	31.1	27.0°
OC	26.75	0.182	109.0	25.1	40.6°
D	53.00	0.336	143.9	34.8	38.4°

Table 3-8: Summary of mechanical properties of all samples.

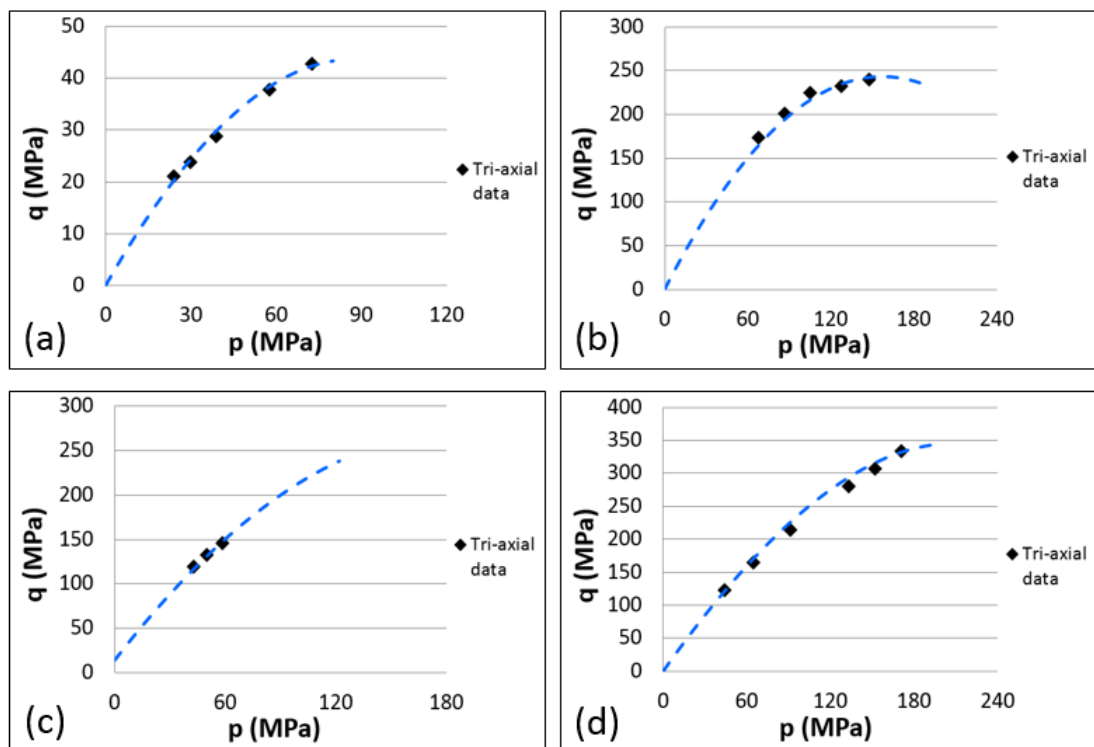


Figure 3-19: Stages at peak principle stresses in  $p$ - $q$  space of (a) WS, (b) KC, (c) OC and (d) D samples.



### 3.3 Discussion

Samples characterization was done based on mineralogical, petrophysical and geomechanical properties. The minerals composition by mass percentage of each sample results were summarized in Table 3-1, obtained from the XRD test. The XRD results were then used to classify shale samples used in this thesis. Valdiviezo-Mijangos and Nicolás-Lopez (2014) published mineralogical classification of shale-gas and shale-oil source rock using published data of mineralogy of shale-gas and shale-oil reservoirs (Rickman et al., 2008; Passey et al., 2010). It was done based on three mineralogical groups :

- Clay: includes clay, illite, smectite and kaolin minerals. Samples with clay content 50-80% are argillaceous lithotype.
- Carbonate: includes calcite, dolomite and siderite minerals. rocks with carbonate content 50-80% are of calcareous lithotype.
- Quartz: includes quartz, albite and feldspars minerals. rocks with carbonate content 50-80% are of siliceous lithotype.

The classification is presented in ternary plot shown in Figure 3-20. Shale-gas and shale-oil lithotypes are enclosed by the brown envelope. The samples used in this research are marked with black dots in the same figure. The difference size of marker represents the different percentages of pyrite content. As it can be seen, the samples used in this research are of a good diversity; three argillaceous rocks, one siliceous, one at the edge of calcareous. The last one, OC, falls in the core of the ternary plot which could be classified as a mixed mudstone (Valdiviezo-Mijangos and Nicolás-Lopez, 2014). TOC plays a role in controlling the stiffness of the sample. Shukla et al. (2013) presented a correlation between TOC and Young's modulus for Wolfcamp shale (Figure 3-21). An increase in the TOC weight percentage from 1% to 7% could result in a reduction of approximately 22% in Young's modulus. The samples used in this thesis has a range of TOC between 0.5% to 6.7% which reduce stiffness significantly.

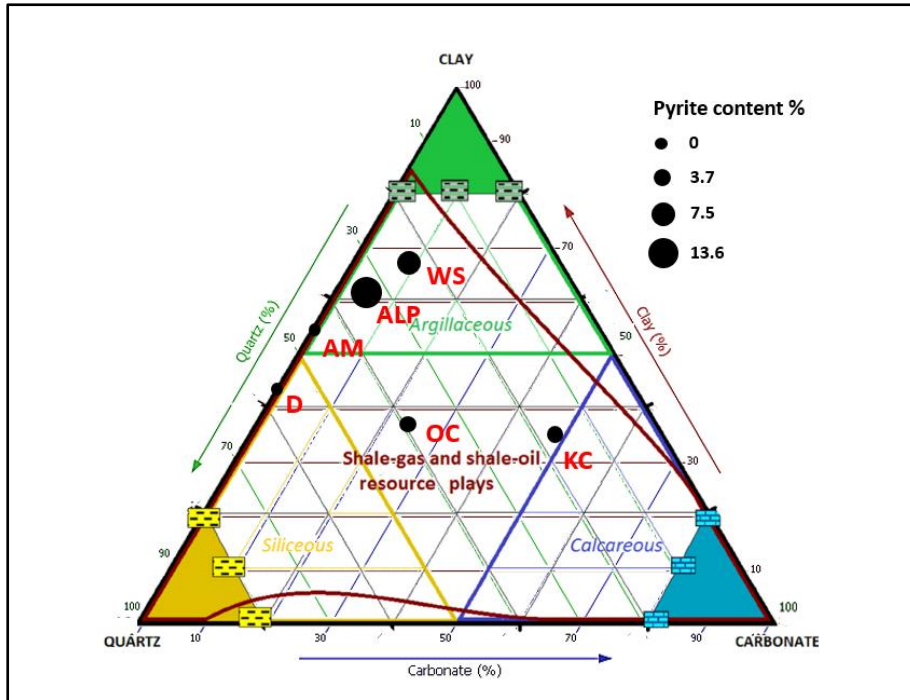


Figure 3-20: Ternary plot of mineral composition of shale rocks. The brown envelope encloses the shale-gas and shale-oil resources based on published data from Rickman et al. (2008) and Passey et al. (2010). The black points are the samples used in this research (Figure taken from Valdiviezo-Mijangos and Nicolás-Lopez, 2014).

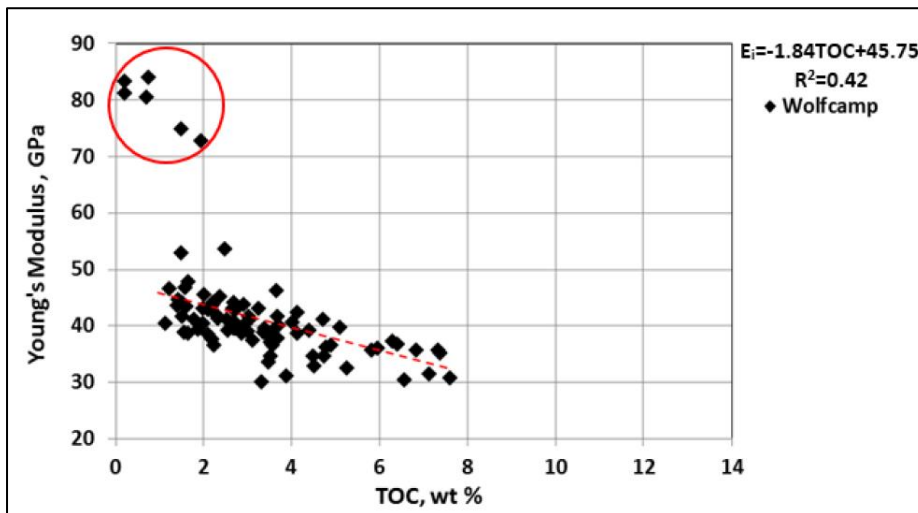


Figure 3-21: Correlation between TOC and Young's modulus for Wolfcamp shale (Shukla et al., 2013).

Porosity determines the capacity of rock to store fluid. It also has a large effect on mechanical properties of shale. For example, Chang et al. (2006) correlated porosity of sedimentary rocks with unconfined compressive strength (UCS) using data from different resources (e.g. Horsrud, 2001; Jizba, 1991; Lama and Vutukuri, 1978).

The data are plotted in Figure 3-22 and it can be clearly seen that the variation of UCS for the samples with porosities less than 10% is very high. For samples with porosity higher than 10%, the variation of UCS is very small.

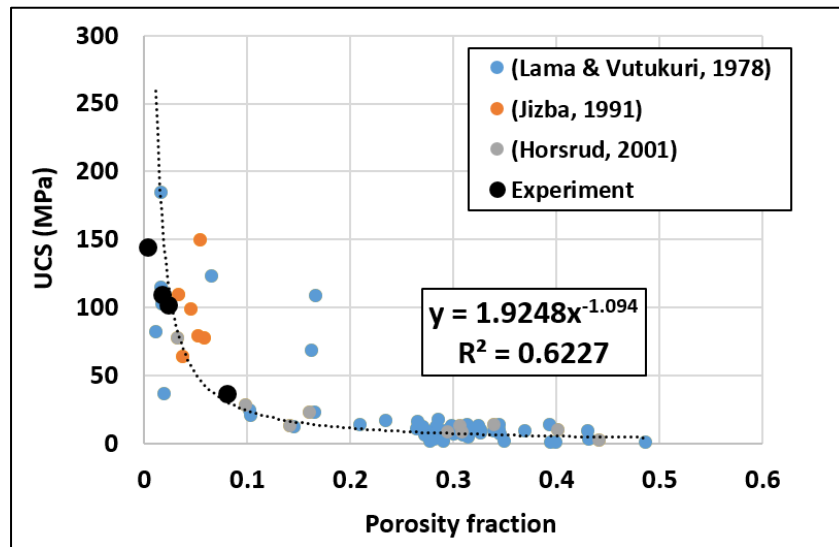


Figure 3-22: Correlation between uniaxial compressive strength and porosity (Chang et al., 2006). Black points are for the samples tested in this thesis.

Petrophysical and geomechanical properties were also measured using above explained techniques. Porosity was estimated using MIP because it is a quick and cheap method to get an understanding of the porosity of shale (Listiyowati, 2018). MIP has a limitation in terms of maximum mercury pressure (60,000 psi) which is equivalent to a pore throat of 3 nm. This means that MIP cannot capture pore spaces with pore throats smaller than 3 nm (Listiyowati, 2018). However, the porosity estimated provides a good fit with the correlation between porosity and unconfined compressive strength as it is shown in Figure 3-22. The porosity variation is about 0.35-8.06%, which provides a wide range of variation in mechanical properties (based on Figure 3-22). This was confirmed by Young's modulus obtained from multistage triaxial tests as it is shown in Figure 3-23. However, the multistage triaxial test was not performed on AM and ALP samples because they were weakly laminated and drilling a long enough core was challenging. TOC-Young's modulus relationship was also presented in Figure 3-24 for samples with triaxial data available. All properties measured for all samples are summarized in Table 3-9.

Sample name	Effective porosity MIP (%)	Threshold pressure (psi)	Clay content (%)	TOC (%)	Bulk Density (g/cc)	Young's modulus Triaxial (GPa)	Poisson's ratio
WS	8.06	13,000	61.9	3.36	2.46	12.89	0.102
ALP	5.04	11,000	52.9	6.53	2.40	-	-
AM	3.01	18,000	54.7	0.80	2.74	-	-
KC	2.35	20,000	32.6	6.70	2.51	24.54	0.299
OC	1.71	20,000	35.5	3.38	2.50	26.75	0.182
D	0.35	400	43.3	0.52	2.72	53.00	0.336

Table 3-9: Summary of samples properties

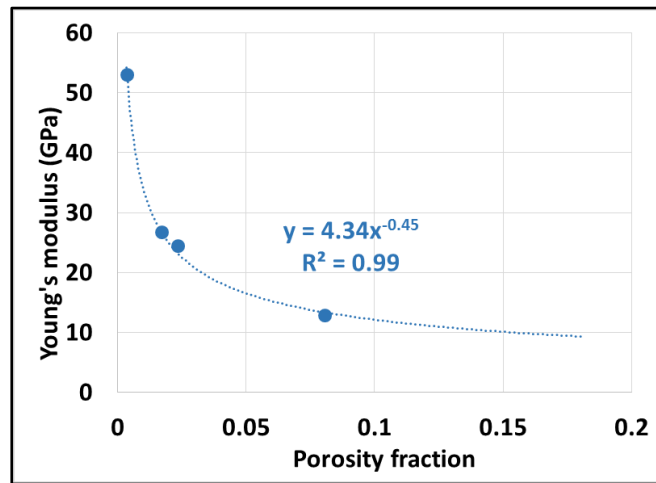


Figure 3-23: Porosity-Young's modulus relationship for shale sample with triaxial test data.

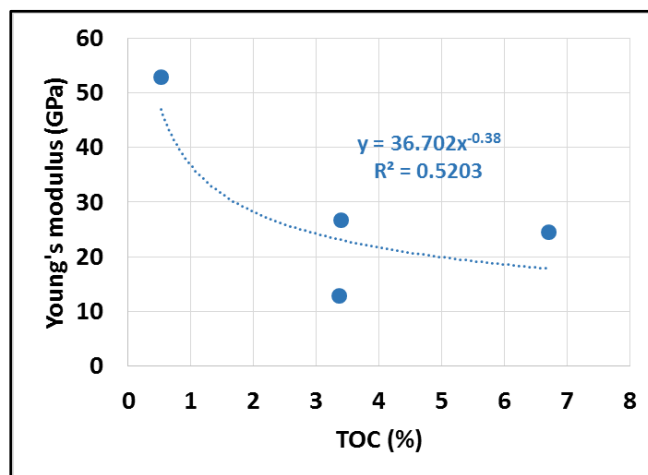


Figure 3-24: TOC- Young's modulus relationship for shale sample with triaxial test data.

### 3.3 Summary

Samples characterization was conducted to determine the mineralogical properties, petrophysical properties and geomechanical properties of the samples tested. The total number of samples used in this thesis is six samples. A set of experiments were performed on these samples to obtain these properties. Regarding mineralogy, XRD and backscatter imaging was conducted to obtain mineralogical and microstructural information. In addition, TOC was also measured using LECO furnace technique. The samples used in this thesis has a wide range in mineralogy; three argillaceous rocks, one siliceous, one calcareous and one of a mixed mudstone type. Range of TOC within the sample is significant (0.5%-6.7%), which will have an impact of stiffness of the sample.

Porosity is one of the main petrophysical properties that controls geomechanical properties of shale. Porosity estimation was done experimentally using the MIP technique. Threshold pressure was also measured using the same technique. For geomechanical properties, a multistage triaxial test was performed only on four samples (WS, KC, OC and D). The reason behind that is ALP and AM samples were weakly laminated and it was impossible to drill a long enough core plug for the test. Unconfined compressive strength (UCS) provides a good correlation with porosity, which agrees with the correlations published in the literature. Shale samples with porosity lower than 10% will have a big variation in mechanical properties while variation in mechanical properties of samples with porosity is higher than 10 % is minimum. All samples used in the thesis have porosity lower than 10 % which guaranty that the samples will have a wide range of mechanical properties.

## **4 Chapter IV: Investigation of controls of matrix flow within shale in deforming and non-deforming flow regimes**

### **4.1 Introduction:**

It has been argued that shale caprock could leak through the matrix by either a non-deforming flow in a form of capillary flow or as a result of flow through fractures formed in the caprock (Watts, 1987). Capillary flow leakage occurs when the pressure difference between the wetting (brine) and non-wetting (oil or gas) phases is high enough to overcome threshold pressure of the caprock (refer to Section 2.3.1). However, in stress sensitive rocks, such as shale, threshold pressure as well as other petrophysical properties vary with stress (Brace et al., 1968; Guise et al., 2017).

Threshold pressure determines sealing capacity of a caprock. Sealing capacity is defined as the petroleum column height that a caprock can seal through as a result of its capillary properties. A caprock would lose its sealing functionality when the buoyance forces exerted by the fluid column below the caprock are high enough to overcome capillary resistance. It should be noted that even if the threshold pressure of caprocks is exceeded, leak rates could be small due to their low permeability. The maximum petroleum column that a caprock can seal is calculated using equation (2-5).

Traditional MIP described earlier is often used to estimate the capillary entry and the threshold pressure of caprocks. However, the measurements are made under unconfined conditions and the threshold pressure is not directly measured but it is estimated based on the shape of the injection curve. The MIP measurements indicate that shale generally has a mercury threshold pressure between 1,000 to 21,000 psi (Almon et al., 2005; Dawson et al., 2003; Fisher et al., 2013). During the MIP test, mercury is exerting a hydrostatic pressure around the sample until mercury starts to invade pore spaces (Mitchell et al., 2003; Brown, 2015). If the threshold pressure in the MIP test is lower than the stress in the subsurface, it would mean that the sample is under a lower stress condition than in the subsurface, which could lead to an underestimation of the sealing capacity. This is due to the fact that the effective stress in the subsurface in some particular cases is higher the initial hydrostatic pressure applied by mercury in MIP before entry. A new instrument to measure mercury

injection parameters on a core sample was developed in the Wolfson Laboratory at the University of Leeds that allowed the sample to be subjected to a net stress during the MIP experiment. In this research, this instrument will be referred to as Mercury Porosimeter Under Confining Stress (MPUCS). The results presented by Guise et al. (2017) using this instrument suggest that for tight rocks, threshold pressure at reservoir condition could be three times higher than the one obtained from traditional MIP measurements. In this research, this instrument is used to investigate the sealing capacity of shale when subjected to confining stress. The threshold pressure under confining stress will be measured and compared against MIP results. Break-through pressure, which is the pressure at which mercury goes through the sample from one end to the other, is also recorded as it represents the pressure at which flow through the rock would start; this is the true threshold pressure of the sample.

Flow through shale could also occur via preferential pathways that are formed by the high fluid pressure as it is claimed by radioactive waste management industry (Horseman et al., 1999). Evidences of existence of these pathways at the micro-scale are still not available as these pathways are stress dependent and could close after reducing pore pressure. All evidences available in the literature are based on changes observed in the samples, such as increase of matrix permeability with increasing pore pressure and of slight volumetric expansion and mechanical deformations with increasing pore pressure (Horseman et al., 1999; Cuss et al., 2014a; Tawara et al., 2014). A new idea in this research is proposed to induce preferential pathways and image these pathways using a Scanning Electron Microscope (SEM). The idea is to heat and force low melting point metal, such as Field's metal, into a sample to form preferential pathways. Field's metal will solidify when cooled and the sample can then be polished and imaged to identify the flow pathways. It is believed that this phenomenon is likely to happen in clay-rich rock such as mudstones. Clay-rich synthetic samples were prepared with different percentages of clay content and compacted using a consistent synthetic sample preparation procedure. Details of samples preparation, experimental method and results followed by a discussion are presented in next sections of this chapter.

## 4.2 Sample preparation

### 4.2.1 Controls of matrix flow within shale by capillary flow

Shale samples were drilled perpendicular to the bedding into cylindrical core plugs and ground at both ends to ensure that they were perfectly parallel. Small (1.5 cm length) cubes were also prepared for MIP. Table 4-1 summarises properties of the samples used for MPUCS. AM and D samples were excluded in these test due to difficulty in drilling a sufficiently long core plug.

Sample	Weight (g)	Length (mm)	Diameter (mm)
KC-M1	110.54	39.90	37.50
OC-M1	69.05	24.77	37.71
WS-M1	69.81	27.40	36.85
ALP-M1	195.93	74.12	39.02

Table 4-1 : Summary of the samples used for MPUCS.

### 4.2.2 Controls of matrix flow within shale by pathway dilation

Synthetic samples were prepared carefully in the laboratory to ensure constituency. Two minerals were used in making samples, kaolin and medium grained silica sand. The used sand in preparing the samples is from Bent Farm quarry and has a density of 2.65 g/cm<sup>3</sup> and average grain size of 271µm. Kaolin had an average grain size of 2 µm. Three samples were prepared with different sand to clay ratios as is shown in Table 4-2. Required weight ratio of the two minerals were mixed together carefully with an aim of producing a mixture that is as homogenous as possible. The mixture is placed in heat shrink and inserted in a compaction assembly designed in-house (Figure 4-1).

Sample	Clay (Weight %)	Sand (Weight %)
SY-1	25	75
SY-2	50	50
SY-3	80	20

Table 4-2: Samples minerals by percentage weight.

Compaction assembly consists of the three main parts; tube; plunger and cap as it is shown in Figure 4-1. All parts are made of aluminium to be able to image the sample later under CT-scanner. Plastic heat shrink material is placed inside the tube



to house the sample and to avoid sample material to flow past the plunger. Plunger is designed with grooves to allow air to escape while compaction. Cap is designed with holes on top to allow Field's metal to flow to the top of the sample. Stress will be applied from both top and bottom of the assembly to compact the sample.

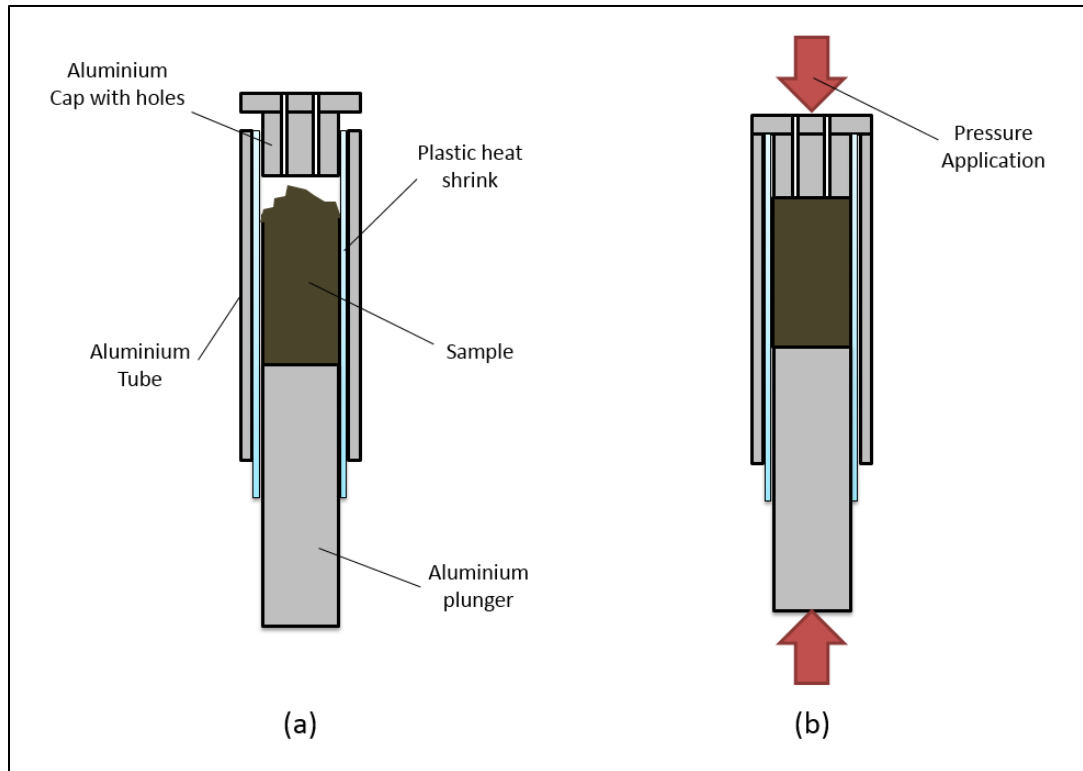


Figure 4-1: Schematic of compaction assembly (a) before compaction, (b) after compaction.

After the right amounts are mixed and placed in the compaction assembly, the assembly then is loaded in a mechanical rig to apply an axial load. Compaction was done in three cycles of loading/unloading; 1000 psi, 1500 psi and 2000 psi. At each loading step, the sample is kept under compression for at least 24 hours to settle. The final compacted sample has a diameter of 31 mm and a length between 27-28 mm (Figure 4-2).

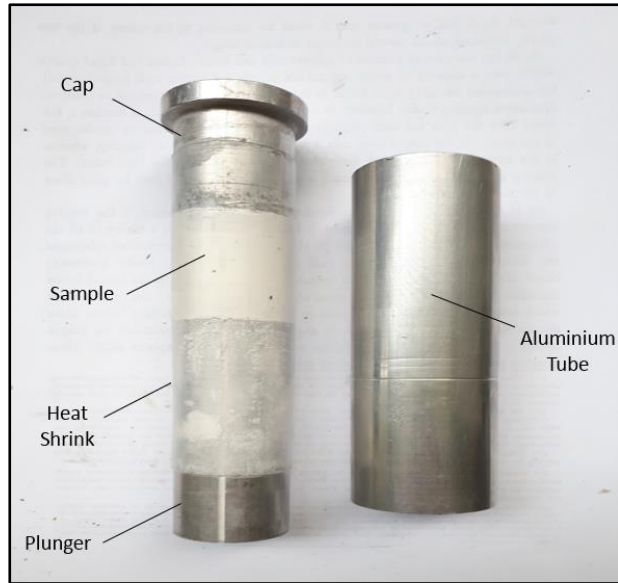


Figure 4-2: Photograph of compaction assembly after compaction.

## 4.3 Experimental method

### 4.3.1 Controls of matrix flow within shale by capillary flow

MPUCS instrument was designed and developed in Wolfson Multiphase Flow Laboratory at University of Leeds (Guise et al., 2017). The setup consists of five main parts; pressure vessel, sample assembly, pumps, instrumentation system and controlling software (Figure 4-3). The pressure vessel houses the sample assembly and it is designed to withstand a pressure of up to 100,000 psi (Figure 4-4). Confining pressure is applied via hydraulic oil supplied by a pump to the pressure vessel. The sample assembly contains the sample and end platens with a sealing system around to avoid confining oil entering the sample. End platens have electric terminals to measure electrical conductivity throughout the experiment. Electrical conductivity will be used as an indication of mercury breaking through the sample. MIP instruments does not have conductivity measurement and breakthrough pressure cannot be measured. Resolution of MIP is better than  $0.1 \mu L$  while resolution of MPUCS is better than  $1.0 \mu L$ ; as the size of the samples for MPUCS is around 10 times that used for MIP, they have similar relative resolution. Unconfined mercury injection was performed using MIP instrument described earlier and the results will be compared against MPUCS results.

Mercury is injected into the sample through a separate pump (Figure 4-3). Confining pressure is applied by a separate pump, which follows injection pump to

maintain the required net stress. This instrument is capable of applying a net stress (difference between confining and pore pressure), between 1,000 to 15,000 psi and maintain this net stress throughout the experiment up to a Hg injection pressure of 50,000 psi. This is the main advantage of MPUCS over MIP as there is no control over net stress in MIP. Computer software controls the injection pressure using an algorithm similar to MIP. Injection pressure is applied in a pre-set pressure steps and the pressure is increased automatically whenever mercury flow rate goes to a pre-set value (0.001 cc/min in this case). The second main advantage is the capability of MPUCS to take electrical measurement across the sample to allow the threshold pressure to be measured as opposed to MIP, where it has to be estimated based on the shape of the curve. All pressures and flow rates are measured and recorded precisely using high accuracy instruments through computer software. The data recorded is filtered and processed through a separate Excel sheet. After applying system and mercury compressibility correction, pore diameter is calculated using Young-Laplace equation presented earlier.

The selection of net stress to be applied on samples are based on the available data of the sample at reservoir conditions. Out of the four samples tested, the only sample with a known burial depth is the ALP-M1 sample. The net stress associated with the burial depth of the sample is about 4,250 psi. WS-M1 and KC-M1 are collected from outcrops and not from cores obtained from actual reservoir. A different strategy was proposed for studying these samples. The plan was to run MPUCS at the maximum net stress expected in a reservoir (about 7,000 psi) and investigate their sealing capacity. If no break-through occurred at 7,000 psi net stress, the sample was run again at low net stress (1,000 psi) to study the effect of stress (assuming only a small amount of mercury has invaded the sample). OC-M1 sample information is confidential and thus is tested using the same procedure as the outcrop samples. All net stresses used in testing these samples are listed in Table 4-3.

Sample	Net stress applied (psi)
KC-M1	1,000 psi and 7,000 psi
OC-M1	1,000 psi and 7,000 psi
WS-M1	1,000 psi and 7,000 psi
ALP-M1	4,250 psi

*Table 4-3 : Summary of net stresses used to test the samples.*

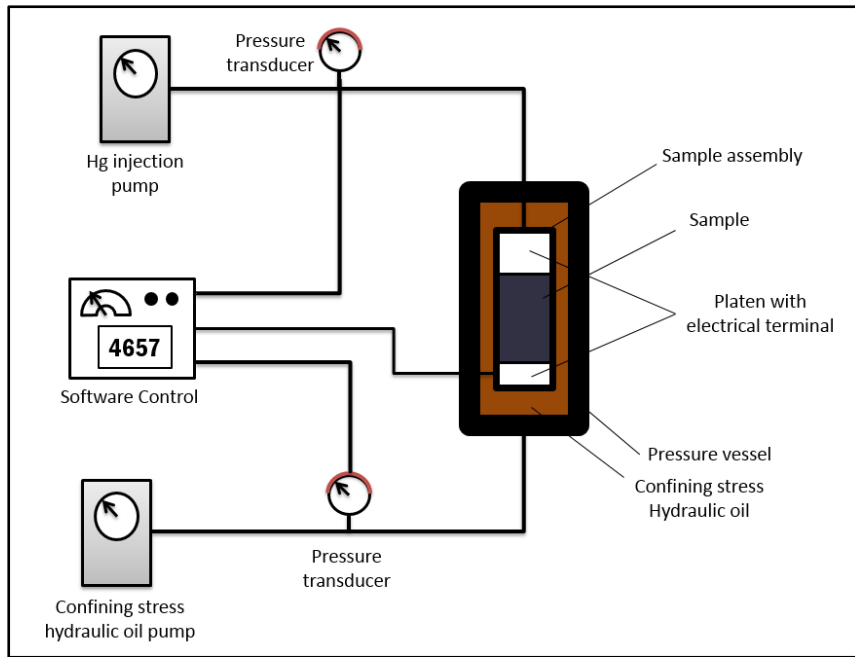


Figure 4-3: Schematic diagram of MPUCS setup (Guise et al., 2017).

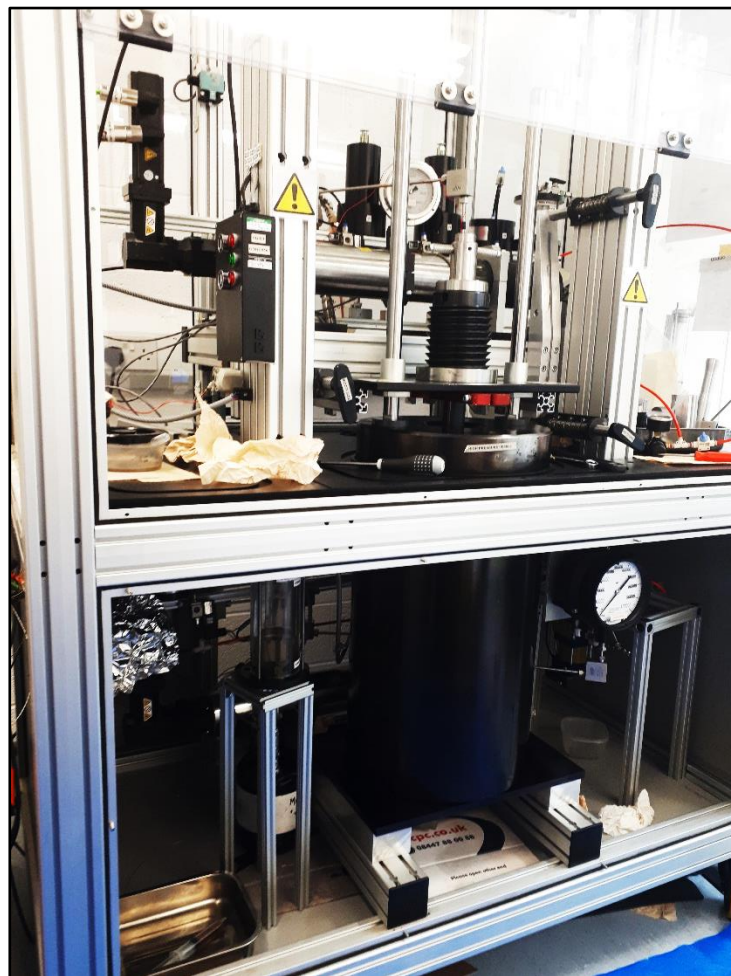


Figure 4-4: Picture of the MPUCS instrument (Guise et al., 2017).

The estimation of the threshold pressure from MIP data is done quantitatively and qualitatively using different methods (Cranganu and Soleymani, 2015). Sutton et al. (2004) suggested that the threshold pressure is the mercury pressure which corresponds to the 10% mercury saturation in the sample. A graphical approach was suggested by Cranganu and Villa (2005) by fitting the best straight line through the points in the pressure vs saturation after the plateau as it is shown in Figure 4-5. The pressure-axis intercept of this line is the threshold pressure. The last qualitative graphical approach was proposed by Daniel and Kaldi (2009), which suggested that the threshold pressure is the pressure which corresponds to the point where the pressure vs saturation curve starts to concave upward. An example of all three methods is shown in Figure 4-5. These methods provide an estimate of the threshold pressure, which might be biased due to heterogeneity of the rock. The threshold estimation for all samples in this thesis were done using Daniel and Kaldi (2009) method.

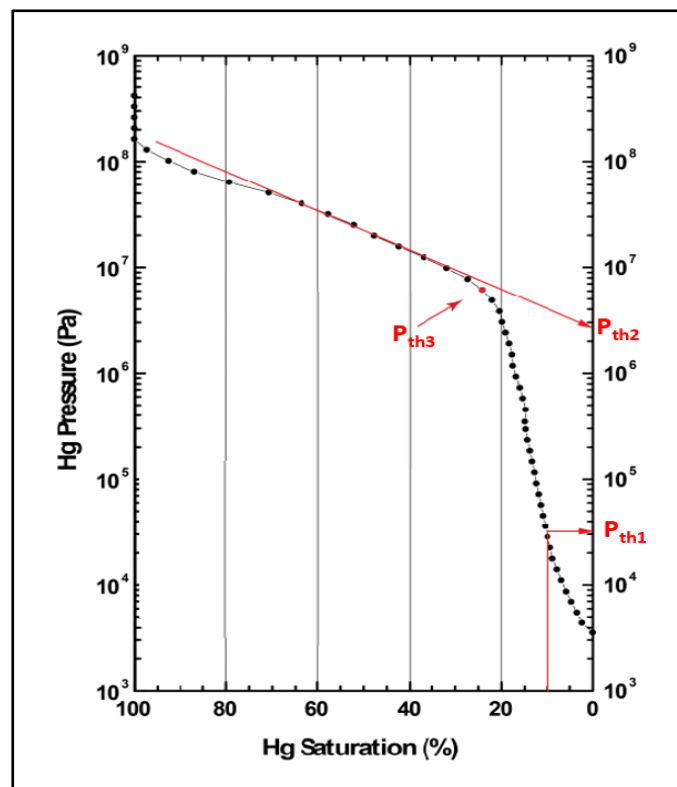


Figure 4-5: Figure showing the an example of threshold pressure measurement using the three different methods;  $P_{th1}$  using Sutton et al. (2004),  $P_{th2}$  using Cranganu and Villa (2005) and  $P_{th3}$  using Daniel and Kaldi (2009); the figure is taken from Cranganu and Soleymani (2015).

### 4.3.2 Controls of matrix flow within shale by pathway dilation

The aim of the experiment is to be able to visualize how preferential pathways form in micro-scale. Field's metal was chosen for injection because it is safe to handle and has a relatively low melting point. Field's metal is an alloy of indium (51.0%), bismuth (32.5%) and tin (16.5%) by weight, which are not toxic (Alfa Aesar, 2006). Field's metal has a melting point of 62 °C, which means that the experiment has to be conducted at temperature higher than 62 °C. There is no direct measurement of wettability of Field's metal published in the literature. Kouraytem et al. (2016) estimated Field's metal liquid surface tension using properties of main components and found it to be 0.41 (N/m).

Field's metal was injected into a sample through a pressure cylinder designed in-house to provide a better control of injection pressure (Figure 4-6-a). The pressure cylinder is basically a hollow cylinder with plunger inside to transmit pressure from water to the melted metal. O-rings are present to provide the required sealing to avoid flow across the plunger.

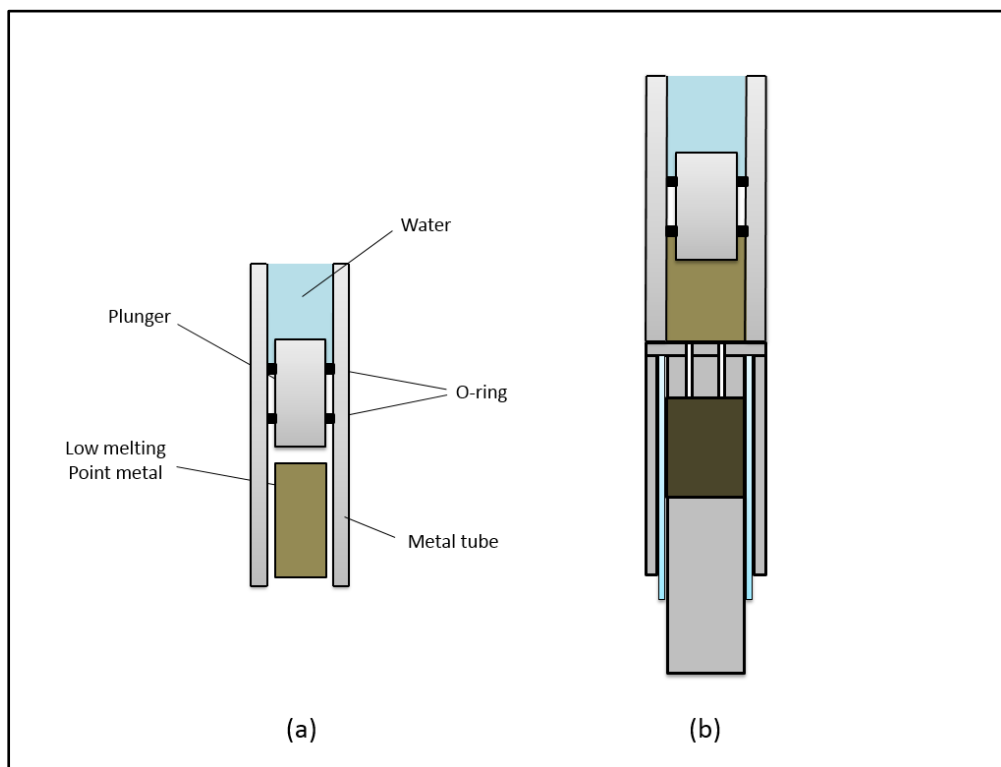


Figure 4-6: Schematics of pressure cylinder assembly (a) components of the pressure cylinder, b) full assembly with the sample and compaction assembly. Sizes of some components are exaggerated for the purpose of clarification.

Pressure cylinder assembly and compaction assembly (Figure 4-6-b) are placed inside a bi-axial core holder that has a hydraulic ram to apply axial stress. This ram is capable of applying a maximum axial stress of 3000 psi under the experiment working conditions. The core holder is then placed in an oven and heated up to a temperature of 100 °C, which is above melting point of Field's metal by 38 °C (Figure 4-7). Temperature is measured by a thermocouple and regulated using a controller. Confining pressure is applied through a rubber sleeve in the core holder using oil supplied by the high pressure pump. The maximum confining pressure that could be applied using this core holder at that temperature is about 3000 psi. Injection pressure is applied using positive displacement pump. The temperature, injection pressure and flow rates are monitored throughout the experiment. The purpose of monitoring flow rates and injection pressure is to be able to anticipate when injection starts and when to stop the experiment. A photograph of the setup is presented in Figure 4-8. Once a significant amount of metal is injected, the experiment will be stopped and left to cool down for a period of 6 hours. Compaction assembly is then removed from the core holder and scanned using CT scanner to visualize the metal within the sample. The CT scanner used is Brivo 385 from General Electric with a maximum resolution of 200  $\mu\text{m}$  in x-direction and 625  $\mu\text{m}$  in y-direction. The sample is then removed from compaction assembly and cut into slices. Some slices will be impregnated in resin for SEM microstructure analysis and others will be fragmented for secondary electron imaging, which is good for topography inspection. The SEM used was FEI Quanta FEG 650, provided from Field Electron Ion Company (FEI).

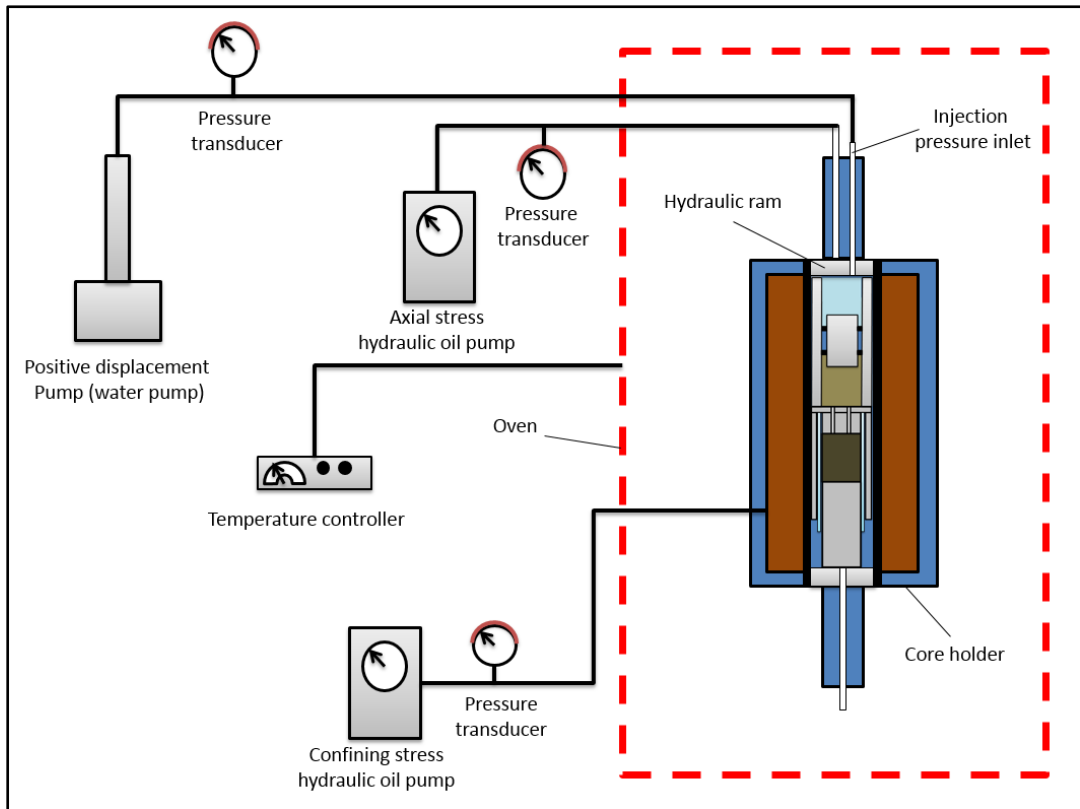


Figure 4-7: Schematic of Field's metal injection experiment setup.



Figure 4-8: Photograph of Field's metal injection experiment setup.



The experimental procedure can be summarized as:

- Inspect the pressure cylinder to make sure it is clean and the O-rings are all in a good condition.
- Calculate the amount of metal required using the following equation:  
Volume of metal required= (porosity of sample\*sample volume)\*1.05
- Shape the metal into a cylindrical ingot with the same diameter as the inner diameter of the pressure cylinder using a die made of Teflon by placing it in 100 °C oven.
- Place the plunger inside the pressure cylinder followed by metal ingot.
- Place the compaction assembly at the Field's metal beside of the pressure cylinder as it is shown in Figure 4-6-b.
- Insert the whole assembly in the core holder as it is shown in Figure 4-7.
- Place the core holder in the oven.
- Connect the pressure cylinder to the pump through the inlet and slowly pump water to fill the injection line with water.
- Apply axial stress of 500 psi. The reason of applying a low axial stress is that when the oven is turned on, the hydraulic oil will expand and hence pressure will increase.
- Apply confining pressure of 500 psi using the high pressure pump. Again, the confining pressure applied is low because oil will expand with increasing temperature which will increase pressure in the core holder.
- Turn on the oven and set the required temperature, which is around 100 °C, using temperature controller and wait for approximately 3 hours until the system is stabilized thermally. During this process, confining and axial stress must be monitored as they might exceed the operating limit due to oil expansion. When the system stabilizes, set the confining pressure to 2000 psi and axial stress to 2000 psi.
- Start applying constant injection pressure steps and monitor the volume flow rate. At each pressure step, wait until the volume flow rate goes close to zero (about 0.001 cm<sup>3</sup>/min) before increasing the pressure to the next step. The volume flow rate gives an indication of whether metal goes into the sample or not.

- The experiment is considered finished when a significant volume of water change between two pressure steps is noticed. This will be an indication that the metal went into the sample.
- Once the experiment finished, turn off the oven and leave the system under pressure for approximately 6 hours to make sure that the metal solidifies and the system is cooled down.
- Compaction assembly is removed and imaged using CT scanner.
- Then, the sample is removed and cut into slices. Some slices are impregnated in resin and polished using standard SEM block preparation procedure to be imaged later. The others are fragmented and also imaged using SEM.

## **4.4 Experimental results**

### **4.4.1 Controls of matrix flow within shale by capillary flow**

MPUCS provides accurate measure of the breakthrough pressure at which flow will start through the sample using electrical conductivity test. This measurement is done at reservoir condition by applying a net effective stress to the sample close to the reservoir condition. Buried petroleum systems are normally subjected to a reservoir net effective stress of 3,000 to 15,000 psi (Guise et al., 2017).

The ALP-M1 sample was the first sample tested. Figure 4-9 shows mercury saturation versus pressure and pore diameter versus fractional incremental intrusion curves for both MIP and MPUCS. MIP threshold pressure is estimated to be 11,000 psi, which is confirmed by pore size distribution curve indicated with a red arrow in Figure 4-9. The threshold pressure in MPUCS could not be estimated graphically as little amount of mercury went in the sample. Mercury did not break-through the sample as no indication of electrical conductivity was noticed even at mercury pressure as high as 60,000 psi.

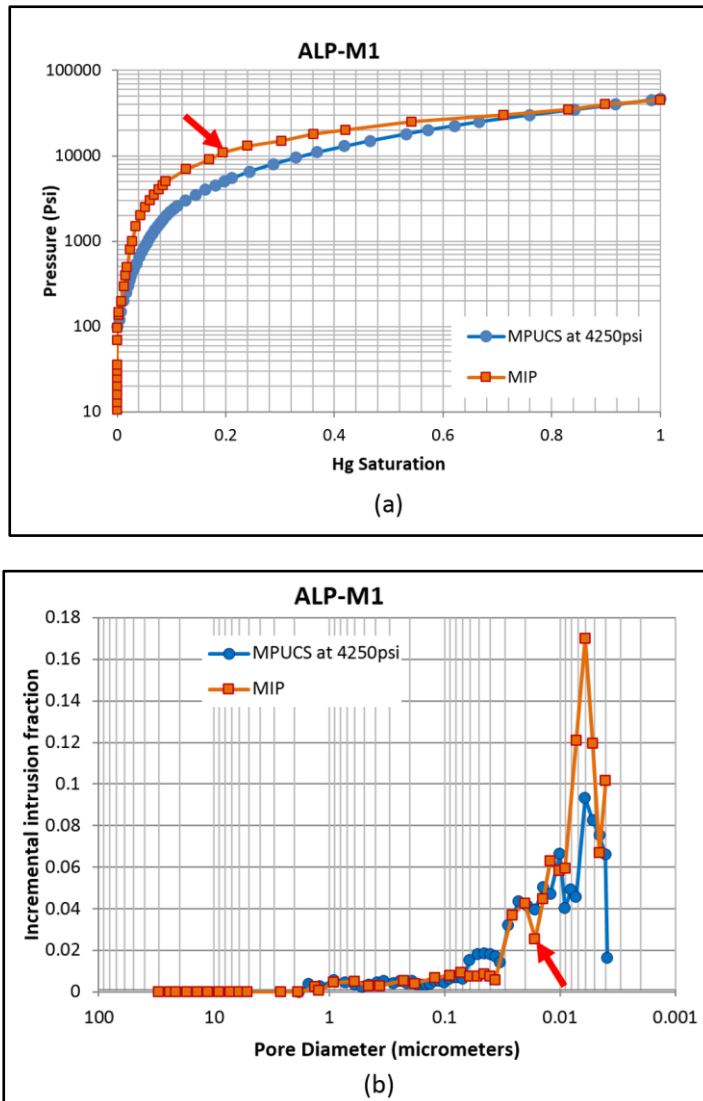


Figure 4-9: ALP-M1 MIP (red) and MPUCS (blue) at 4250 psi net stress ((a) is the mercury saturation vs pressure; (b) is pore diameter vs fractional incremental intrusion) . Red arrow indicates estimate of threshold pressure from MIP.

The second sample tested was the KC sample in two stages; at 7000 psi and 1000 psi net stress. Figure 4-10 represents data of KC-M1 sample of MIP and MPUCS at 7000 psi net stress. Break-through of mercury did not occur using MPUCS at this net stress, even when the mercury pressure was increased to 60,000 psi. The threshold pressure for MIP was found to be about 20,000 psi and shown on the graphs in Figure 4-10.

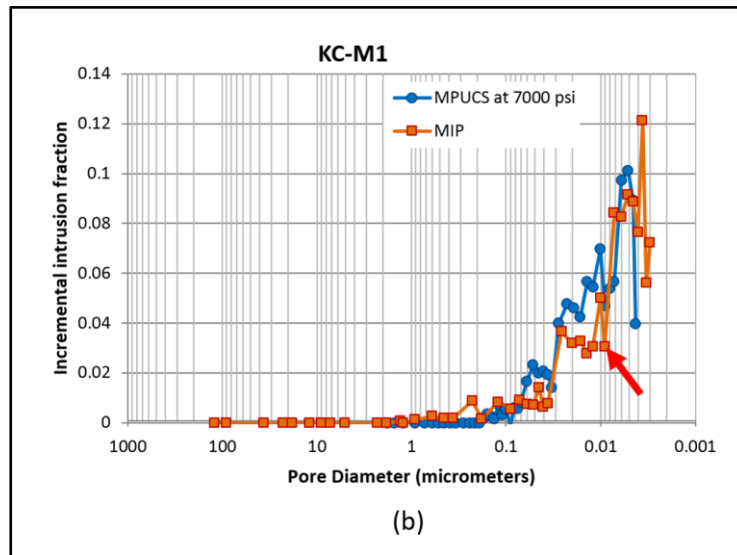
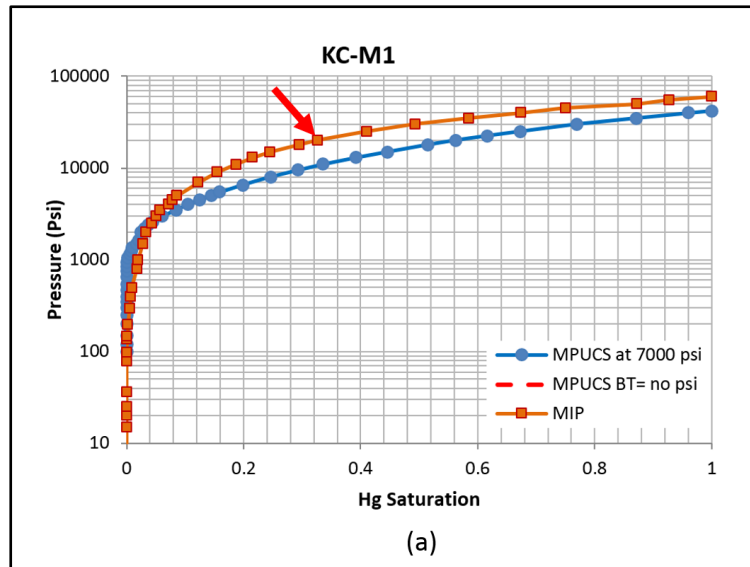


Figure 4-10: KC-M1 MIP (red) and MPUCS (blue) at 7000 psi net stress ((a) is the mercury saturation vs pressure; (b) is pore diameter vs fractional incremental intrusion) Red arrow indicates estimate of threshold pressure from MIP.

The sample (KC-M1) was reanalysed using MPUCS at a low net stress to observe mercury breakthrough pressure. The net stress was set to be 1000 psi and the experiment was run again to 60,000 psi. Electrical conductivity was detected at a mercury injection pressure of 50,000 psi, which indicates mercury breakthrough as it is shown in Figure 4-11.

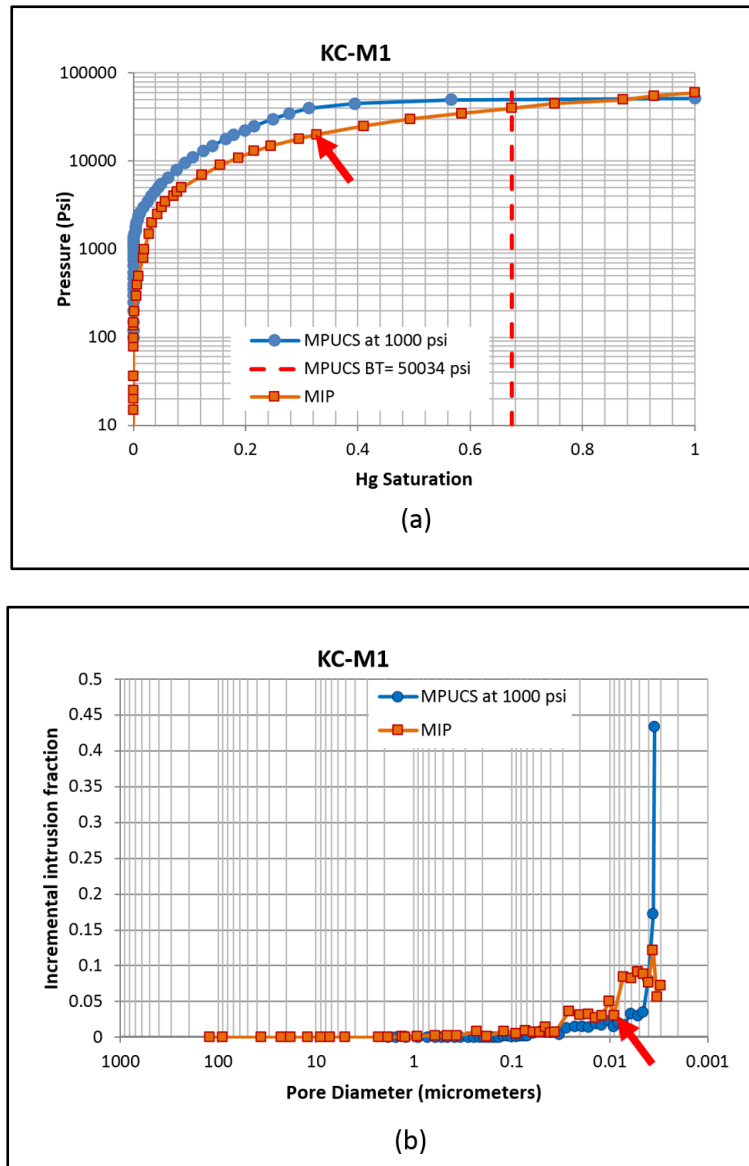


Figure 4-11: KC-M1 MIP (red) and MPUCS (blue) at 1000 psi net stress ((a) is the mercury saturation vs pressure; (b) is pore diameter vs fractional incremental intrusion). Red arrow indicates estimate of threshold pressure from MIP and dashed line indicates the mercury breakthrough recorded.

OC-M1 was processed using the same procedure as KC-M1. Figure 4-12 presented the data obtained from MIP and MPUCS at 7000 psi net stress. OC-M1 has similar mechanical properties and mineral composition as KC-M1 and it was expected that their behaviour will be similar as well. At 7,000 psi, no mercury breakthrough was noticed in OC-M1 throughout the experiment. The threshold pressure estimated from MIP was found to be 20,000 psi, which is the same value as KC-M1. When the net stress of MPUCS was reduced to 1,000 psi, breakthrough in OC-1M sample occurred at 39,000 psi as it is shown in Figure 4-13.

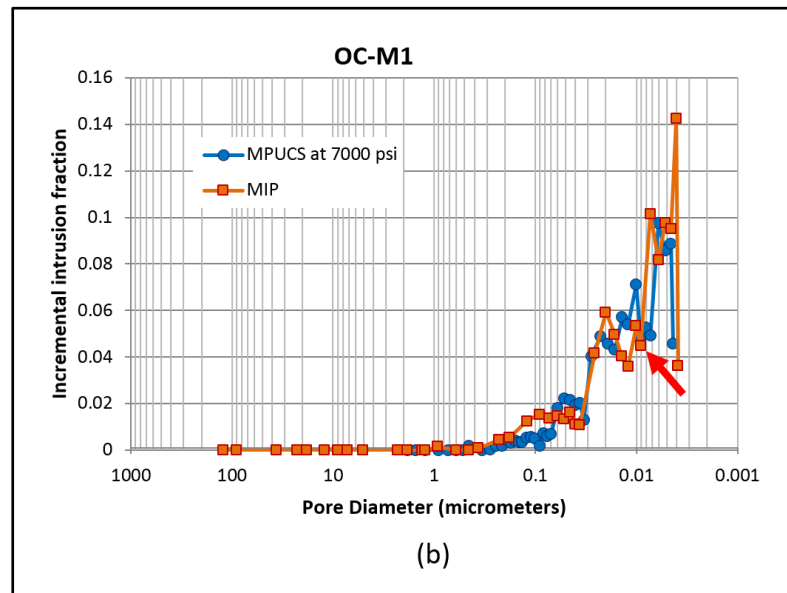
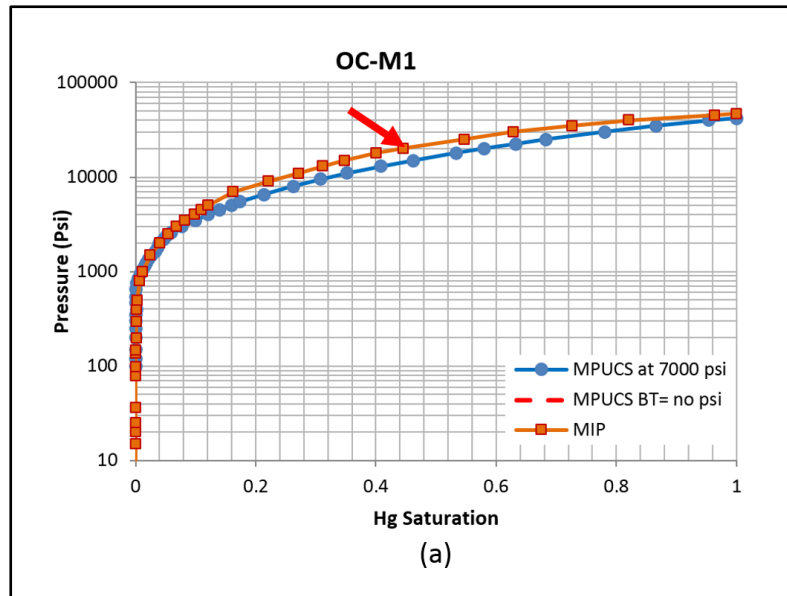


Figure 4-12: OC-M1 MIP (red) and MPUCS (blue) at 7000 psi net stress ((a) is the mercury saturation vs pressure; (b) is pore diameter vs fractional incremental intrusion).

Red arrow indicates estimate of threshold pressure from MIP.

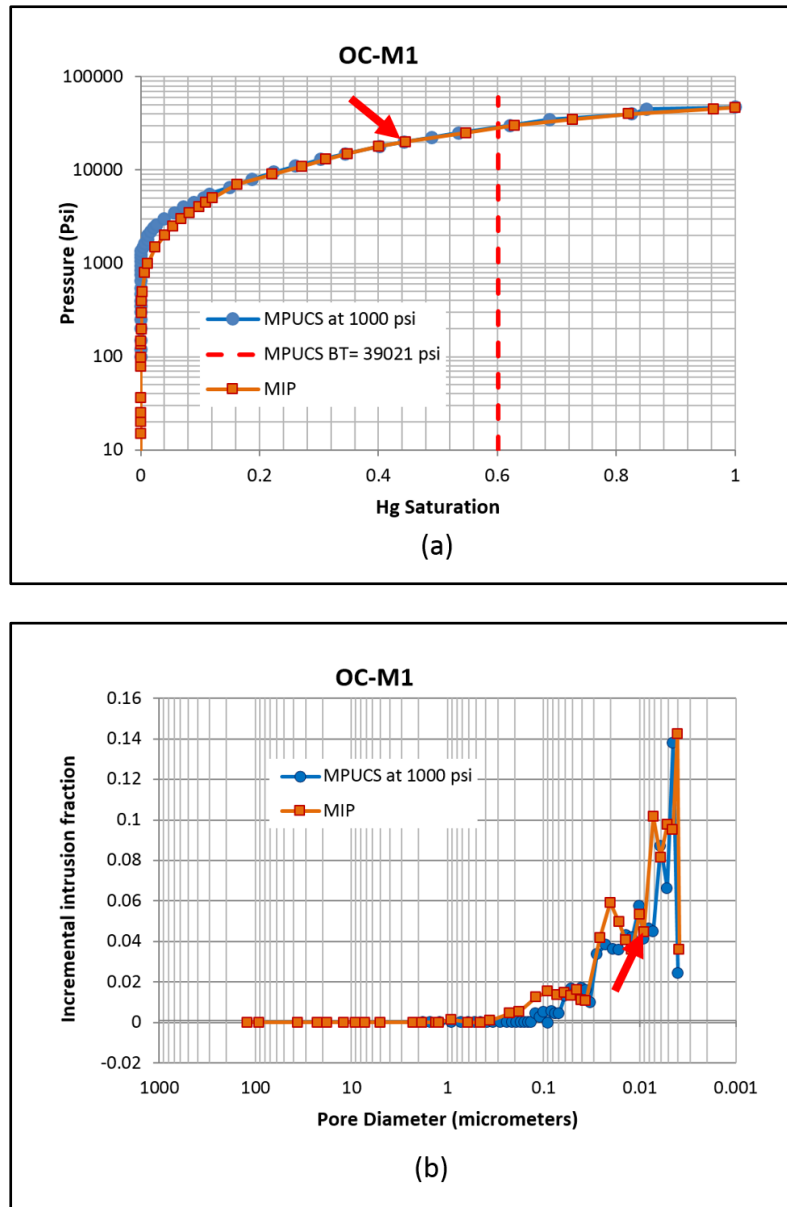


Figure 4-13: OC-M1 MIP (red) and MPUCS (blue) at 1000 psi net stress ((a) is the mercury saturation vs pressure; (b) is pore diameter vs fractional incremental intrusion). Red arrow indicates estimate of threshold pressure from MIP and dashed line indicates the mercury breakthrough recorded.

The last sample tested was WS-1M, which is a weakly laminated. The sample behaved similar to the others with no mercury breakthrough notice even at 60,000 psi injection pressure when MPUCS was run at net stress 7000 (Figure 4-14). The threshold pressure was estimated to be around 13,000 psi using MIP technique.

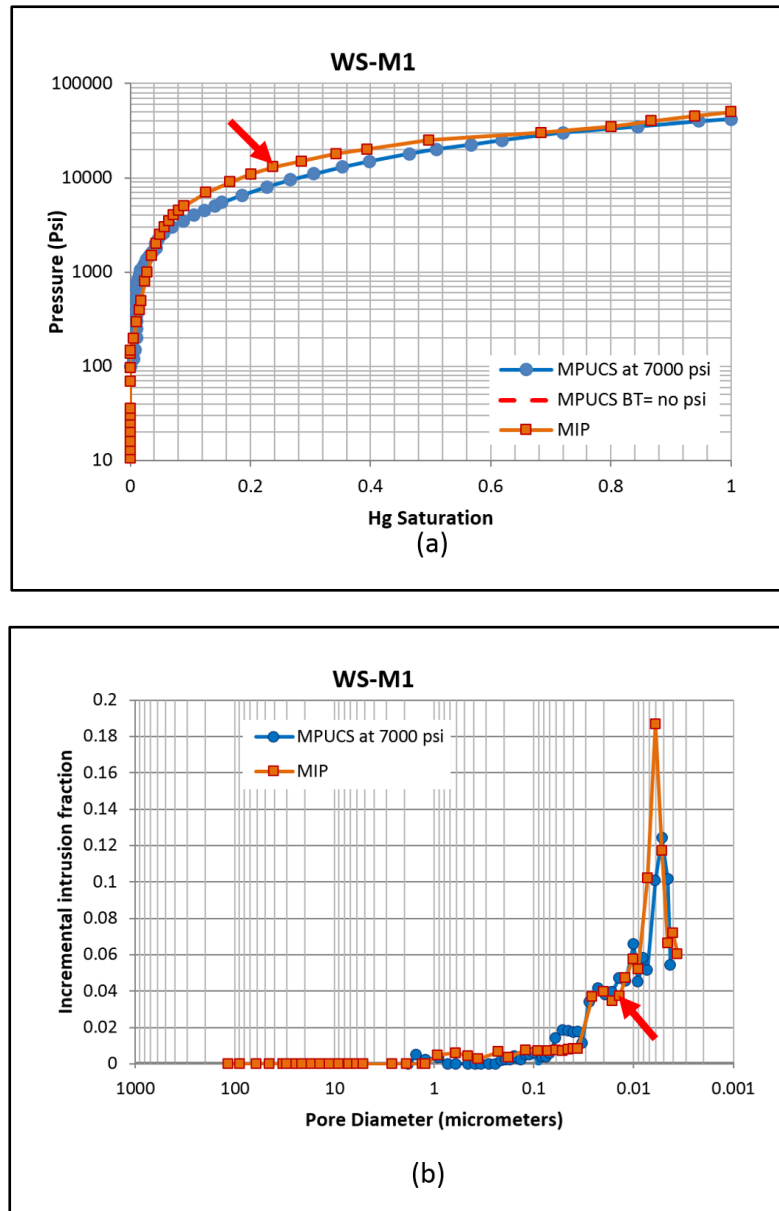


Figure 4-14: : WS-M1 MIP (red) and MPUCS (blue) at 7000 psi net stress ((a) is the mercury saturation vs pressure; (b) is pore diameter vs fractional incremental intrusion).

Red arrow indicates estimate of threshold pressure from MIP.

However, when the net stress was reduced to 1,000 psi for the second MPUCS run, breakthrough was detected at around 3,500 psi, which is far lower than estimated using MIP. The reason behind this behaviour is either the sample developed a crack when it was stressed and unstressed during the previous test or due to an error during the test. However, looking at the data in Figure 4-15, MPUCS, the threshold pressure was estimated to be 25,000 psi using the graphical approach. A summary of all results obtained using the tests is presented in Table 4-4.



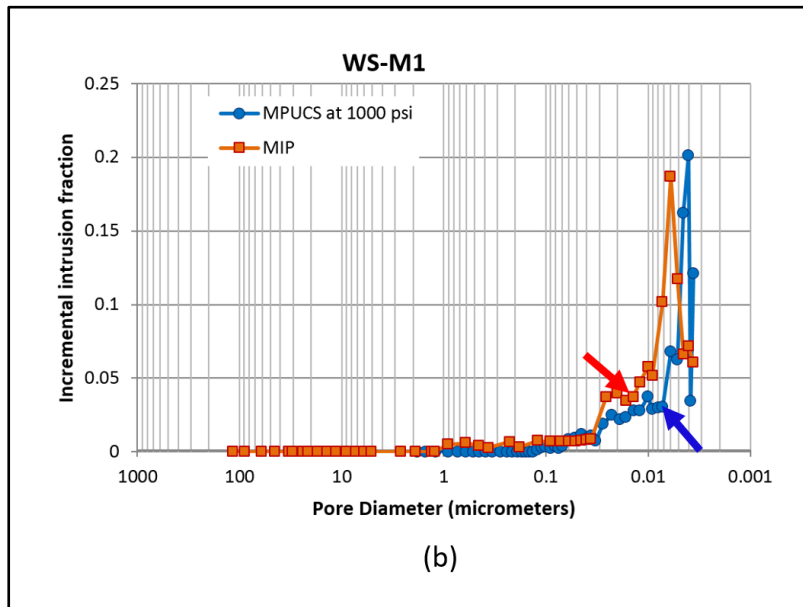
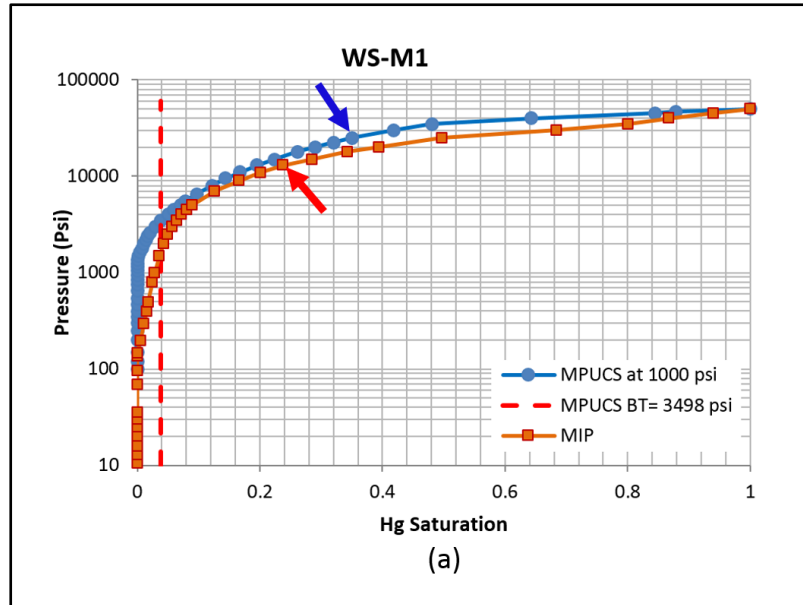


Figure 4-15: WS-M1 MIP (red) and MPUCS (blue) at 1000 psi net stress ((a) is the mercury saturation vs pressure; (b) is pore diameter vs fractional incremental intrusion). Red arrow indicates estimate of threshold pressure from MIP and blue arrow indicates estimate of threshold pressure from MPUCS. Dashed line indicates the mercury breakthrough recorded.

Sample	Threshold pressure MIP (psi)	Breakthrough pressure MPUCS (psi)	
		7000 psi net stress	1000 psi net stress
ALP-M1	11,000	*No breakthrough	
WS-M1	13,000	No breakthrough	25,000
KC-M1	20,000	No breakthrough	50,000
OC-M1	20,000	No breakthrough	39,000

Table 4-4: Summary of the results of MPUCS against MIP. \* ALP-M1 was test at a net stress of 4,250 psi.

#### 4.4.2 Controls of matrix flow within shale by pathway dilation

The first step before conducting the experiment was to determine all pressure losses within the system due to friction. To estimate the losses, the pressure cylinder was loaded in the core holder without the compaction assembly and placed in the oven. The systems took around 3 hours for the confining pressure and axial stress to stabilize. A constant flow rate of water (5 cm<sup>3</sup>/min) was injected into the core holder while observing the injection pressure. Pressure and time are plotted in Figure 4-16. It can be clearly seen that the system needed at least 77 psi to overcome friction (marked as P<sub>min</sub>) and then 48 psi to continuously move the piston (marked as P<sub>mov</sub>).

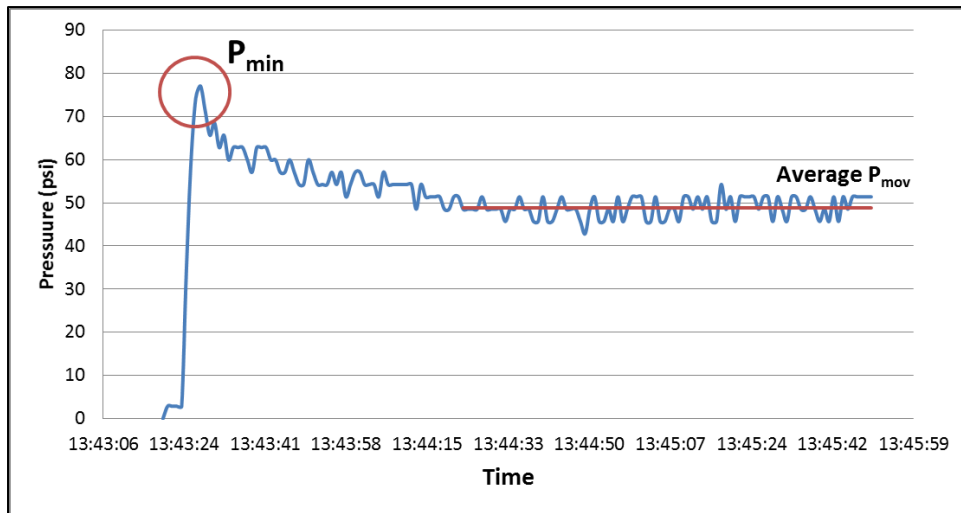


Figure 4-16: Hydraulic pressure versus time plot to estimate friction.

SY-1 was loaded in the core holder and placed inside the oven and then heated to 100 °C until the system is stabilized. Initially, 55 psi injection pressure was applied to overcome friction. The pressure was then increased in steps of 5 psi while monitoring the volume flow rate. Volume flow rate was stabilizing quickly (about 15

minutes) at each pressure step until pressure reached 115.7 psi. The volume flow rate took around one hour to stabilize at that particular pressure. This pressure point is believed to be the pressure where the metal started going in the sample and it is estimated to be 67.7 psi after removing friction effect (Figure 4-17). The injection pressure was then increased and large volumes of water pumped in were recorded. The experiment was then stopped at a pressure of 137 psi (89 psi after removing friction effect) and the system was left under pressure until it was cooled down and the metal was solidified. Helical CT scan images of the sample were then taken and combined to form a 3D image shown in Figure 4-18, where the sample was set to be transparent and metal in white using ImageJ.

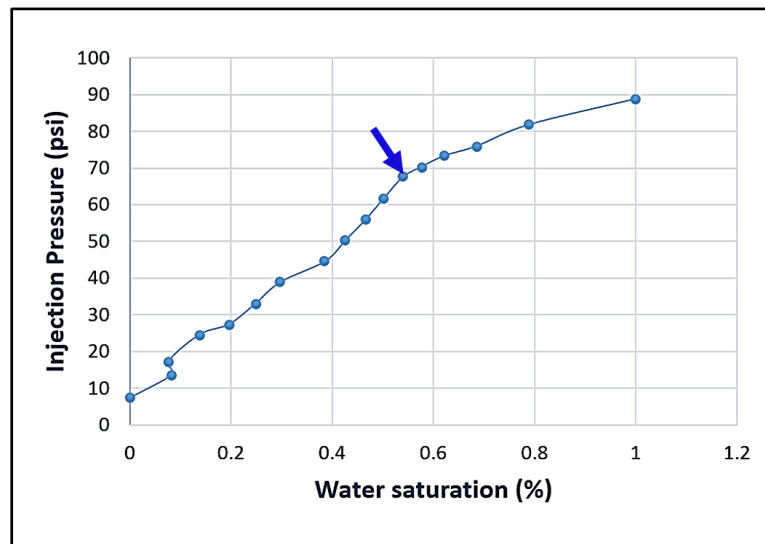


Figure 4-17: SY-1 injection pressure vs saturation of the water used to apply injection pressure after removing friction effect. Blue arrow points at the threshold pressure.

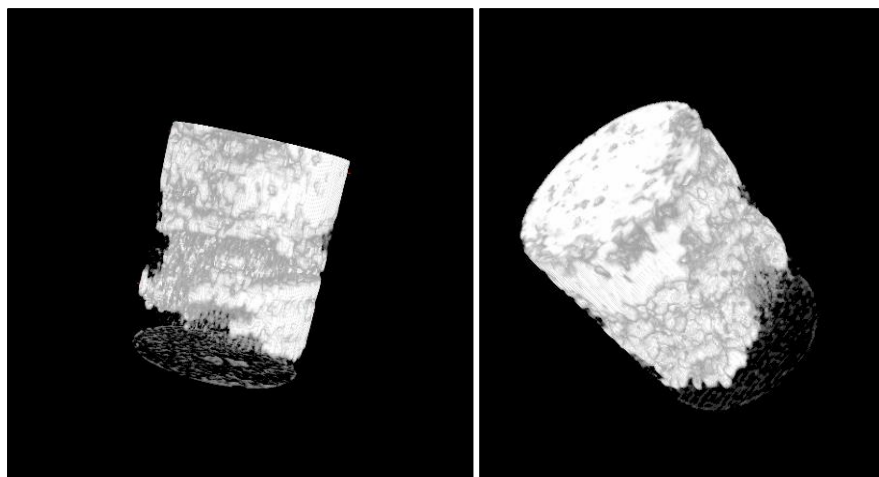


Figure 4-18: 3D Image of SY-1 generated from CT images using ImageJ. The sample is set to be transparent and the metal is shown in white.

After removing SY-1 from compaction assembly, it was sliced into three slices; two slices were impregnated in resin and one slice was disaggregated. Figure 4-19 are SEM Images of two slices from top and bottom of the sample with metal shown in white colour. The maximum diameter of the metal filaments was found to be about 200  $\mu\text{m}$ . Figure 4-20 are magnified images at a different location in the surface, which confirms the same observations.

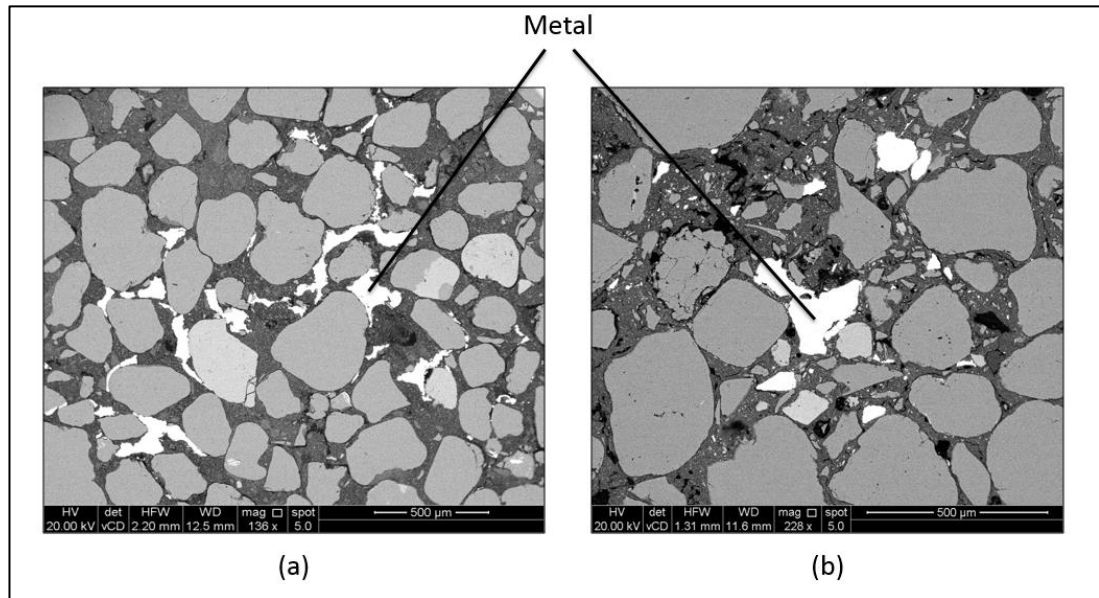


Figure 4-19: SEM images of SY-1 (a) Top segment and (b) bottom segment.

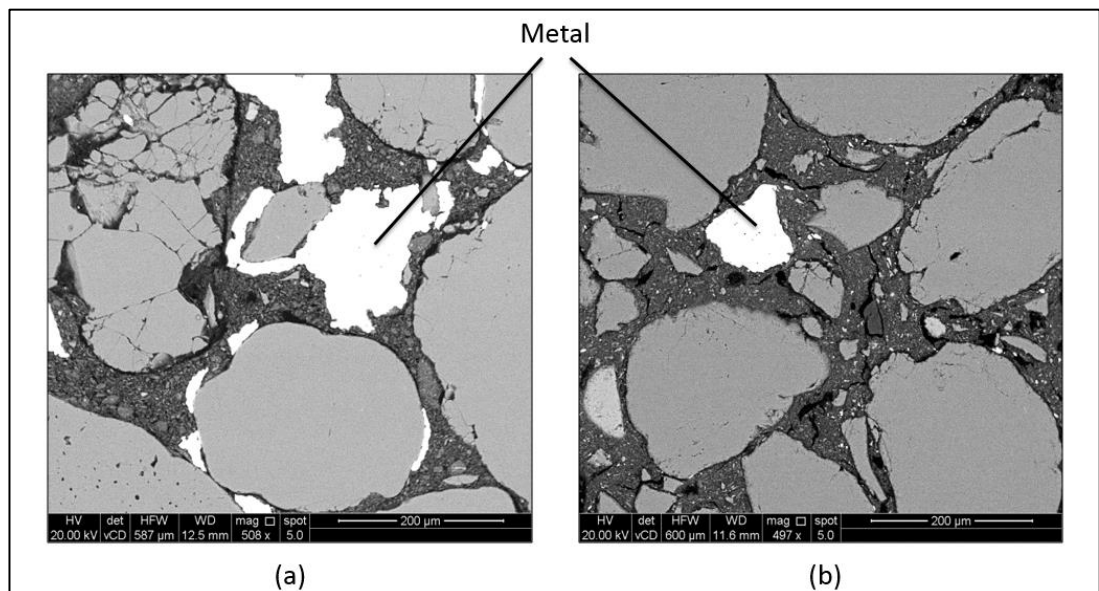
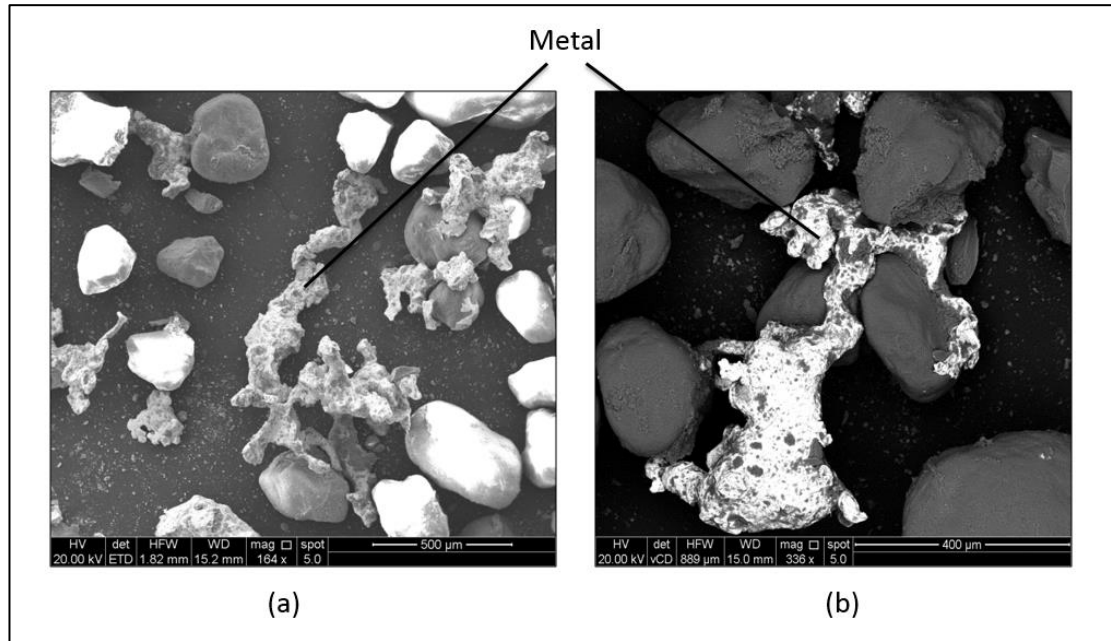


Figure 4-20: Magnified SEM Images of SY-1 (a) Top segment and (b) bottom segment.

The secondary electron image of disaggregated SY-1 showed long pieces of metal as is shown in Figure 4-21a. A long piece of metal, about 1000  $\mu\text{m}$  long and average width of 150  $\mu\text{m}$  with irregular shape was observed. Figure 4-21b shows how the metal is moving around sand grains during injection, which describes why the metal observed have irregular shape.



*Figure 4-21: Secondary electron microscopy images of fragmented segment of SY-1 (a) Long metal piece (b) Field's metal flowing around the grains.*

The second sample to test was SY-2. Similarly, the initial injection pressure applied was 55 psi to overcome friction. The pressure was then increased in steps of 5 psi using the same procedure (Figure 4-22). The hydraulic ram had a fault when the injection pressure reached 212.7 psi and reduced the axial stress, which caused injection pump to overshoot to 635 psi and hence large volume of water was detected. 3D image using CT scan images shows that a significant amount of metal went in the sample Figure 4-23.

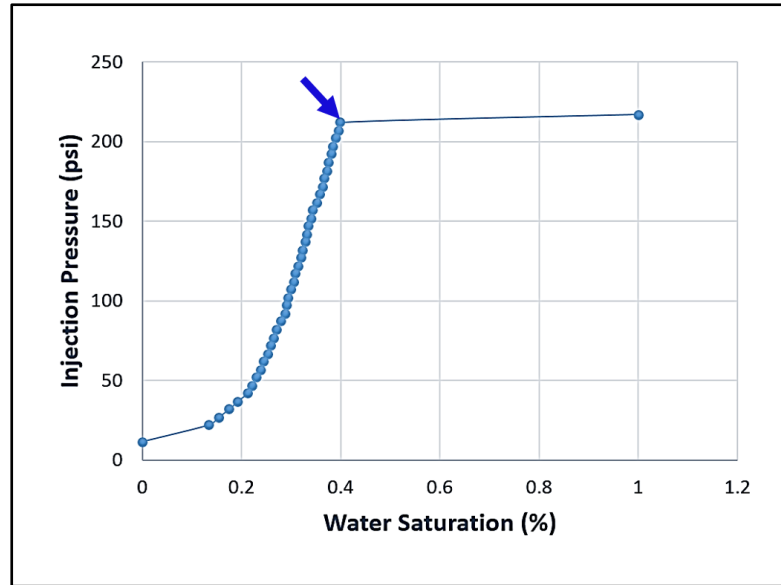


Figure 4-22: SY-2 injection pressure vs saturation of the water used to apply injection pressure after removing friction effect. Blue arrow points at the threshold pressure.

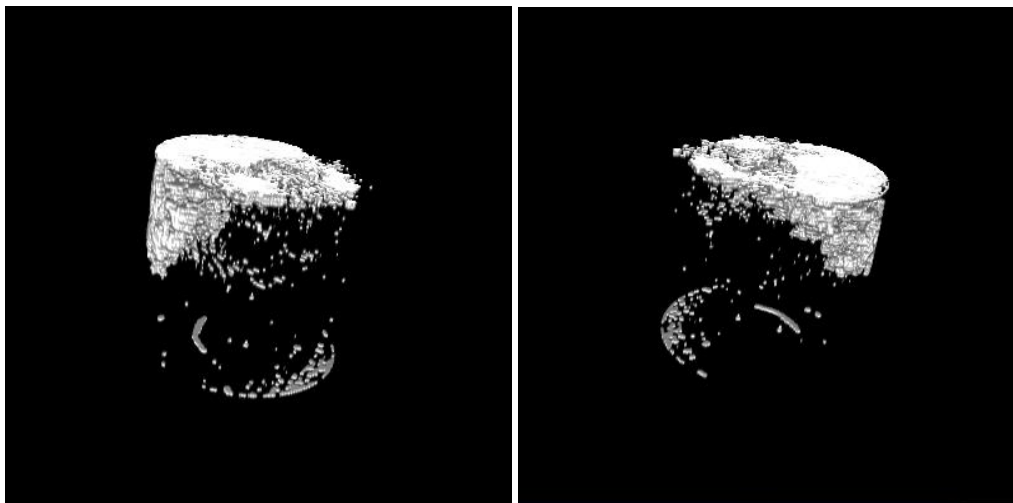


Figure 4-23: 3D image of SY-2 generated from CT images using ImageJ. The sample is set to be transparent and the metal is shown in white. The free hanging dots in the middle of the sample is not metal, they appear when the colour threshold was applied; this is due to low resolution of CT scan used.

Field's metal penetrated halfway into the sample (Figure 4-23) only although injection pressure overshoot to 635 psi. Figure 4-24 represents SEM images of SY-2 sample showing metal in between sand grains. The size of the metal filaments are far smaller than the ones formed in SY-1. The metal filaments observed have a width of 30  $\mu\text{m}$  or less as it is shown in Figure 4-25. Secondary electron images were taken for disaggregated part of SY-2 sample and shown in Figure 4-26. A long piece of metal (about 200  $\mu\text{m}$ ) was captured and shown in Figure 4-26a.

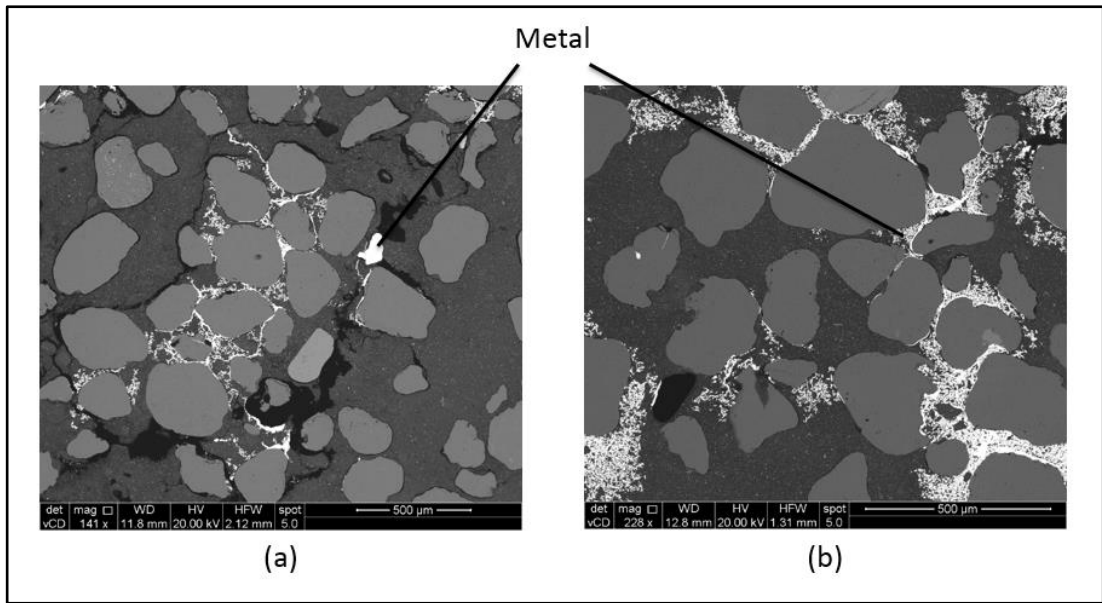


Figure 4-24: SEM images of SY-2 sample.

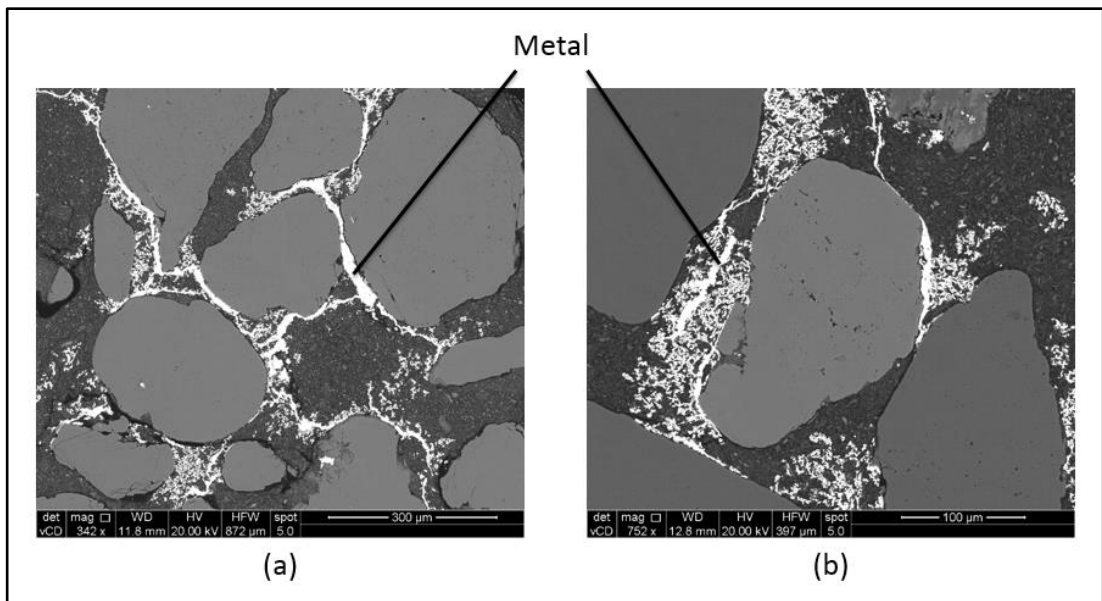


Figure 4-25: Magnified SEM Images of SY-2 sample.

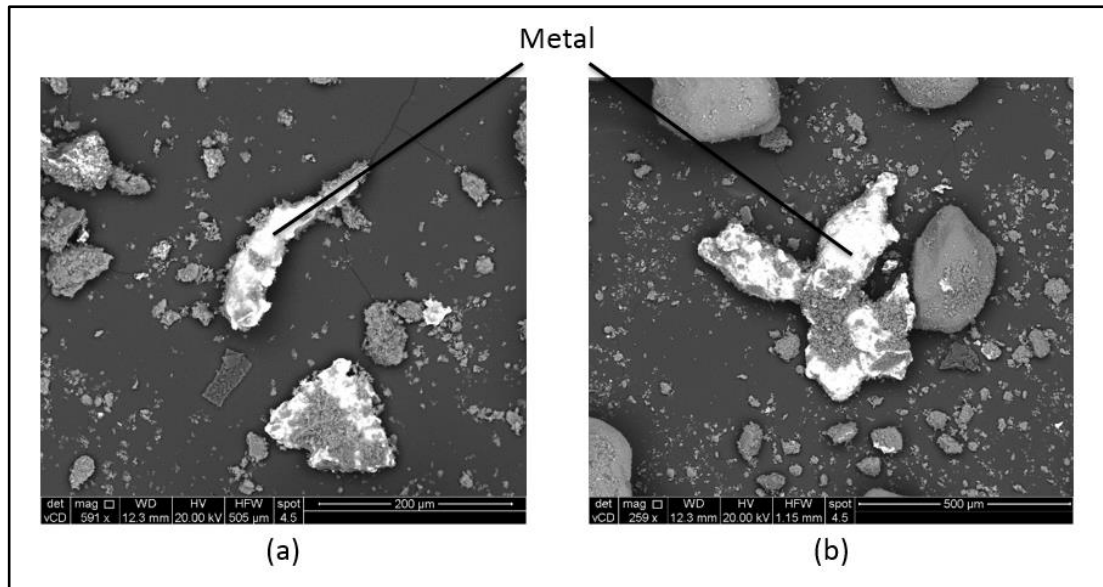


Figure 4-26: Secondary electron microscopy images of fragmented bottom segment of SY-2  
 (a) Long metal piece (b) Field's metal flowing around the grains.

SY-3 has the highest clay to sand ratio among the samples prepared for this test. It was noticed from the previous two samples that the threshold pressure increases with increasing clay content. Thus, it was expected that the threshold pressure of SY-3 will be higher than 200 psi. So, injection pressure step while running this sample was set to be 10 psi per step. Injection pressure versus water saturation plot of SY-3 is shown in Figure 4-27. The threshold pressure was found to be 516 psi where large volume of water was injected. CT images show that metal flowed past the sample between heat-shrink and aluminium tube (Figure 4-28a). However, the image slices of the helical CT scan suggest that a small amount of metal has actually penetrated the sample (about 4 mm) from the other end of the sample (Figure 4-28b). Figure 4-29 shows the SEM images of SY-3 sample with metal filaments around the sand grains. The size of the filaments was similar to the ones observed in SY-2. A magnified images of the filaments are shown in Figure 4-30.



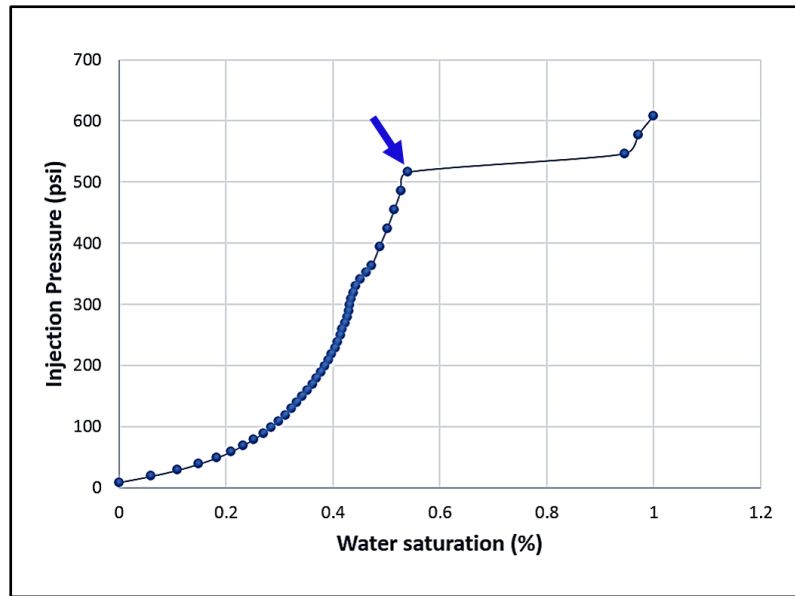


Figure 4-27: SY-3 injection pressure vs saturation of the water used to apply injection pressure. Blue arrow points at the threshold pressure.

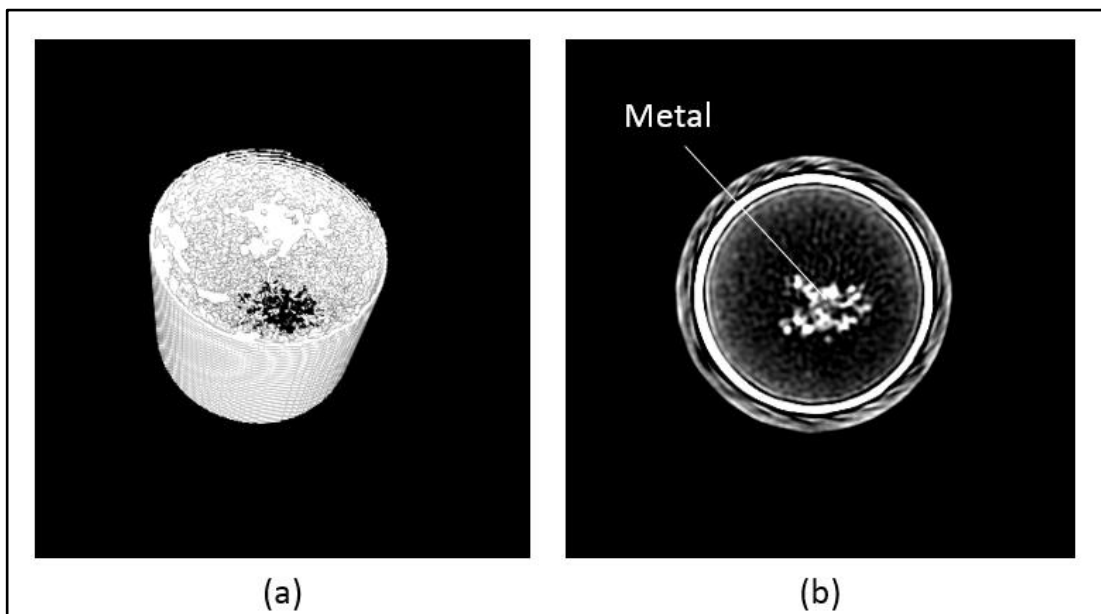


Figure 4-28: (a) 3D Image of SY-3 generated from CT images using ImageJ. The sample appeared to be full white because Field's, metal flew in between the aluminium tube and heat shrink of the compaction assembly ;( b) is a slice of CT image set showing Field's metal in the sample.

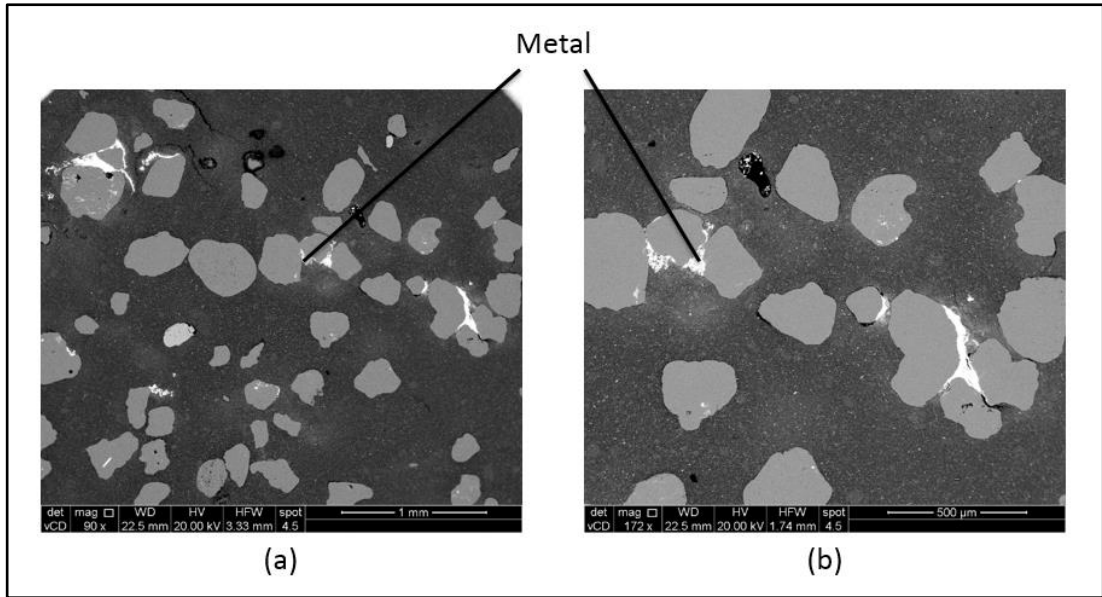


Figure 4-29: SEM images of SY-3 sample.

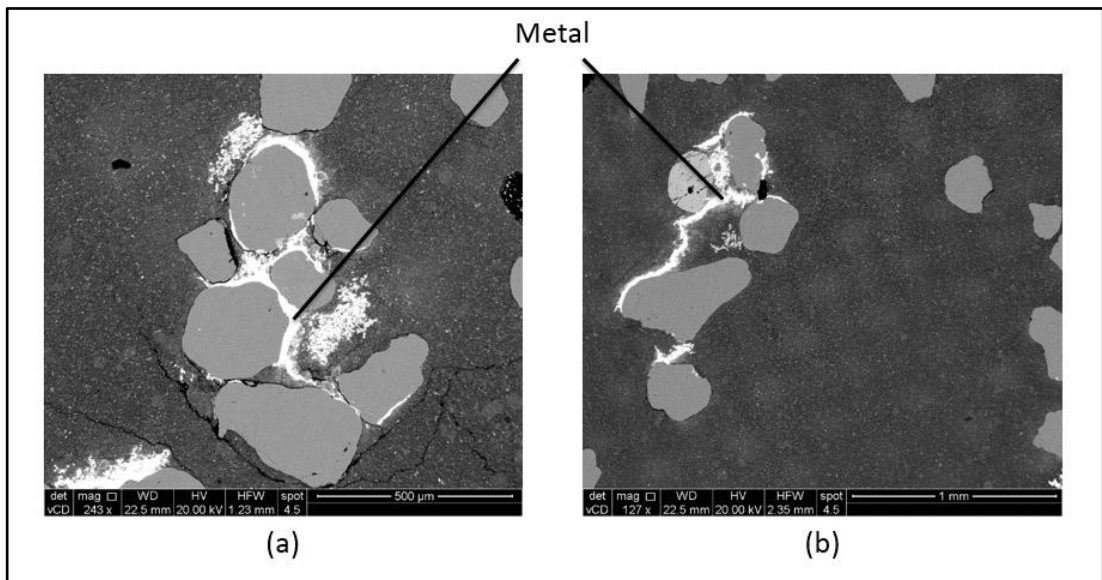


Figure 4-30: Magnified SEM Images of SY-3 sample.

## 4.5 Discussion

### 4.5.1 Controls of matrix flow within shale by capillary flow

#### 4.5.1.1 Sealing capacity

For the four samples tested using MPUCS, breakthrough pressure measured was always higher than estimated threshold pressure using MIP. This will result in an increase in the sealing capacity of the caprock. Sealing capacity is calculated using the equation (2-4) provided earlier. However, the threshold pressure estimated and measured earlier has to be converted to reservoir condition fluid system. This can be done using the following equation (Purcell, 1949):

$$P_{CR} = P_{CM} \left( \frac{2\sigma_R \cos \theta_R}{2\sigma_M \cos \theta_M} \right) \quad (4-1)$$

where  $P_{CM}$  and  $P_{CR}$  are the pressures for air-mercury system from MIP and reservoir condition respectively,  $(\sigma_M, \theta_M)$  and  $(\sigma_R, \theta_R)$  are the interfacial tension and contact angle for both air-mercury system and reservoir condition respectively. The assumption in this thesis is that caprock is water-wet, which means that interfacial tension and contact angle would be for oil-water system or gas-water system. The interfacial tension and contact angle values used in converting threshold pressure are shown in Table 4-5.

Fluid system	Interfacial tension (dynes/cm)	Contact angle (degrees)
Mercury-air system	485	140
Water-oil system	35	0
Water-gas system	72	0

*Table 4-5: Interfacial tension and contact angle for all fluid systems assuming shale is strongly water-wet (Chilingarian et al., 1996).*

The sealing capacity of each test was calculated assuming densities of water, oil and gas to be 1.1g/cc, 0.7 g/cc and 0.2 g/cc respectively. The calculated sealing capacities are listed in Table 4-6. For the tests where no breakthrough was measured, the exact sealing capacity is not measured but the maximum testing pressure will represent the lower limit of the sealing capacity.

Sample	Sealing capacity MIP (km)	Sealing capacity MPUCS (km)	
		7000 psi net stress	1000 psi net stress
ALP-M1	1.8 oil or 1.7 gas	*at least 9.9 oil or 9.1 gas	
WS-M1	2.2 oil or 2.0 gas	*at least 9.9 oil or 9.1 gas	4.1 oil or 3.8 gas
KC-M1	3.3 oil or 3.0 gas	*at least 9.9 oil or 9.1 gas	8.3 oil or 7.6 gas
OC-M1	3.3 oil or 3.0 gas	*at least 9.9 oil or 9.1 gas	6.5 oil or 5.9 gas

Table 4-6: Summary of the results of MPUCS against MIP. \*ALP-M1 was test at a net stress of 4,250 psi.

The sealing capacity estimated was very large (in a range of km) as it is presented in Table 4-6. This means that, for these shale sample, hydrocarbon column has to be very large for leakage to start. The structural closure is definitely not in a range of kilometres, which suggests that leakage via buoyancy forces induced by hydrocarbon column below the top seal is highly unlikely to occur for reservoirs capped by shale.

The net stress applied on the sample during the MPUCS test presents the mean effective stress subjected to the rock in reservoir condition. Under the assumption of the linear elasticity and zero lateral strain, the horizontal stress,  $\sigma_h$ , is approximated using the following equation (Fjaer et al., 2008):

$$\sigma_h = 0.5 \sigma_v \quad (4-2)$$

Where  $\sigma_v$  is the vertical lithostatic stress. Using the assumption of lithostatic gradient of 1 psi/ft, the corresponding depth in feet,  $D_{\sigma_h}$ , at which the net stress is applied is given by:

$$D_{\sigma_h} = \frac{\sigma_h}{0.5} \quad (4-3)$$

The estimated sealing capacity using MPUCS was around two times higher than the ones estimated by MIP for a net stress as small as 1000 psi. The burial depth associated with this net stress is approximately 610 m. The sealing capacity was at least three times higher than the one estimated using MIP when the net stress was increased to 7000 psi (about 14,000 feet burial depth). This suggests that the sealing capacity is stress sensitive and a small change in the net stress would result in a change in the sealing capacity.

#### 4.5.1.2 Effect of microfractures within the shale matrix

As it was explained in **Chapter 2**, brittle failure of shale results in formation discrete slip planes while ductile failure is in a form of shear enhanced compaction. Formation of fractures within the shale matrix affects permeability and threshold pressure. Holland et al. (2006) studied experimentally clay-rich sediments and observed an increase in pore size and reduction in capillary-entry pressure in faulted samples compared to the unfaulted ones.

It is important to understand faulting in shale rocks to be able to assess whether faults will be dilatant resulting in increase in permeability or compactive which will result in reduction in permeability. This can be done using overconsolidation ratio as it was suggested by Nygård et al. (2006). Overconsolidation ratio, OCR is estimated by:

$$OCR = \frac{\sigma_{v,max}}{\sigma_v} \quad (4-4)$$

Where  $\sigma_{v, max}$  is the maximum effective stress the rock was subjected to during its history and  $\sigma_v$  is the effective stress the rock subjected to at present time. Nygård et al. (2006) suggested that OCR value of 2.5 is considered as the threshold value above which dilatant fractures will form. This means that shale rock has to experience significant uplift to undergo embrittlement form dilatant fractures.

In this thesis, capillary entry pressures estimated using MIP for all samples were less 1,000 psi. The capillary entry pressures of MPUCS showed a behaviour similar to Holland et al. (2006) observation. Figure 4-31 presents incremental intrusion fraction against pore diameter of all sample at 1,000 psi net stress expect ALP-M1 which was tested at 4,250 psi net stress. Large pore sizes were observed in MIP data, which explain the reason of having low entry pressures. The large pores closed (which are technically microfractures) and entry pressure has increased when the same rock was subjected to a net stress of 1,000 psi. Although a net stress of 4,250 psi was applied, ALP-M1 sample did not experience any change in entry pressure, which suggests that ALP sample did not undergo embrittlement and dilatant fractures were not formed.

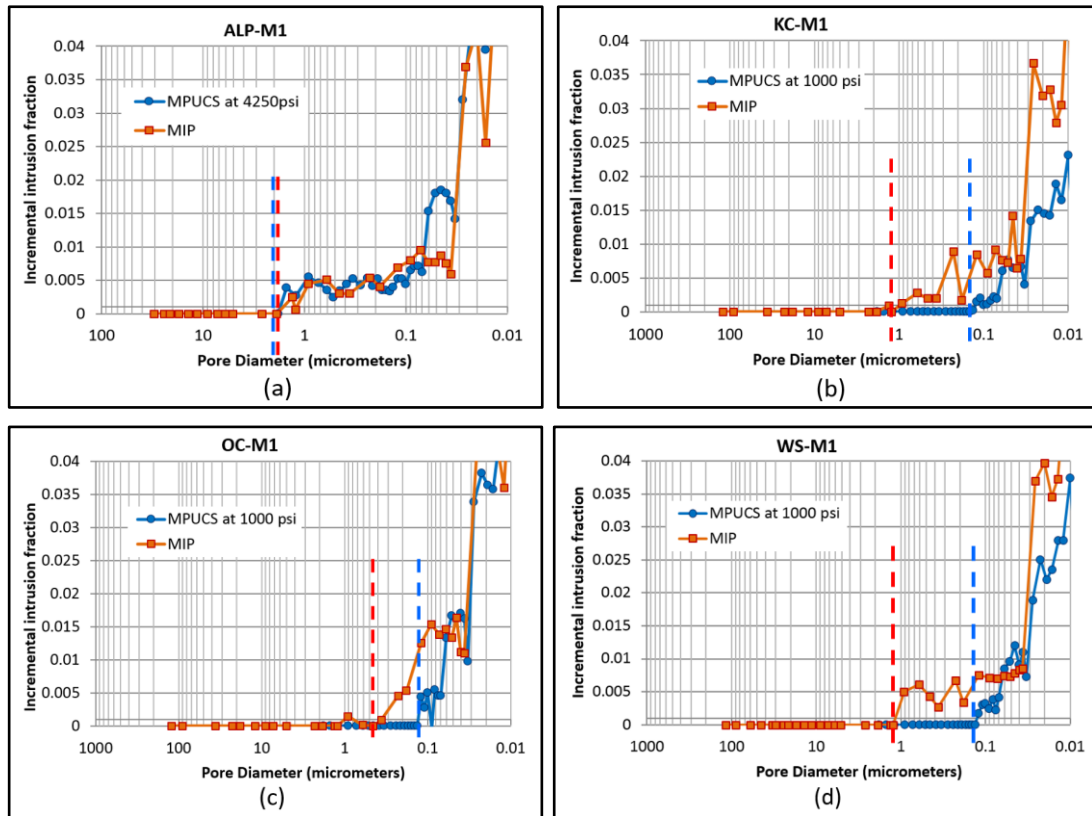


Figure 4-31: A zoomed in plot of incremental intrusion fraction against pore diameter for (a) ALP-M1, (b) KC-M1, (c) OC-M1 and (d) WS-M1 samples for both MIP and MPUCS and net stress of 1000 psi except for ALP-M1 sample. Red dashed line is capillary entry pressure using MIP technique and Blue dashed line is capillary entry pressure using MPUCS.

#### 4.5.2 Controls of matrix flow within shale by pathway dilation

Field's metal entry pressure increased with increasing clay content of the sample. This is because permeability of shale rock decreases with increasing clay content (Yang and Aplin, 2010). Using the estimated interfacial tension of Field's metal (0.41  $N/m$ ) provided by (Kouraytem et al., 2016) and contact angle of mercury-air system ( $140^\circ$ ), the corresponding pore diameter to Field's metal entry pressure is shown in Table 4-7. However, it is important to mention that Field's metal pressure measurement is subjected to error and was used as an indication of the point where metal starts to flow in the sample.

Sample	Clay (wt %)	Entry pressure (psi)	Pore radius ( $\mu\text{m}$ )
SY-1	25	68	1.34
SY-2	50	217	0.42
SY-3	80	516	0.18

Table 4-7: Field's metal entry pressure and their corresponding pore diameter for all samples.

In the sample with the lowest clay content, SY-1, the size of metal filaments shown in SEM images (about 200  $\mu\text{m}$ ) suggests that Field's metal did not travel through pore space but it actually formed pathways within the sample. This was confirmed by long pieces of metal seen in the secondary electron images. SY-2 and SY-3 behaved similar to the SY-1 and metal flowed within the sample forming preferential pathways observed in SEM images and secondary electron images. However, the sizes of the filaments were relatively small compared to the previous samples.

Irregular shapes of the injected metal shown in secondary electron images of the segregated parts suggest that Field's metal flows in the least resistance path within the sample. As it can be seen in Figure 4-32, the three samples had preferential pathways formed by injecting Field's metal in between sand grains. This is because of the arching of sand grain after compaction, which protects clay particles as it is shown in Figure 4-33. All the stress is being accommodated by sand grains, which protects the clay from compaction/stress making pathway dilation easier along those pathways.

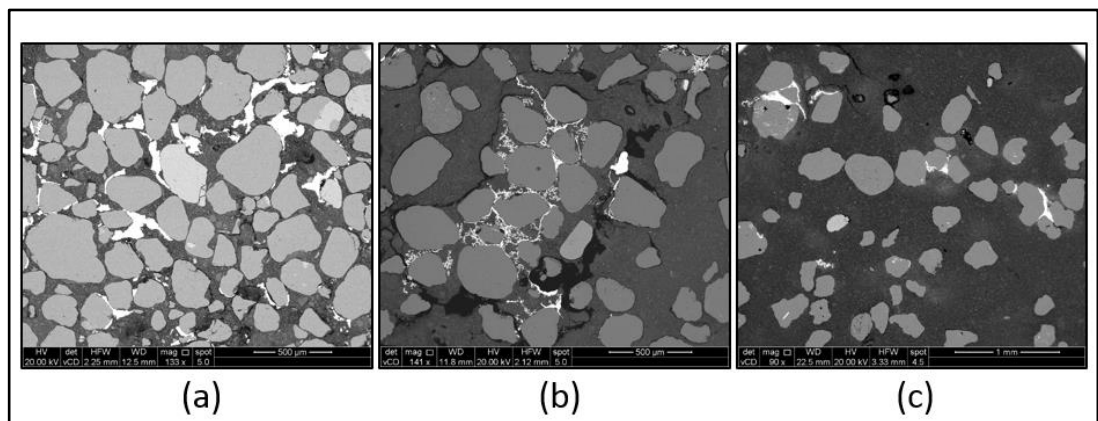
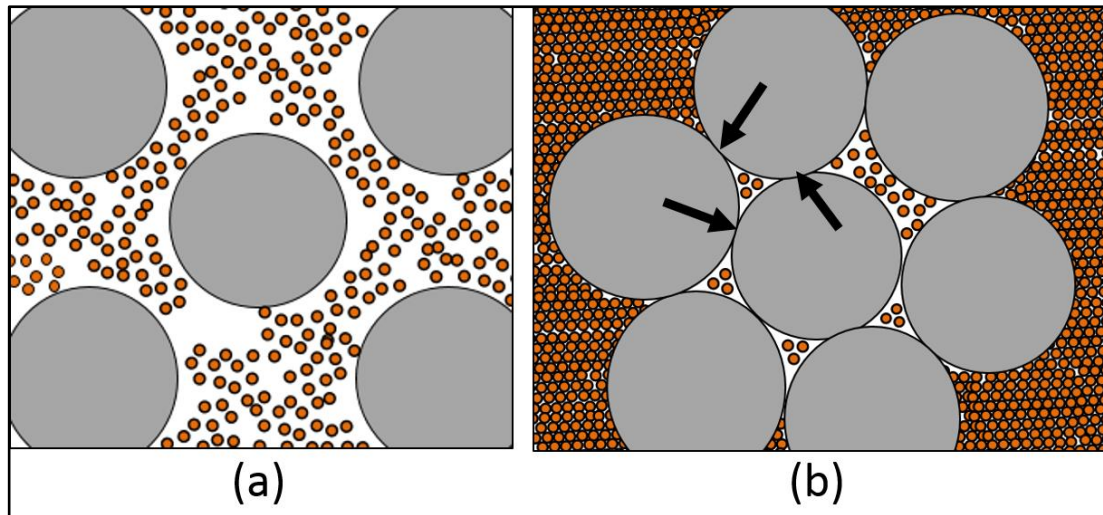


Figure 4-32: SEM images showing Field's metal flowing around sand grains for samples (a) SY-1, (b) SY-2 and (c) SY-3.



*Figure 4-33: Diagram showing clay particles (orange) and sand grains (grey) (a) before compaction and (b) after compaction. The black arrows shows arching of sand grains*

As it was explained in **Chapter 2**, chemical diagenesis plays an important role in compaction causing a reducing porosity whether it was in a form of calcite cementation or illitization. Chemical diagenesis becomes significant at deep depth and high temperature (Ramm, 1992; Ramm, 1994; Giles, 1997; Kalani et al, 2015). Cuss et al. (2014a) pathway dilation experiment was performed on a sample from Callovo-Oxfordian claystone, which is used in a Laboratory in Bure-France as a host rock for geological disposal of radioactive waste. Callovo-Oxfordian claystone was only subjected to a maximum burial depth of 850 m, which is considered small for diagenesis to be significant (Mazurek et al., 2008). Compaction of Callovo-Oxfordian claystone was mostly mechanical with formation of carbonates cement and no sign of illitization (Andra, 2005). Chemical diagenesis causes changes in microstructures of shale which might lead to reduction of potential pathways generated by arching.

The observations of the samples compacted mechanically presented in this thesis were similar to the observations made by (Cuss et al., 2014a) from gas flow experiment on Callovo-Oxfordian claystone sample. Preferential pathways formed in both cases could be due to the absence of chemical diagenesis. Weak zones or pore spaces generated between sand grains during compaction, which Field's metal has pushed clay and flown through, has made the sample prone to formation of preferential pathways.



Wiseall et al. (2015) performed pathway dilation experiment and visualized formation and dilation of localized pathways on clay paste. It was suggested that dilation causes compression of surrounding clay paste. Similarly in this experiment, the metal flowed through preferential pathways at a certain pressure pushing the sample radially causing a reduction in effective stress and changes in the volume of the sample. This agrees with the findings of Cuss et al. (2014a) where a change in the samples' volume was detected when preferential pathways were formed.

The results above suggest that the deformations associated with pathway dilation are plastic deformation because Field's metal is pushing the clay to flow through the spaces between sand grains causing a permanent change in microstructure and hence, change in petrophysical properties. This was also observed in gas migration experiment in clay performed by Horseman et al., (1999). It was noticed that when the gas pressure reaches the threshold and flow starts, pathways form and get dilated with time. After stopping the flow and re-establishing it again, it was noticed that the gas threshold pressure has experienced a significant reduction. Horseman et al. (1999) suggested that presence of residual gas filled voids accumulated at these pathways is the reason behind gas threshold pressure reduction. However, the changes in the microstructure of the sample change pore-size distribution, which will result in changes in capillary entry pressure.

## **4.6 Conclusions**

The petrophysical properties of shale are stress sensitive, so the measurements of petrophysical properties should be conducted at in situ stress conditions. The common practice to determine sealing capacity is to use the threshold pressure estimated by MIP. MIP threshold pressure is estimated graphically and its accuracy is questionable. In addition, the MIP threshold pressure is estimated under stressed condition only until mercury starts to invade the sample. In some of the cases, the mercury entry pressure is lower than the actual stress subjected to rock at in situ condition. At this condition, the MIP threshold pressure estimated is at unstressed condition and lower than the actual one at in situ condition.

A new equipment was developed in Wolfson multiphase laboratory is capable to measure mercury breakthrough pressure at any required effective stress referred to as MPUCS. The measurement of breakthrough pressure was done by measuring

electrical conductivity across the two sample ends. The measured breakthrough pressure of shale samples using MPUCS at net stress of 1,000 psi was around two times higher than the threshold pressure estimated using MIP. This is probably a result of closure of microfractures present within the sample which were formed when the rock experienced a significant uplift. At 7,000 psi net stress, the samples were capable to seal up to 9.9 km of oil column and 9.1 km gas column with no mercury breakthrough detected.

Formation of preferential pathways in shale rocks was investigated by injecting molten Field's metal into synthetic samples prepared in the laboratory. The synthetic samples were compacted in loading-unloading cycles using sand and kaolinite. The samples tested were of a different clay to sand ratio with same exact preparation method. The experiments were conducted in the oven under controlled temperature of 100 C° to ensure that Field's metal is in the liquid phase. The injection pressure was applied in steps until a significant amount of metal gets injected into the sample. The samples were scanned using CT scanner and then cut into slices and polished for SEM imaging.

Metal entry pressure increases with increasing clay content due to reduction in sample permeability. The SEM images of the polished slices showed metal filaments in between sand grains. These filaments were too large to represent undeformed matrix flow through porous media. One slice was disaggregated for secondary electron microscopy, which showed long pieces of Field's metal flowing around sand grains. These pieces are actual pathways formed by injection of slightly wetting fluid. These pathways were found only around sand grains, which was the easiest path for the metal to flow. The compressive stress was accommodated mostly by the sand grains due to arching, which protected clay minerals in between sand grains. The metal used these un-compacted zones created by arching to form preferential pathways. It was suggested that the presence of these zones could be eliminated when chemical diagenesis plays a role during compaction. Formation and dilation of these pathways is associated with plastic deformations and changes in microstructure of the sample which leads to changes in petrophysical properties of the rock.

# 5 Chapter V: Determination of geomechanical properties of shale using micro-indentation and Mercury Intrusion Porosimetry (MIP)

## 5.1 Introduction

Measurement of geomechanical properties of a rock is very important to be able to characterize it in terms of strength, elasticity and to be able to use correlations provided in the literature to estimate other rock properties. The standard practice used in the industry is to perform triaxial tests to obtain elastic and plastic properties of rock. Shale is often laminated, which makes it difficult to prepare core plugs that are sufficiently long to perform standard mechanical test. As an alternative, micro-indentation was proposed to measure hardness, fracture toughness and Young's modulus using small rock samples, which provided encouraging results (Shukla et al., 2013).

Microindentation is a breakthrough technology that can provide a measure of some mechanical properties regardless of the sample size. In fact, nanoindentation can be used to measure mechanical properties of small features and thin films as it is performed on a relatively small scale (Oliver and Pharr, 2003). The method of measuring hardness and modulus of elasticity introduced by Oliver and Pharr (1992) and Pharr et al. (1992) has been used widely in the industry to characterize the mechanical behaviour of materials at small scales (Oliver and Pharr, 2003). Many authors used this technique to mechanically characterize shale (e.g. Liu, 2015; Shukla et al., 2013; Corapcioglu et al., 2014). A comparison of mechanical properties estimated by microindentation and conventional multistage will be presented to investigate the reliability of results obtained using indentation techniques.

The sample is normally cut flat and polished before performing any indentation. The indentation force and depth data are measured during the microindentation test and are then used to estimate Young's modulus. Later, SEM images of the indenter impression on sample's surface are taken to estimate hardness and fracture toughness. The dimensions of the indentation impression measured from SEM images are used to estimate hardness. As the indenter goes inside the sample, it generates cracks at the corners of the indenter. Crack length obtained from SEM is

used to estimate fracture toughness of the sample. A step by step sample preparation together with the experimental method used are discussed later in this chapter.

Acid is being widely used as a stimulation fluid to enhance permeability and porosity of oil and gas production wells near wellbore for the purpose of improving production (Schechter, 1992). Acid is injected into the formation to either dissolve some of the rock minerals to create wormholes or to dissolve any materials (debris) blocking the channels between the formation and wellbore. This process increases porosity, which in turn will reduce the strength of the rock. The impact of acid treatment on the mechanical properties of shale is studied as well using microindentation technique to investigate the effect of acid on mechanical properties of shale.

The apparent preconsolidation pressure is a very important material property and incorrect assumption of this parameter could lead to overestimation or underestimation of rock strength and wrong determination of the failure mode. Preconsolidation pressure measurement of shale using traditional methods takes a long time as it has to be done in drained conditions allowing the fluid present in the sample to drain out during the test similar to Wong et al. (1997). For the case of tight materials such as shale, it takes a long time for the fluid to drain. As it was mentioned earlier, there are only few measurements of the apparent preconsolidation pressure of shale available in the literature. On the other hand, there is well developed theory to estimate preconsolidation pressure for sandstones because it is relatively easy to perform triaxial compression in drained condition for permeable rocks. Zhu and Wong (1997) studied mechanical behaviour and failure modes (brittle and ductile) in relation to the transition from brittle faulting to shear enhanced compaction for a range of sandstone samples using a triaxial rig. In addition, Wong et al. (1997) managed to measure the critical effective pressure ( $p^*$ ) for a group of sandstones using the same setup.

Wong et al. (1997) developed yield/failure criterion similar to those used in critical-state soil mechanics. It is basically the same  $p$ - $q$  plot but each axis is normalized to critical effective pressure ( $p^*$ ) (Figure 5-1a). The failure envelope presented by Wong et al. (1997) shown in Figure 5-1-a was approximated by Fisher et al. (2007) to an elliptical form shown in the same figure (Figure 5-1b). The initial approximation would be that dilatant brittle failure occurs when  $p/p^* > 0.25$ , brittle-

ductile deformation when  $0.25 < p/p^* < 0.4$  and finally cataclastic flow when  $p/p^* > 0.4$  (Fisher et al., 2007).

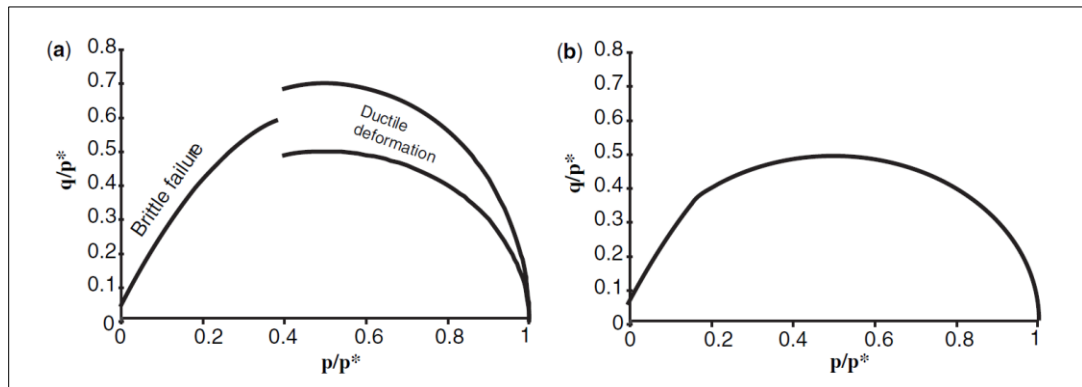


Figure 5-1: Yield-failure envelope developed by Wong et al. (1997); (b) the elliptical form for the yield-failure envelope proposed by Fisher et al. (2007).

As there is a well-developed knowledge in the literature about mechanical deformation for sandstone (Wong et al., 1997; Fisher et al., 2007), a better understanding of failure envelopes for shale is certainly needed. Unfortunately, sandstone theory cannot be applied to shale because differences in mineralogy and grain size mean that deformation mechanisms are likely to be different.

In this research, a new technique is proposed of measuring critical effective pressure ( $p^*$ ), which is technically the preconsolidation pressure under hydrostatic loading using the MIP technique. The test takes a relatively short time and is capable of applying high compression pressures (up to 60,000 psi using the Autopore IV 9520 system). MIP is traditionally used to measure pore throats but a slight modification to the process might lead to measurement of mechanical deformation (Figure 5-2). Normally for pore throat measurement, a small dried piece of rock sample is placed in the cup and mercury is pumped into the sample. The idea proposed is to seal the sample and pump mercury around it to provide pressure and pressurize it until porosity collapses. The sample will be stressed hydrostatically until porosity collapses following the red path shown in Figure 2-17. The mercury pressure and the volume of mercury pumped in will be a representative data for the deformations resulted.

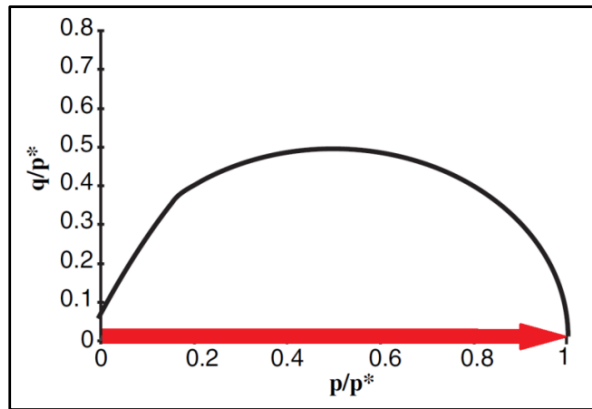


Figure 5-2: Load path for measuring  $p^*$  marked by a red line on the elliptical failure envelope approximated by Fisher et al. (2007).

## 5.2 Sample preparation

### 5.2.1 Measurement of mechanical properties using micro-indentation

Microindentation is a sensitive process and samples have to be prepared carefully to control sources of bias in the measurement. In addition, the sample has to be well polished because the surface can be imaged using SEM to assess indenter impressions and cracks generated. The indentation surface should be:

- Polished to minimum grit size possible to minimize effect of high surface roughness.
- Perpendicular to the indentation direction.
- Flat with minimum variation across the surface.

First, the samples are cut into regular shapes and ground in one face to be able to mount them on flat glass using thermal wax for further processing as it is shown in Figure 5-3. The sample is then cut flat using a Petrothin cutting and grinding machine shown in Figure 5-4. This machine is normally used for preparing thin section slides for microstructural analysis and it is accurate enough to produce a good flat surface. The surfaces produced using this process were within maximum of 40  $\mu\text{m}$  variation.



Figure 5-3: Samples after mounting them on a flat glass.

The samples are then removed from the glass and mounted on SEM stub in preparation for polishing. All the samples were mechanically polished using Buehler grinding and polishing machine (Figure 5-4). The polish was done gradually using 9 $\mu$ m to 0.25 $\mu$ m diamond. Figure 5-5 shows the gradual grits sizes used in the process of polishing the samples.

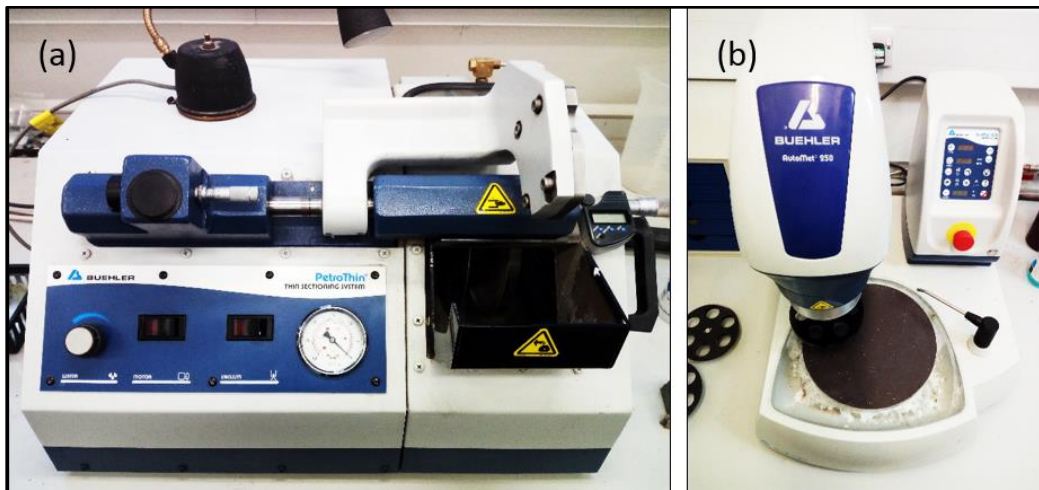


Figure 5-4: Petrothin (a) grinding and (b) polishing machines from Buehler.

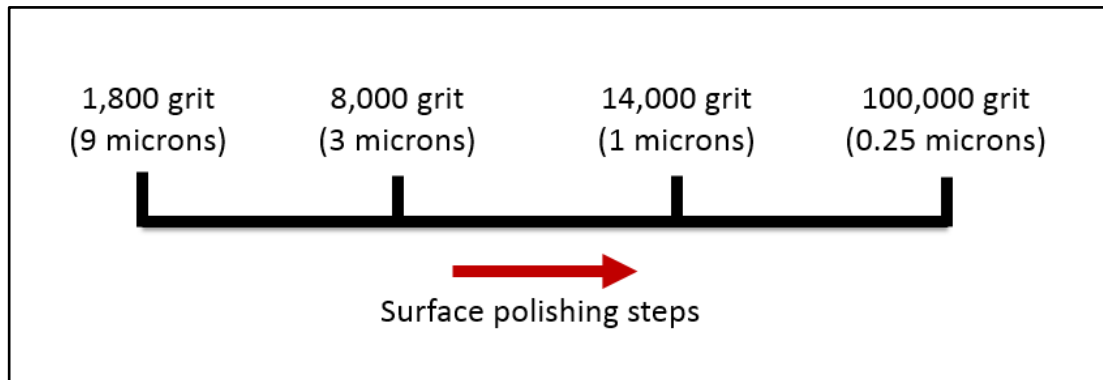


Figure 5-5: Gradual surface polishing steps.

As it was mentioned earlier, the plan was to investigate the applicability of microindentation technique to shale. For this purpose, laboratory dry samples were prepared for microindentation, which are in same condition as the samples used for triaxial testing. In addition, the effect of acid on elastic properties was investigated for all samples by exposing them to 5% HCL for a period of one month. The samples have to be fully prepared using the above mentioned procedure before exposure to acid to avoid any harsh treatment to the indentation surface. After acid exposure, the samples are then mounted on SEM stubs and kept dry ready for performing the experiment.

### **5.2.2 Estimation of critical effective stress ( $p^*$ ) of shale using MIP technique**

The most critical part of this experiment is to select a suitable sealing material and to develop an effective sealing method that is strong enough to keep the samples sealed at high pressures. A couple of trails have been made to achieve this goal, which was at the end achieved successfully. Initially, the samples were kept in a 60 C° oven until the weight stabilizes to ensure that the samples are dry and no moisture is present inside.

The primary adhesive material chosen for sealing the samples is an epoxy adhesive from Araldite, specifically “Araldite 2011”. The reasons behind choosing this adhesive is that it has good resistance to dynamic loading in addition to its ability to elongate up to 9% (Huntsman, 2013). It has good mechanical properties and requires a few days to harden. The first trail made was done to sample with shale cubes similar to the ones prepared for normal MIP test for pore throat characterization. It was noticed that epoxy tends to flow down the sample and accumulate at the bottom (Figure 5-6). Epoxy mixture has air bubbles generated while mixing, which might generate vugs in the sealing system. In addition, it was difficult to place sufficient amount of epoxy around the sharp edges which acted as weak points in the sealing. As a result, the sealing system has failed and all the failures occurred at the edges of the sample and in air bubbles, which acted as stress concentration points.



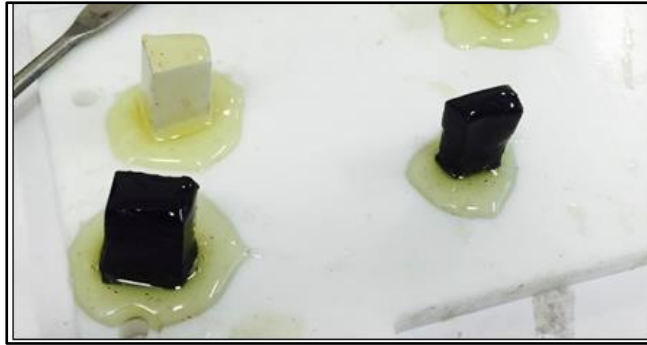


*Figure 5-6: Cubic samples sealing application using Araldite 2011.*

Sharp edges, air bubbles are believed to be the weak points that cause failure. To minimize sharp edges, the samples were drilled into small 16 mm diameters cylindrical cores. The remaining shape edges (top and bottom) are then smoothed using sand paper. The bubbles generated while mixing the epoxy are very hard to remove because of the viscosity of the adhesive. To reduce epoxy viscosity, acetone was added to the mixture, which significantly lowered its viscosity. The mixture was then placed under vacuum to remove all the air bubbles. Acetone to epoxy mixture weight ratio was always set to be 0.113 to ensure consistency in samples preparation.

To ensure that the epoxy is placed evenly around the sample and not accumulating at the bottom of the sample, a cylindrical mould made of Teflon was prepared. The inner diameter of the mould is 18 mm, which will ensure a 1 mm layer of epoxy around the sample provided that the sample is centralized. After placing the sample in the mould and the resin is poured, the sample is centralized using a needle. The sample is then left for two days inside the mould until the epoxy hardens. Figure 5-7 shows the mould and the sample after the epoxy is hardened. This sample survived in MIP and was able to sustain pressure up to 60,000 psi.



*Figure 5-7: Teflon mould and sample after sealing placement*

## 5.3 Experimental methods

### 5.3.1 Measurement of mechanical properties using micro-indentation

Micro and nano-indentation techniques are widely used by researchers nowadays due to their simplicity and time effectiveness. They provide wide range elastic properties measurements with little effort in relatively short time. Micro-indentation was used in this thesis to minimize the bias generated by surface roughness and to make sure that each indentation covers multiple grains and representative to the matrix mechanical properties.

The machine used is an Instron5566 Universal testing machine, which is widely used in the industry for mechanical compression and tension testing. It consists of four main components; load frame; crosshead, load cell and a control system (Instron, 2005). As it is shown in Figure 5-8, the sample is mounted on the load cell and the indenter is mounted on the crosshead. The indenter moves down to apply the force on the samples (Figure 5-9). Load, displacement and speed are programmed and recorded using the control system. This machine has a capability of applying compressive or tensile force as high as 10 kN at a speed between 0.005-500 mm/min (Instron, 2005).

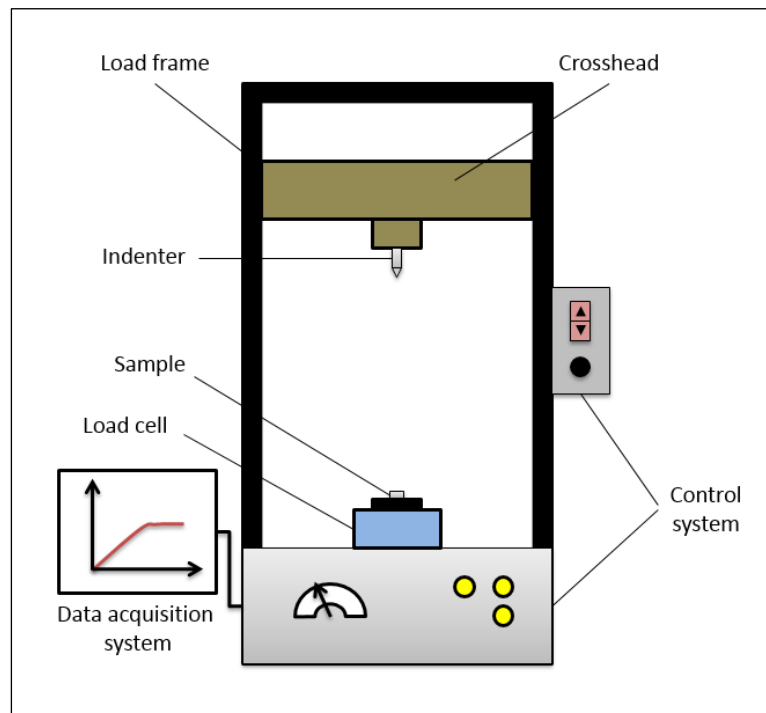
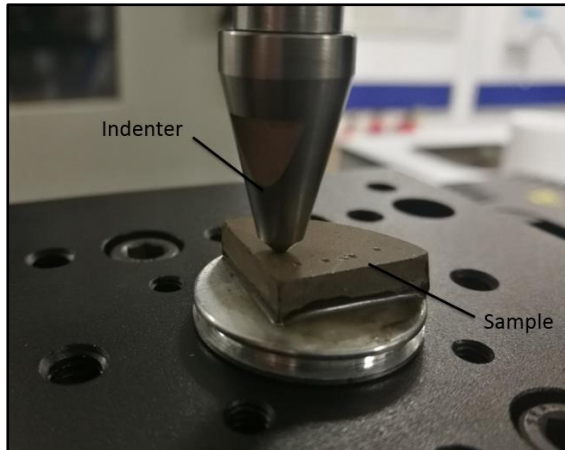
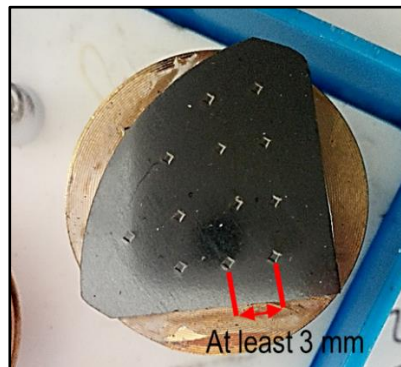


Figure 5-8: Instron5599 Universal testing machine.



*Figure 5-9: Indentation process in a rock sample.*

The indenter used in all the tests is Vickers diamond indenter from Gilmore Diamond Tools. Each sample will have 8-12 indentations on its polished surface with at least 3 mm distance between indentations to minimize the interference between them (Figure 5-10).



*Figure 5-10: Sample with indentations impressions on the polished surface. The space between indentations was at least 3mm.*

The indentation program has to be pre-set in advance using the software associated with the machine. The first step was to specify maximum indentation load for that particular measurement. Penetration speed of  $8 \mu\text{m/s}$  was applied until the maximum load is reached. At the pre-specified maximum load point, the load was held constant for 30 seconds to allow the system to stabilize. Finally, the load was released gradually until it goes to zero (Figure 5-11). All loads and displacements of the indentation will be recorded accurately using data question system and then indenter impressions are imaged using SEM. Data recorded are then used to calculate Young's modulus, hardness and fracture toughness. However, the deformations recorded represent the deformations of the sample in addition to deformation of the machine.

The deformations of the machine can be found by running the machine without the sample. Before performing any calculations, these two deformations have to be decoupled by subtracting deformations of the machine from deformations of the sample plus machine. Ignoring this step will introduce errors in calculated parameters.

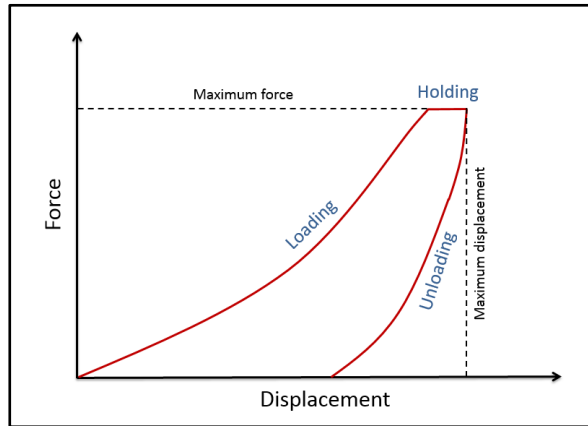


Figure 5-11: Schematic of load-displacement curve illustrating the indentation program used.

Elastic and plastic deformation take place while the indenter is penetrating the sample during the loading stage (Oliver and Pharr, 2003). The plastic deformation is reflected by the permanent impression induced by the indenter, which is used to estimate hardness. Hardness is basically a measure of the materials resistance to deform plastically. During the unloading stage, the deformation recovered is assumed to be pure elastic and the data is used to estimate elastic properties (Figure 5-12 and Figure 5-13).

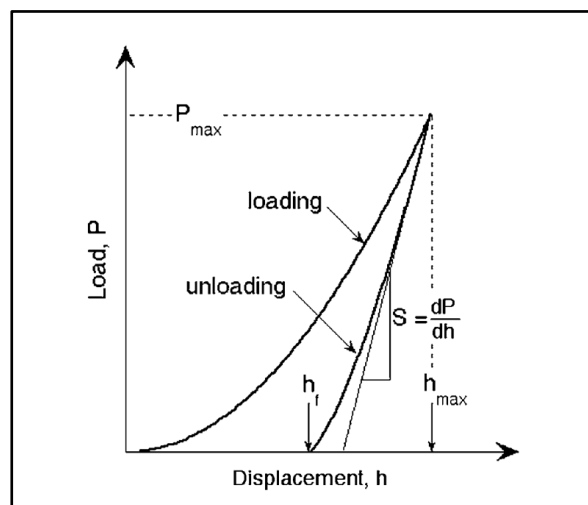


Figure 5-12: Schematic showing load-displacement data with the important parameters obtained from the plot (Figure taken from Oliver and Pharr (1992)).

Hardness ( $H_h$ ) can be calculated using the equation:

$$H_h = \frac{P_{max}}{a_c} \quad (5-1)$$

Where  $P_{max}$  is the maximum load applied by the indenter and  $a_c$  is the contact area between the indenter and the sample. Contact area can be found using the geometry of the indenter and the average diagonal length ( $d_c$ ) of the impression made by the indenter (Figure 5-13-a). Vickers indenter has pyramidal shape with angle of  $136^\circ$  at the tip of the indenter which makes the contact area in terms of  $d_c$  to be (Guder et al., 2011):

$$H_V = \frac{(9.81E-3)*0.1891 P_{max}}{d_c^2} \quad (5-2)$$

Where  $H_V$  is Vickers hardness in (GPa),  $P_{max}$  is in (N) and  $d_c$  is in (mm).

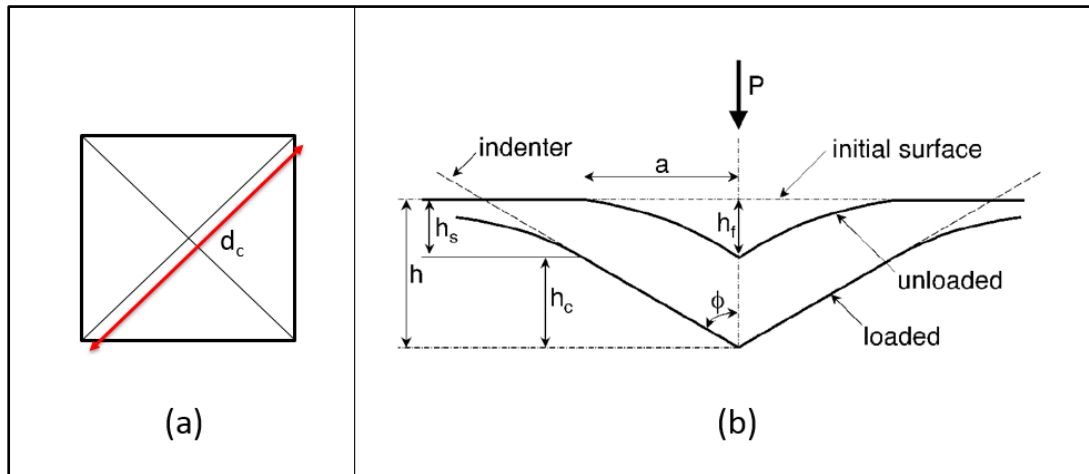


Figure 5-13: schematic showing (a) impression of Vickers indenter with a diagonal  $d_c$  indicated with a red arrow and (b) the response of the material during loading and unloading with the parameters required to estimate mechanical properties (Figure taken from Oliver and Pharr (1992)).

Young's modulus could be estimated using the elastic deformation part of the indentation process, i.e. during the unloading stage. Effective Young's modulus is related to the slope of the unloading curve (Figure 5-12) and the projected contact area between the indenter and the sample. The relationship is given by Oliver and Pharr (2003):

$$E_{eff} = \frac{S}{2\beta_i} \sqrt{\frac{\pi}{A_p}} \quad (5-3)$$

where  $E_{eff}$  is effective Young's modulus (MPa),  $S$  is the slope of the unloading curve (N/mm),  $A_p$  is projected contact area (mm<sup>2</sup>) and  $\beta_i$  is a constant which depends on the type of indenter. For Vickers indenter, the constant  $\beta$  is about 1.012. Determining the projected contact area for the elastic part is not straight forward. It can be determined using the displacement of the indenter using area function or indenter shape function. For Vickers indenter, the area function is (Kang et al., 2009):

$$A_p = 24.5 h_c^2 \quad (5-4)$$

Where  $h_c$  is the displacement of the indenter recovered when the load is released which can be determined using (Oliver and Pharr, 2003):

$$h_c = h_{max} - \epsilon \frac{P_{max}}{S} \quad (5-5)$$

Where  $\epsilon$  is a dimensionless constant that depends on the shape of the indenter; it is 0.75 for the Vickers indenter.

Once all the parameters are determined and  $E_{eff}$  is calculated, Young's modulus of the material tested can be calculated using the equation (Oliver and Pharr, 2003):

$$\frac{1}{E_{eff}} = \frac{1-\nu^2}{E} + \frac{1-\nu_i^2}{E_i} \quad (5-6)$$

Where  $\nu$ ,  $\nu_i$  are Poisson's ratios of the sample and the indenter respectively and  $E$ ,  $E_i$  are Young's modulus for the sample and the indenter respectively. Looking at equation (5-6), knowledge of Poisson's ratio of the sample is required to calculate Young's modulus. However, the selectivity to this parameter is weak and a 40% change in Poisson's ratio will only change calculated Young's modulus by 5% only (Hay, 2009). Thus, Poisson's ratio in all calculation performed in this chapter was assumed to be 0.25.

Fracture toughness is a measure of materials resistance against fracture. It is an important material property to anticipate crack growth in materials subjected to stress. Fracture toughness can be estimated using the cracks generated at the corners of the indentation impression as it is shown in Figure 5-14. The length of the crack measured from the tip of the indenter,  $c$ , is fed into fracture toughness models to calculate fracture toughness. The commonly used fracture toughness models available

in literature are based on half-penny crack model or by curve-fitting (Moradkhani, 2013). Curve fitting models are semi-empirical and coefficients were determined using experimental data obtained from tests using Vickers indenter. The models are summarized in Table 5-1.

Evans and Charles (1976) model is a commonly used fracture toughness model due to its simplicity. It is a semi-empirical model based on half-penny crack model and it takes into account the maximum load and the length of the crack. This model was developed further by Lawn et al. (1980) and Anstis et al. (1981) to include properties of the tested material. On the other hand, Shetty et al. (1985) introduced a model based on curve-fitting, which is frequently used in the literature. This model is unique because it takes into account the four sides crack length into account with hardness. Japanese Industrial Standards (1990) introduced a model similar to Lawn et al. (1980) and Anstis et al. (1981) model using curve-fitting technique.

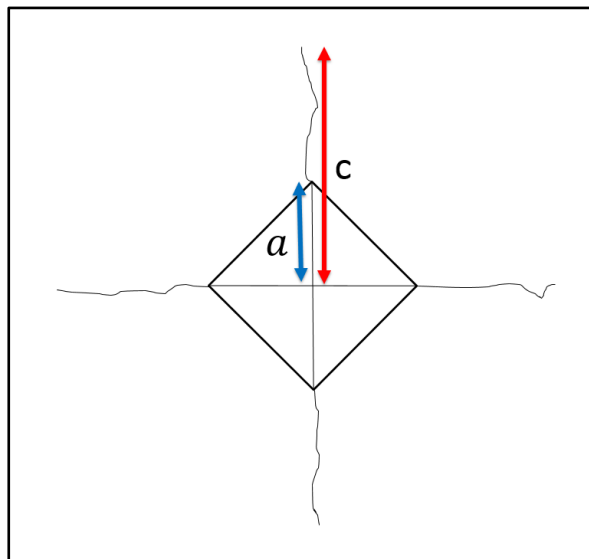


*Figure 5-14: Vickers indenter impressions with cracks generated at the corners. The red arrow indicates the crack length,  $c$ , used in fracture toughness calculations and  $a$  is half of the diagonal length (blue arrow).*

Equation	Crack model	Reference
$K_{IC} = 0.016 \left( \frac{E}{H_V} \right)^{\frac{1}{2}} \frac{P}{c^{\frac{3}{2}}}$	Half-penny	(Anstis et al., 1981)
$K_{IC} = 0.0752 \frac{P}{c^{\frac{3}{2}}}$	Half-penny	(Evans and Charles, 1976)
$K_{IC} = 0.067 H_V a^{\frac{1}{2}} \left( \frac{E}{H_V} \right)^{\frac{2}{5}} \left( \frac{c}{a} \right)^{-\frac{1}{2}}$	Half-penny	(Niihara et al., 1982)
$K_{IC} = 0.0726 \frac{P}{c^{\frac{3}{2}}}$	Half-penny	(Lawn and Fuller, 1975)
$K_{IC} = 0.014 \left( \frac{E}{H_V} \right)^{\frac{1}{2}} \frac{P}{c^{\frac{3}{2}}}$	Half-penny	(Lawn et al., 1980)
$K_{IC} = 0.0089 \left( \frac{E}{H_V} \right)^{\frac{2}{5}} \frac{P}{ac^{\frac{1}{2}}}$	Curve-fitting	(Niihara et al., 1982)
$K_{IC} = 0.0889 \left( \frac{H_V P}{\sum_{i=1}^4 c_i} \right)^{\frac{1}{2}}$	Curve-fitting	(Shetty et al., 1985)
$K_{IC} = 0.4636 \left( \frac{E}{H_V} \right)^{\frac{2}{5}} \frac{P}{a^{\frac{3}{2}}} 10^F$	Curve-fitting	(Evans, 1979)
$K_{IC} = 0.018 \left( \frac{E}{H_V} \right)^{\frac{1}{2}} \frac{P}{c^{\frac{3}{2}}}$	Curve-fitting	(Japanese Industrial Standards, 1990)
$K_{IC} = H_V a^{\frac{1}{2}} \left( \frac{E}{H_V} \right)^{\frac{2}{5}} 10^y$	Curve-fitting	(Evans, 1979)

Table 5-1: Summary of famous fracture toughness equations (Moradkhani, 2013).

### 5.3.2 Estimation of critical effective stress ( $p^*$ ) of shale using MIP technique

MIP equipment is normally used for pore throat characterization of rock samples and not for measuring mechanical deformation. However, Hildenbrand and Urai (2003) suggested that for low permeability shale, mercury does not enter the pore spaces and the volume of mercury pumped in can be viewed as mechanical deformation in a form of reduction in bulk volume of the sample. The idea proposed in this thesis is to alternatively seal the rock sample with a different material to stop mercury entering the pore space, so that the mercury volume and pressure change represent pure mechanical deformation. The results of the sealed samples will be compared against the unsealed samples to validate Hildenbrand and Urai (2003) results and suggestions.



As it was explained earlier, shale rocks experience ductile failure by shear enhanced compaction and porosity collapse. Thus, the sample is expected to have lower volumetric strain after it undergoes porosity collapse. The point at which the volumetric strain changes would be the  $p^*$  we are after.

To perform this test, the same procedure of standard MIP will be used. The equipment used is Micromeritics Autopore IV 9520 system explained in **Chapter 3**. The only difference would be that the sample in this case is sealed to avoid mercury invading pore space as it is shown in Figure 5-15.

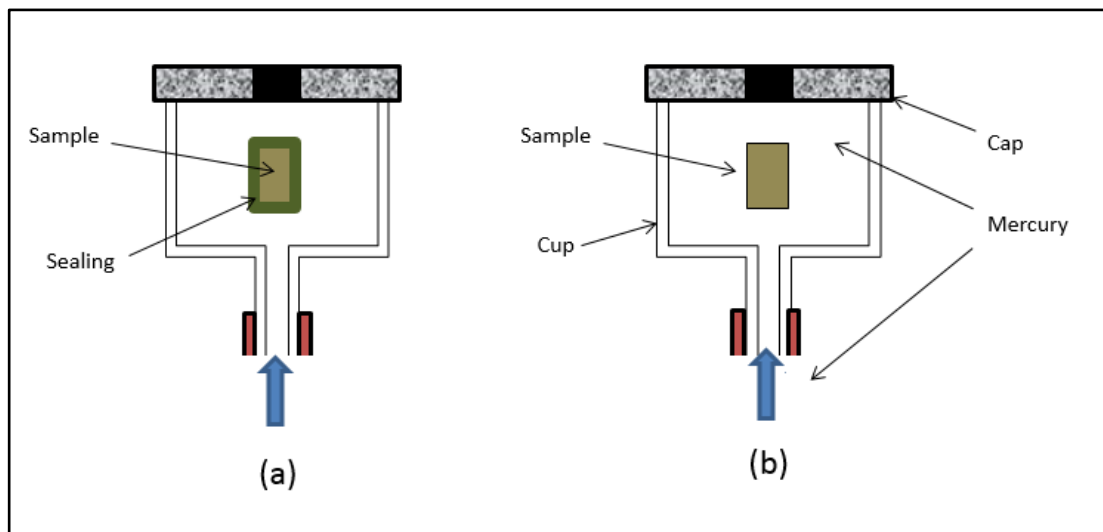


Figure 5-15: Mercury Intrusion Porosimetry (MIP) assembly for (a) mechanical deformation and (b) pore throat characterization.

## 5.4 Experimental results

### 5.4.1 Measurement of mechanical properties using micro-indentation

#### 5.4.1.1 Laboratory-dry samples

Micro-indentation was performed to all samples at laboratory-dry condition to be comparable with multistage triaxial results. Initially, tests were performed to identify the suitable loading for each sample that initiate crack without breaking the sample. It was found that the load required to initiate a crack in shale rocks is between 100-450 N depending on the stiffness of the sample. Table 5-2 shows the loads determined for each sample. Three different loads were used for each sample to estimate mechanical properties at different penetration depth.

Sample	Loads applied (N)
WS	100-150-200
ALP	150-200-250
AM	200-225-250
OC	250-275-300
KC	350-375-400
D	350-375-400

Table 5-2: Indentation loads determined for each shale rock.

Load displacement curves resulted from indentation process for all samples are shown in the figures below. SEM images of the indentations were also taken (shown in the below figures) and indenter impression and crack dimensions were measured for fracture toughness and hardness calculations. Some of the indentation results were excluded from these results due to chipping of rock material out of the surface during indentation which leads to bias calculation of mechanical properties.

Fracture toughness is calculated using four models (Evans and Charles, 1976; Anstis et al., 1981; Shetty et al., 1985; Japanese Industrial Standards, 1990) and the average value of these models is considered as fracture toughness of the rock. Detailed parameters obtained from micro-indentation data and SEM images are summarized in Table 5-3, Table 5-4, and Table 5-5. These tables also include the calculated effective Young's modulus, hardness and fracture toughness.

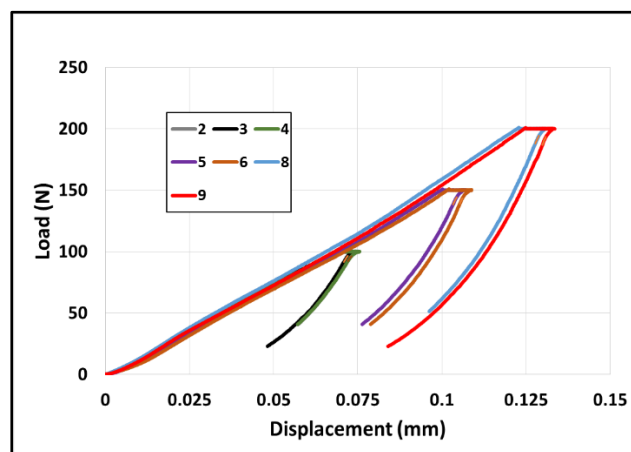


Figure 5-16: Load-displacement curves for the successful indentation made on WS sample.

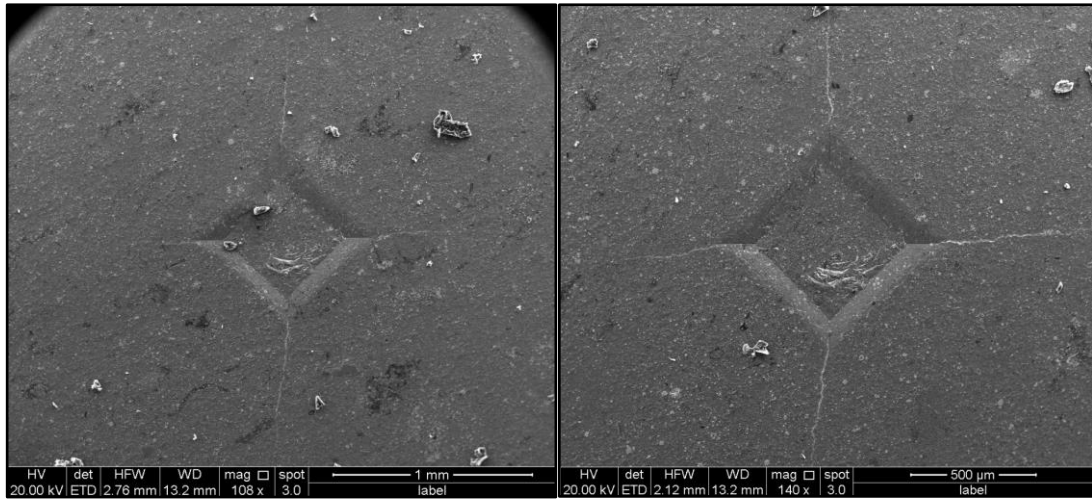


Figure 5-17: SEM images of the impression made by indents number 2 (left) and 4 (right) taken from WS sample..

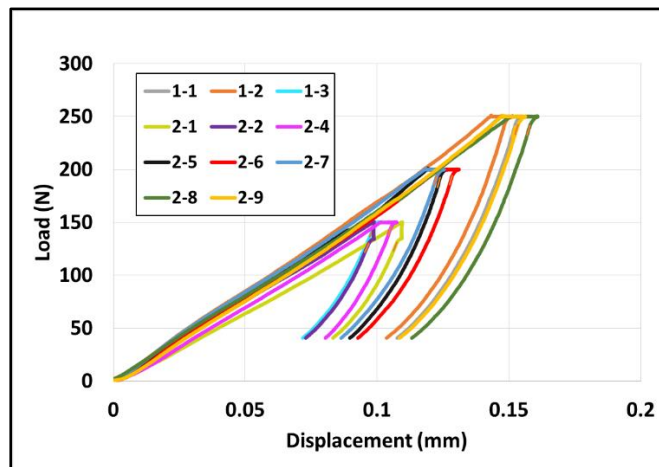


Figure 5-18: Load-displacement curves for the successful indentation made on ALP sample.

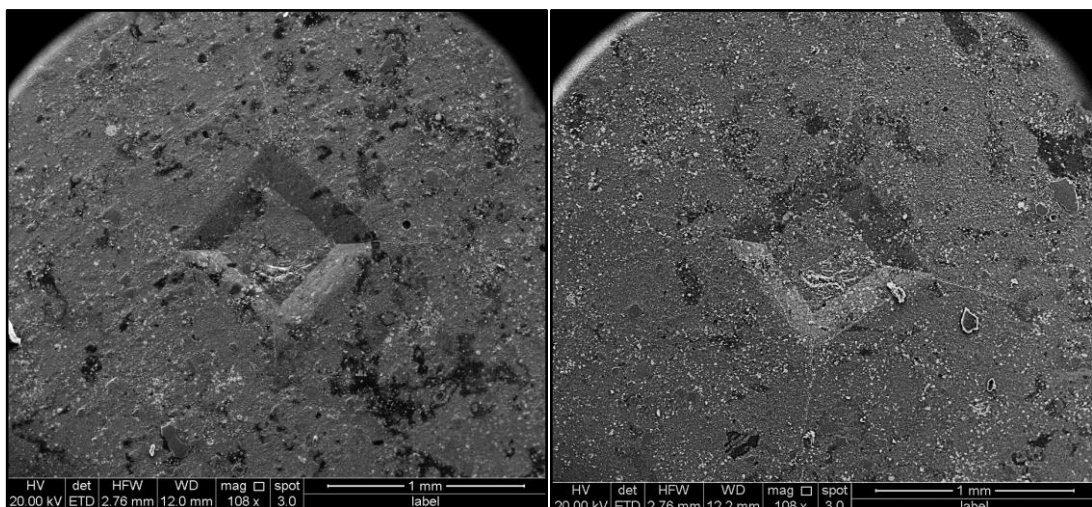


Figure 5-19: SEM images of the impression made by indents number 1-3 (left) and 2-1 (right) taken from ALP sample.

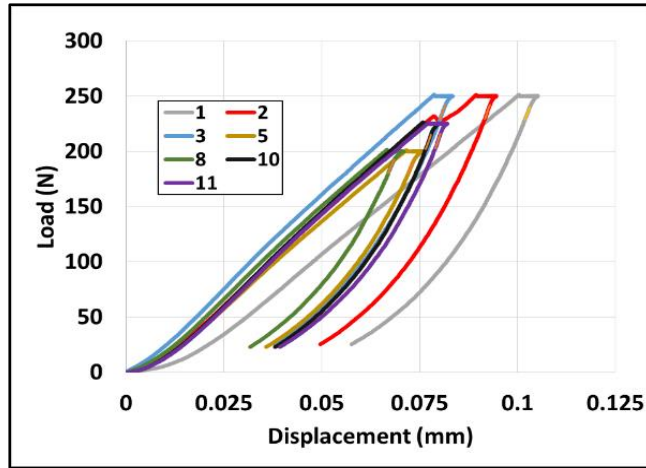


Figure 5-20: Load-displacement curves for the successful indentation made on AM sample.

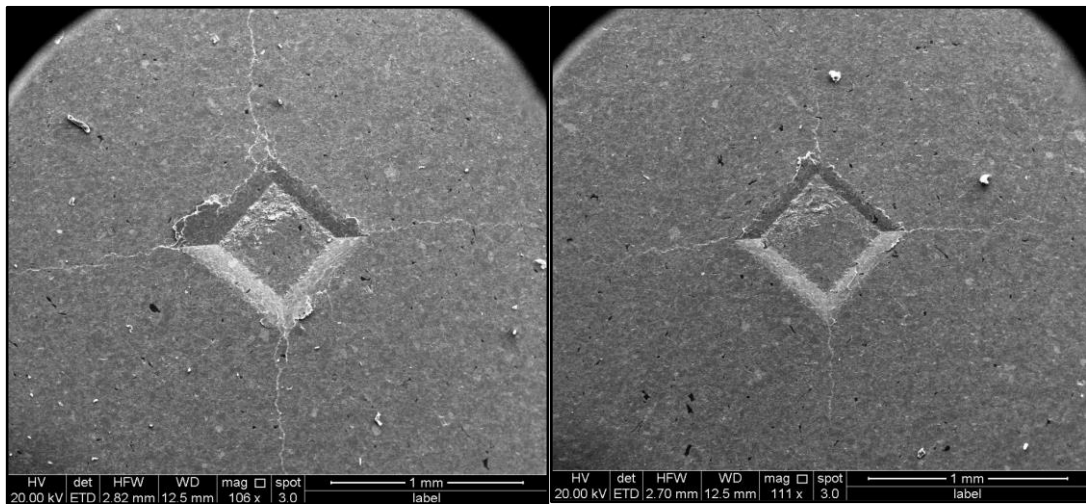


Figure 5-21: SEM images of the impression made by indents number 1 (left) and 5 (right) taken from AM sample.

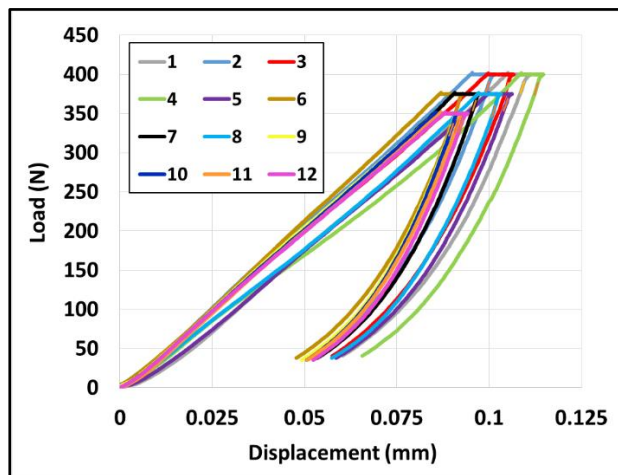


Figure 5-22: Load-displacement curves for the successful indentation made on KC sample.

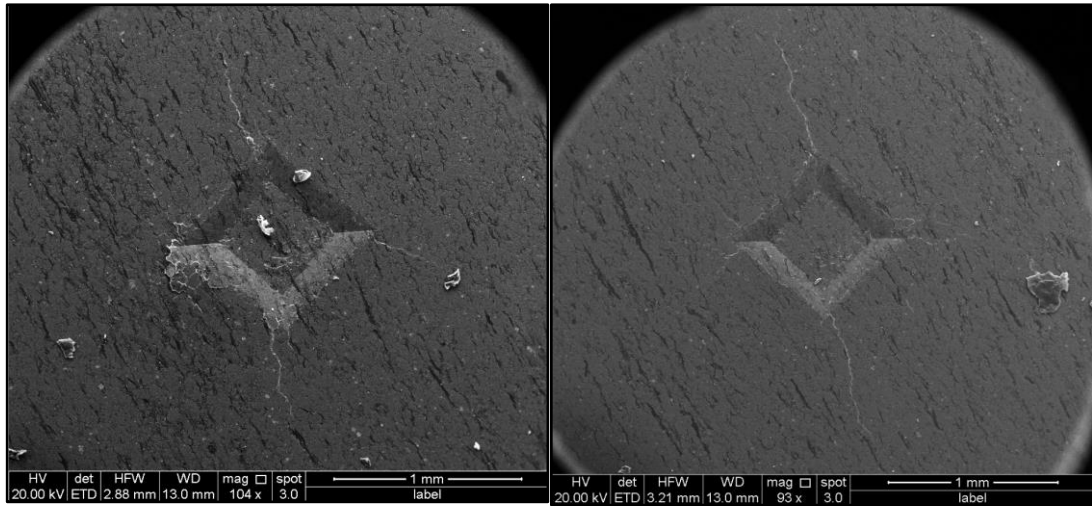


Figure 5-23: SEM images of the impression made by indents number 3 (left) and 12 (right) taken from KC sample.

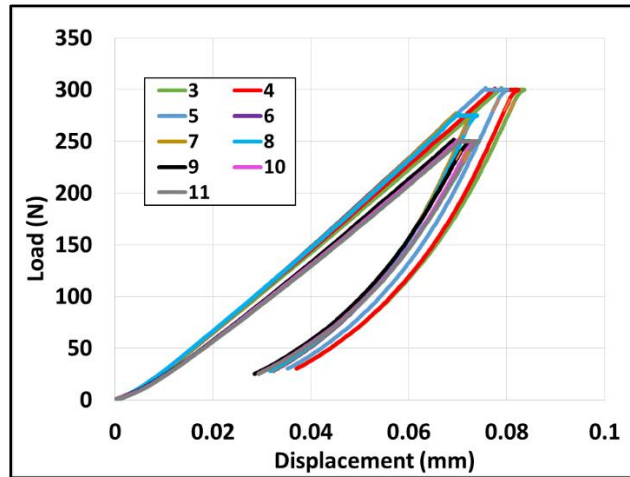


Figure 5-24: Load-displacement curves for the successful indentation made on OC sample.

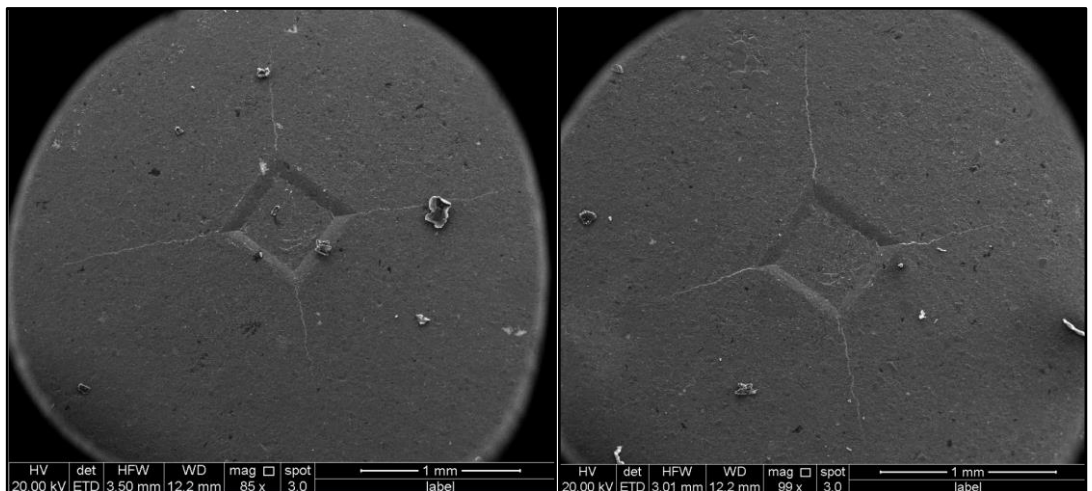


Figure 5-25: SEM images of the impression made by indents number 4 (left) and 6 (right) taken from OC sample.

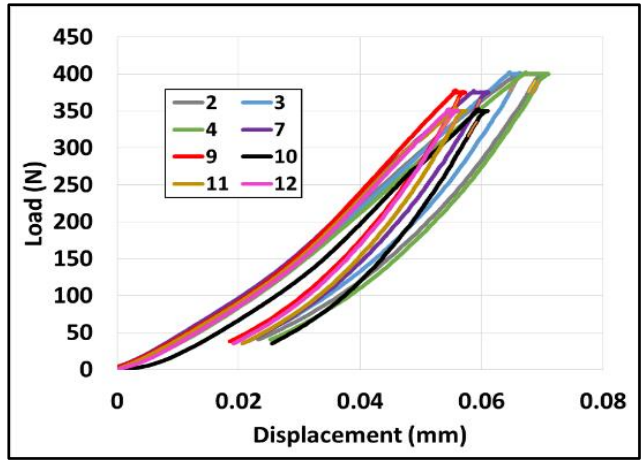


Figure 5-26: Load-displacement curves for the successful indentation made on D sample.

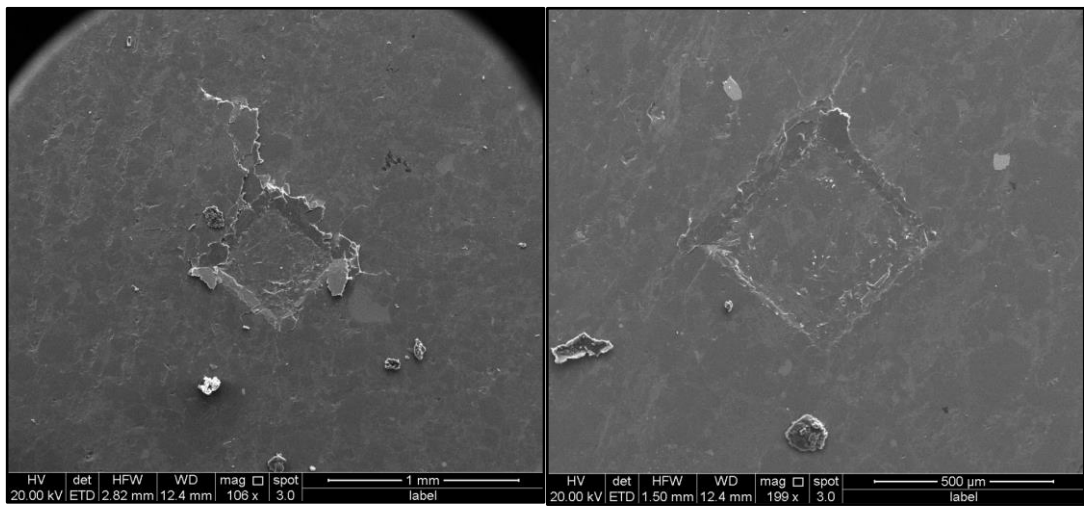


Figure 5-27: SEM images of the impression made by indents number 4 (left) and 12 (right) taken from D sample.

Indent number	Load (N)	Maximum displacement (mm)	Average $a$ (mm)	Average $c$ (mm)	Slope (N/mm)	$E_{eff}$ (GPa)	$H_V$ (GPa)	$K_{IC\_HP}$ (Evans & Charles, 1976)	$K_{IC\_HP}$ (Anstis et al., 1981)	$K_{IC\_CF}$ (Shetty et al., 1985)	$K_{IC\_CF}$ (Japanese Industrial Standard, 1990)
WS Sample											
2	100	0.075	0.46	0.92	4.37E+03	13.4	0.22	0.27	0.41	0.22	0.46
3	100	0.074	-	-	4.27E+03	13.4	-	-	-	-	-
4	100	0.076	0.47	0.96	3.70E+03	11.9	0.22	0.25	0.38	0.21	0.43
5	150	0.107	0.53	1.36	5.73E+03	11.6	0.25	0.22	0.32	0.23	0.36
6	150	0.109	-	-	5.80E+03	11.5	0.22	-	-	-	-
8	200	0.131	0.62	1.52	5.97E+03	10.0	0.25	0.25	0.36	0.25	0.41
9	200	0.134	0.64	1.66	6.53E+03	10.5	0.23	0.22	0.33	0.23	0.37
Average						11.8	0.23	0.25	0.36	0.23	0.40
ALP Sample											
1-1	250	0.155	0.70	1.49	8.57E+03	11.4	0.24	0.33	0.48	0.28	0.54
1-2	250	0.151	0.68	1.39	8.70E+03	11.9	0.25	0.36	0.52	0.30	0.58
1-3	150	0.102	0.55	0.95	5.65E+03	12.3	0.24	0.39	0.58	0.27	0.65
2-1	150	0.118	0.54	1.07	6.10E+03	10.9	0.24	0.32	0.48	0.26	0.54
2-2	150	0.099	0.68	1.39	5.52E+03	12.4	0.15	0.22	0.40	0.18	0.45
2-4	150	0.108	-	-	7.04E+03	13.6	-	-	-	-	-
2-5	200	0.127	-	-	9.55E+03	15.2	-	-	-	-	-
2-6	200	0.131	0.62	1.25	8.67E+03	13.5	0.25	0.34	0.49	0.28	0.55
2-7	200	0.125	0.63	1.23	7.76E+03	12.9	0.24	0.35	0.51	0.28	0.57
2-8	250	0.160	-	-	8.31E+03	10.6	-	-	-	-	-
2-9	250	0.156	-	-	7.99E+03	10.7	-	-	-	-	-
Average						12.3	0.23	0.33	0.49	0.26	0.56

Table 5-3 : Summary of parameters obtained from indentation data and the calculated properties using these parameters. This table is for WS and ALP samples.

Indent number	Load (N)	Maximum displacement (mm)	Average $a$ (mm)	Average $c$ (mm)	Slope (N/mm)	$E_{eff}$ (GPa)	$H_V$ (GPa)	$K_{IC\_HP}$ (Evans & Charles, 1976)	$K_{IC\_HP}$ (Anstis et al., 1981)	$K_{IC\_CF}$ (Shetty et al., 1985)	$K_{IC\_CF}$ (Japanese Industrial Standard, 1990)
AM Sample											
1	250	0.105	0.49	1.51	9.03E+03	19.0	0.49	0.32	0.48	0.40	0.54
2	250	0.095	0.53	1.24	1.03E+04	23.9	0.43	0.43	0.68	0.41	0.77
3	250	0.084	0.44	1.10	9.57E+03	26.6	0.62	0.51	0.68	0.53	0.77
5	200	0.076	0.43	1.02	8.64E+03	26.1	0.51	0.46	0.67	0.44	0.75
8	200	0.071	0.39	0.80	8.02E+03	27.3	0.62	0.66	0.87	0.55	0.98
10	225	0.080	0.43	0.95	9.74E+03	27.7	0.57	0.58	0.79	0.52	0.89
11	225	0.082	0.44	0.93	1.06E+04	28.4	0.56	0.60	0.83	0.52	0.93
Average						25.57	0.54	0.51	0.72	0.48	0.80
KC Sample											
1	400	0.111	0.66	1.04	1.41E+04	27.9	0.44	0.90	1.57	0.58	1.77
2	400	0.102	0.48	0.95	1.41E+04	31.2	0.81	1.02	1.31	0.82	1.47
3	400	0.107	0.50	0.94	1.51E+04	30.8	0.75	1.05	1.39	0.80	1.57
4	400	0.115	-	-	1.59E+04	29.5	-	-	-	-	-
5	375	0.106	0.50	0.78	1.32E+04	27.6	0.70	1.28	1.76	0.82	1.98
6	375	0.093	0.48	0.80	1.61E+04	31.1	0.77	1.24	1.64	0.84	1.84
7	375	0.098	0.51	0.82	1.46E+04	33.2	0.68	1.21	1.69	0.79	1.90
8	375	0.103	0.51	0.92	1.54E+04	32.2	0.67	1.01	1.42	0.73	1.60
9	350	0.092	0.49	0.73	1.35E+04	33.1	0.70	1.33	1.83	0.81	2.06
10	350	0.092	0.49	0.80	1.37E+04	33.5	0.70	1.17	1.61	0.78	1.81
11	350	0.093	0.49	0.89	1.41E+04	33.7	0.70	0.99	1.37	0.74	1.54
12	350	0.094	0.49	1.02	1.31E+04	31.3	0.70	0.81	1.12	0.69	1.26
Average						31.3	0.69	1.09	1.52	0.76	1.71

Table 5-4: Summary of parameters obtained from indentation data and the calculated properties using these parameters. This table is for AM and KC samples.



Indent number	Load (N)	Maximum displacement (mm)	Average $a$ (mm)	Average $c$ (mm)	Slope (N/mm)	$E_{eff}$ (GPa)	$H_V$ (GPa)	$K_{IC\_HP}$ (Evans & Charles, 1976)	$K_{IC\_HP}$ (Anstis et al., 1981)	$K_{IC\_CF}$ (Shetty et al., 1985)	$K_{IC\_CF}$ (Japanese Industrial Standard, 1990)
OC Sample											
3	300	0.084	0.44	1.29	1.07E+04	30.2	0.73	0.48	0.66	0.58	0.74
4	300	0.082	0.45	1.28	9.87E+03	29.4	0.72	0.49	0.68	0.58	0.76
5	300	0.080	0.45	1.19	9.47E+03	29.8	0.72	0.55	0.76	0.60	0.85
6	275	0.074	0.43	1.06	1.08E+04	35.2	0.71	0.60	0.83	0.60	0.93
7	275	0.073	0.43	0.98	1.09E+04	35.6	0.72	0.68	0.93	0.63	1.04
8	275	0.074	0.42	1.04	1.08E+04	34.9	0.73	0.61	0.83	0.62	0.94
9	250	0.073	0.42	0.75	8.56E+03	29.9	0.68	0.92	1.29	0.67	1.45
10	250	0.074	-	-	9.37E+03	30.9	-	-	-	-	-
11	250	0.074	0.40	0.92	8.95E+03	29.7	0.72	0.67	0.91	0.62	1.03
Average						31.7	0.72	0.63	0.86	0.61	0.97
D Sample											
2	400	0.070	0.36	0.57	1.39E+04	50.5	1.45	2.23	2.98	1.42	3.36
3	400	0.067	0.36	0.53	1.52E+04	57.0	1.44	2.46	3.30	1.47	3.72
4	400	0.071	0.37	0.66	1.54E+04	53.0	1.35	1.79	2.49	1.27	2.80
7	375	0.061	0.36	0.63	1.74E+04	68.7	1.37	1.80	2.49	1.27	2.80
9	375	0.057	0.35	0.56	1.61E+04	71.8	1.48	2.11	2.79	1.40	3.14
10	350	0.061	0.34	0.48	1.37E+04	58.2	1.44	2.53	3.39	1.45	3.81
11	350	0.057	0.33	0.48	1.53E+04	67.5	1.53	2.51	3.27	1.49	3.68
12	350	0.056	-	-	1.32E+04	64.6	-	-	-	-	-
Average						61.4	1.44	2.21	2.96	1.39	3.33

Table 5-5: Summary of parameters obtained from indentation data and the calculated properties using these parameters. This table is for OC and D samples.

Using the assumption of 0.25 Poisson’s ratio for all samples, the actual Young’s modulus of the samples are calculated and listed in Table 5-6. This table includes the average hardness and fracture toughness as well.

Sample	$E$ (GPa)	$H_V$ (GPa)	$K_{IC}$ (MPa. m <sup>1/2</sup> )
WS	11.1	0.23	0.31
ALP	11.6	0.23	0.41
AM	24.0	0.54	0.63
KC	29.3	0.69	1.27
OC	29.7	0.72	0.77
D	57.6	1.44	2.47

*Table 5-6: Summary of mechanical properties estimated using micro-indentation technique for lab-dry samples.*

#### 5.4.1.2 Acid exposed samples

Acid is expected to weaken the rock mechanically especially those with a high carbonates content. Thus, lower indentation loads are required to avoid damaging the samples. A new set of indentation loads were determined on acid exposed shale samples. Indentation loads for each shale sample are listed in Table 5-7. KC sample has the highest carbonates content among all samples used in this test. After acid exposure, KC sample become very weak and a load as low as 50 N caused damage to the sample. Thus, it was excluded from acid exposure test.

Sample	Loads applied (N)
WS	100-125-150
ALP	100-150
AM	100-150-175
OC	100-150-175
D	100-150-200

*Table 5-7: Indentation loads determined for all acid exposed shale samples.*

Young’s modulus and hardness of the samples were estimated using load-displacement data and SEM images. However, fracture toughness was not estimated for these samples because some of SEM images were not very clear due to damage on the indentation surface caused by acid exposure. Load-displacement curves and SEM

images for all samples are shown in the below figures (Figure 5-28 to Figure 5-37). Detailed calculation of indentation parameters and mechanical properties are found in Table 5-9 and Table 5-10. Using the similar assumption of Poisson's ratio, actual Young's modulus and final average hardness are listed in Table 5-8.

Sample	$E$ (GPa)	$H_V$ (GPa)
WS	6.5	0.15
ALP	7.6	0.19
AM	13.2	0.30
OC	11.6	0.17
D	30.7	0.57

Table 5-8: Summary of mechanical properties estimated using micro-indentation technique for acid exposed samples.

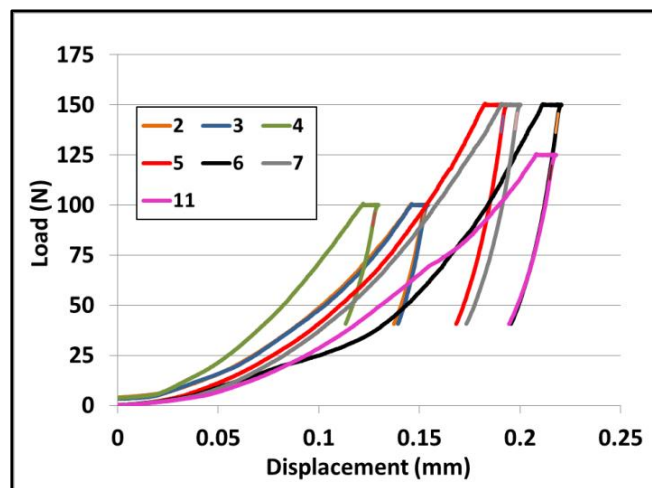


Figure 5-28: Load-displacement curves for the successful indentation made on acid exposed WS sample.

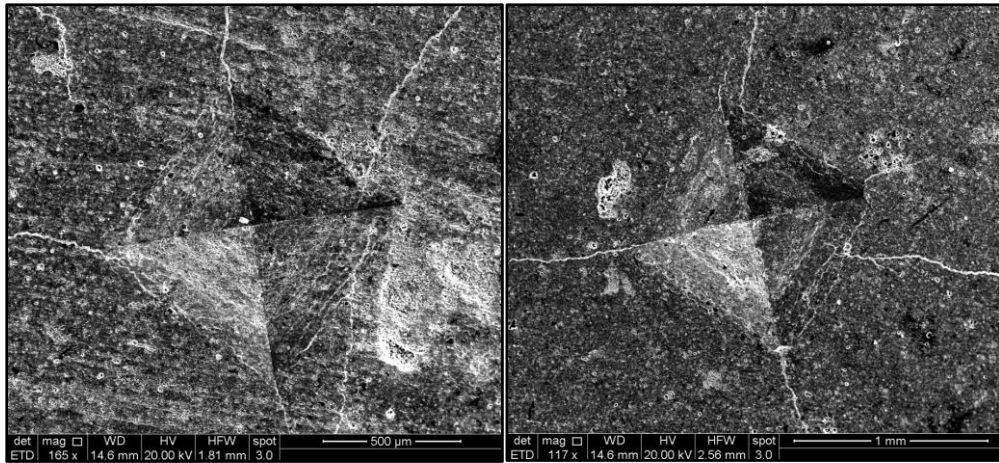


Figure 5-29: SEM images of the impression made by indents number 2 (left) and 5 (right) taken from acid exposed WS sample.

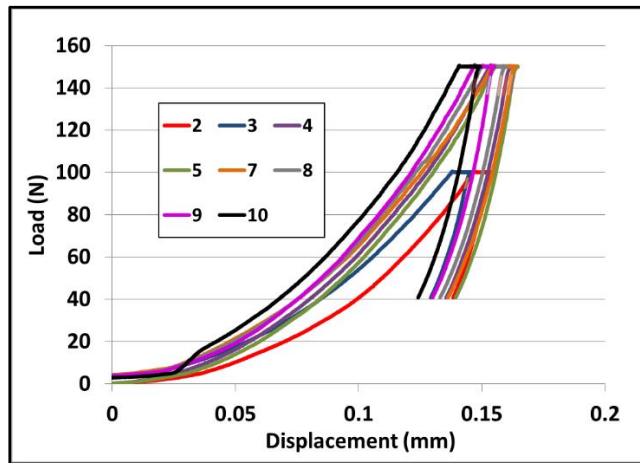


Figure 5-30: Load-displacement curves for the successful indentation made on acid exposed ALP sample.

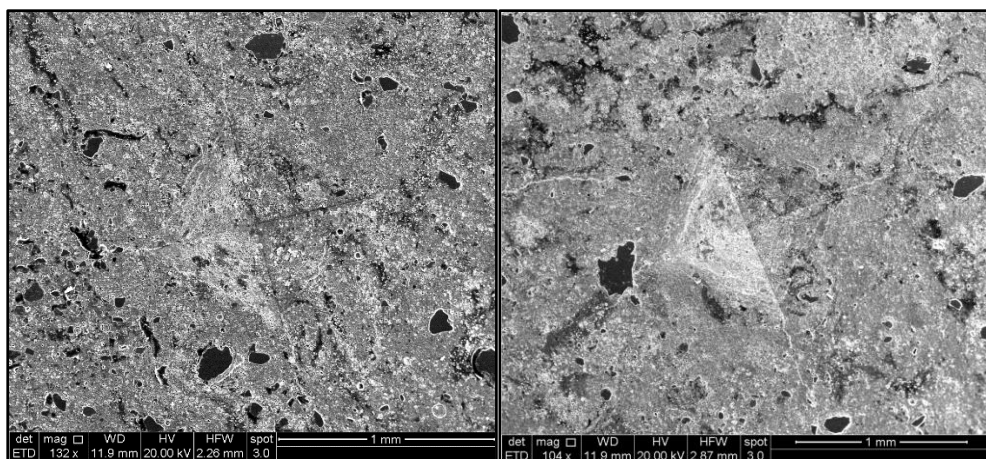


Figure 5-31: SEM images of the impression made by indents number 3 (left) and 4 (right) taken from acid exposed ALP sample.

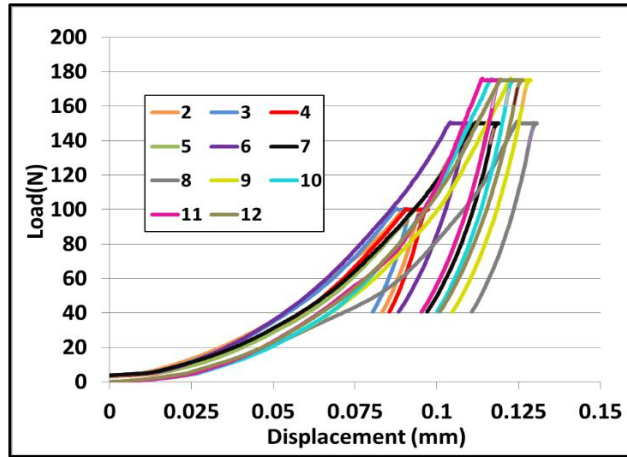


Figure 5-32: Load-displacement curves for the successful indentation made on acid exposed AM sample.

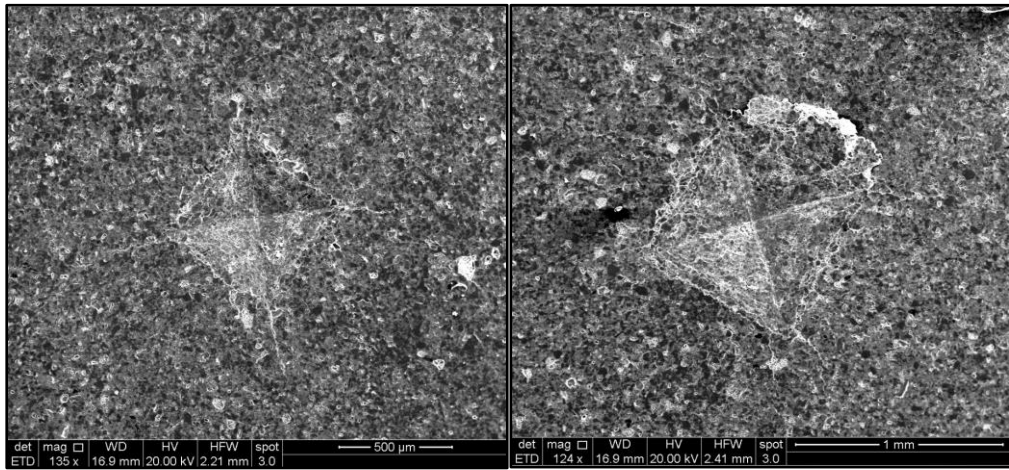


Figure 5-33: SEM images of the impression made by indents number 3 (left) and 9 (right) taken from acid exposed AM sample.

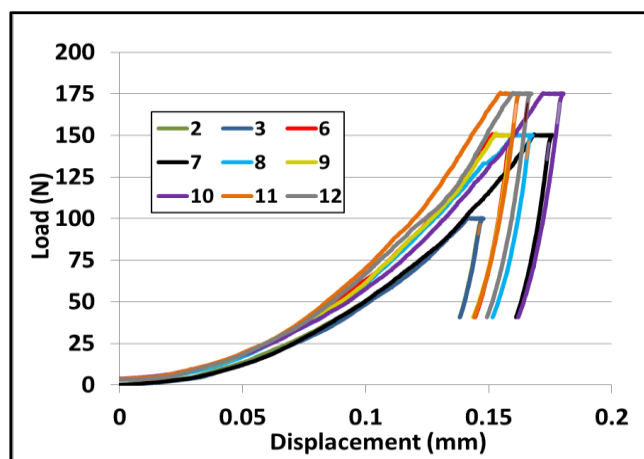


Figure 5-34: Load-displacement curves for the successful indentation made on acid exposed OC sample.

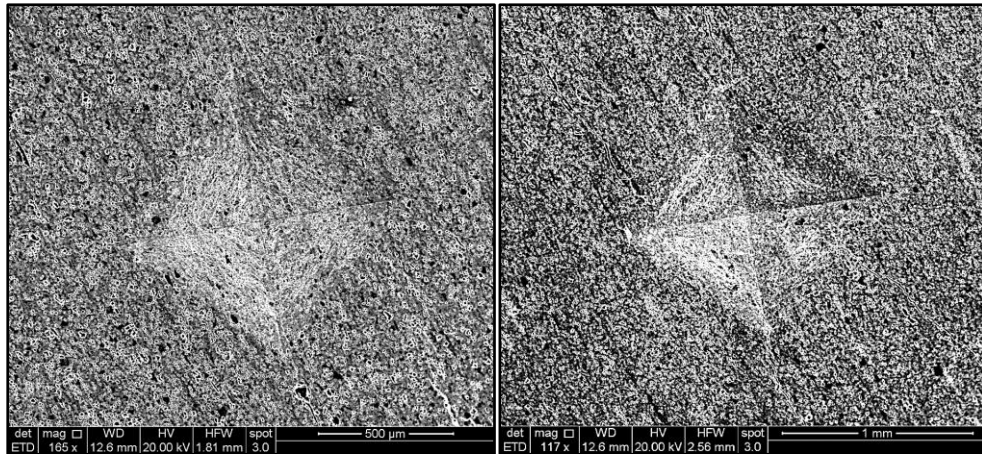


Figure 5-35: SEM images of the impression made by indents number 3 (left) and 12 (right) taken from acid exposed OC sample.

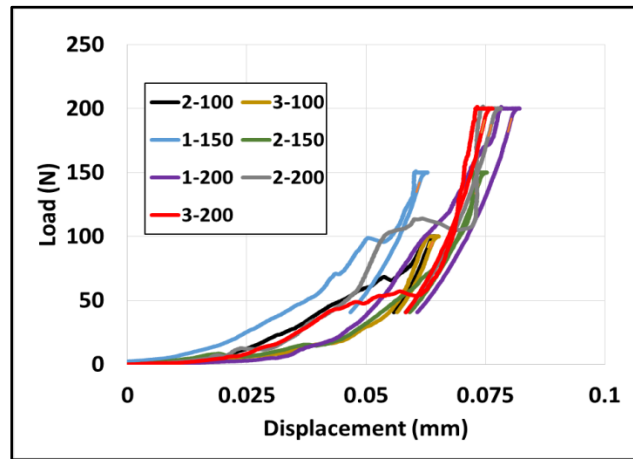


Figure 5-36: Load-displacement curves for the successful indentation made on acid exposed D sample.

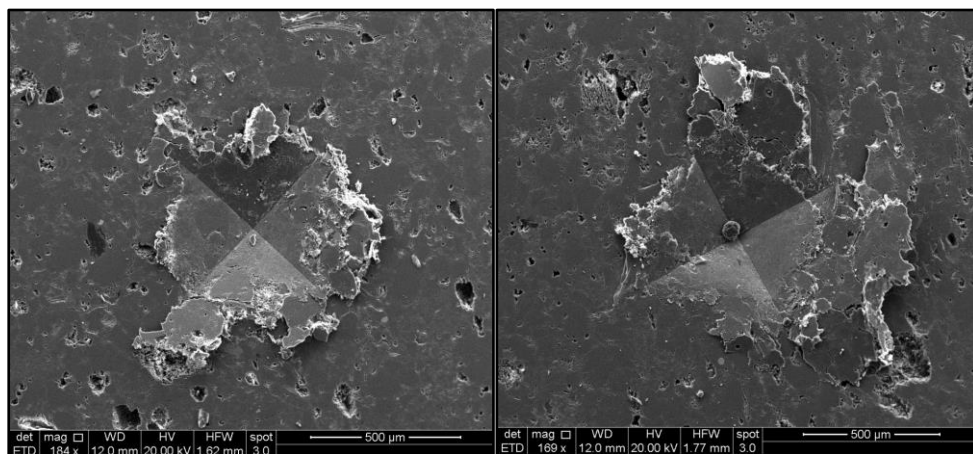


Figure 5-37: SEM images of the impression made by indents number 2-150 (left) and 1-200 (right) taken from acid exposed D sample.

Indent number	Load (N)	Maximum displacement (mm)	Average $a$ (mm)	Slope (N/mm)	$E_{eff}$ (GPa)	HV (GPa)
WS sample						
2	100	0.154	0.55	5.04E+03	6.4	0.16
3	100	0.154	0.59	5.87E+03	7.3	0.14
4	100	0.130	0.58	5.50E+03	8.4	0.14
5	150	0.194	0.66	7.54E+03	7.5	0.16
6	150	0.221	-	7.22E+03	6.6	-
7	150	0.200	0.66	6.81E+03	6.6	0.16
11	125	0.218	0.71	6.05E+03	5.3	0.12
Average					6.9	0.15
ALP sample						
2	100	0.154	-	6.12E+03	7.6	-
3	100	0.146	0.52	4.50E+03	6.2	0.18
4	150	0.162	0.55	6.43E+03	7.9	0.24
5	150	0.165	0.61	6.86E+03	8.2	0.19
7	150	0.164	-	6.50E+03	7.8	-
8	150	0.160	-	7.04E+03	8.7	-
9	150	0.155	0.60	7.14E+03	9.1	0.20
10	150	0.149	0.64	7.28E+03	9.6	0.18
Average					8.1	0.19
AM sample						
2	100	0.096	0.41	5.90E+03	12.6	0.29
3	100	0.093	0.39	6.39E+03	13.9	0.32
4	100	0.097	0.36	6.75E+03	13.8	0.37
5	150	0.117	0.48	8.45E+03	14.4	0.31
6	150	0.111	-	7.75E+03	14.3	-
7	150	0.112	0.51	7.47E+03	12.7	0.27
8	150	0.131	0.51	8.02E+03	12.2	0.27
9	175	0.129	0.57	9.93E+03	15.2	0.26
10	175	0.124	-	9.28E+03	15.0	-
11	175	0.120	0.52	9.61E+03	16.1	0.31
12	175	0.126	-	9.17E+03	14.5	
Average					14.1	0.30

*Table 5-9: Summary of parameters obtained from indentation data and the calculated properties using these parameters. This table is for acid exposed WS, ALP and AM samples.*

Indent number	Load (N)	Maximum displacement (mm)	Average $a$ (mm)	Slope (N/mm)	E <sub>eff</sub> (GPa)	HV (GPa)
OC sample						
2	100	0.148	0.57	7.96E+03	10.2	0.15
3	100	0.148	0.50	7.95E+03	10.2	0.19
6	150	0.160	0.66	1.11E+04	13.2	0.16
7	150	0.176	0.67	1.12E+04	11.9	0.16
8	150	0.168	0.65	1.14E+04	12.8	0.17
9	150	0.160	-	1.16E+04	13.6	-
10	175	0.180	0.74	1.21E+04	12.6	0.15
11	175	0.163	0.69	1.17E+04	13.6	0.18
12	175	0.167	0.69	1.20E+04	13.6	0.18
Average					12.4	0.17
D sample						
2-100	100	0.065	0.28	9.85E+03	30.6	0.62
3-100	100	0.065	0.31	8.80E+03	27.5	0.48
1-150	150	0.063	0.36	1.11E+04	37.4	0.54
2-150	150	0.075	0.33	1.08E+04	29.5	0.64
1-200	200	0.082	0.37	1.43E+04	35.2	0.68
2-200	200	0.078	0.44	1.43E+04	37.4	0.48
3-200	200	0.077	0.42	1.13E+04	31.6	0.54
Average					30.7	0.57

Table 5-10: Summary of parameters obtained from indentation data and the calculated properties using these parameters. This table is for acid exposed OC and D samples.

#### 5.4.2 Estimation of critical effective stress ( $p^*$ ) of shale using MIP technique

Samples from all six shale rock were prepared using the above mentioned procedure. For each shale rock, two samples were prepared and tested; one is unsealed and the other is sealed. Volumetric strain was calculated at each pressure step and plotted against pressure. Volumetric strain ( $V/V_o$ ) is calculated using the following equation:

$$\frac{V}{V_o} = \frac{Hg_{inc}}{V_o} \quad (5-7)$$



Where  $V$  is change in sample volume,  $V_o$  is initial sample volume and  $Hg_{inc}$  is cumulative mercury intrusion recorded by MIP equipment at each pressure step.

The first sample tested was WS sample which has the highest porosity and clay content among all samples. The results from unsealed sample showed a clear change in strain rate at hydrostatic stress of 25,000 psi as it is seen in Figure 5-38. If we assume all the mercury pumped in is compressing the sample and not invading the pore space, 25,000 psi would be the  $p^*$  of WS sample. Volumetric strain of the sealed WS sample shown in Figure 5-39 is the strain of rock and epoxy together. WS sealed sample showed also a change in strain between 20,000 psi to 30,000 psi. Using the linear approximation of both strain rates before and after compaction, the intersection between the two linear curves is about 23,169 psi. This is believed to be the  $p^*$  of WS sample.

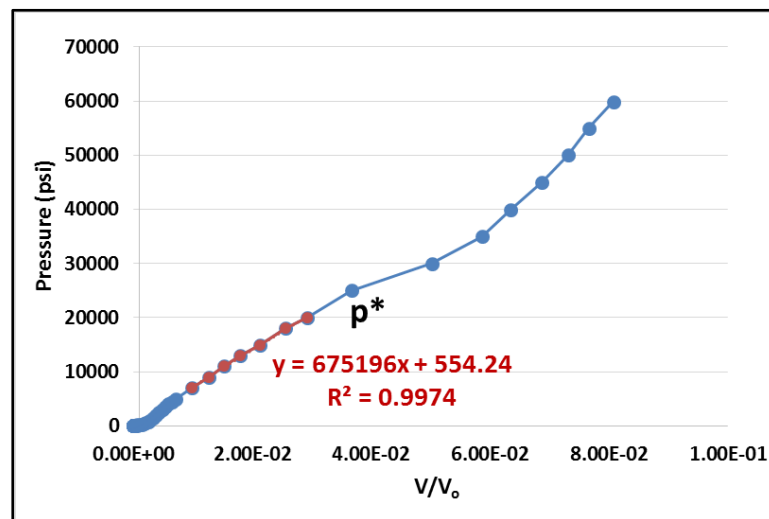


Figure 5-38: Volumetric strain at each pressure step for unsealed WS shale rock sample.  
Data is obtained from MIP test results.

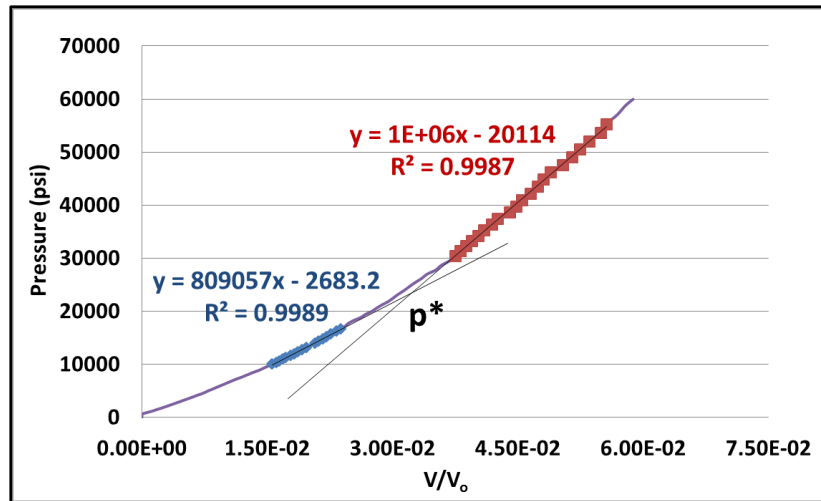


Figure 5-39: Volumetric strain at each pressure step for sealed WS shale rock sample. Volumetric strain plotted is for rock and sample together. Data is obtained from MIP test results.

ALP sample is a high clay content shale sample and relatively high porosity (about 5%). Unsealed ALP sample showed similar strain behaviour to unsealed WS sample. However, ALP unsealed estimated  $p^*$  was about 30,000 psi which is slightly higher than unsealed WS sample (Figure 5-40). ALP sealed sample  $p^*$  was found to be slightly higher than the unsealed sample (about 32,000 psi) as it is shown in Figure 5-41.

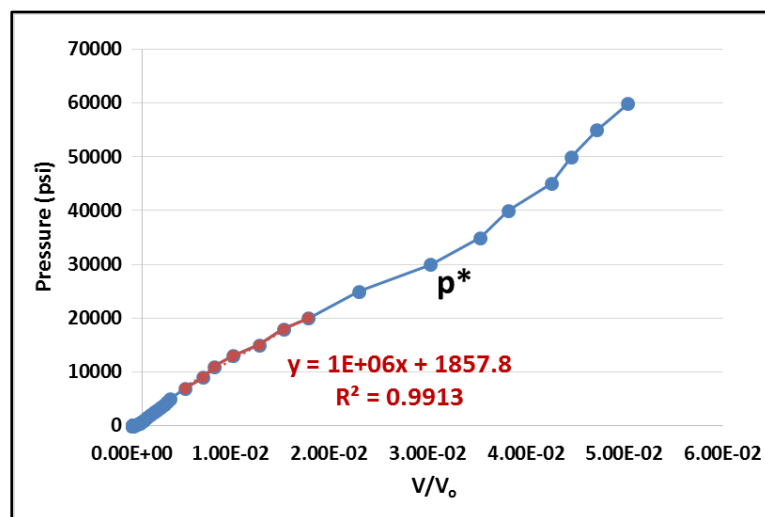


Figure 5-40: Volumetric strain at each pressure step for unsealed ALP shale rock sample. Data is obtained from MIP test results.

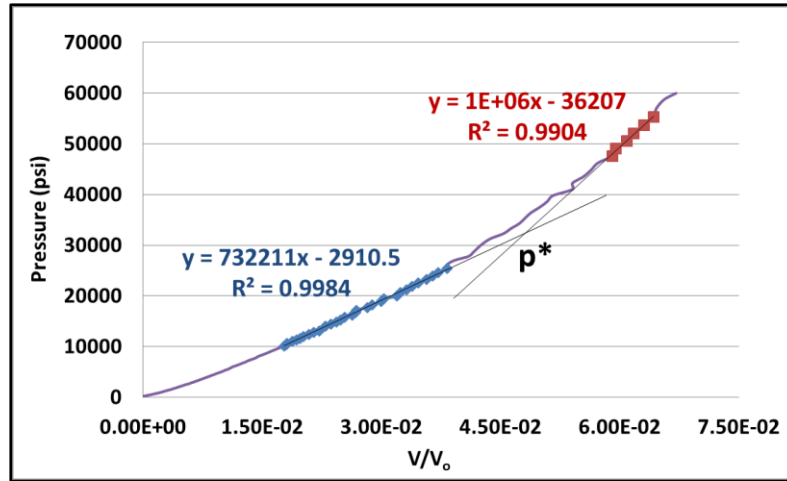


Figure 5-41: Volumetric strain at each pressure step for sealed ALP shale rock sample. Volumetric strain plotted is for rock and sample together. Data is obtained from MIP test results.

AM has a relatively high clay content but has a low porosity compared to the pervious samples. Estimation of  $p^*$  was less obvious in unsealed AM sample and it was found to be 36,400 psi as it is shown in Figure 5-42. The sealed AM sample  $p^*$  was slightly higher than the unsealed  $p^*$  similar to pervious shale rock samples (Figure 5-43). Although AM sample has relatively low porosity,  $p^*$  was quite high compared to previous samples.

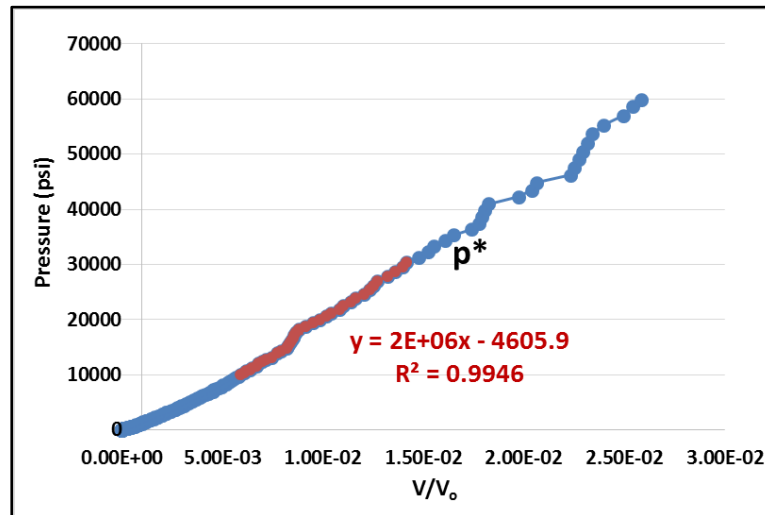


Figure 5-42: Volumetric strain at each pressure step for unsealed AM shale rock sample. Data is obtained from MIP test results.

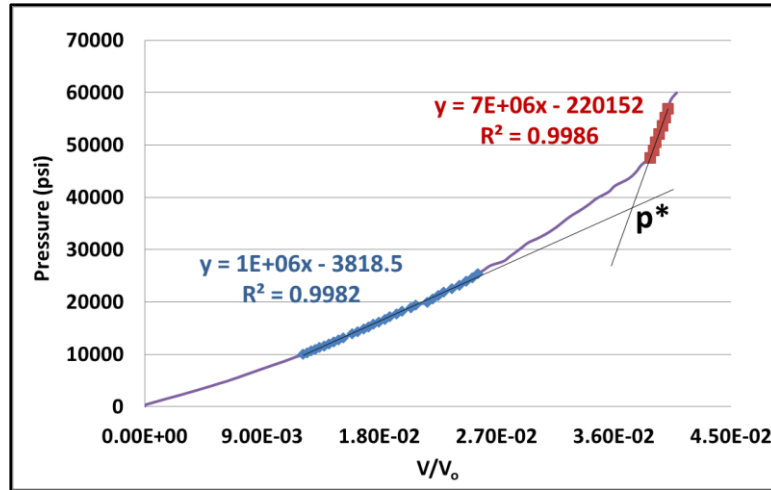


Figure 5-43: Volumetric strain at each pressure step for sealed AM shale rock sample. Volumetric strain plotted is for rock and sample together. Data is obtained from MIP test results.

All the pervious test samples had relatively high clay content. KC sample has relatively low clay content and is very carbonate-rich. The porosity of this shale sample is about 2.35% which is considered in the low side of this set of samples. According to the trend of pervious tested samples, KC sample was expected to have high  $p^*$  value. It was found that  $p^*$  for both unsealed and sealed samples agrees with the expectation and the values were 45,000 psi and 45,725 psi respectively. Volumetric strain curves for both unsealed and sealed samples are shown in Figure 5-44 and Figure 5-45 respectively.

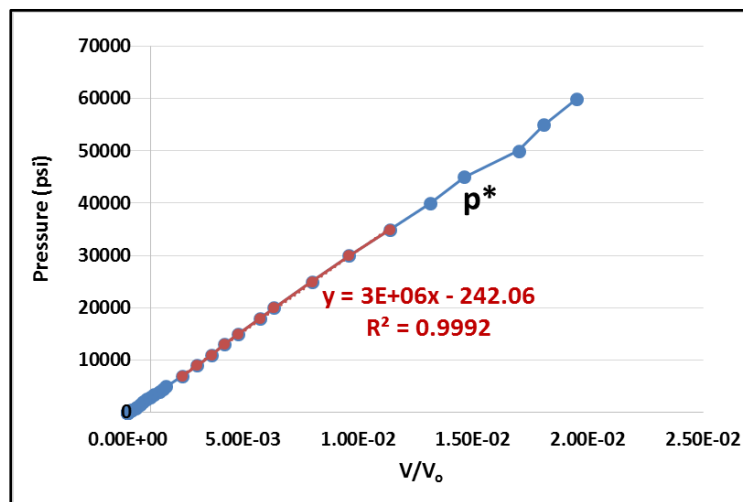


Figure 5-44: Volumetric strain at each pressure step for unsealed KC shale rock sample. Data is obtained from MIP test results.

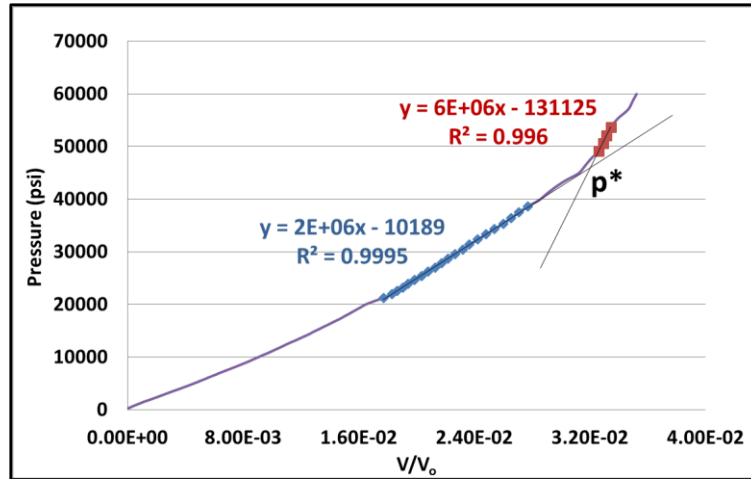


Figure 5-45: Volumetric strain at each pressure step for sealed KC shale rock sample. Volumetric strain plotted is for rock and sample together. Data is obtained from MIP test results.

OC sample is among the hardest samples in the set and has relatively low porosity and clay content. In addition, this sample is carbonate-rich (about 22.8%) which induces extra hardness. According to  $p^*$  trend observed from the previous samples, OC sample should have  $p^*$  slightly higher than KC sample because porosity of OC sample (about 1.71%) is slightly lower than KC sample porosity. The  $p^*$  of OC unsealed sample was easy to identify at around 46,620 psi which agrees with the expectations (Figure 5-46). The sealed OC sample  $p^*$  was found to be 49,305 psi, which is slightly higher than the sealed sample as it is shown in Figure 5-47.

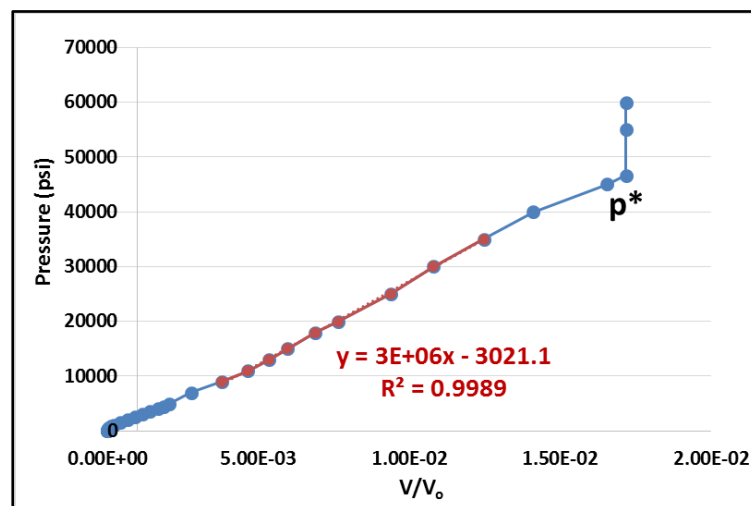


Figure 5-46: Volumetric strain at each pressure step for unsealed OC shale rock sample. Data is obtained from MIP test results.

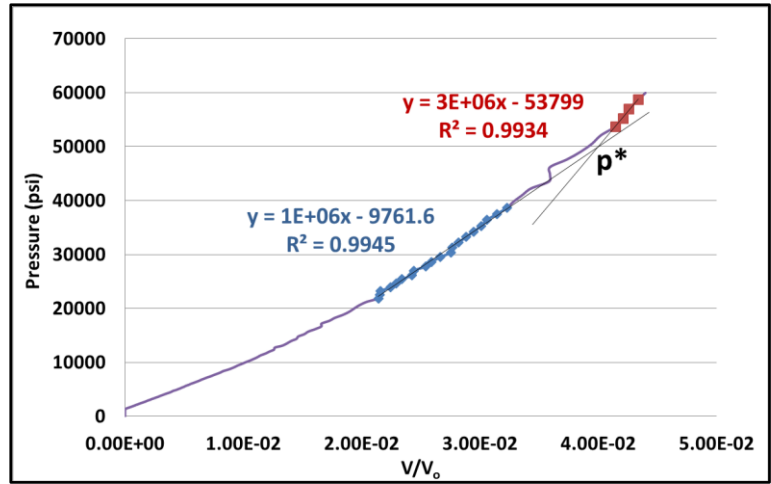


Figure 5-47: Volumetric strain at each pressure step for sealed OC shale rock sample. Volumetric strain plotted is for rock and sample together. Data is obtained from MIP test results.

The D sample is the hardest sample in the set with very high quartz content (about 57.3 %) and extremely low porosity (0.35 %). This sample has relatively moderate clay content and no carbonates, which leads to the conclusion that quartz is the source of large hardness. The unsealed D sample did not actually show any sign of compaction and strain did not change at all from 9,000 psi (Figure 5-48). However, the sealed D sample experienced a slight compaction between 40,000 psi and 50,000 psi as it is shown in Figure 5-49. The sealed D sample  $p^*$  was estimated to be 47,514 psi.

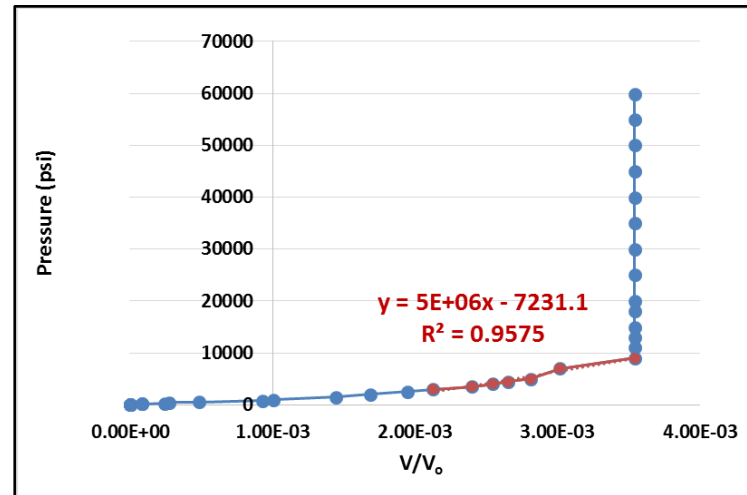


Figure 5-48: Volumetric strain at each pressure step for unsealed D shale rock sample. Data is obtained from MIP test results.

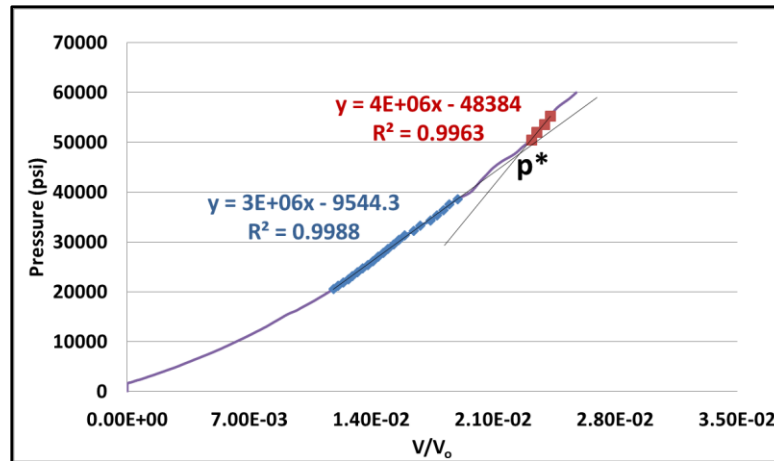


Figure 5-49: Volumetric strain at each pressure step for sealed D shale rock sample. Volumetric strain plotted is for rock and sample together. Data is obtained from MIP test results.

## 5.5 Discussion

### 5.5.1 Measurement of mechanical properties using micro-indentation

#### 5.5.1.1 Effect of mineral composition

Many authors conducted studies on the effect of mineralogy on geomechanical properties particularly Young's modulus (e.g. Shukla et al., 2013; Rybacki et al., 2014). Generally, Young's modulus is inversely proportional to both clay content and TOC (Figure 5-50 and Figure 5-51). This means that the presence of clay and organic contents decreases Young's modulus making shale rocks soft. On the other hand, the presence of quartz and carbonates minerals increases Young's modulus and thus makes shale rocks stiffer as it shown in Figure 5-52.

For all samples used in this thesis, total clay content, TOC and summation of quartz and carbonates content are calculated and listed in Table 5-11. The variation in total clay content between the samples was about 32.6-61.9%. For such variation, Young's modulus will have average variation of about 40-50 GPa using the data in Figure 5-50. The total quartz and carbonates weight content has similar variation to clay content (about 30.4-62.6%) and reflected variation in Young's modulus was about 40-50 GPa. In this set of samples, the component that will control stiffness of the shale sample is TOC. Total variation in TOC in this set of samples is 0.52-6.70% which according to Figure 5-51 will induce average variation of 35-70 GPa in Young's modulus.

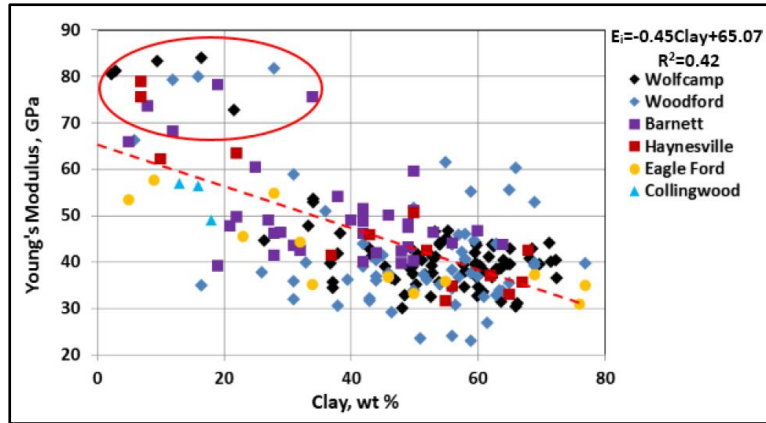


Figure 5-50: Young's modulus obtained by nanoindentation versus clay content different shale samples. points encircled in red are outliers. There is an inverse relation between the two paramters but has weak correlation coefficient (Shukla et al.,2013).

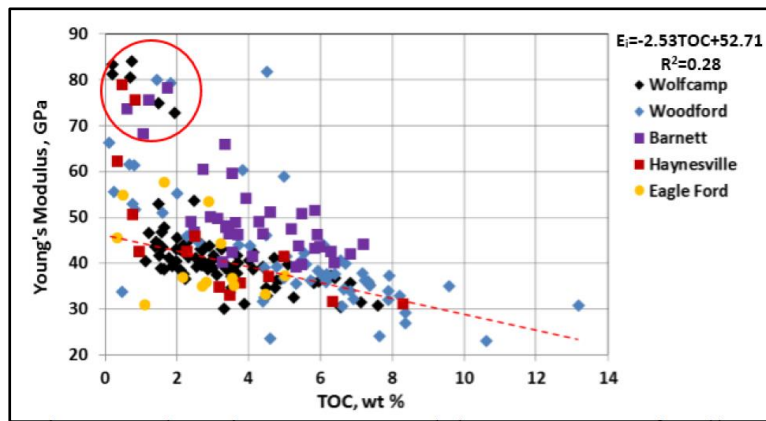


Figure 5-51: Young's modulus obtained by nanoindentation versus TOC for different shale samples. points encircled in red are outliers. Overall, there is an inverse porpotionality between the two paramters and data is less scattered at higher TOC values (Shukla et al.,2013).

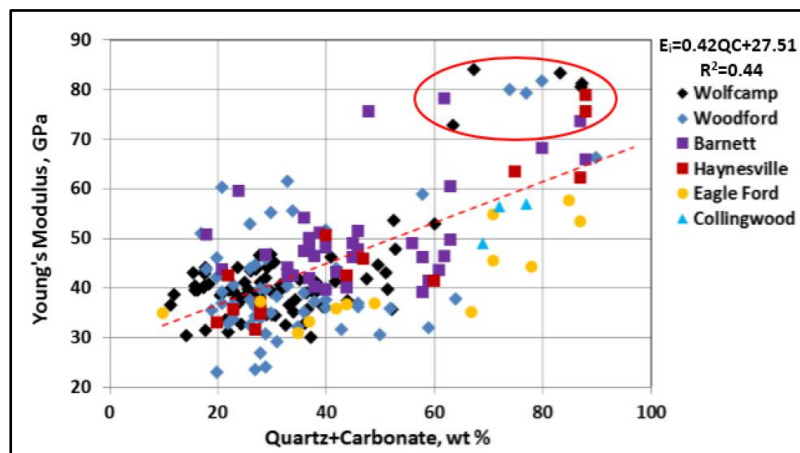


Figure 5-52: Young's modulus obtained by nanoindentation versus (quartz+carbonate) for different shale samples. points encircled in red are outliers. There is a direct proportionality between the two paramters(Shukla et al.,2013).



Sample	Clay content (%)	TOC (%)	Quartz and carbonates (%)	Quartz (%)
WS	61.9	3.4	30.4	21.7
ALP	52.9	6.5	33.8	28.4
AM	54.7	0.8	45.9	45.9
KC	32.6	6.7	62.6	16.3
OC	35.5	3.4	61.0	38.2
D	43.3	0.5	57.3	57.3

*Table 5-11: Total weight percentage of clay, TOC and quartz & carbonates minerals for all samples.*

Total clay content weight percentage was plotted against Young's modulus to highlight the effect of mineralogy on Young's modulus (Figure 5-53). It can be seen that the measured Young's modulus is inversely proportional to clay content of shale samples. The D sample has the highest Young's modulus among all samples. This sample has relatively moderate clay content with respect to other samples (about 43.3%) and the lowest TOC, which is about 0.5%. However, it has relatively high quartz and carbonates content (about 57.3%) which is mostly quartz. Quartz is considered a strong mineral, carbonates are of intermediate strength and clay minerals are considered mechanically weak (Rybacki et al., 2014). High quartz content present in the D sample is responsible for stiffness of the sample and increase in Young's modulus. The black arrow in Figure 5-53 represents the effect of quartz mineral on the elastic properties of shale.

The AM sample has slightly higher TOC than the D sample (about 0.8%) and relatively high clay content, which is about 54.7%. Quartz content is high but lower than the D sample. The increase in TOC and clay content together with reduction in quartz content has made this sample softer and hence has lower Young's modulus.

The rest of the samples (WS, ALP, KC and OC) have a relatively moderate to low quartz content. WS and ALP samples have relatively high clay content, which is about 61.9% and 52.9% respectively. WS and ALP are the softest samples in the set and have Young's modulus similar to each other, 11.1 GPa and 11.6 GPa respectively. Although there is a big difference in clay content, both samples show similar Young's modulus due to the high TOC content in the ALP sample which made it much softer. The WS sample have moderate clay content (about 3.4%), which gave the sample extra more softness. The effect of TOC is highlighted with a red arrow in Figure 5-53.

The KC and OC samples are considered stiff and have almost the same Young's modulus, 29.3 GPa and 29.7 GPa respectively. Both samples have a relatively low clay content and high quartz and carbonates content, which will actually explain the stiff nature of the samples. The 62.6 % quartz and carbonate content present in KC sample consists of 16.3% quartz, 35.5% dolomite and 10.8 % calcite. Dolomite has very high strength and increases Young's modulus dramatically in dolomite-rich samples. However, KC sample has high TOC content (about 6.7%), which will reduce Young's modulus dramatically and hence increase softness of the sample. The OC sample has a quartz and carbonate content of 61.0%, which consists of 38.2% quartz, 19.2% calcite and 3.6 % dolomite. This sample has a TOC of 3.4%, which is relatively moderate and will reduce Young's modulus. The effect of TOC for both KC and OC samples are indicated with a red arrow in Figure 5-53.

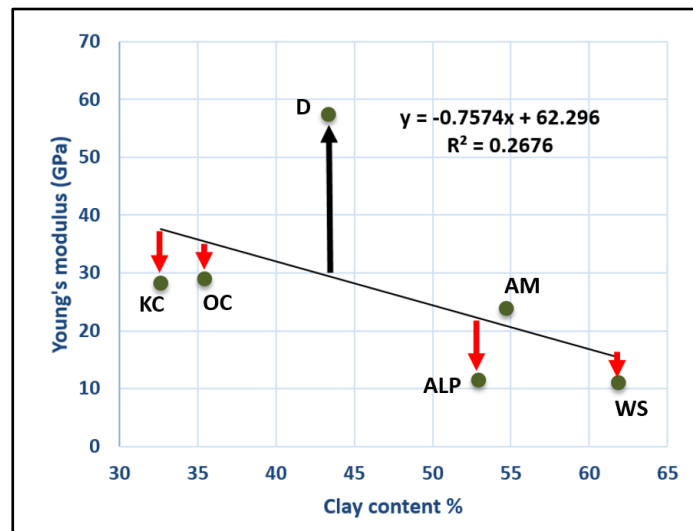


Figure 5-53: Young's modulus obtained by microindentation for all samples versus total weight % of clay content. The red arrow indicates the effect of TOC and black arrow indicate the effect of total weight content of quartz & carbonates minerals.

### 5.5.1.2 Relationship between Young's modulus, hardness and fracture toughness

To validate microindentation elastic results, Young's modulus obtained by micro-indentation is compared against the one obtained by triaxial testing. Figure 5-54 represents a comparison between the two methods with respect to 1:1 straight line with a good correlation between the results of these two measurement methods. The comparison suggests that micro-indentation technique is capable of providing reliable measurement of elastic modulus for shales.

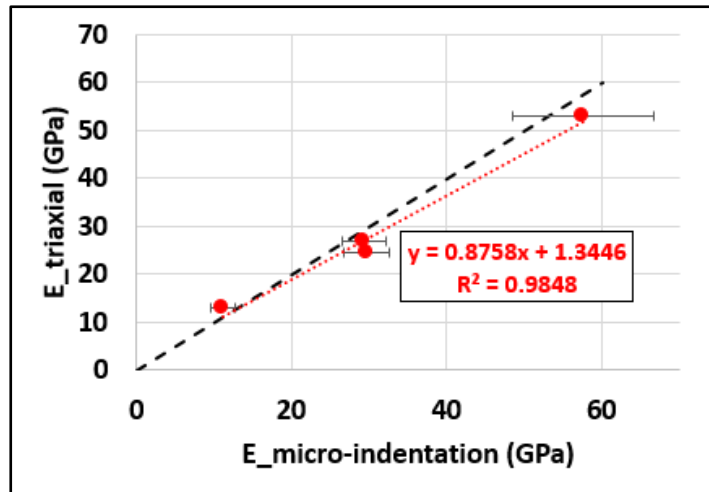


Figure 5-54: Estimated Young's modulus using triaxial test against micro-indentation. The dashed black represents 1:1 relationship.

Normally, Young's modulus is directly proportional to hardness for shales (e.g. Kumar et al., 2012; Corapcioglu, 2014; Shukla et al., 2013). Figure 5-55 presents the relationship between Young's modulus and hardness obtained by micro-indentation, which shows a clear proportionality with excellent correlation. In addition, experimental results showed good agreement with the general hardness-Young's modulus relationship trend as it is clearly seen in Figure 5-56.

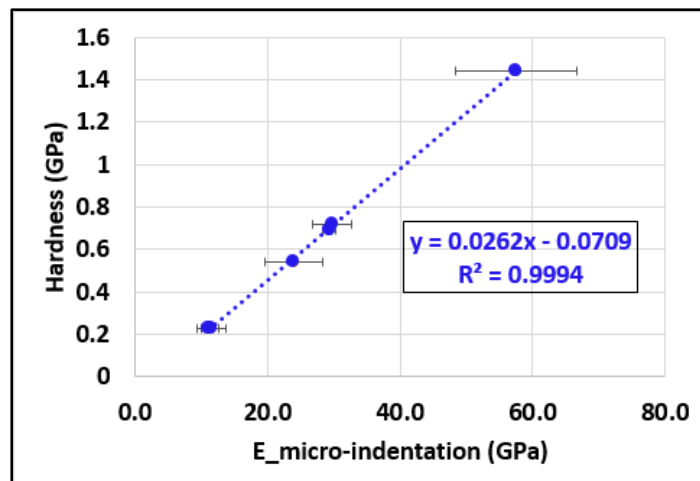


Figure 5-55: Relationship between Young's modulus and hardness obtained by micro-indentation technique. This data is for lab dry samples.

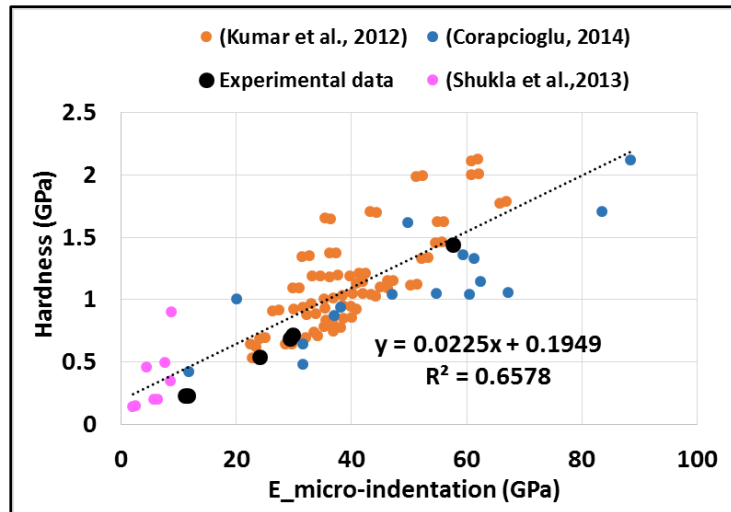


Figure 5-56: Relationship between Young's modulus and hardness from different authors. Data obtained from Kumar et al. (2012), Corapcioglu (2014) and Shukla et al.(2013).

Fracture toughness has a great influence on understanding fracture propagation especially in hydraulic fracturing. Only few data are available of measured fracture toughness of shale in the literature. Figure 5-57 represents fracture toughness measurement available in the literature against Young's modulus from Chandler et al. (2016) and Liu (2015). Fracture toughness is directly proportional to estimated Young's modulus with relatively acceptable correlation ( $R^2=0.745$ ). The fracture toughness estimated in the research follows the same trend as the published measurements in the literature. This suggests that soft samples with low Young's modulus have lower resistance to a fracture than the stiff samples with large Young's modulus.

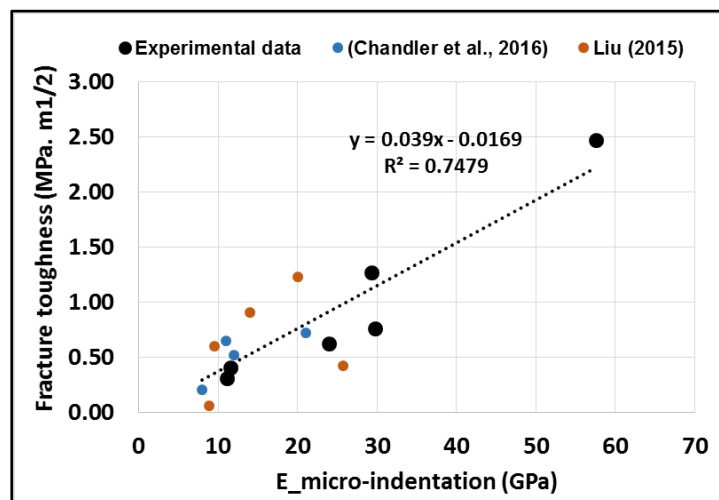


Figure 5-57: Young's modulus against fracture toughness for shale rocks. Data obtained from Chandler et al. (2016) and Liu (2015).

### 5.5.1.3 Effect of acid on mechanical properties of shale

Micro-indentation results for acid-exposed samples had similar behaviour as lab-dry samples. Estimated Young's modulus was directly proportional to hardness and the trend matches perfectly with other data as it shown in Figure 5-58. The KC sample had the highest carbonates content which explains the weakening of the sample after acid exposure. This made performing micro-indentation with the suggested experimental setup difficult.

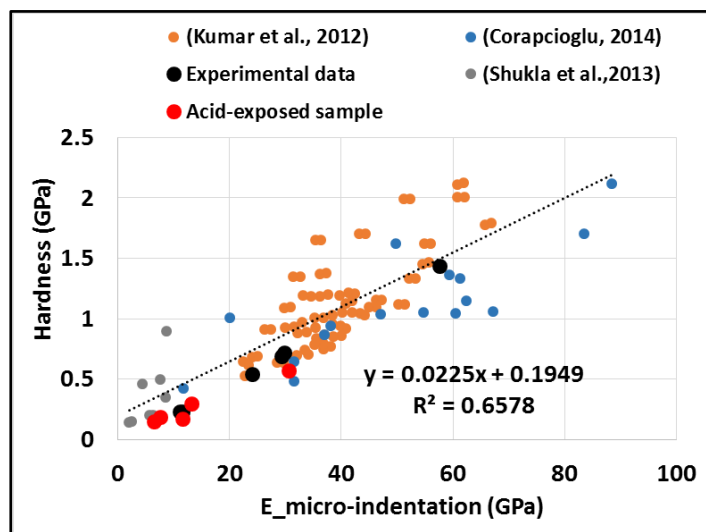


Figure 5-58: Relationship between Young's modulus and hardness from different authors including lab-dry samples and acid-exposed samples results. Data obtained from Kumar et al. (2012), Corapcioglu (2014) and Shukla et al.(2013).

All samples subjected to acid experienced a reduction in Young's modulus by at least 34%. Samples which have carbonate minerals were expected to have a significant reduction in strength due to the reaction between acid and carbonate minerals. However, it was noticed that even samples with no carbonates content underwent a reduction in Young's modulus of about 45%. The OC sample has large carbonates content (23%) and results in a reduction of 61% in Young's modulus after acid exposure. The WS and ALP samples had similar carbonates content (9% and 5 % respectively) and had the lowest reduction in Young's modulus among all samples (41% and 34% respectively).

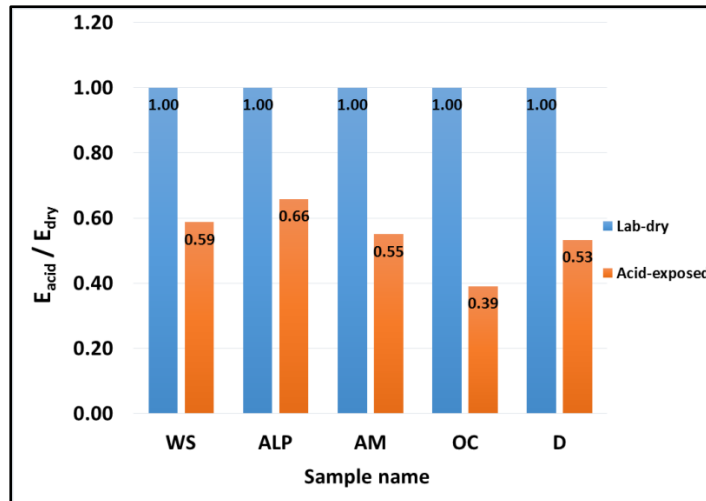


Figure 5-59: Bar chart describing reduction in Young's modulus due to acid exposure for a period of one month.

## 5.5.2 Estimation of critical effective stress ( $p^*$ ) of shale using MIP technique

### 5.5.2.1 $P^*$ results validation

According to critical state theory, size of failure envelope in  $p$ - $q$  spaces with increasing burial depth. As porosity decreases with burial, the size of failure envelope will increase with decreasing porosity. Hence, preconsolidation pressure is inversely proportional to porosity and will increase with decreasing porosity. Figure 5-60 represents the effect of porosity on size of failure envelope and preconsolidation pressure.

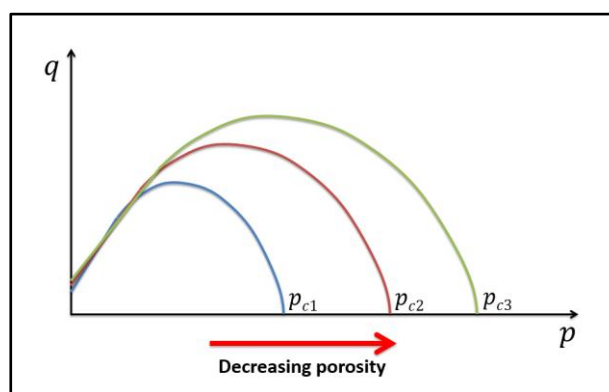


Figure 5-60: Effect of porosity on preconsolidation pressure of rocks.

The data of  $p^*$  measurement presented by Wong et al. (1997) showed an inverse proportionality to porosity. Using the results of Wong et al. (1997), Fisher et al. (2007) developed an inverse linear relationship between ( $p^*$ ) and the product of

porosity and grain size ( $R\phi$ ) in log-log space Figure 5-61. The regression line through the data is:

$$\log(p^*) = 3.9 - 1.1 \log(R\phi) \quad (5-8)$$

where:  $p^*$  is in (MPa),  $R$  is in ( $\mu\text{m}$ ) and  $\phi$  is porosity fraction. This model is extremely simple and can be considered semi-quantitative. However, the results of this model showed constituency with observation made from several hundred petroleum reservoirs around the world (Fisher et al., 2007).

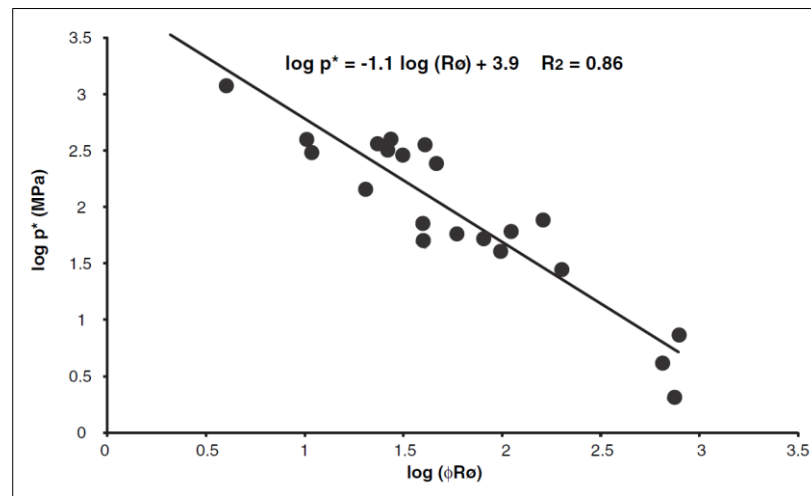


Figure 5-61: Log–log plot of  $p^*$  against the product of grain radius and porosity developed by Fisher et al. (2007). Included is the regression line through the data (black). The grey line and equation represent the minimum boundary to the data and were used to calculate  $p^*$  values in the simulations presented. Data are from Wong et al. (1997).

$p^*$  measured for both sealed and unsealed samples showed a decreasing trend with increasing porosity as it can be seen in Figure 5-62. Shale rocks are very fine sediments and grain size does not have much significance in determining strength. Thus, a relationship similar to the one developed by Fisher et al. (2007) was presented between porosity and  $p^*$  in a form of linear relationship given as:

$$\text{Sealed:} \quad p^* = -3579.7 * (\phi) + 51540 \quad (5-9)$$

$$\text{Unsealed:} \quad p^* = -4175.8 * (\phi) + 52446 \quad (5-10)$$

where  $p^*$  is in (psi) and  $\phi$  is porosity is in %. Both data for sealed and unsealed samples had a good fitting with linear models as it is shown in Figure 5-63.

Sample	Porosity (%)	unsealed $p^*$ (psi)	sealed $p^*$ (psi)
ALP	5.04	30,000	32,000
AM	3.01	36,386	38,069
D	0.35	***	47,514
OC	1.71	46,620	49,305
WS	8.06	20,000	23,169
KC	2.35	45,000	45,725

Figure 5-62: Summary of all shale rocks  $p^*$  estimated for sealed and unsealed samples.

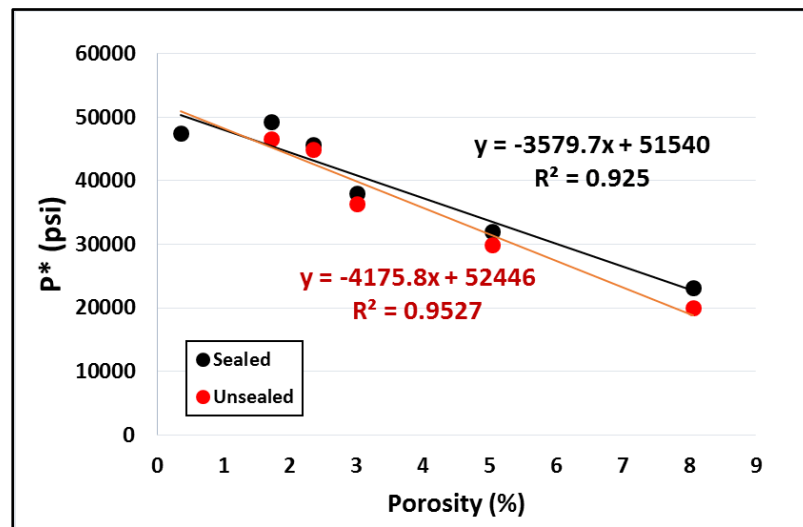


Figure 5-63: Porosity versus  $p^*$  relationship showing a decreasing trend of  $p^*$  with increasing porosity.

Shale rocks are fine grained sediments and they are likely to have a ductile failure by shear enhanced compaction or porosity collapse rather than grain crushing. Chalks are also fine grained sediment and expected to behave similarly to shale in ductile regime. Since  $p^*$  is actually the pressure at which the sample undergoes ductile failure by compaction or porosity collapse,  $p^*$  for both rocks should be comparable. Figure 5-64 shows porosity- $p^*$  relationship for chalk using  $p^*$  values measured in the laboratory (unpublished data). It can be seen that  $p^*$  for shale measured using the above described method falls perfectly in porosity-  $p^*$  trend for chalks.



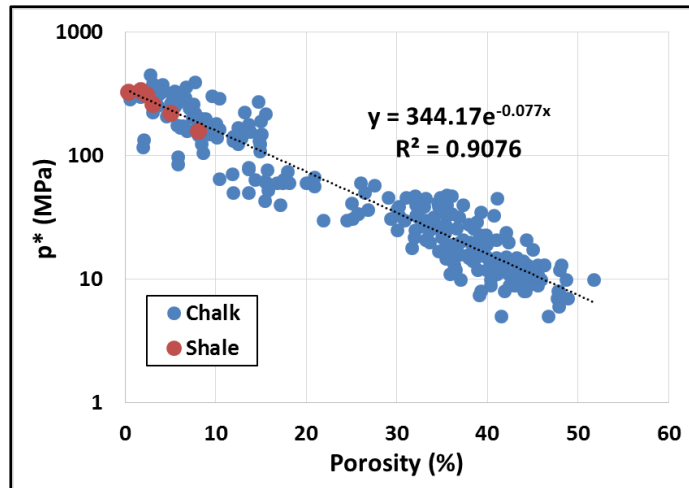


Figure 5-64: porosity versus measured  $p^*$  (in log-space) for chalk (Blue). Red data points are measure  $p^*$  for shale.

### 5.5.2.2 Effect of mineralogy and permeability on estimating elastic properties of the samples

Unsealed  $p^*$  was similar to sealed  $p^*$  in most of the samples. Unsealed  $p^*$  in some of the samples was easy to recognize from volumetric strain and stress curve. However, in other samples, it was not obvious and in the D sample in particular, it was not possible to identify. Looking at the curves for unsealed OC and D samples (Figure 5-46 and Figure 5-48 respectively), it seems that mercury invaded all the effective pore spaces before reaching crushing pressure  $p^*$ . Volumetric strain becomes constant when mercury invades all effective pore spaces, even if the pressure is increased further. The point at which effective pore space is filled completely with mercury is estimated to be 46,620 psi and 8,979 psi from the data provided in Figure 5-46 and Figure 5-48 for OC and D samples respectively.

According to Hildenbrand and Urai (2003), mercury pumped in is deforming the sample and does not enter effective pore space for tight samples with low permeability. As it was discussed in **Chapter 2**, shale permeability varies with porosity and mineralogy. Figure 5-65 presents permeability and porosity relationship shown earlier for various mudrocks with different clay content. The red square represent the range of porosities and the corresponding range of permeabilities for the samples used in this test. It can be seen in Figure 5-65 that for the set of the samples tested, permeability variation could be up to two order of magnitudes. Low clay content samples have larger permeability than high clay content samples. Thus, KC,

OC and D samples will have larger permeability than WS, ALP and AM samples. This explains why D and OC samples had their effective pore spaces filled with mercury before compaction occurs. The KC sample has low clay content but did not behave like D and OC samples due to its high carbonates content which will reduce permeability dramatically. These observations agree with Hildenbrand and Urai (2003) suggestions.

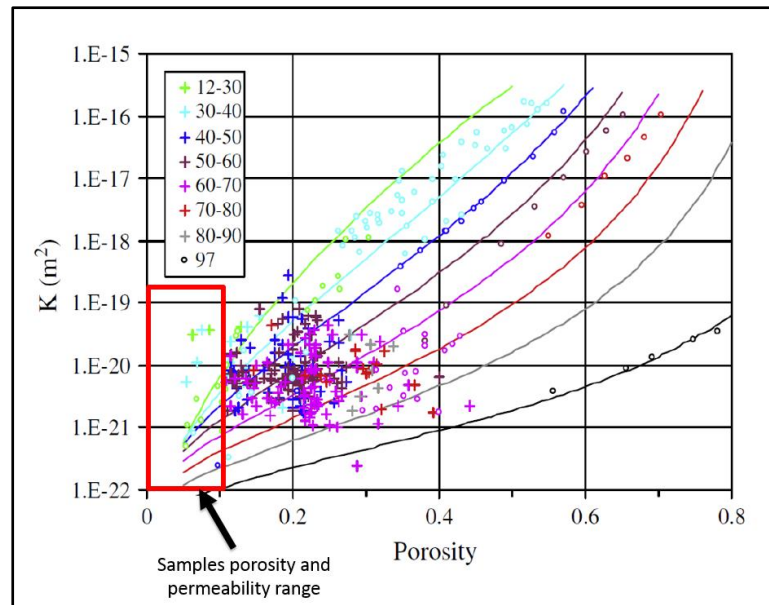


Figure 5-65: Permeability/Porosity relationships for mudrocks (from Yang and Aplin 2010). The red box represent porosity and the corresponding permeability range for the samples used in this test.

The effect of permeability could also be analysed using compressibility of the rock sample. The slope of the straight line before compaction in volumetric strain versus pressure curves for unsealed samples is actually the reciprocal of the compressibility of the rock. The equation is given by:

$$Slope = \frac{\Delta y}{\Delta x} = \frac{\Delta P}{\Delta V} V_o \quad (5-11)$$

Where  $\Delta P$  is change in pressure,  $\Delta V$  is change in volume and  $V_o$  is the original sample volume. Reciprocal of compressibility is bulk modulus of the sample which is the resistance of the sample against hydrostatic compression (Fjaer et al., 2008). If mercury pumped into the cup is deforming the sample and not invading the effective pore space, bulk modulus calculated using MIP data should be close to the bulk modulus calculated using elastic properties ( $E, \nu$ ). Bulk modulus can be calculated by:

$$K = \frac{E}{3(1-2\nu)} \quad (5-12)$$

Figure 5-66 summarizes bulk modulus calculated using elastic properties obtained using microindentation technique against the ones calculated using MIP unsealed data. For microindentation data, Poisson's ratio is assumed to be 0.25 for all rock samples. Bulk modulus for both techniques were similar as it is shown in Figure 5-67. However, when Young's modulus and Poisson's ratio obtained from triaxial test were used to calculate bulk modulus, OC and D samples showed a significant difference in bulk modulus (Figure 5-69). This difference highlights the importance of estimating the correct Poisson's ratio. Details of the calculated bulk modulus using triaxial stat are shown in Figure 5-68.

Sample	$E$ from microindentation (GPa)	$\nu$	$K$ from ( $E, \nu$ ) (GPa)	$K$ from MIP (psi)	$K$ from MIP (GPa)
WS	11.02	0.25	7.35	6.75E+05	4.66
ALP	11.45	0.25	7.63	1.00E+06	6.89
AM	23.91	0.25	15.94	2.00E+06	13.79
KC	29.31	0.25	19.54	3.00E+06	20.68
OC	28.97	0.25	19.31	3.00E+06	20.68
D	57.37	0.25	38.25	5.00E+06	34.47

Figure 5-66: Comparison of bulk modulus calculated using Young's modulus obtained using microindentation technique against bulk modulus obtained from MIP data. Poisson's ratio is assumed to 0.25 for all samples.

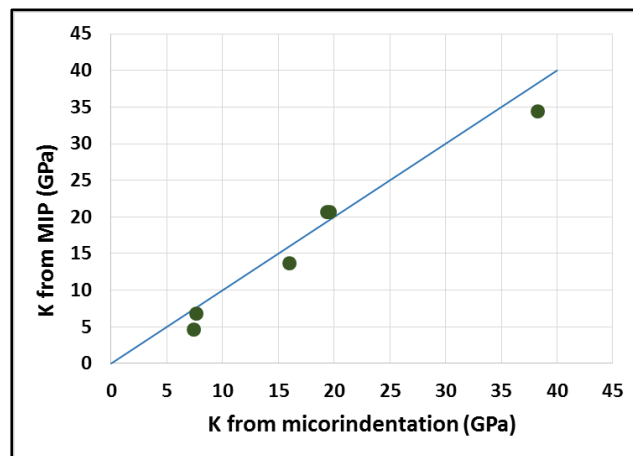


Figure 5-67: Bulk modulus, calculated using microindentation technique against bulk modulus estimated using MIP data. The blue line represents 1:1 relationship.

Sample	$E$ from triaxial test (GPa)	$\nu$	$K$ from ( $E, \nu$ ) (GPa)	$K$ from MIP (GPa)
WS	12.89	0.102	5.40	4.66
ALP	-	-	0.00	6.89
AM	-	-	0.00	13.79
KC	24.54	0.299	20.35	20.68
OC	26.75	0.182	14.02	20.68
D	53	0.336	53.86	34.47

Figure 5-68: Comparison of bulk modulus calculated using  $E$  &  $\nu$  obtained using triaxial test against bulk modulus obtained from MIP data. There is no triaxial data for ALP and AM samples.

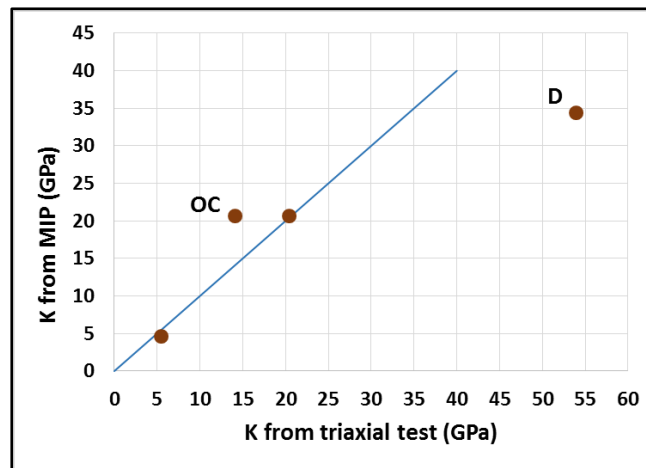


Figure 5-69: Bulk modulus, calculated using triaxial test results against bulk modulus estimated using MIP data. The blue line represent 1:1 relationship.

## 5.6 Conclusions

Micro-indentation is a powerful technique to estimate mechanical properties of material which can be effectively utilized in oil and gas industry. It can be used to determine mechanical properties of rock sample using rock cuttings collected while drilling without the need to core a sample of that rock. The samples were prepared carefully to ensure that they have minimum variation in height across the surface. In addition, the samples were polished to the minimum grit size possible to be able to see indentation impression clearly under the SEM. Indentation load for each sample was determined using a series of indentation tests.

Results of micro-indentation tests on shale samples falls in the trend of the published results in the literature. Young's modulus using micro-indentation was very

close to the Young's modulus obtained by micro-indentation, which makes micro-indentation technique a reliable technique to estimate Young's modulus of shale rocks. Soft rock tends to have low Young's modulus while stiff rocks tend to have high Young's modulus. Sample mineralogy plays an important role in controlling stiffness of the rock. It was shown that the presence of clay and organic matter makes the samples soft while on the other hand, the presence of quartz makes the samples stiff and increases its Young's modulus.

Hardness was also estimated using the indentation impression captured by SEM images. Fracture toughness was also estimated using fracture toughness models available in the literature. Both results perfectly follow the same trend as the published data in the literature. Fracture toughness and hardness are directly proportional to Young's modulus estimated by micro-indentation.

Rocks tend to weaken when they are exposed to acid as the acid reacts and dissolves some minerals. The effect of acid was studied by exposing all samples to acid (5% HCL) for a period of month. Indentation was then performed on these samples to estimate Young's modulus and hardness. Fracture toughness was not estimated because acid damaged the indentation surface and SEM images were not clear enough to do so. Young's modulus was reduced in all samples by at least 34% due to acid reacting with carbonates minerals within the sample. In addition, estimated hardness followed the same trend in the Young's modulus-hardness relationship as the pervious results which makes estimated results valid. The KC sample (carbonate-rich sample) exposed to acid got very weak and no measurement was possible to make.

Preconsolidation pressure is an essential material property for estimating the deformational behaviour of rock under a range of stress conditions. Normally, estimation of preconsolidation pressure is difficult and take long time for tight rock such as shale rocks. This is because this test is done in drained condition allowing all the fluid within the rock sample to drain out. In this thesis, a new method was proposed to estimate preconsolidation pressure under hydrostatic stress condition known as,  $p^*$ . The method is basically to seal rock samples with an adhesive and then use standard Mercury Intrusion Porosimetry (MIP) instrument to pressurize the sample with the adhesive until it undergoes compaction. Volume of mercury pumped in and its pressure recorded by MIP instrument was processed and converted to volumetric

strain. The pressure at which volumetric strain started to change was believed to be the  $p^*$  of the sample.

Sealed samples of all shale rock samples were tested using this method and results obtained were acceptable. Unsealed samples were run and processed as well to investigate if  $p^*$  could be measured if the rock samples are unsealed. However, it was not possible to measure  $p^*$  for some of the samples due to mercury invading the samples before compaction. It was shown that  $p^*$  can be measured in unsealed condition if the sample has low  $p^*$  and low permeability. This was also confirmed by bulk modulus estimation using compressibility of the sample using MIP data and bulk modulus estimated from triaxial data. It was found that in sample with clear sign of  $p^*$  in unsealed condition had similar bulk modulus using both methods.

According to compaction theory,  $p^*$  is inversely proportional to porosity. All  $p^*$  measurement for sealed and unsealed samples were inversely proportional to porosity of the sample. As there was no much  $p^*$  for shale available in the literature, the results were compared with  $p^*$  measurement of chinks. Chink is fined grained rocks like shale and will have the same ductile failure by shear enhanced compaction. Estimated shale  $p^*$  falls perfectly with porosity-  $p^*$  trend of chink samples. This makes this method reliable to measure  $p^*$  of shale under partially drained condition.

## 6 Chapter VI: Experimental investigation of controls of fracture closure in shale

### 6.1 Introduction

Experiments were conducted to investigate the closure of artificial fractures within shale. The key goal of these experiments is to determine the controls of fracture closure in shale. Fracture closure experiments were conducted to the maximum confining pressure the apparatus can withstand. Results are then extended further using closure model to predict complete fracture closure, which will reflect self-sealing capacity of the rock.

Fracture closure is controlled by three factors; geomechanical properties, effective stress and fracture surface morphology (Duan et al., 2000). Normally, there is no control on surface morphology of a fracture and every fracture has its unique surface morphology. To control surface morphology, an artificial fracture with a single proppant layer was used to study controls of fracture closure in shale. This proppant layer will represent surface morphology, which will technically be similar in each sample. Core plugs were cut laterally into two halves and packed with single layer of proppant in between as it is shown in Figure 6-1. Proppant is harder than the rock, so it tends to become embedded into the fracture wall resulting in reduction in the fracture aperture and hence reduction in fracture conductivity. The proppant used in this study is the same proppant used to pack artificial fracture in hydraulic fracturing application.

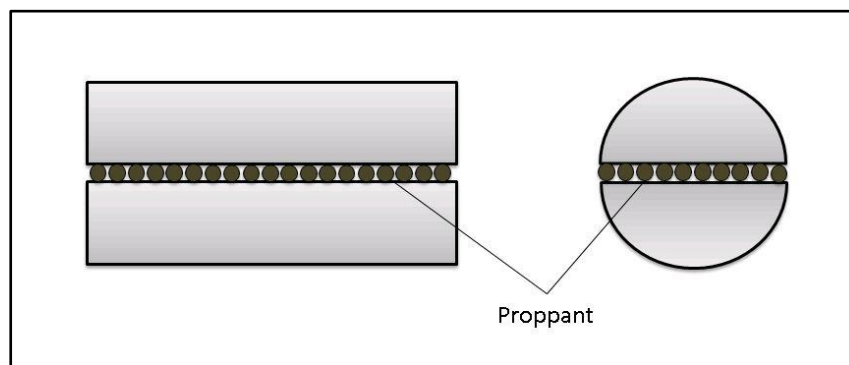


*Figure 6-1: Front and side view of sample with proppant pack.*

Experiments were designed and planned to be conducted in the laboratory for various shale rock samples with different mechanical and petrophysical properties under various stress conditions. Samples were tested in a biaxial core holder and kept

under a confining pressure for a period of time to investigate creep. Shale with high clay content tend to experience creep deformation especially the ones with high clay content (Sone and Zoback, 2010). Fracture conductivity was measured frequently and changes in conductivity will reflect in fracture closure due to embedment of proppant into the sample.

CT images were taken at each confining pressure to visualize fracture closure. CT images were then analysed and exported to 3D image processing software known as Avizo developed by FEI Visualization Sciences Group. Avizo has the capability of performing quantitative analysis using sets of 3D images obtained from CT and other imaging instruments.

## 6.2 Sample preparation

Sample preparation is a crucial part of the experiment as surface morphology has to be similar in all samples to ensure consistency in results. It is quite important to make sure that the surfaces of the fracture are as flat as possible to ensure that any change in aperture is caused by proppant embedment and not by proppant moving and resting between asperities. First, samples are cored into 38 mm (1.5 in) diameter cylindrical cores and ground in both ends to make the end surfaces flat. Samples are then cut in the middle using a thin saw in the lateral direction, both inner surfaces will then represent fracture walls. Fracture walls were then ground carefully to make them as flat as possible as it is shown in Figure 6-2. Finally, the sample is saturated with water by placing a core in water and subjecting it to vacuum pressure to be ready for proppant placement.

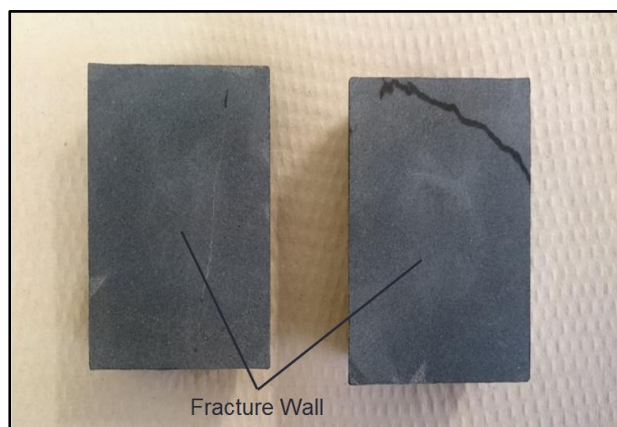


*Figure 6-2: Sample under preparation with ground fracture walls.*



Proppant particles have a small variation in terms of particles sizes and shape. The proppant used in this experiments is intermediate strength proppant “InterProp 16/30” from Saint-Gobain. Proppant mesh size is 16/30, which means that particles diameter is in a range of 600-1180  $\mu\text{m}$ . Krumbein and Sloss (1963) developed a method to quantify roundness and sphericity based on visual and manual methods. Using Krumbein and Sloss (1963) quantification, the proppant used in these tests has roundness of 0.9 and sphericity of 0.9. A visualization of proppant shape using roundness and sphericity can be seen in Figure 6-3. Although this proppant has high roundness and sphericity, the variation in diameter is still large. Given the fact that proppant has a large variation in diameter, the number of proppant particles in contact with fracture walls will be different in each sample. Hence, proppant particles have been sieved to a size range of 770-840  $\mu\text{m}$  to reduce the effect of proppant size variation.

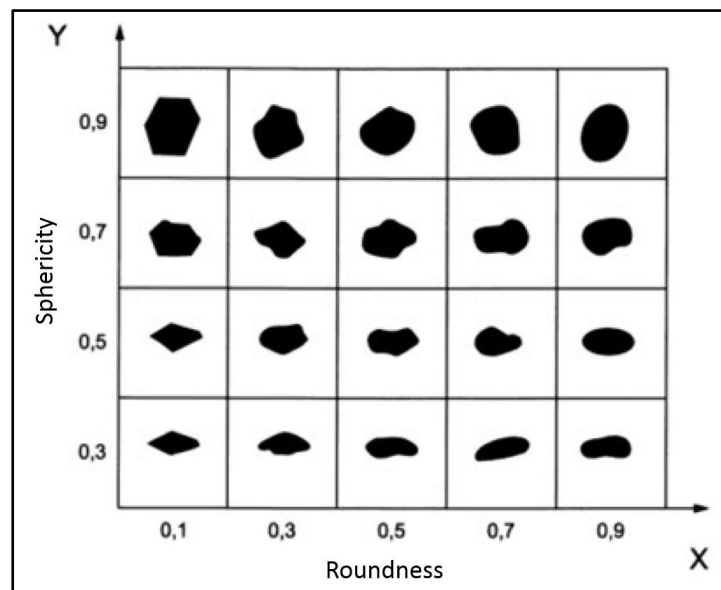
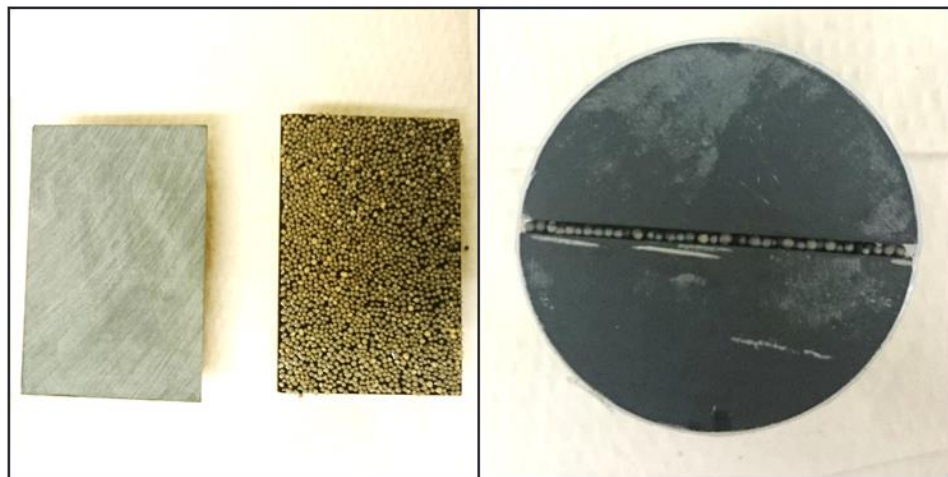


Figure 6-3: Diagram showing visual estimation of sphericity and roundness of proppant (Horiba, 2012).

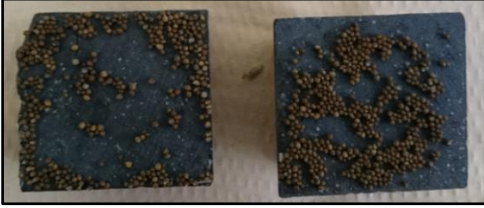
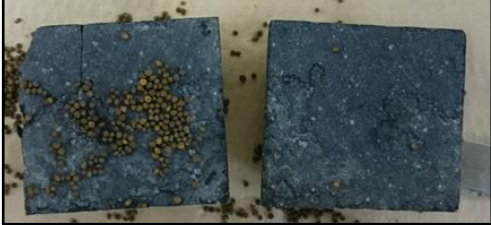
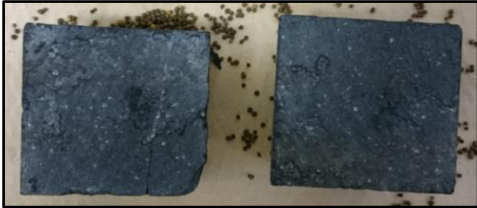
It was important to create an even layer of proppant on the surface of the fracture that was reproducible between different experiments. Initial attempts to place the proppant directly on the fracture wall proved futile as the proppant is very mobile. It was therefore decided to mix the proppant with a bonding material to allow it to be spread evenly along the surface of the fracture in a reproducible manner. It is, however, important that the bonding material can be removed prior to the experiments. A series of experiments were therefore conducted to identify a proppant bonding material that

could be used which met these criteria. Three bonding materials were used; PVA glue, Pritt Stick and honey. Proppant was placed using the three mentioned materials in the fracture wall. Then, the two pieces of the sample were put together and jacketed with plastic heat shrink to hold everything together (Figure 6-4). The sample was then loaded in a core holder and placed under a confining pressure of 500 psi to stabilize the sample and proppant. Water was pumped into the sample to flush the bonding material. Table 6-1 summarizes the observations made after flushing distilled water through the sample. It was found that honey bonds the proppant very well and can be easily flushed in short period of time.

To ensure consistency, honey density, which is the amount of honey per fracture wall area, and proppant density, which is the amount of proppant per fracture wall area, were similar in all samples. Table 6-2 provides full description of all samples tested. Proppant weight per fracture wall was about  $(1.08 \pm 0.05 \text{ kg/m}^2)$  and honey weigh per fracture wall area was about  $((4.59 \pm 0.31) \text{ E-2}) \text{ kg/m}^2$ .



*Figure 6-4: Proppant embedment test sample.*

Material	Observation after flushing water	Picture of the sample after flushing water
PVA glue	Most of the glue was flushed out. Little amount of glue was observed at the edges. Proppant particles were loose at the centre but cemented at the edges.	
Pritt stick	It did not flush out at all. A thin layer of the glue was still there at the fracture wall.	
Honey	All proppant particles were loose and all honey was flushed out.	

*Table 6-1: observation noticed after flushing water through the sample for each bonding material tested.*

Sample	Length (mm)	Width (mm)	Proppant density (kg/m <sup>2</sup> )	Honey density (kg/m <sup>2</sup> ) 10 <sup>-2</sup>
WS	22.2	36.8	1.12	4.90
ALP	41.4	38.1	1.07	4.31
AM	36.4	37.3	1.09	4.28
KC	33.4	37.1	1.03	4.84
OC	22.8	37.7	1.04	4.77
D	37.4	37.2	1.06	4.89

*Table 6-2: Fracture closure samples description.*

The sample preparation process can be summarized as:

- Sample is cored into 38 mm diameters cylindrical core plugs (1.5 in diameter) and ground flat at both ends.
- The core plug is cut into two halves using a thin saw and both inner surfaces referred as “fracture walls” are ground flat.
- Sample is then saturated with water for 24 hours by placing it into water and subjecting it to vacuum pressure.
- Honey is spread in one of the fracture walls. Honey weight to fracture wall area ratio has to be around  $4.59\text{E-}2 \text{ kg/m}^2$ .
- Proppant particles are scattered carefully by hand on the honey covered surface to form only one layer of proppant. It has to fill the fracture wall area completely and uniformly as it is shown in Figure 6-4 and have weight to fracture area ratio of  $1.08 \text{ kg/m}^2$ .
- Sample is jacketed with plastic heat shrink to secure the configuration.
- Finally, the sample is placed in a core holder and flushed through with distilled water to remove all the honey.

### **6.3 Experimental method**

Fracture closure is determined by measurement of the change in hydraulic conductivity of the proppant packed fracture shown in Figure 6-4 due to confining pressure application. It can be also measured using CT images but the resolution of the CT scanner used is similar to the fracture width. Fracture conductivity was measured using the steady-state technique because the proppant packed fracture was expected to have high conductivity especially at low confining pressures. The permeant used in this experiment is distilled water. Water is pumped through the fracture at constant flow rate and differential pressure across the sample is measured in real-time. The steady-state is reached when the differential pressure becomes stable with acceptable variation. Differential pressures and volume flow rates are used later to calculate fracture conductivity. The apparatus used for the steady-state method is shown in Figure 6-5 and Figure 6-6. It is composed of the following components:

- Positive displacement pump (Isco pump)
- Pressure transducers
- Core holder

- Data acquisition system
- Compressed air pump

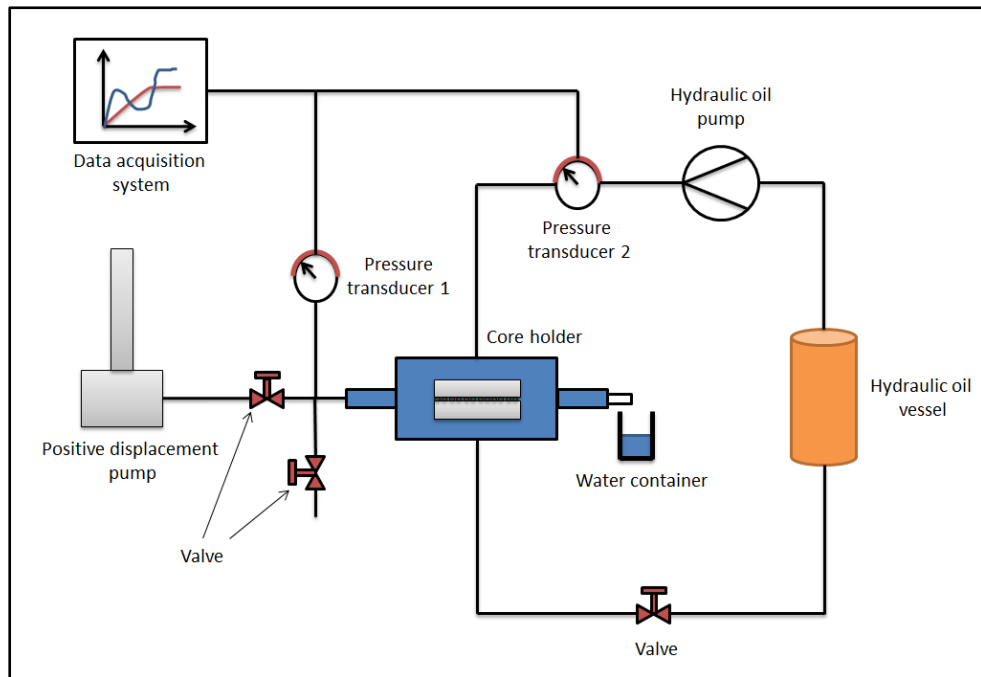


Figure 6-5: Experimental setup of fracture closure experiment.

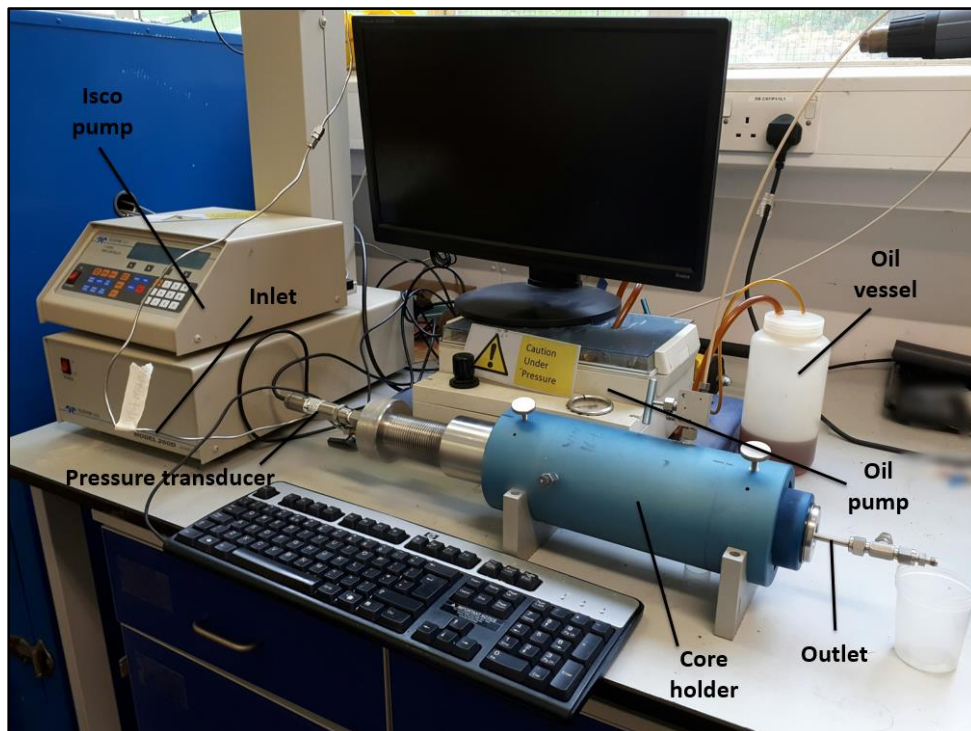


Figure 6-6: Picture of the setup used in fracture closure experiment.

The Isco pump was connected to the inlet port of the core holder to provide required volume flow rate to the sample in the core holder. This pump has a capability of providing a constant inlet flow rate throughout the experiment. It can pump fluids at flow rates in quite a big range (0.001-100 cm<sup>3</sup>/min) with a good accuracy. A pressure transducer is attached to the inlet line to provide real time inlet pressure measurement to the data acquisition system to be recorded and plotted in real time. The other end of the core holder (outlet) is open to atmospheric pressure. Hence, the pressure reading from the transducer at the inlet will represent the differential pressure across the sample. Fracture conductivity is measured in both directions (forward and reverse) as it is shown in Figure 6-7. The fracture conductivity reported is the average conductivity obtained by flowing fluid forward and reverse directions. Confining pressure is applied using a simple hydraulic system, which uses mineral oil as a hydraulic fluid. A compressed air pump is used to pump the hydraulic oil from the vessel to the core holder. A pump is then used to pressurize the oil to apply a confining pressure to the sample.

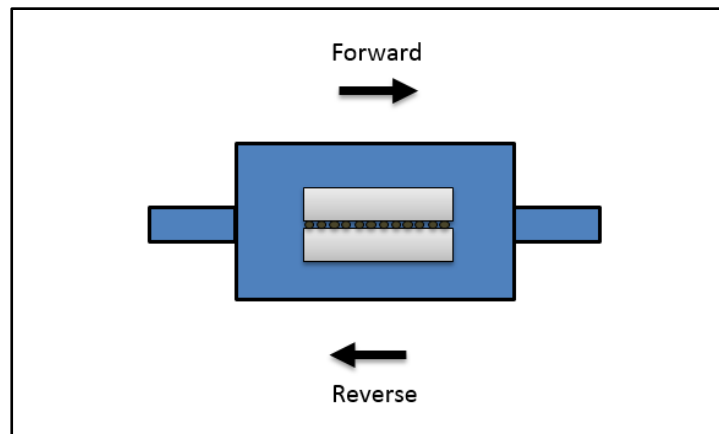


Figure 6-7: Diagram showing fluid flow directions during conductivity measurement.

Fracture hydraulic conductivity ( $C_f$ ) of a proppant pack can be calculated using the following equation (API RP-19D, 2008):

$$C_f = kW_f = \frac{Q\mu L}{W\Delta P} \quad (6-1)$$

Where  $k$  is proppant pack permeability,  $W_f$  is proppant pack thickness (fracture aperture),  $Q$  is volume flow rate of the test fluid,  $L$  is length of the fracture,  $W$  is width of the fracture,  $\mu$  is viscosity of the test fluid and  $\Delta P$  is differential pressure. This setup has some limitation in terms duration and accuracy. Low fracture conductivities are

difficult to measure using the steady-state methods because it takes a long time. This setup is well tested for any potential leak for few days before running any sample to minimize the error.

The fracture conductivity equation (6-1) is derived from Darcy's equation. For Darcy's equation to be valid, flow rate has to be laminar through the porous media. At high flow rates, fluid flow in porous media tends to become turbulent which leads to wrong calculation of fracture conductivity. A dimensionless number known as the Reynolds number is used to characterize flow rate through any media. For a flow in porous media, Chilton and Colburn (1931) conducted experiments of packed particles and defined Reynolds number to be:

$$Re = \frac{\rho D_p v_f}{\mu} \quad (6-2)$$

Where  $\rho$  ( $\text{kg/m}^3$ ) is fluid density,  $D_p$  (m) is the particle's diameter;  $v_f$  is velocity of the fluid (m/s),  $\mu$  ( $\text{kg/m}\cdot\text{s}$ ) is the dynamic viscosity of the fluid. Fancher and Lewis (1933) used the same above definition and flowed crude oil, water and air through unconsolidated sands, lead shot, and consolidated sandstones; their results are shown in

*Table 6-3.* In this proposed experiment, the proppant size is about 770-840  $\mu\text{m}$ . Assuming the Reynold's number of 1000, the maximum volume flow rate to keep the flow laminar though the proppant packed fracture is about 20  $\text{cm}^3/\text{min}$ . This suggests that while conducting the experiment, flow rates have to be 20  $\text{cm}^3/\text{min}$  or less.

Sand Type	Reynolds Number
unconsolidated porous media	10-1000
loosely consolidated rocks	0.4-3

*Table 6-3: Results of Fancher and Lewis (1933).*

Confining pressure was increased in steps of 1000 psi to a maximum of 4000 psi. Fracture conductivity was measured every 24 hours to capture creep behaviour. Once creep ends and fracture conductivity is fluctuating around a constant value, confining pressure is increased to the next step. Differential and confining pressures were measured using transducers with a maximum error of  $\pm 0.005$  psi to capture small creep rates. CT scan images were taken at the beginning of the experiment and at the

end of each pressure step. These images will be used later in Avizo to quantify fracture parameters. The CT scanner used is Brivo 385 from General Electric with a maximum resolution of 200  $\mu\text{m}$  in the x-direction and 625  $\mu\text{m}$  in the y-direction.

The experimental procedure can be summarized as:

1. Fill the positive displacement pump with distilled water. Make sure that you remove all trapped air by flowing some of the water out after filling.
2. Make sure that there is sufficient oil in the hydraulic oil vessel.
3. Load the sample into the core holder.
4. Apply required confining pressure.
5. Take a CT image of the sample.
6. Turn on data acquisition system and start recording the readings.
7. Start flowing water at a constant flow rate through the sample and wait until system reaches a steady state. Make sure that the pressure measured is within the transducer operating limits.
8. Repeat step 7 for at least 3-4 times using different flow rate steps in the forward direction.
9. Repeat step 7 for at least 3-4 times using different flow rate steps in the reverse direction.
10. Turn off data acquisition system and make sure to save the data.
11. Repeat steps 6-10 every day at the same time until fracture conductivity stabilizes a steady state value.
12. Take a CT image of the sample.
13. Repeat steps 4-12 for every confining pressure step.

## 6.4 Experimental results

Fractures experience closure when confining pressure is increased, which makes determining the initial condition of the fracture challenging. For this purpose, a special sample made of borosilicate glass rod, which is quite a stiff material ( $E = 63$  GPa), was prepared using the same procedure explained earlier to represent the initial state of the fracture before closure. Borosilicate glass is very stiff and will not experience proppant embedment at low stresses. A description of the glass sample is presented in Table 6-4.



Sample	Glass
Fracture wall area (mm <sup>2</sup> )	38.8(L)*36.7(W)
Proppant density (kg/m <sup>2</sup> )	1.08
Honey density (kg/m <sup>2</sup> )	4.64 E-02

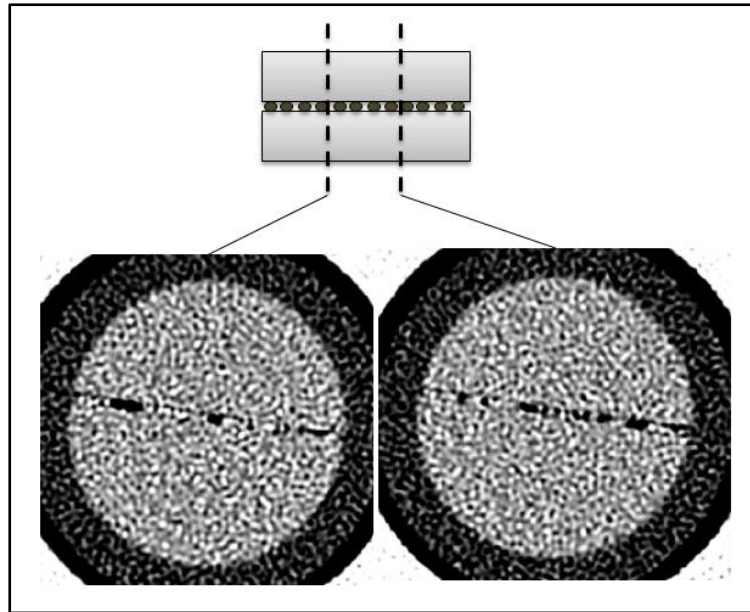
Table 6-4: Properties of the glass sample used to determine initial fracture parameters.

The sample was loaded in a core holder and pressurized to 500 psi confining pressure. Fracture conductivity was measured in both directions and the average fracture conductivity was found to be 1.71 E-13 m<sup>3</sup>. This will be used as the initial fracture conductivity of all samples. Table 6-5 presents forward and reverse differential pressures and flow rates.

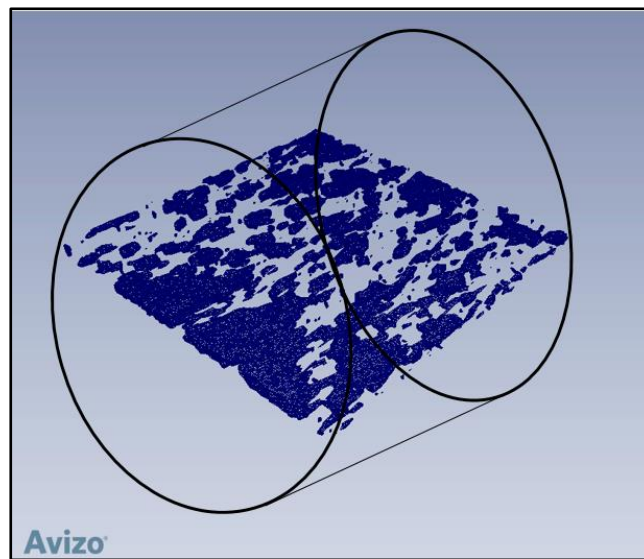
Flow rate (cc/min)	Differential pressure (psi)	Conductivity (m <sup>3</sup> )
Forward		
4	0.069	1.33 E-13
8	0.13	1.42 E-13
12	0.207	1.33 E-13
16	0.285	1.29 E-13
Reverse		
4	0.045	2.05 E-13
8	0.087	2.12 E-13
12	0.134	2.06 E-13
16	0.178	2.07 E-13
Average conductivity (m <sup>3</sup> )		1.71 E-13

Table 6-5: Flow rate steps and their corresponding differential pressures together with fracture conductivity for glass sample at 500 psi confining pressure.

The CT images of the glass sample taken at 1/3 and 2/3 of the length of the sample are shown in Figure 6-8 . CT images set is then exported to Avizo to form a 3D model of the sample. A threshold tool was then used to remove proppant material and rock material from the model and keep the void space which represents fracture fluid flow conduits. Figure 6-9 presents the void spaces (in blue) after applying the threshold and removing rock and proppant material.



*Figure 6-8: CT images of glass sample taken at 1/3 and 2/3 of the length of the sample. These images for glass sample taken at 500 psi confining pressure.*



*Figure 6-9: Void spaces (blue surfaces) that acts as conduits to fluid flow in glass sample at 500 psi confining pressure. This picture is generated by Avizo.*

Avizo is capable of quantifying void space geometry in terms of volume, surface area and thickness. Thickness of the void space is the fracture aperture,  $W_f$  in Equation 6-1, which was found to be 0.59 mm. This is taken to represent the initial fracture aperture of the proppant packed fracture. Summary of Avizo are found in Table 6-6.

Sample	Glass
Void surface area (mm <sup>2</sup> )	2018.65
Void volume (mm <sup>3</sup> )	503.69
Fracture thickness (mm)	0.59

Table 6-6: Avizo results for glass sample at 500 psi.

Initial voids surface area and volume of glass sample presented in Table 6-6 were used to estimate initial voids surface area and volume. Since these parameters are related to fracture wall area, initial voids surface area and volume for any sample can be calculated using the following equations:

$$A_s = \frac{A_s \text{ of glass}}{A_F \text{ of glass}} * A_F \text{ of sample} \quad (6-3)$$

$$V_s = \frac{V_s \text{ of glass}}{A_F \text{ of glass}} * A_F \text{ of sample} \quad (6-4)$$

Where  $A_s$  is Initial void surface area (mm<sup>2</sup>),  $A_F$  is fracture wall area (mm<sup>2</sup>) and  $V_s$  is initial voids volume (mm<sup>3</sup>).

#### 6.4.1 Fracture closure of the WS sample

The first sample tested was WS sample, which had the lowest Young's modulus of all samples tested. It was loaded to a confining pressure of 1000, 2000, 3000 and 4000 psi for a total period of 32 days. Initial proppant pack fracture parameters estimated using the previous mentioned procedure are summarized in Table 6-7.

Sample	WS
Initial void surface area (mm <sup>2</sup> )	1159
Initial void volume (mm <sup>3</sup> )	289
Initial fracture conductivity (m <sup>3</sup> )	1.71 E-13

Table 6-7: Initial fracture parameters of WS sample.

Fracture conductivity reduction with time due to confining pressure application for WS sample is shown in Figure 6-10. At 1000 psi confining pressure, this sample experienced a reduction of 70% in fracture conductivity over 10 days. Fracture conductivity started to stabilize on the fourth day of this pressure step. After conductivity stabilization, confining pressure was then increased to 2000 psi and the

sample was kept under this pressure for a period of 8 days. Fracture conductivity started to stabilize starting from the third day of this stage. Average conductivity at the end of this stage was about  $2.07 \text{ E-}14 \text{ m}^3$ , which makes the total reduction in fracture conductivity up till the end of 2000 psi confining pressure stage about 88%. At 3000 psi confining pressure, conductivity was reduced by two order of magnitude compared to the previous stage. In this confining pressure step, the system was kept under pressure for 7 days and fracture conductivity started to plateau on the third day. Total reduction in hydraulic conductivity was 99.9% compared to initial fracture conductivity. Final average fracture conductivity was about  $1.29 \text{ E-}16 \text{ m}^3$ . Fracture conductivity experienced the largest reduction when confining pressure was increased to 4000 psi. This stage lasted for 7 days and fracture conductivity started to stabilize on the fourth day. Fracture conductivity has reduced to about seven orders of magnitude with reference to initial fracture conductivity. The average conductivity measured at the end of the experiment was about  $8.76 \text{ E-}20 \text{ m}^3$  which suggests that fracture conductivity reduction was about 99.99% throughout the experiment. Table 6-8 summarizes the last conductivity test results carried out at the end end of each confining pressure step. The average conductivity shown in this table is the average conductivity value at the plateau of the curves shown in Figure 6-10.

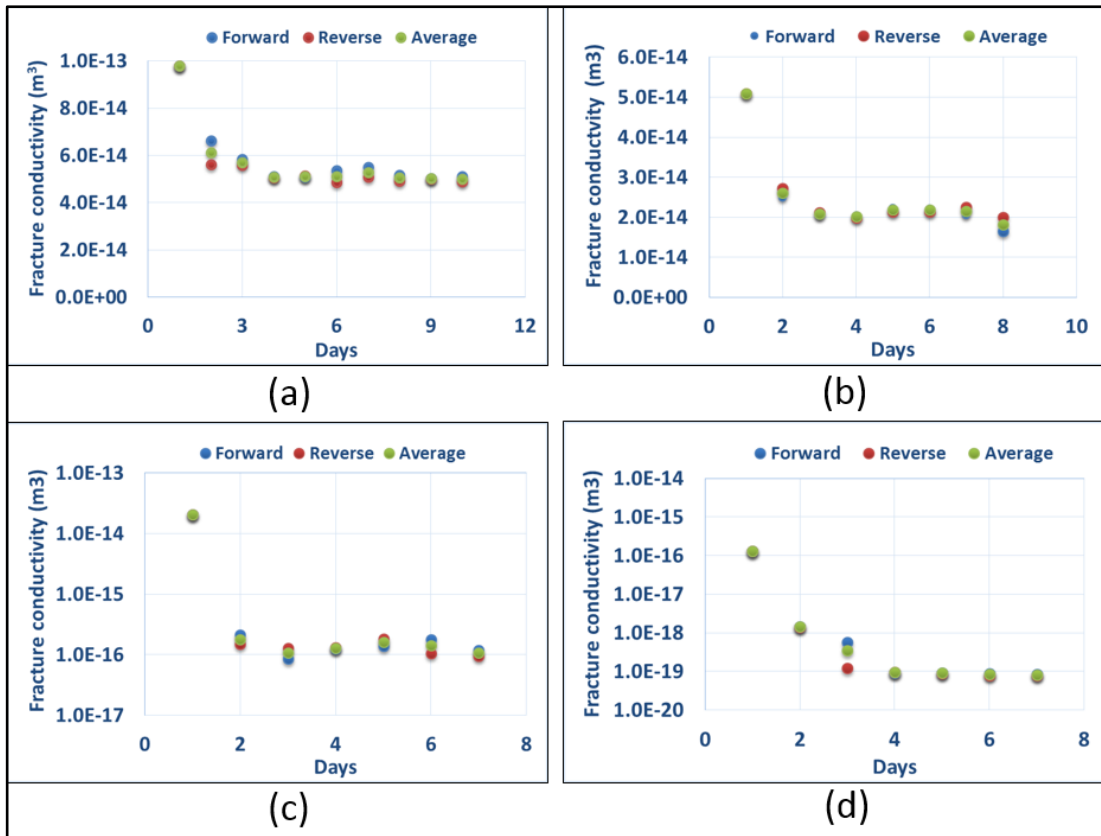


Figure 6-10: Fracture conductivity reduction with time for WS sample at (a) 1000 psi, (b) 2000 psi, (c) 3000 psi and (d) 4000 psi. Fracture conductivity in (c) and (d) is in log-scale.

Confining pressure (psi)	Forward			Reverse		
	Flow rate (cc/min)	Differential pressure (psi)	Conductivity (m <sup>3</sup> )	Flow rate (cm <sup>3</sup> /min)	Differential pressure (psi)	Conductivity (m <sup>3</sup> )
1000	12	0.347	4.54 E-14	12	0.357	4.41 E-14
	9	0.244	4.84 E-14	9	0.259	4.56 E-14
	6	0.148	5.32 E-14	6	0.153	5.15 E-14
	3	0.069	5.71 E-14	3	0.072	5.47 E-14
	Average conductivity (m <sup>3</sup> )			5.10 E-14		
2000	10	0.865	1.52 E-14	12	0.850	1.85 E-14
	9	0.759	1.56 E-14	9	0.601	1.97 E-14
	6	0.474	1.66 E-14	6	0.366	2.15 E-14
	3	0.217	1.81 E-14	3	0.190	2.07 E-14
	Average conductivity (m <sup>3</sup> )			2.07 E-14		
3000	5	60.1	1.09 E-16	5	72.4	9.06 E-17
	4	45.8	1.15 E-16	4	57.7	9.10 E-17
	3	32.8	1.20 E-16	3	42.0	9.37 E-17
	2	19.6	1.34 E-16	2	26.1	1.01 E-16
	Average conductivity (m <sup>3</sup> )			1.29 E-16		
4000	0.05	493.8	1.33 E-19	0.05	501.1	1.31 E-19
	0.03	471.7	8.35 E-20	0.03	500.7	7.86 E-20
	0.01	368.6	3.56 E-20	0.01	480.9	2.73 E-20
	Average conductivity (m <sup>3</sup> )			8.76 E-20		

*Table 6-8: Results of fracture conductivity test at the end of each confining pressure stage for WS sample. The average conductivity reported is the average at the plateau of the curves shown in Figure 6-10.*

Figure 6-11 shows CT Images at 1/3 and 2/3 of the sample length at the end of the first and last confining pressure stages showing clearly the reduction in fracture aperture through out the experiment. The whole images set is as well exported and analysed in Avizo and resulted void space can be seen in Figure 6-11. Properties of the void space computed by Avizo for all confining pressure stages are tabulated in Table 6-9. Using fracture aperture estimated by Avizo, fracture closure at the end of 1000 psi confining pressure stage was almost 29%. At 2000 psi confining pressure, total reduction in fracture aperture was about 42% with reference to initial condition. Volume of the void spaces was reduced by 50% during this stage only. Significant reduction in void space was recorded at the end of 3000 psi confining pressure stage. Reduction in void space volume was about 79% compared to the previous confining pressure stage. Reduction in aperture up till the end of this stage was about 52%. The CT images taken at the end of 4000 psi confining pressure stage show that fracture is almost closed (Figure 6-11). Only a few fracture void spaces are present in the Avizo

3D reconstructed model (Figure 6-11). However, fracture aperture reduction was very small (about 1%) compared to the previous stage. On the other hand, reduction in void spaces volume was about 59% compared to previous stage.

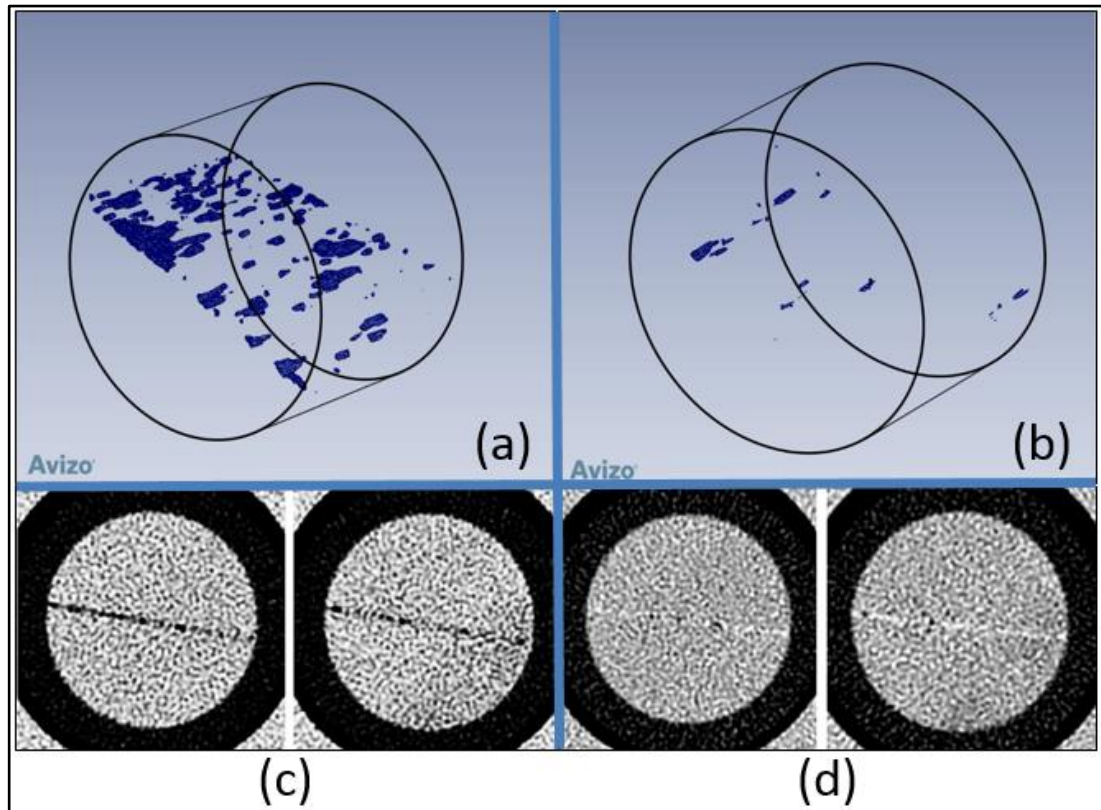


Figure 6-11: Void spaces (blue surfaces) that acts as conduits to fluid flow in WS sample at (a) 1000 psi and (b) 4000 psi. CT images of sample at 1/3 and 2/3 of the length of the sample for (c)1000 psi and (d) 4000 psi confining pressure stages.

Confining pressure (psi)	1000	2000	3000	4000
Void surface area (mm <sup>2</sup> )	451.3	270.8	73.21	30.52
Void volume (mm <sup>3</sup> )	74	35	7	3
Fracture aperture (aperture)(mm)	0.42	0.34	0.285	0.282

Table 6-9: Avizo results for WS sample for all confining pressure stages.

Fracture conductivity normalized to the initial fracture conductivity is plotted against time in days for all confining pressure steps in Figure 6-12. Larger conductivity reductions occurred at higher confining stresses (3000 and 4000 psi). Figure 6-13 shows a photograph of the fracture walls of the sample after performing the experiment; clear impressions of proppant embedment can be seen in fracture walls due to confining pressure application.

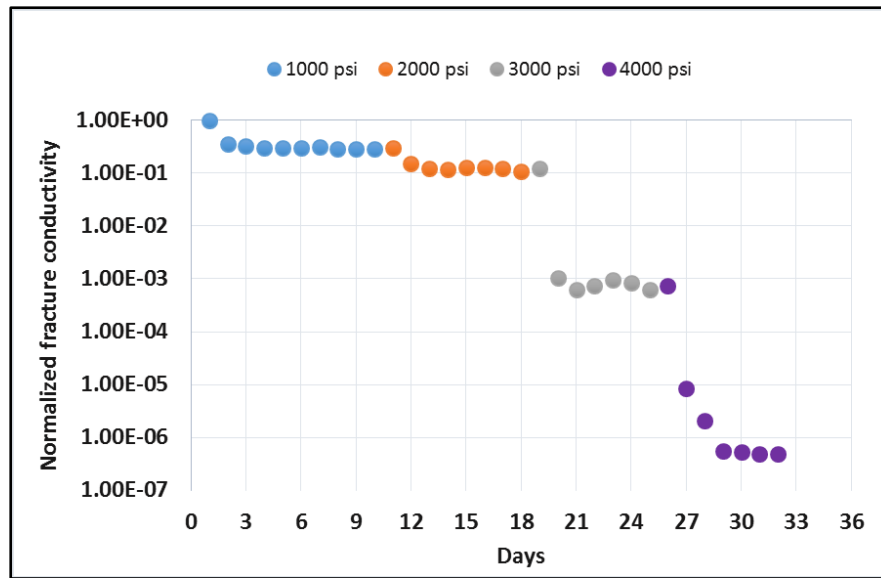


Figure 6-12: Normalized fracture conductivity of WS sample (in log scale) vs. time for all confining pressure steps.



Figure 6-13: WS sample fracture walls after performing the experiment showing impressions of the proppant embedment into fracture wall.



#### 6.4.2 Fracture closure of the ALP sample

The ALP sample was expected to have large fracture closure because it is relatively soft and has a Young's modulus similar to the WS sample. Total experiment time for all confining pressure steps was about 53 days. Initial parameters estimated for ALP sample proppant pack fracture are summarized in Table 6-10.

Sample	ALP
Initial void surface area (mm <sup>2</sup> )	2236
Initial void volume (mm <sup>3</sup> )	558
Initial fracture conductivity (m <sup>3</sup> )	1.71 E-13

Table 6-10: Initial fracture parameters of the ALP sample.

The ALP sample fracture conductivity took longer to plateau at each confining pressure step compared to the WS sample. The ALP sample was kept under 1000 confining pressure on the first step for 15 days. Fracture conductivity started to stabilize after 8 days. Final average conductivity calculated from the plateau was about 3.25 E-14 m<sup>3</sup>, which is 81% less than the initial conductivity.

Fracture conductivity did not change significantly compared to the previous stage when confining pressure was increased to 2000 psi. The system was pressurized in this stage for a period of 8 days and conductivity started to stabilize on the 2<sup>nd</sup> day. Average measured conductivity was found to be 2.07 E-14 m<sup>3</sup> compared to the 3.25 E-14 m<sup>3</sup> in the previous stage. Change in conductivity between the two stages is about 36%.

A large reduction in fracture conductivity was noticed when confining pressure was increased to 3000 psi; this stage lasted for 15 days and fracture conductivity started to stabilize on the 3<sup>rd</sup> day. Fracture conductivity reduced by two order of magnitudes to a final average value of 9.66 E-16 m<sup>3</sup>. Confining pressure was then increased on the final stage to 4000 psi for a period of 15 days. Fracture conductivity started to stabilize on the 6<sup>th</sup> day and was reduced by two orders of magnitude to a final value of 4.43 E-18 m<sup>3</sup>. Differential pressure and flowrates measured while testing this sample are presented in Table 6-11. Daily conductivity change with time is presented in Figure 6-14 for all four stages.

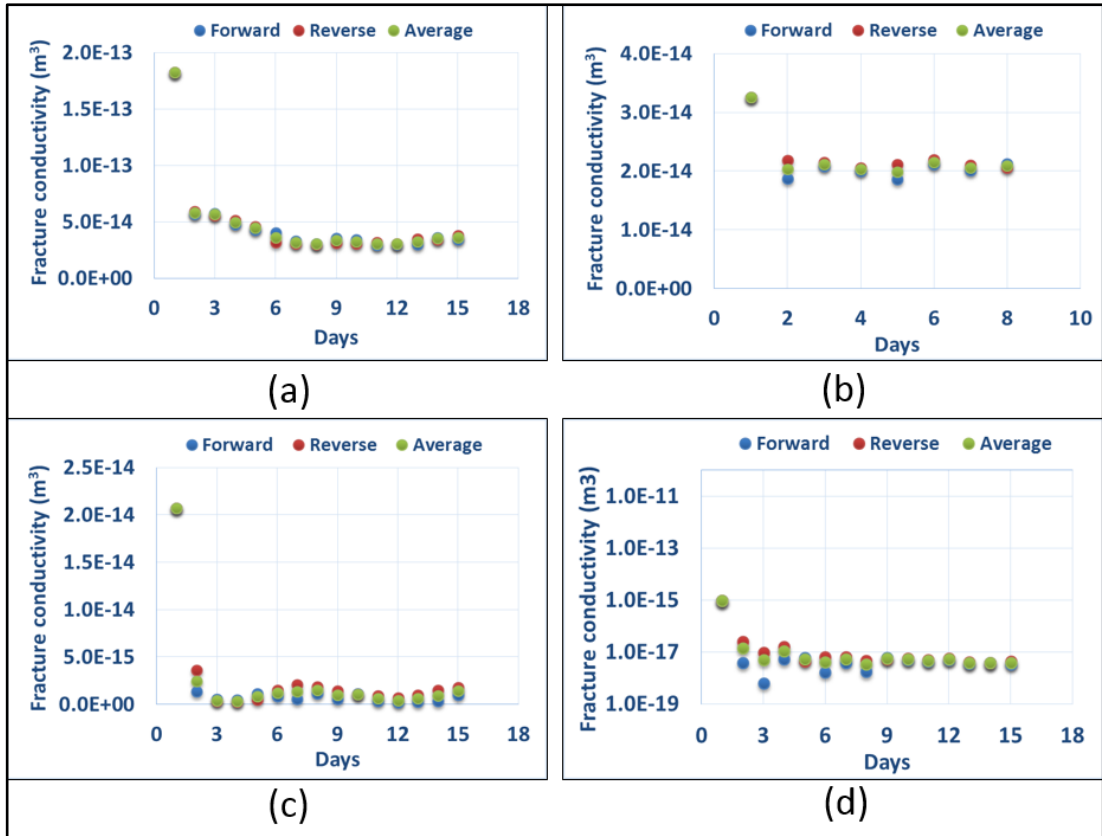


Figure 6-14: Fracture conductivity reduction with time for ALP sample at (a) 1000 psi, (b) 2000 psi, (c) 3000 psi and (d) 4000 psi. Fracture conductivity in (d) is in log-scale.

Confining pressure (psi)	Forward			Reverse		
	Flow rate (cc/min)	Differential pressure (psi)	Conductivity (m <sup>3</sup> )	Flow rate (cc/min)	Differential pressure (psi)	Conductivity (m <sup>3</sup> )
1000	2.5	0.172	3.43 E-14	2.5	0.157	3.76 E-14
	2.1	0.145	3.42 E-14	2.1	0.129	3.84 E-14
	1.7	0.119	3.37 E-14	1.7	0.105	3.82 E-14
	1.3	0.091	3.37E-14	1.3	0.083	3.70 E-14
	Average conductivity (m <sup>3</sup> )			3.25 E-14		
2000	2.5	0.277	2.13 E-14	2.5	0.293	2.01 E-14
	2	0.222	2.13 E-14	2	0.228	2.07 E-14
	1.5	0.165	2.15 E-14	1.5	0.171	2.07 E-14
	1	0.111	2.13 E-14	1	0.113	2.09 E-14
	Average conductivity (m <sup>3</sup> )			2.07 E-14		
3000	3	7.25	9.77 E-16	3	3.9	1.82 E-15
	2.5	5.9	1.00 E-15	2.5	3.3	1.79 E-15
	2	4.55	1.04 E-15	2	2.7	1.75 E-15
	1.5	3.231	1.10 E-15	1.5	2.0	1.77 E-15
	Average conductivity (m <sup>3</sup> )			9.66 E-16		
4000	0.6	379.2	3.73 E-18	0.6	293	4.83 E-18
	0.5	337.9	3.49 E-18	0.5	263.1	4.48 E-18
	0.4	293.5	3.22 E-18	0.4	224.9	4.20 E-18
	0.3	235.3	3.01 E-18	0.3	185.4	3.82 E-18
	Average conductivity (m <sup>3</sup> )			4.43 E-18		

Table 6-11: Results of fracture conductivity test at the end of each confining pressure stage for the ALP sample. The average conductivity reported is the average at the plateau of the curves shown in Figure 6-14.

CT images taken at the end of initial and final stage presented in Figure 6-15 showing progression of fracture closure with increasing confining pressure. Corresponding Avizo models with void spaces are shown in Figure 6-15. Calculated properties of void spaces by Avizo are summarized in Table 6-12. At 1000 psi confining pressure, a large reduction in fracture aperture is observed in conductivity results is confirmed by Avizo results shown in Table 6-12. Calculated reduction in fracture aperture using Avizo results was about 40 %. The void spaces volume at the end of this stage was about 131 mm<sup>3</sup>.

At 2000 psi confining pressure, change in fracture conductivity was very small, which complies with change in void spaces. Change in void space volume between 1000 psi and 2000 psi stages was about 21 %. However, at 3000 psi confining pressure, void surfaces generated by Avizo have experienced a large reduction and their volume has reduced by 91 % compared to the previous stage. Total reduction in fracture

aperture due to closure was 57% with respect to initial fracture aperture. At 4000 psi confining pressure, fracture aperture remained constant and was about 0.255 mm compared to 0.251 mm in the previous stage. On the other hand, change in the void spaces volume was about 40% with respect to the previous stage causing a reduction in fracture conductivity reported earlier.

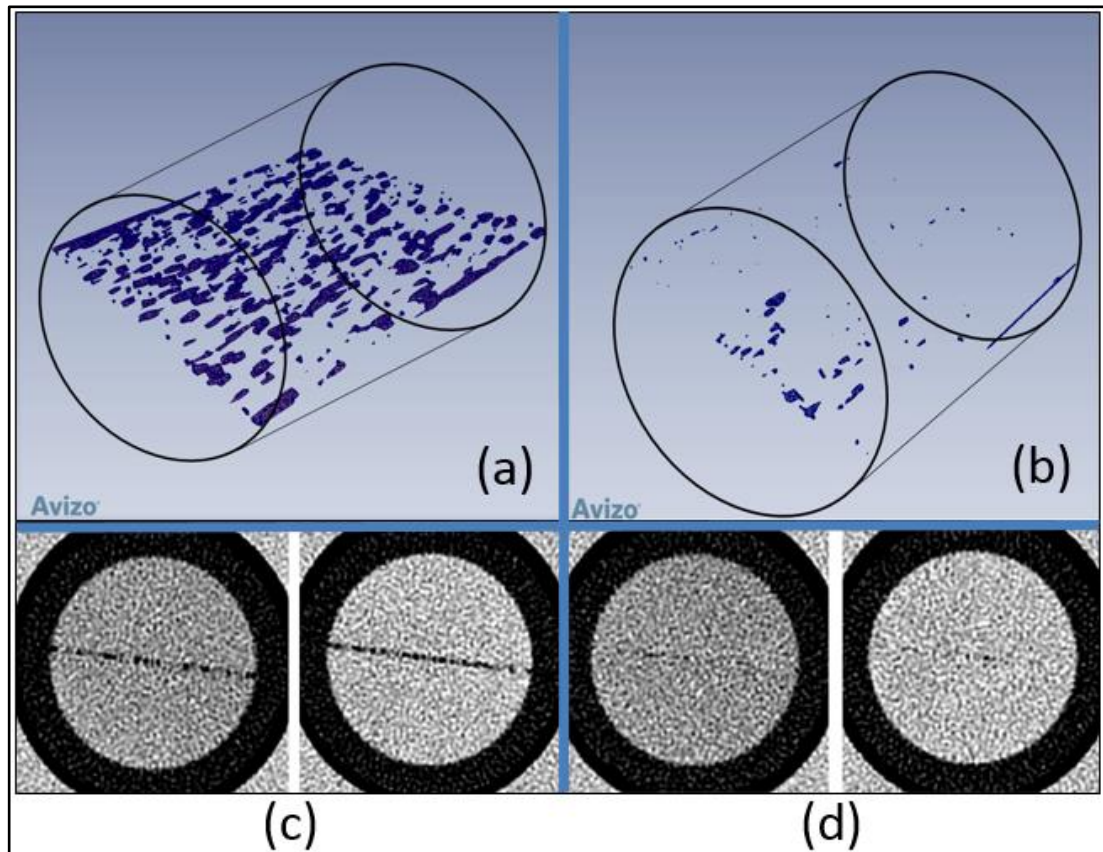


Figure 6-15: Void spaces (blue surfaces) that acts as conduits to fluid flow in ALP sample at (a) 1000 psi and (b) 4000 psi. CT images of sample at 1/3 and 2/3 of the length of the sample for (c) 1000 psi and (d) 4000 psi confining pressure stages.

Confining pressure (psi)	1000	2000	3000	4000
Void surface area (mm <sup>2</sup> )	1025	808	116	66.93
Void volume (mm <sup>3</sup> )	131	94	9	5
Fracture thickness/aperture (mm)	0.355	0.33	0.251	0.255

Table 6-12: Avizo results for ALP sample for all confining pressure stages.

The ALP sample fracture conductivity reduced by five orders of magnitude throughout the experiment (Figure 6-16). Large reduction in fracture conductivity were captured in the last two stages (3000 psi and 4000 psi). A photograph of the sample after performing the experiment is shown in Figure 6-17 with clear impressions of proppant embedment on fracture walls.

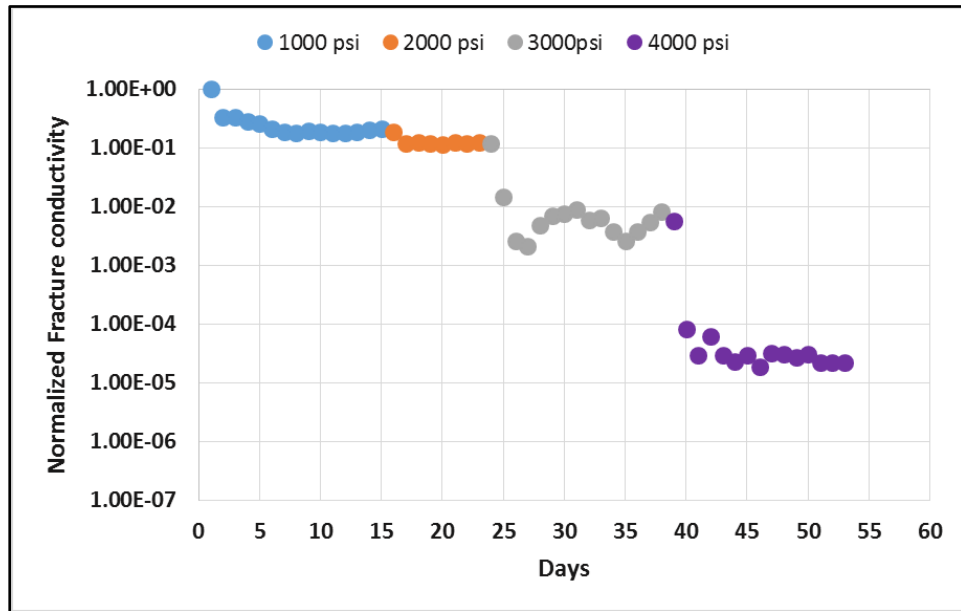


Figure 6-16: Normalized fracture conductivity of the ALP sample (in log scale) vs. time for all confining pressure steps.

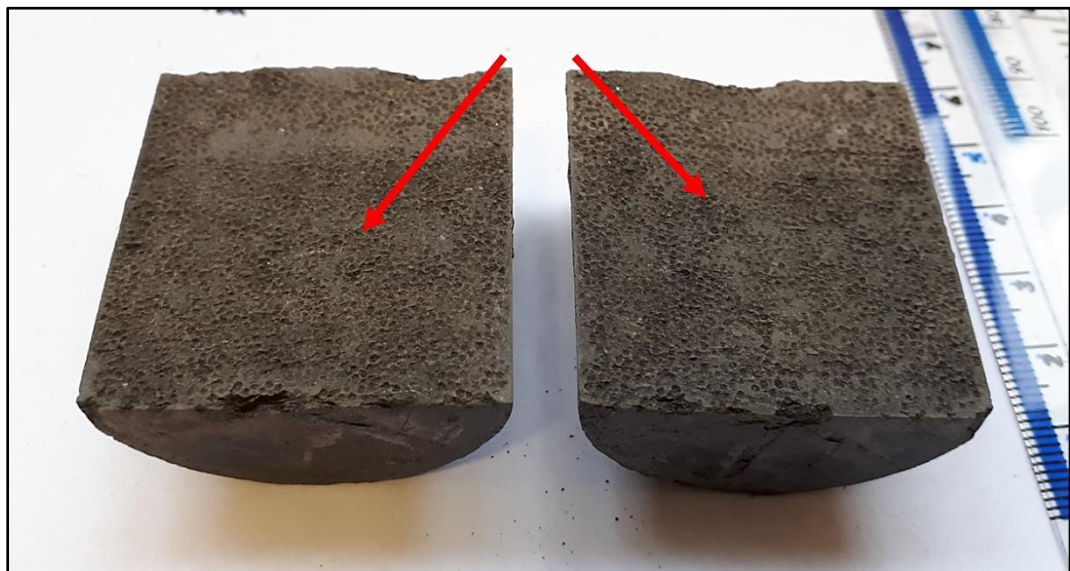


Figure 6-17: ALP sample fracture walls after performing the experiment showing impressions of the proppant embedment into fracture wall.

### 6.4.3 Fracture closure of the AM sample

The AM sample was tested under the pre-described procedure for a period of 52 days. Initial proppant pack fracture parameters are listed in Table 6-13.

Sample	AM
Initial void surface area (mm <sup>2</sup> )	1924
Initial void volume (mm <sup>3</sup> )	480
Initial fracture conductivity (m <sup>3</sup> )	1.71 E-13

*Table 6-13: Initial fracture parameters of AM sample.*

Fracture conductivity change over time for all stages is shown in Figure 6-18. At 1000 psi, sample was kept under confining pressure at this stage for a period of 15 days. Fracture conductivity started to plateau on the 8<sup>th</sup> day of this stage. By the end of this stage, conductivity had a total average reduction of 87% to final value of 2.21 E-14 m<sup>3</sup>.

Fracture conductivity did not have significant reduction in a 12 day period when confining pressure was increased to 2000 psi. It has reduced by 8 % only throughout this stage to a final average value of 2.04 E-13 m<sup>3</sup> compared to the previous stage. This behaviour continued even when confining pressure was increased to 3000 psi. The sample was kept under confining pressure in this stage for a period of 14 days. Final average conductivity was found to be 1.97 E-14 m<sup>3</sup>, which is about 3.5% less than the conductivity in the previous stage.

Fracture conductivity went through larger reduction at 4000 psi confining pressure stage which lasted for 11 days. It started to stabilize on the 4th day to an average final value of 1.51 E-14 m<sup>3</sup>. Reduction in fracture conductivity was about 24% compared to the previous stage. The last conductivity measurement parameters for the measurement done at the end of each stage are listed in Table 6-14.

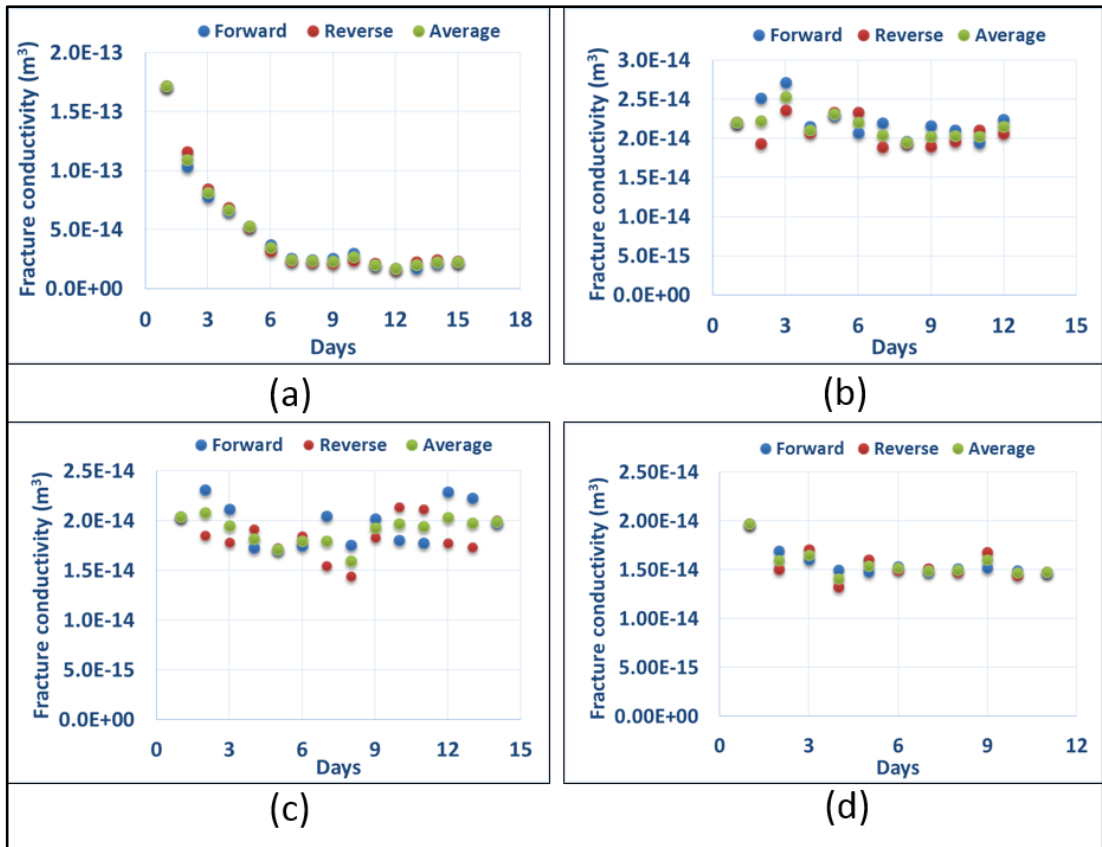


Figure 6-18: Fracture conductivity reduction with time for the AM sample at (a) 1000 psi, (b) 2000 psi, (c) 3000 psi and (d) 4000 psi.

Confining pressure (psi)	Forward			Reverse		
	Flow rate (cc/min)	Differential pressure (psi)	Conductivity (m <sup>3</sup> )	Flow rate (cc/min)	Differential pressure (psi)	Conductivity (m <sup>3</sup> )
1000	1.5	0.124	2.56 E-14	1.5	0.125	2.54 E-14
	1.2	0.108	2.36 E-14	1.2	0.108	2.36 E-14
	0.9	0.088	2.17 E-14	0.9	0.087	2.19 E-14
	0.6	0.064	1.99 E-14	0.6	0.061	2.09 E-14
	Average conductivity (m <sup>3</sup> )			2.21 E-14		
2000	2.5	0.235	2.26 E-14	2.5	0.251	2.11 E-14
	2	0.185	2.29 E-14	2	0.204	2.08 E-14
	1.5	0.142	2.24 E-14	1.5	0.153	2.08 E-14
	1	0.097	2.19 E-14	1	0.108	1.96 E-14
	Average conductivity (m <sup>3</sup> )			2.04 E-14		
3000	2.5	0.271	1.96 E-14	2.5	0.248	2.14 E-14
	2	0.217	1.95 E-14	2	0.205	2.07 E-14
	1.5	0.154	2.07 E-14	1.5	0.168	1.89 E-14
	1	0.109	1.95 E-14	1	0.11	1.93 E-14
	Average conductivity (m <sup>3</sup> )			1.97 E-14		
4000	2.5	0.363	1.46 E-14	2.5	0.382	1.39 E-14
	2	0.286	1.48 E-14	2	0.292	1.45 E-14
	1.5	0.212	1.50 E-14	1.5	0.211	1.51 E-14
	1	0.146	1.45 E-14	1	0.135	1.57 E-14
	Average conductivity (m <sup>3</sup> )			1.51 E-14		

Table 6-14: Results of fracture conductivity test at the end of each confining pressure stage for AM sample. The average conductivity reported is the average at the plateau of the curves shown in Figure 6-18.

Figure 6-19 presents CT images taken at the beginning and end of the experiment shows a slight reduction in fracture aperture over stages. Re-construction of CT images using Avizo are shown in Figure 6-19 with the calculations results listed in Table 6-15. At the end of 1000 psi stage, fracture aperture calculated by Avizo was 0.383 mm, which is about 65% of the initial fracture aperture. Void spaces generated by Avizo within the fracture have reduced as well by 66%.

Fracture conductivity results showed minor change in fracture conductivity for the 2000 psi and 3000 psi stages. At the end of 2000 psi stage, Avizo results agree with the observations and reduction in fracture aperture was about 6% with reference to the previous stage. Reduction in void spaces was slightly higher and had a final value of 120 mm<sup>3</sup> compared to 163 mm<sup>3</sup> in the previous stage. Similar observations were made when confining pressure was increased to 3000 psi. Avizo estimated fracture aperture to be 0.328 mm, which is about 9% less than the previous stage.



However, the sample experienced large reduction in voids volume which was about 38% with respect to the previous stage.

The large reduction in fracture conductivity was not reflected in fracture aperture calculated by Avizo. Using Avizo calculations, fracture aperture has reduced by 4.9% only compared to the previous stage. However, the reduction in conductivity was reflected in voids volume, which experiences a reduction of 50%.

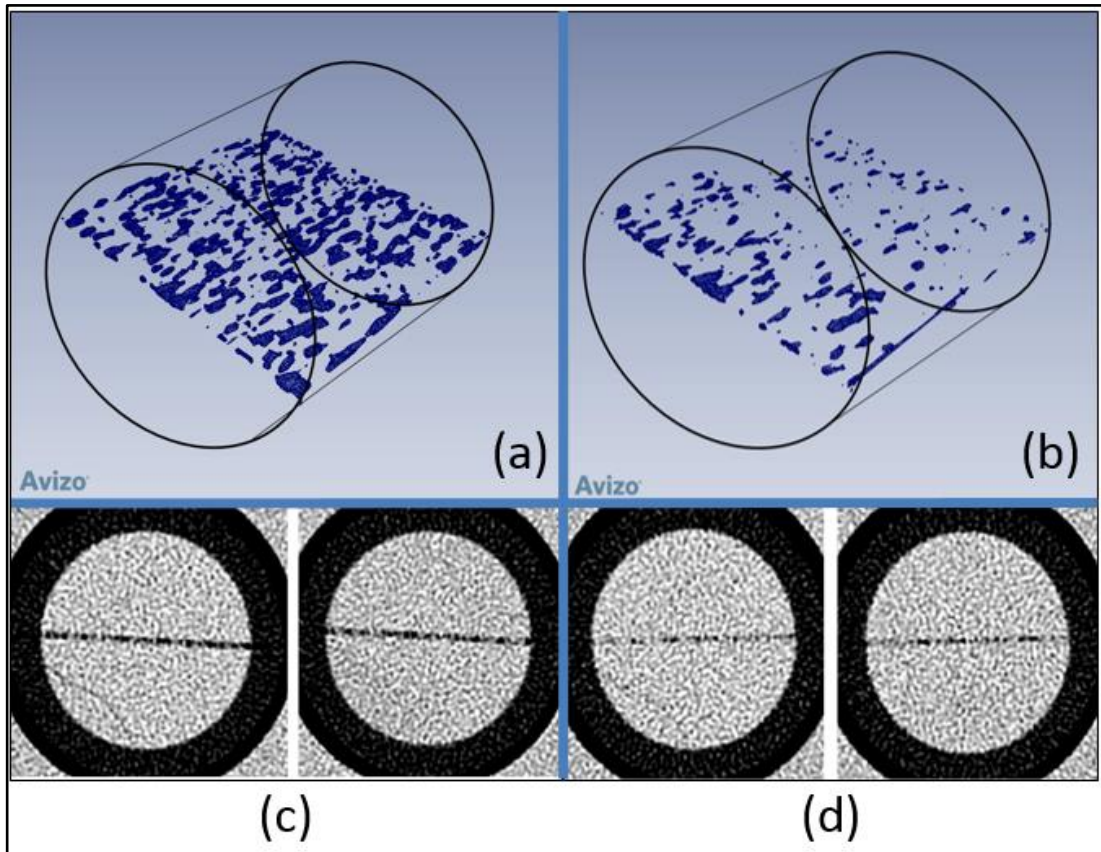


Figure 6-19: Void spaces (blue surfaces) that acts as conduits to fluid flow in AM sample at (a) 1000 psi and (b) 4000 psi. CT images of sample at 1/3 and 2/3 of the length of the sample for (c)1000 psi and (d) 4000 psi confining pressure stages.

Confining pressure (psi)	1000	2000	3000	4000
Void surface area (mm <sup>2</sup> )	1161	924	661	360
Void volume (mm <sup>3</sup> )	163	120	75	37
Fracture thickness (aperture)(mm)	0.383	0.361	0.328	0.312

Table 6-15: Avizo results for the AM sample for all confining pressure stage.

Fracture conductivity normalized to the initial fracture conductivity results against time are plotted in Figure 6-20, which suggests that most conductivity reduction was actually at low confining stress on the first stage. Very minor reduction in fracture closure and fracture conductivity was measured at higher stresses. Total conductivity reduction throughout the experiment was 92%. It can be seen clearly in fracture walls of the sample shown in Figure 6-21 as the sample underwent proppant embedment during the experiment.

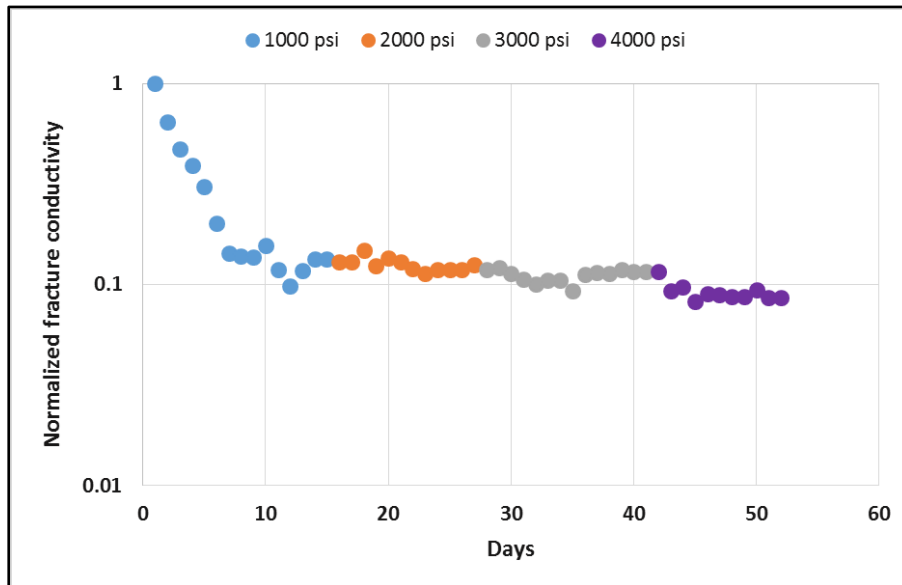


Figure 6-20: Normalized fracture conductivity of the AM sample (in log scale) vs. time for all confining pressure steps.

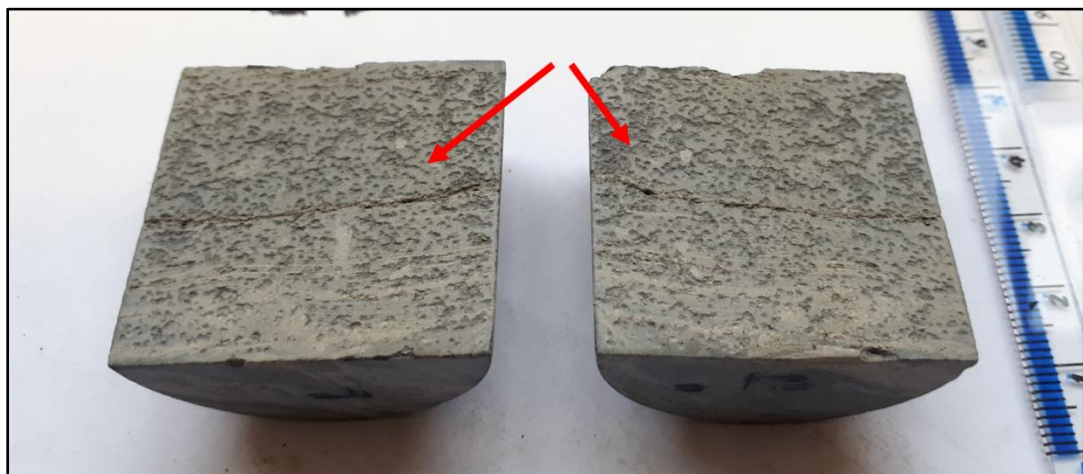


Figure 6-21: ALP sample fracture walls after performing the experiment showing impressions of the proppant embedment into fracture wall.

#### 6.4.4 Fracture closure of the KC sample

The previous samples tested before were relatively soft compared to the other samples. The KC sample is stiffer than the previous samples and expected to experience far less fracture closure than the softer samples. Initial fracture parameters are listed in Table 6-16.

Sample	KC
Initial void surface area (mm <sup>2</sup> )	1758
Initial void volume (mm <sup>3</sup> )	439
Initial fracture conductivity (m <sup>3</sup> )	1.71 E-13

Table 6-16: Initial fracture parameters of KC sample.

Fracture conductivity variation with time is presented in Figure 6-22 for all four stages. Final conductivity measurement for these stages is as well presented in Figure 6 23. KC sample was tested for about 35 days under all confining pressure stages. In 1000 psi confining pressure stage, fracture conductivity reduced significantly and it took around 8 days to start to plateau. The sample was kept under 1000 psi confining pressure for a period of 14 days. The average final conductivity was about  $7.58 \text{ E-}14 \text{ m}^3$ , which is about 56% less than the initial condition.

The sample showed a quick response when confining pressure was increased to 2000 psi and conductivity stabilized straight away on the second day of this stage. This stage lasted for 7 days and fracture conductivity stabilized to an average value of  $5.90 \text{ E-}14 \text{ m}^3$ , which means the reduction in conductivity was 22% during this stage.

At 3000 psi confining pressure, fracture conductivity took a long time to stabilize. Sample was kept at this confining pressure for 8 days and fracture conductivity started to plateau on the 5th day. However, the change in conductivity was not large, (about 18%) compared to the previous stage.

Fracture conductivity remained relatively constant even when confining pressure was increased to 4000 psi. The sample was kept under this confining pressure for a period of 6 days. Final average conductivity over this stage was  $4.95 \text{ E-}14 \text{ m}^3$ . The slight difference in conductivity between the two stages is due the variation of the measurement across the days.

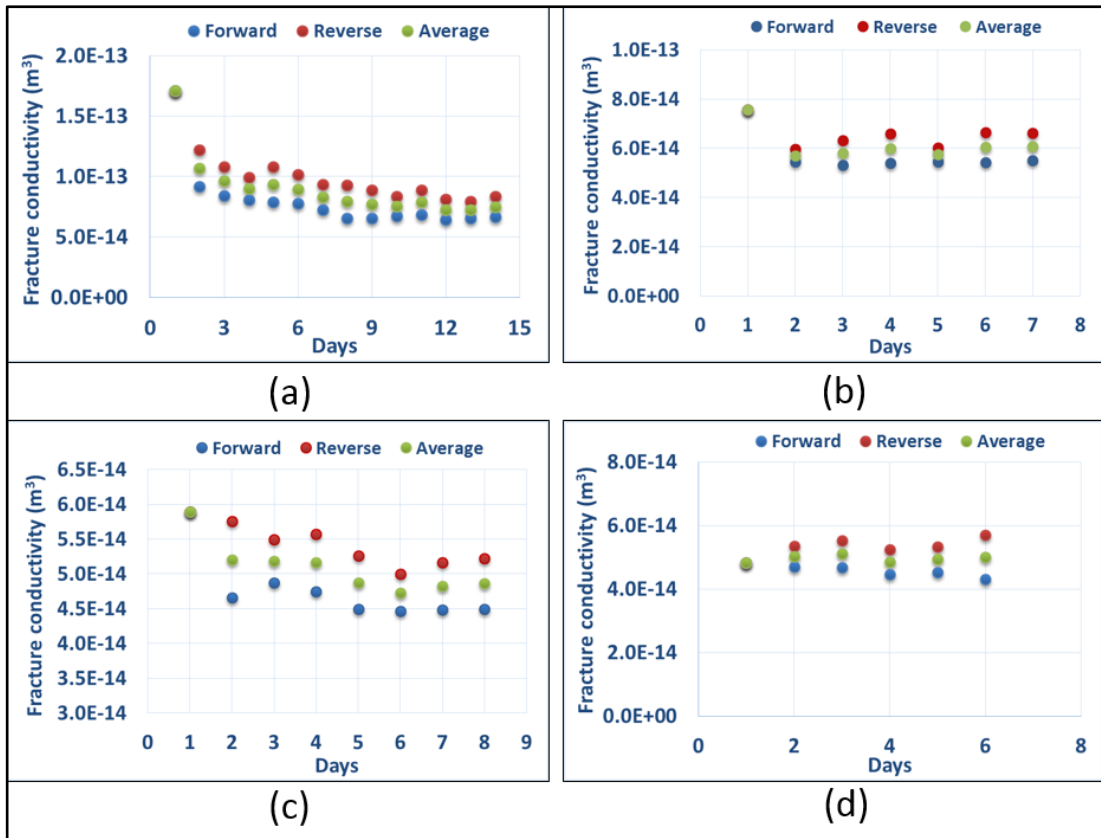


Figure 6-22: Fracture conductivity reduction with time for the KC sample at (a) 1000 psi, (b) 2000 psi, (c) 3000 psi and (d) 4000 psi.

Confining pressure (psi)	Forward			Reverse		
	Flow rate (cc/min)	Differential pressure (psi)	Conductivity (m <sup>3</sup> )	Flow rate (cc/min)	Differential pressure (psi)	Conductivity (m <sup>3</sup> )
1000	15	0.468	6.29 E-14	15	0.386	7.63 E-14
	12	0.367	6.42 E-14	12	0.295	7.99 E-14
	9	0.262	6.75 E-14	9	0.211	8.38 E-14
	6	0.166	7.10 E-14	6	0.125	9.43 E-14
	Average conductivity (m <sup>3</sup> )			7.58 E-14		
2000	12	0.423	5.57 E-14	12	0.331	7.12 E-14
	9	0.304	5.81 E-14	9	0.240	7.36 E-14
	6	0.198	5.95 E-14	6	0.155	7.60 E-14
	3	0.095	6.20 E-14	3	0.079	7.46 E-14
	Average conductivity (m <sup>3</sup> )			5.90 E-14		
3000	10	0.457	4.30 E-14	10	0.357	5.50 E-14
	8	0.353	4.45 E-14	8	0.281	5.59 E-14
	6	0.257	4.58 E-14	6	0.193	6.10 E-14
	4	0.162	4.85 E-14	4	0.115	6.83 E-14
	Average conductivity (m <sup>3</sup> )			4.82 E-14		
4000	10	0.473	4.15 E-14	10	0.375	5.24 E-14
	8	0.373	4.21 E-14	8	0.295	5.32 E-14
	6	0.273	4.32 E-14	6	0.209	5.64 E-14
	4	0.174	4.51 E-14	4	0.119	6.60 E-14
	Average conductivity (m <sup>3</sup> )			4.95 E-14		

*Table 6-17: Results of fracture conductivity test at the end of each confining pressure stage for KC sample. The average conductivity reported is the average at the plateau of the curves shown in Figure 6-22.*

Evolution of fracture closure between initial and final stage can be seen visually in CT images presented in Figure 6-23. Avizo 3D reconstructed model for these two stages are also shown in Figure 6-23. At 1000 psi, fracture aperture has reduced by 34% according to the quantitative analysis done by Avizo. Volume of void spaces has also reduced by 57 % to a final value of 190 m<sup>3</sup>.

As reduction in conductivity was relatively low, a minor change in Avizo results was also noticed when confining pressure was increased to 2000 psi. Avizo calculated the final aperture and was found to be 0.382 mm, which is just 1.8 % less than the previous stage. Void spaces volume has reduced by 17% with respect to the previous stage. At 3000 psi, reduction in fracture conductivity was relatively low which was reflected in Avizo results. Similar to the previous stage, fracture aperture change was minor according to Avizo results. Aperture has reduced to 0.370 mm

compared to 0.382 mm in the previous stage. Volume of void spaces also underwent a minor reduction of 14% with respect to the previous stage.

At 4000 psi, fracture aperture calculated from CT images using Avizo was almost the same as the previous stage, which agrees with conductivity results. Fracture aperture was about 0.367 mm compared to 0.370 mm in the previous stage. A slight reduction in void spaces volume (about 12%) was calculated using Avizo at the end of this stage.

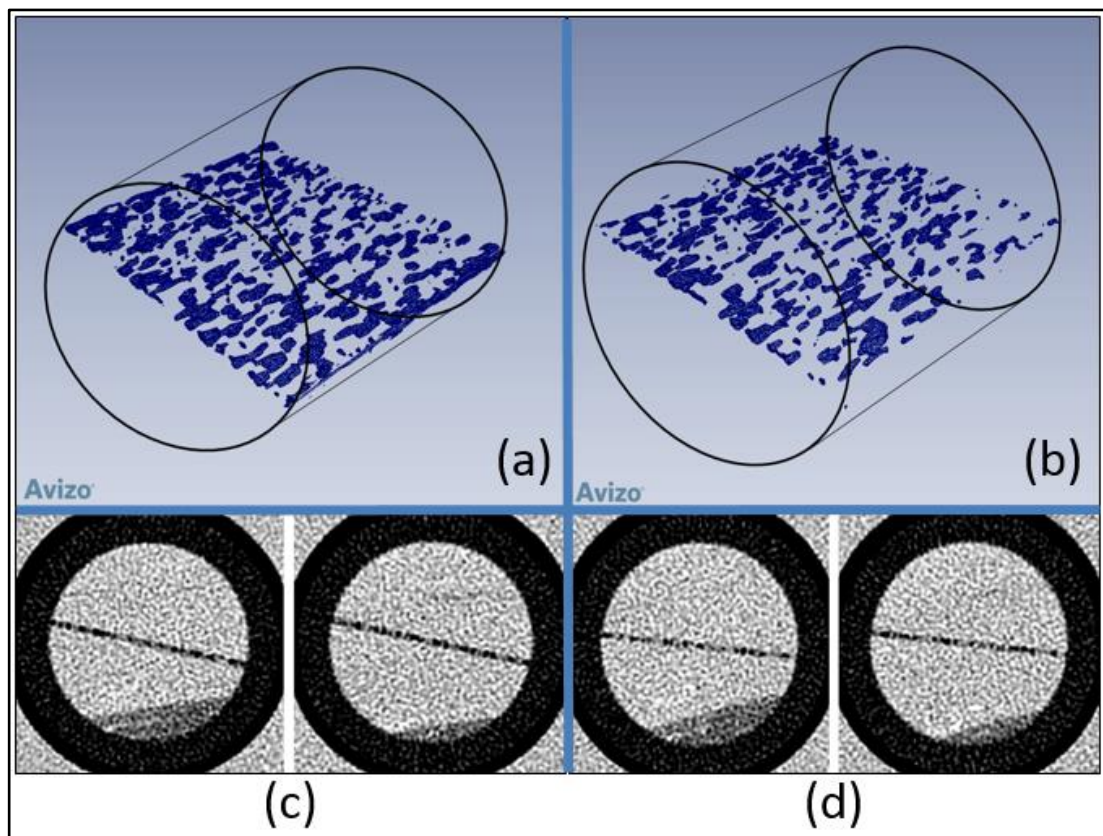


Figure 6-23: Void spaces (blue surfaces) that acts as conduits to fluid flow in KC sample at (a) 1000 psi and (b) 4000 psi. CT images of sample at 1/3 and 2/3 of the length of the sample for (c)1000 psi and (d) 4000 psi confining pressure stages.

Confining pressure (psi)	1000	2000	3000	4000
Void surface area (mm <sup>2</sup> )	1313	1127	1000	904
Void volume (mm <sup>3</sup> )	190	158	136	119
Fracture thickness (aperture)(mm)	0.389	0.382	0.370	0.367

Table 6-18: Avizo results for the KC sample for all confining pressure stages.

Figure 6-24 represent reduction in fracture conductivity throughout the experiment. It can be seen that most of the reduction took place at low stress at 1000 psi and partially at 2000 and 3000 psi. Most of fracture closure occurred at low stresses during 1000 psi and 2000 psi confining pressure stages. Fracture conductivity reduction during these two stages was about 66%. Total reduction in conductivity throughout the experiment is about 71%. KC sample proppant embedment was less than the other samples tested before because fracture closure was less (Figure 6-25).

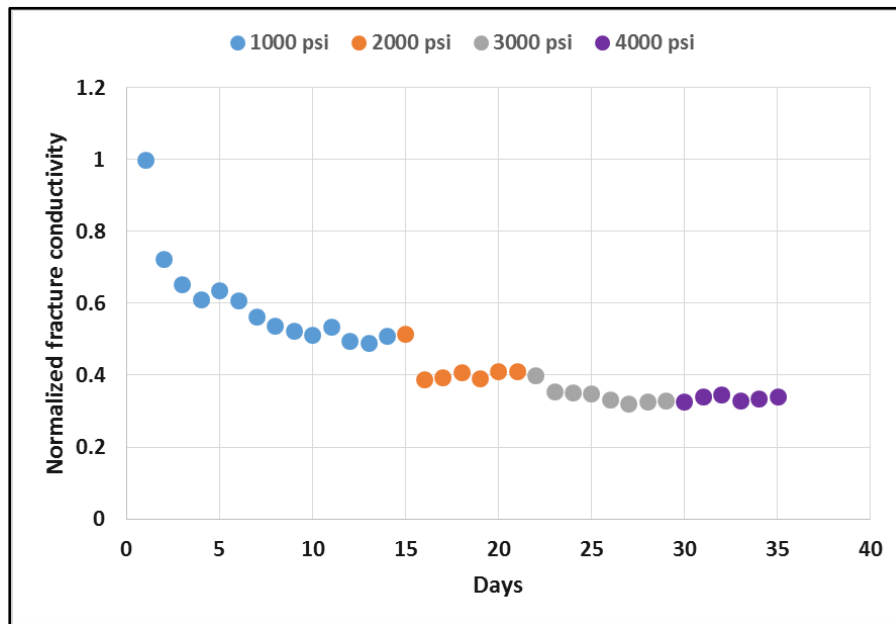


Figure 6-24: Normalized fracture conductivity of the KC sample vs. time for all confining pressure steps.

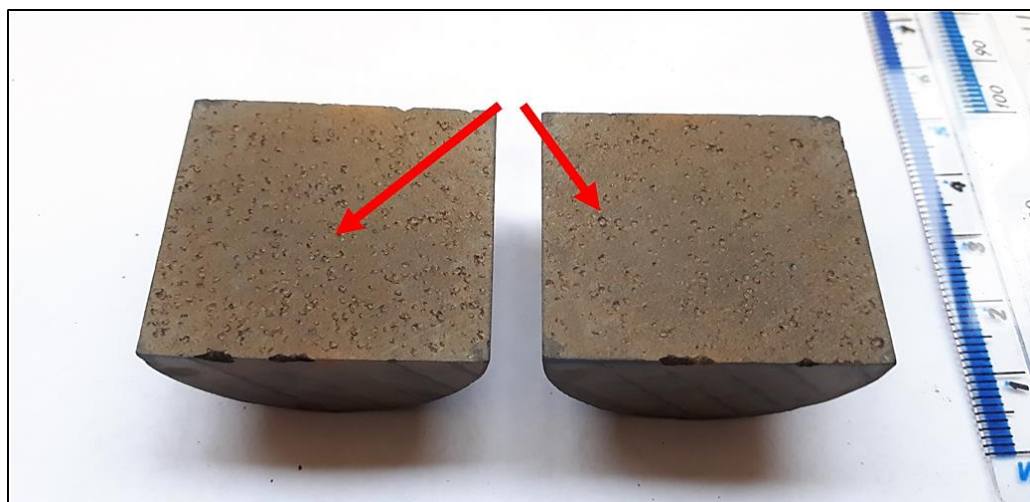


Figure 6-25: KC sample fracture walls after performing the experiment showing impressions of the proppant embedment into fracture wall.

#### 6.4.5 Fracture closure of the OC sample

OC sample is quite a stiff shale sample with relatively high Young's modulus (26.8 GPa). Initial fracture parameters estimated are shown in Table 6-19.

Sample	OC
Initial void surface area (mm <sup>2</sup> )	1220
Initial void volume (mm <sup>3</sup> )	304
Initial fracture conductivity (m <sup>3</sup> )	1.71 E-13

*Table 6-19: Initial fracture parameters of the OC sample.*

The OC sample hydraulic conductivity reduction with time are plotted for all stages in Figure 6-26. Details of the last conductivity measurement and average conductivity at the plateau are presented in Table 6-20. Total experiment time was about 30 days because creep failure rate and fracture closure were less compared to previous samples. First, sample was subjected to 1000 psi confining pressure for a period of 6 days. Fracture conductivity reached a plateau on the 3<sup>rd</sup> day, which is relatively fast compared to other samples. Reduction in fracture conductivity during this stage was about 45%. Average final conductivity at this stage was found to be 9.37 E-14 m<sup>3</sup>.

At 2000 psi confining pressure, fracture conductivity continuously reduced until the 6<sup>th</sup> day where a plateau was observed. Sample was kept under this confining pressure for period of 12 days. Average fracture conductivity at the plateau was 7.02 E-14 m<sup>3</sup>, which is 25 % less than the previous stage.

Minor reduction in fracture conductivity was found when confining pressure was increased to 3000 psi. Conductivity plateau straight away on the 2<sup>nd</sup> day of this stage, which suggests that fracture closure was very minimum at this stage. Average conductivity at the end of this stage was about 6.79 E-14 m<sup>3</sup>, which is just less than the previous stage by 3% only. Similar behaviour was also noticed in the final stage at 4000 psi confining pressure, which lasted for a period of 5 days. Fracture conductivity reduction was minor as well (about 9%) and final average conductivity measured was about 6.16 E-14 m<sup>3</sup>.



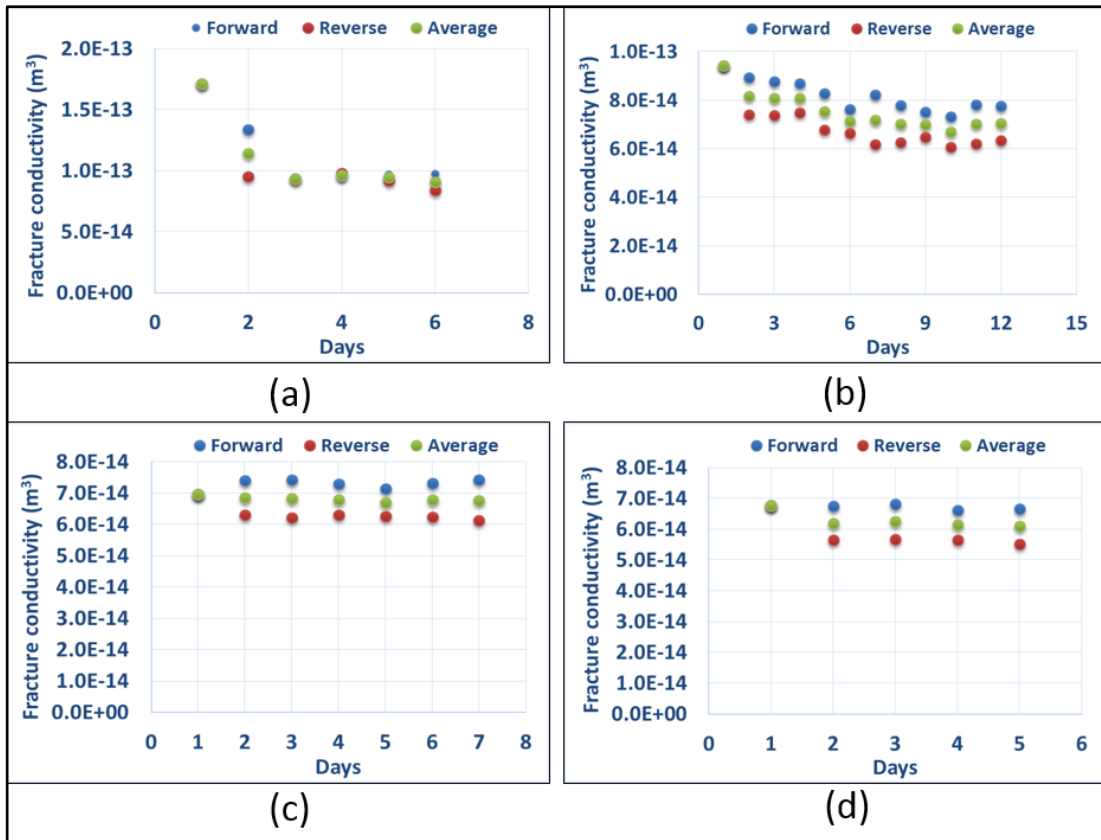


Figure 6-26: Fracture conductivity reduction with time for OC sample at (a) 1000 psi, (b) 2000 psi, (c) 3000 psi and (d) 4000 psi.

Confining pressure (psi)	Forward			Reverse		
	Flow rate (cc/min)	Differential pressure (psi)	Conductivity (m <sup>3</sup> )	Flow rate (cc/min)	Differential pressure (psi)	Conductivity (m <sup>3</sup> )
1000	20	0.294	8.95 E-14	20	0.349	7.54 E-14
	15	0.204	9.67 E-14	15	0.243	8.12 E-14
	10	0.126	1.04 E-13	10	0.15	8.77 E-14
	5	0.066	9.97 E-14	5	0.072	9.14 E-14
	Average conductivity (m <sup>3</sup> )			9.37 E-14		
2000	20	0.383	6.87 E-14	20	0.471	5.59 E-14
	15	0.261	7.56 E-14	15	0.32	6.17 E-14
	10	0.163	8.07 E-14	10	0.194	6.78 E-14
	5	0.077	8.54 E-14	5	0.097	6.78 E-14
	Average conductivity (m <sup>3</sup> )			7.02 E-14		
3000	20	0.393	6.70 E-14	20	0.471	5.59 E-14
	15	0.27	7.31 E-14	15	0.331	5.96 E-14
	10	0.167	7.88 E-14	10	0.201	6.55 E-14
	5	0.084	7.83 E-14	5	0.103	6.39 E-14
	Average conductivity (m <sup>3</sup> )			6.79 E-14		
4000	20	0.440	5.98 E-14	20	0.521	5.05 E-14
	15	0.305	6.47 E-14	15	0.366	5.39 E-14
	10	0.193	6.82 E-14	10	0.228	5.77 E-14
	5	0.089	7.39 E-14	5	0.113	5.82 E-14
	Average conductivity (m <sup>3</sup> )			6.16 E-14		

*Table 6-20: Results of fracture conductivity test at the end of each confining pressure stage for OC sample. The average conductivity reported is the average at the plateau of the curves shown in Figure 6-26.*

CT images taken on the last day of each confining pressure stage are shown in Figure 6-27 which were used to construct Avizo model shown in Figure 6-27. The results of Avizo modelling are tabulated in Table 6-21. Reduction in fracture conductivity was the largest during the first stage. Avizo calculated all dimensions of void spaces within the fracture and found fracture aperture to be 0.41 mm at the end of this stage which suggests that fracture has closed by 31%. Volume of void spaces underwent a reduction of 60% to a final value of 123 mm<sup>3</sup>.

Fracture closure was minor at 2000 psi confining pressure, which complies with fracture conductivity results. Fracture aperture has reduced by 5% with respect to the previous stage to a final value of 0.389 mm. Reduction in volume of the void spaces was about 22%, which is similar to the reduction in fracture conductivity. The final volume of void spaces at the end of this stage was 95 mm<sup>3</sup> as it is shown in Figure 6-27.

At 3000 psi, it was very difficult to notice a change in fracture aperture visually from CT images and Avizo 3D model because change in fracture conductivity was very small. Avizo image processing estimated fracture aperture to be 0.383 mm, which is just 1.5% less than the previous stage. Void spaces underwent a reduction in volume of about 8.7% to final value of 87 mm<sup>3</sup>. The sample underwent minor fracture closure at 4000 psi confining pressure, which agrees with fracture conductivity results. Fracture aperture reduction was about 2.4% and the final fracture aperture at the end of this stage was 0.374 mm. Void spaces generated by Avizo have reduced to 82 mm<sup>3</sup>, which is 6% less than void volumes in the previous stage.

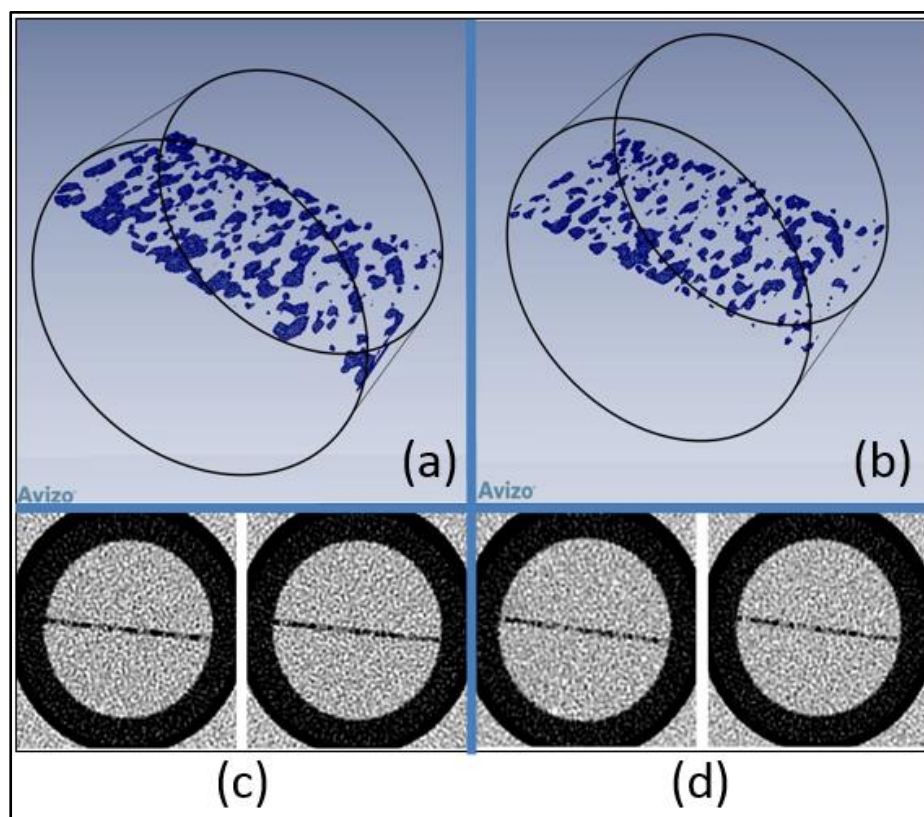


Figure 6-27: Void spaces (blue surfaces) that acts as conduits to fluid flow in OC sample at (a) 1000 psi and (b) 4000 psi. CT images of sample at 1/3 and 2/3 of the length of the sample for (c)1000 psi and (d) 4000 psi confining pressure stages..

Confining pressure (psi)	1000	2000	3000	4000
Void surface area (mm <sup>2</sup> )	789	655	615	596
Void volume (mm <sup>3</sup> )	123	95	87	82
Fracture thickness (aperture)(mm)	0.410	0.389	0.383	0.374

Table 6-21: Avizo results for the OC sample for all confining pressure stages.

Normalized fracture conductivity against time graph for the OC sample under the four confining pressure stages is presented in Figure 6-28. Sample experienced most fracture closure during the first two stages were most reduction of fracture conductivity occurred. The sample had very minor fracture closure at high confining pressure stages (3000 and 4000 psi). Total reduction in conductivity was about 64%. Proppant embedment in the OC sample was less than the one observed in previous samples because fracture closure was less.

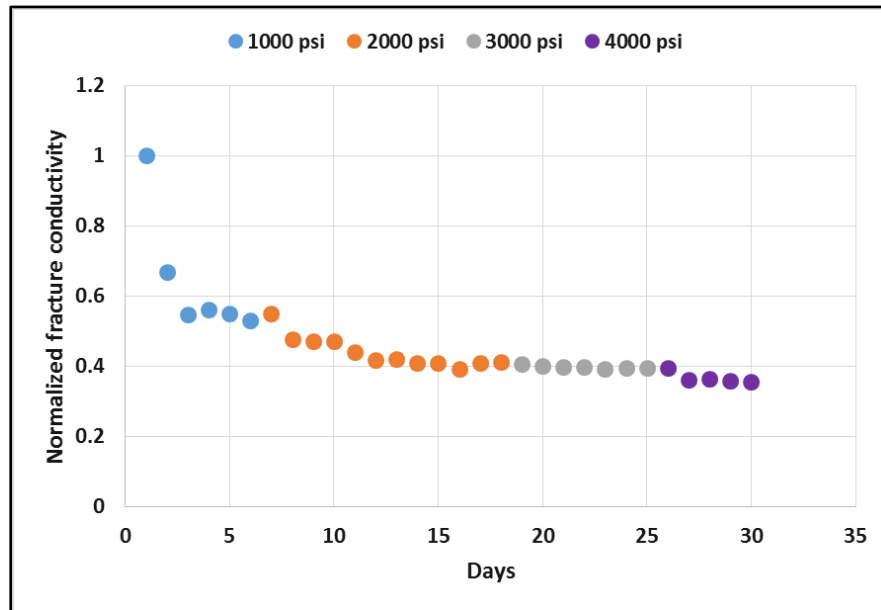


Figure 6-28: Normalized fracture conductivity of OC sample vs. time for all confining pressure steps.

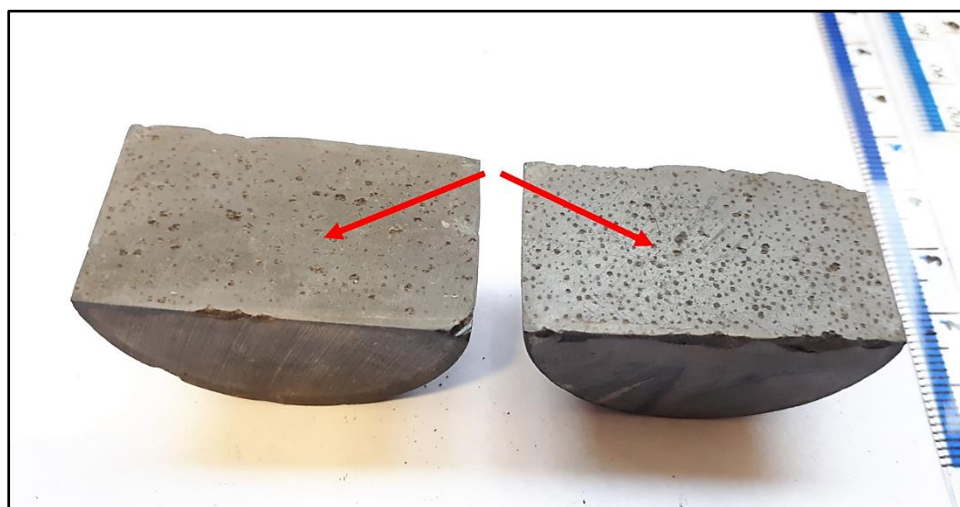


Figure 6-29: OC sample fracture walls after performing the experiment showing impressions of the proppant embedment into fracture wall.

#### 6.4.6 Fracture closure of the D sample

The D sample is the stiffest sample used in this series of experiments; it has a relatively high Young's modulus (53.0 GPa). Initial fracture parameters estimated are shown in Table 6-22.

Sample	D
Initial void surface area (mm <sup>2</sup> )	1973
Initial void volume (mm <sup>3</sup> )	492
Initial fracture conductivity (m <sup>3</sup> )	1.71 E-13

Table 6-22: Initial fracture parameters of D sample.

D sample experienced the lowest total fracture closure among all samples tested. Total experiment time was 31 days for all four stages. Fracture conductivity variation with time was very small compared with others as it is shown in Figure 6-30. Flow rates and pressure drops of the last measurement done at the end of every stage are shown in Table 6-23. Initially, the sample was subjected to 1000 psi confining pressure for a period of 10 days. Fracture conductivity reduced under the effective stress and started to plateau on the 3<sup>rd</sup> day of this stage. The final average conductivity was found to be 9.42 E-14 m<sup>3</sup>, which is 45% less than the initial stage.

The D sample underwent fracture closure and reduction in fracture conductivity as well at 2000 psi confining pressure stage. Sample was subjected to this confining pressure for a period of 7 days and fracture conductivity started to stabilize on the 3<sup>rd</sup> day. Conductivity has reduced to 7.12 E-14 m<sup>3</sup>, which is about 24 % less than the previous stage.

Similar behaviour to OC sample was noticed in the D sample on 3000 psi stage. Fracture conductivity stabilized straight away on the 2<sup>nd</sup> day and reduction was very minor (about 3%) compared to the previous stage. The final average conductivity at the end of this stage was 6.90 E-14 m<sup>3</sup>.

On the last stage, fracture conductivity had a minor reduction as well and showed no signs of fracture closure. This stage lasted for a period of 7 days and conductivity started to plateau on the 2<sup>nd</sup> day of this stage. The final average conductivity was found to be 6.79 E-14 m<sup>3</sup>, which is less than the previous stage by only 1.6%.

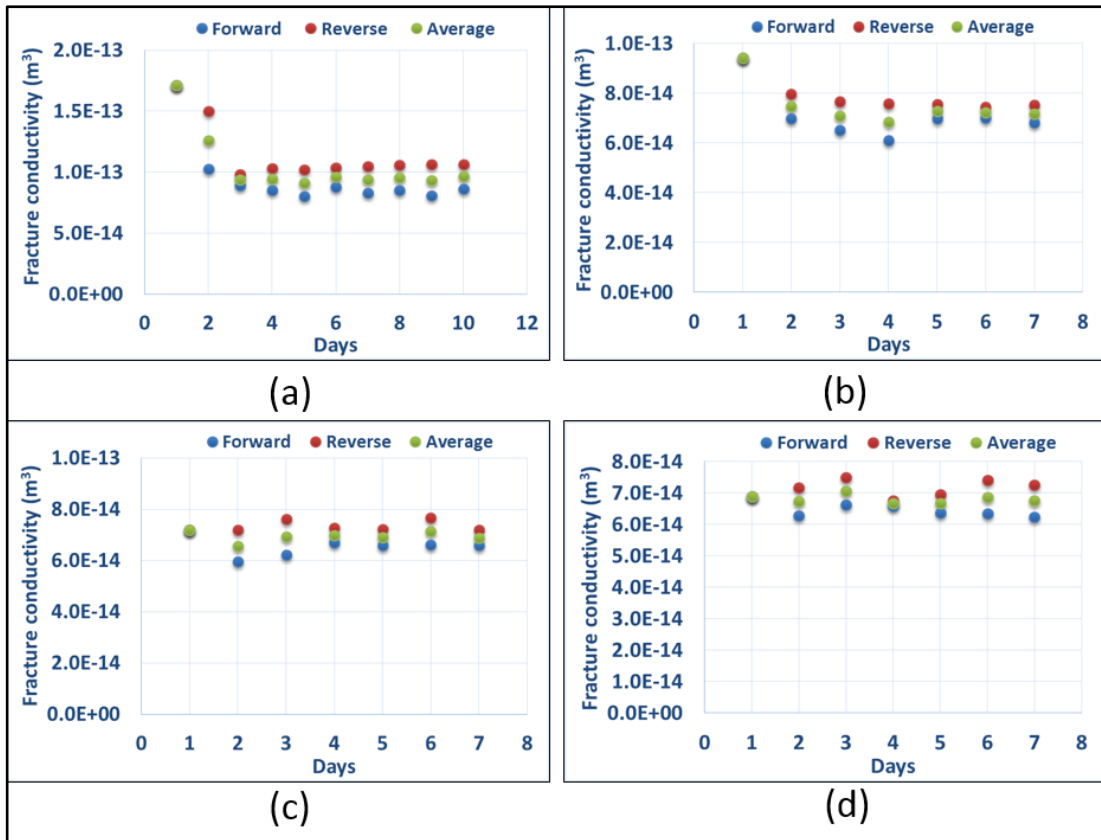


Figure 6-30: Fracture conductivity reduction with time for the D sample at (a) 1000 psi, (b) 2000 psi, (c) 3000 psi and (d) 4000 psi.

Confining pressure (psi)	Forward			Reverse		
	Flow rate (cc/min)	Differential pressure (psi)	Conductivity (m <sup>3</sup> )	Flow rate (cc/min)	Differential pressure (psi)	Conductivity (m <sup>3</sup> )
1000	15	0.394	8.33 E-14	15	0.318	1.03 E-13
	12	0.308	8.52 E-14	12	0.252	1.04 E-13
	9	0.224	8.79 E-14	9	0.187	1.05 E-13
	6	0.148	8.87 E-14	6	0.117	1.12 E-13
	Average conductivity (m <sup>3</sup> )			9.42 E-14		
2000	12	0.401	6.55 E-14	12	0.345	7.61 E-14
	9	0.291	6.77 E-14	9	0.261	7.54 E-14
	6	0.189	6.95 E-14	6	0.174	7.54 E-14
	3	0.094	6.98 E-14	3	0.089	7.37 E-14
	Average conductivity (m <sup>3</sup> )			7.12E-14		
3000	10	0.340	6.43 E-14	10	0.269	8.13 E-14
	8	0.268	6.53 E-14	8	0.242	7.23 E-14
	6	0.198	6.63 E-14	6	0.192	6.84 E-14
	4	0.130	6.73 E-14	4	0.134	6.53 E-14
	Average conductivity (m <sup>3</sup> )			6.90 E-14		
4000	10	0.371	5.90 E-14	10	0.305	7.17 E-14
	8	0.292	5.99 E-14	8	0.254	6.89 E-14
	6	0.216	6.08 E-14	6	0.179	7.33 E-14
	4	0.126	6.95 E-14	4	0.114	7.68 E-14
	Average conductivity (m <sup>3</sup> )			6.79 E-14		

*Table 6-23: Results of fracture conductivity test at the end of each confining pressure stage for the D sample. The average conductivity reported is the average at the plateau of the curves shown in Figure 6-30.*

CT images of the initial and final stage showed qualitatively that no major change in fracture aperture throughout the experiment as it is shown in Figure 6-31. Reconstructed Avizo model and its calculation results are shown in Figure 6-31 and Table 6-24 respectively. Fracture closure was about 24% during the first stage, and final fracture aperture was about 0.452 mm. Void spaces volume has reduced by 47 % to a final a value 260 mm<sup>3</sup>. However, minor reduction in fracture aperture was calculated by Avizo model at the end of the 2000 psi confining pressure stage which was a reflection of fracture conductivity results measured earlier. Aperture change was about 1.6% and volume reduction was minor as well and found to be 4.3% with respect to the previous stage.

Fracture closure was very minimum in the last two stages (3000 psi and 4000 psi). Fracture aperture estimated using Avizo at the end of 3000 psi stage was about 0.447 mm, which is almost the same as the previous stage. Calculated voids volume

at the end of this stage was found to be 238 mm<sup>3</sup>, which is 4.4% less than the volume estimated in the previous stage. The same scenario continued when confining pressure was increased to 4000 ps. Fracture conductivity reduction was very minor which was also reflected in Avizo results. The aperture calculated from CT images by Avizo was 0.423 mm, which is 5.4 % less than the previous stage. Void spaces volume reduction was also minor, (about 13%) with respect to the previous stage.

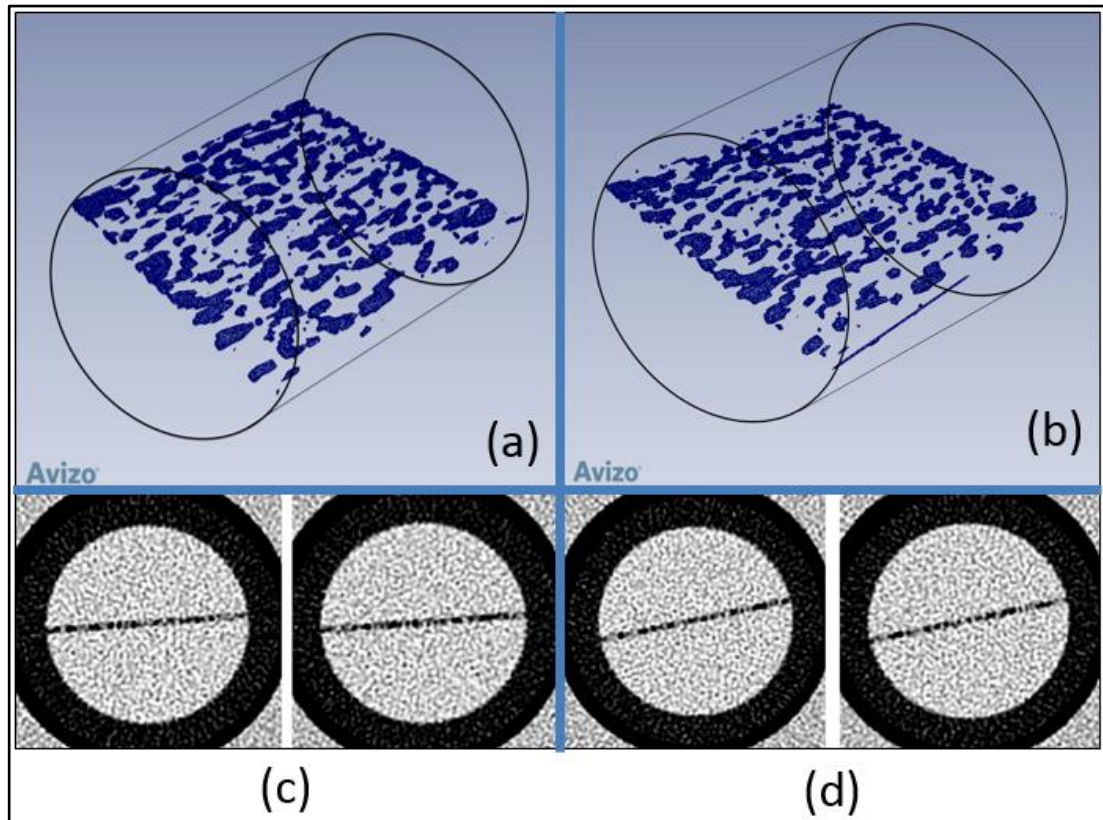


Figure 6-31: Void spaces (blue surfaces) that acts as conduits to fluid flow in D sample at (a) 1000 psi and (b) 4000 psi. CT images of sample at 1/3 and 2/3 of the length of the sample for (c) 1000 psi and (d) 4000 psi confining pressure stages.

Confining pressure (psi)	1000	2000	3000	4000
Void surface area (mm <sup>2</sup> )	1483	1441	1378	1273
Void volume (mm <sup>3</sup> )	260	249	238	206
Fracture thickness (aperture)(mm)	0.452	0.445	0.447	0.423

Table 6-24: Avizo results for the D sample for all confining pressure stages.



Overall, the behaviour of sample D was very similar to the OC sample. Figure 6-32 shows normalized fracture conductivity against time for all four stages of the experiment. Fracture closure occurred mainly at low stresses (1000 and 2000 psi) where most of reduction in fracture conductivity took place. Minor fracture closure occurred at higher stresses (3000 and 4000 psi). Proppant embedment impressions into fracture walls were very similar to the OC sample (Figure 6-33).

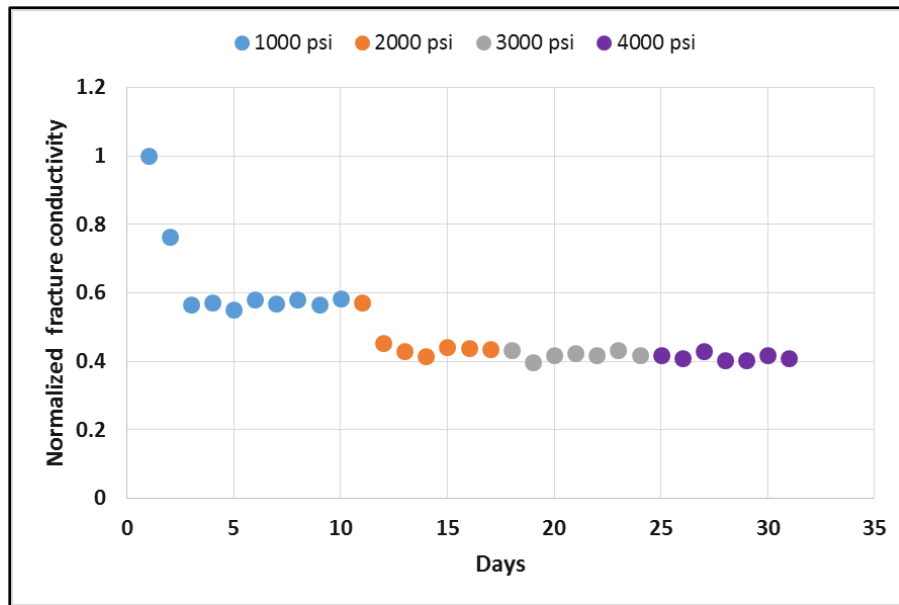


Figure 6-32: Normalized fracture conductivity of the D sample vs. time for all confining pressure steps.

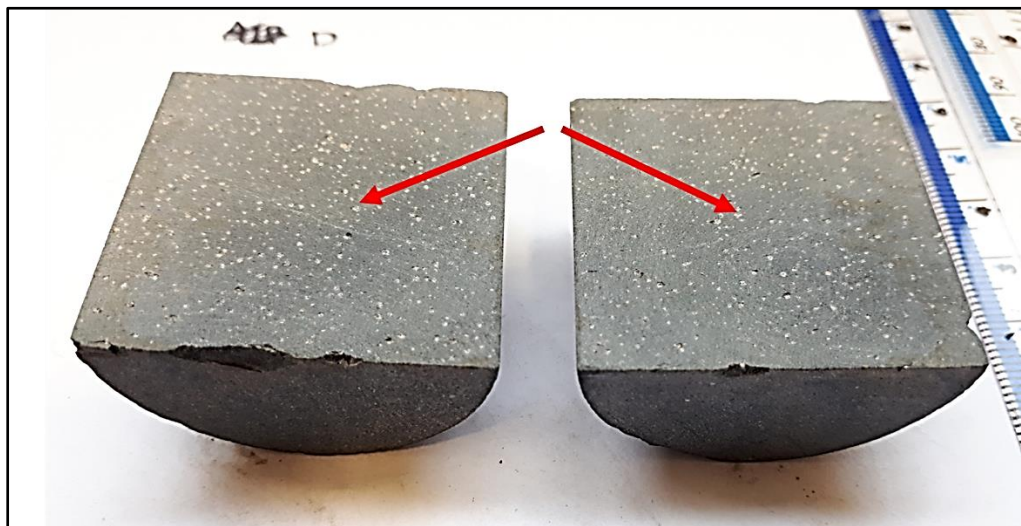


Figure 6-33: D sample fracture walls after performing the experiment showing impressions of the proppant embedment into fracture wall.

## 6.5 Discussion

### 6.5.1 Accuracy of the results

Experimental fracture aperture was estimated using the Avizo software. Avizo converts helical CT images into 3D geometries. The maximum resolution could be achieved with the CT scanner used in this thesis is  $200\ \mu\text{m}$  in the x-direction,  $200\ \mu\text{m}$  in the y-direction and  $625\ \mu\text{m}$  in the z-direction. The voxel size with respect to the scanning direction is shown in Figure 6-34. This means that in fracture aperture estimation, the error caused by image resolution is about  $\pm 200\ \mu\text{m}$ .

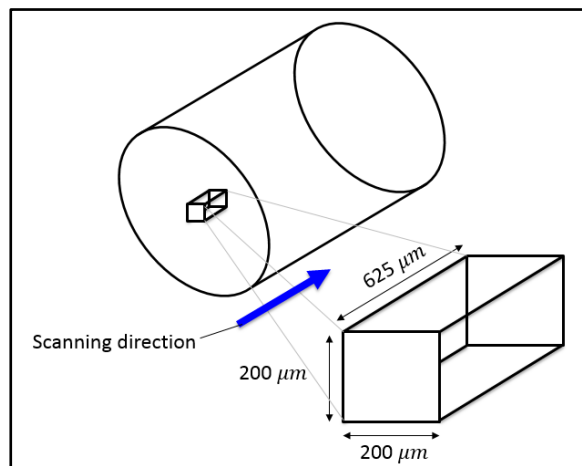


Figure 6-34 : Diagram showing the resolution of CT images in the scanning direction.

### 6.5.2 Deformations during fracture closure

Images of the fracture walls after performing fracture closure experiments showed evidence of some plastic deformations in a form of proppant embedment impressions. Elastic deformation is recoverable where the impressions confirm the existence of plastic deformations. It is important to understand the stress condition of the sample during fracture closure experiment to understand the type of deformations associated with this process. Stress at the interaction between proppant and sample is concentrated and higher than the confining pressure applied due to the difference in contact area. Considering a slice of the core, the force applied on the proppant by the sample,  $F$ , is equal to the reaction force generated by the proppant,  $F_R$  (Figure 6-35a). Thus, the stress at the contact is controlled by contact area between proppant and fracture wall.

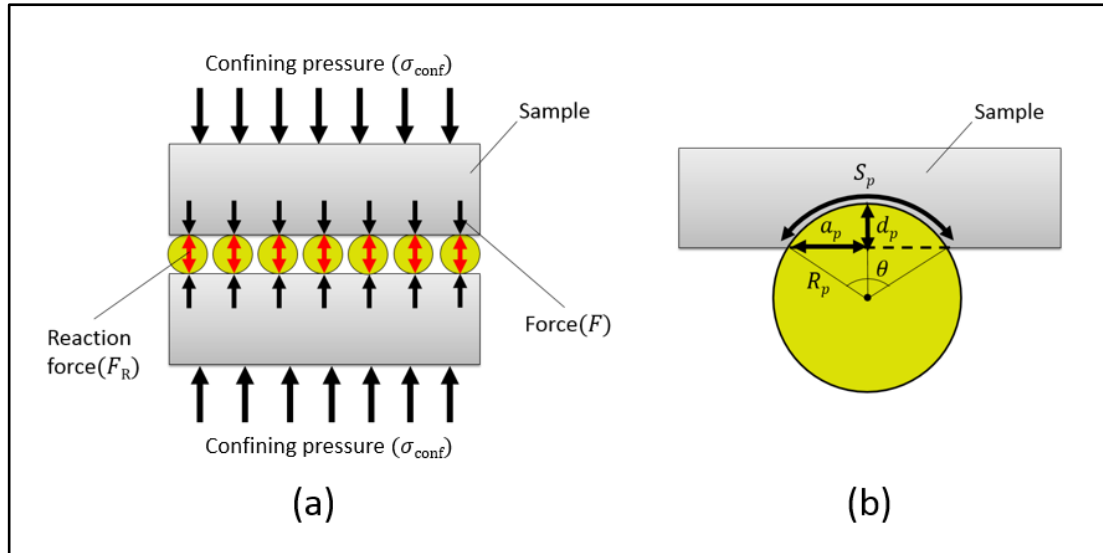


Figure 6-35: Diagram showing (a) forces associated with fracture closure and (b) parameters used to determine contact area between sample and proppant.

Considering one piece of proppant, the forces are balanced such that;

$$F = F_R \quad (6-5)$$

Stress is force per unit area, which makes the maximum stress at the proppant,  $\sigma_p$ , to be:

$$\sigma_p = \sigma_{conf} \frac{A_F}{N_p S_p} \quad (6-6)$$

Where  $A_F$  is area of the fracture wall ( $\text{mm}^2$ ),  $N_p$  is number of proppant and  $S_p$  is the area of the spherical cap of a single proppant particle in contact with fracture wall ( $\text{mm}^2$ ). The area of the spherical cap of a single proppant is calculated using geometry of proppant and embedment depth shown in Figure 6-35b. The equation given by (Polyanin and Manzhirov, 2006):

$$S_p = 2\pi R_p d_p \quad (6-7)$$

Where  $R_p$  is the radius of the proppant particle used and  $d_p$  is the depth of the embedment.

To understand the deformations, stress state at the proppant interface has to be calculated and compared against failure envelopes estimated in **Chapter 5**. Stress state was defined for the four samples (WS, KC, OC and D) as they are the only samples

which have triaxial test data available. Assuming the embedment depth values are close to real embedment, principal stresses are calculated using the stress at the proppant-sample interface. They are then used to calculate deviatoric and effective stresses which determine the stress state. All stresses calculated at each confining pressure step are presented in Table 6-25.

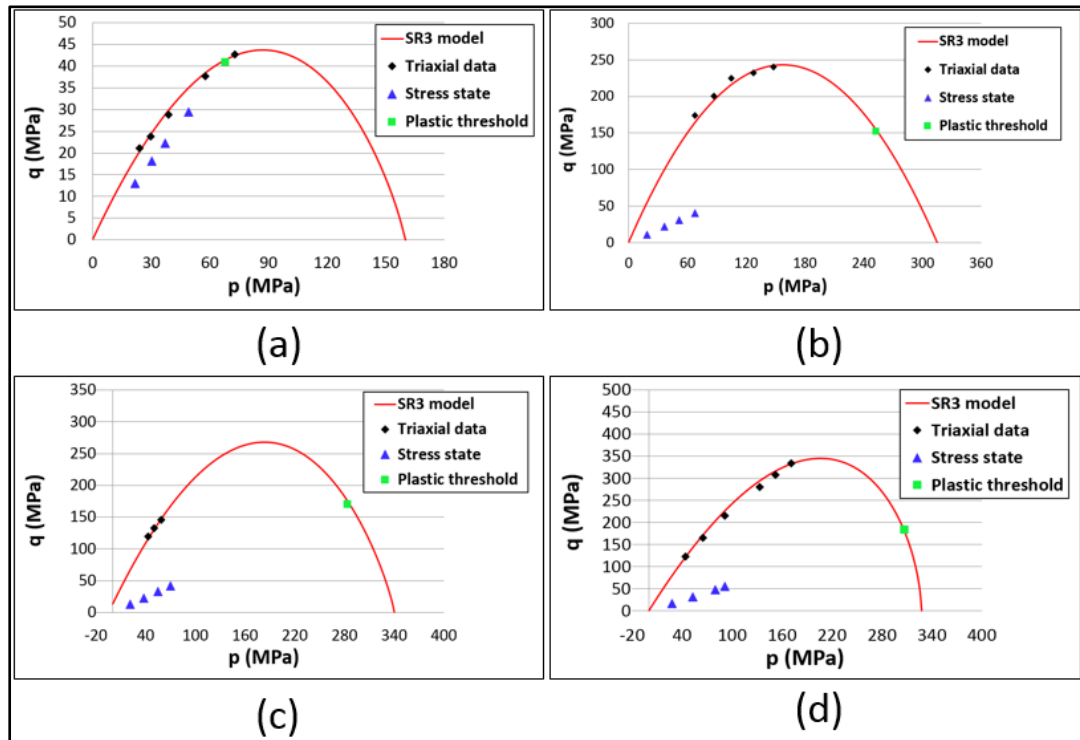


Figure 6-36: Failure envelope of (a) WS, (b) KC, (c) OC and (d) D samples with stress state (blue point) for all four confining pressure stages. Green points at which plastic deformation ends and elastic deformation begins.

Sample	Confining pressure (psi)	$\sigma_c = \sigma_1 = \sigma_2$ (MPa)	$\sigma_3 = 0.5 * \sigma_1$ (MPa)	$p$ (MPa)	$q$ (MPa)
WS	1000	26.1	13.0	21.7	13.0
	2000	36.4	18.2	30.3	18.2
	3000	44.5	22.2	37.1	22.2
	4000	58.9	29.4	49.1	29.4
KC	1000	22.6	11.3	18.8	11.3
	2000	43.6	21.8	36.3	21.8
	3000	61.8	30.9	51.5	30.9
	4000	81.3	40.7	67.8	40.7
OC	1000	25.3	12.6	21.1	12.6
	2000	45.1	22.6	37.6	22.6
	3000	65.8	32.9	54.8	32.9
	4000	84.3	42.1	70.2	42.1
D	1000	33.2	16.6	27.7	16.6
	2000	63.0	31.5	52.5	31.5
	3000	95.6	47.8	79.6	47.8
	4000	109.2	54.6	91.0	54.6

Table 6-25: Principal stresses calculated using stress calculated at the proppant-sample interface. Deviatoric and effective stresses are also estimated using calculated principal stresses.

Initially, when confining stress is applied and proppant started touching the fracture wall, contact area was very small, which made stress at the contact very high thus deformation occurred in the plastic region. Plastic deformations in the form of proppant embedment took place causing an increase in the contact area, which in return reduced stress at the interface and pushed the stress state to the elastic region. The stress state at which the deformations change from plastic to elastic is marked as “plastic threshold” in Figure 6-36. The proppant embedment depths corresponding to the plastic threshold stress state for the four samples are shown in Table 6-26, which are relatively small compared to embedment depths obtained by experiments. This suggests that there are other mechanisms inducing fracture closure in proppant packed fracture.

Sample	$p$ (MPa)	$q$ (MPa)	$d_p$ (mm)
WS	68.1	40.8	2.8 E-02
KC	252.9	151.7	1.0 E-02
OC	283.5	170.1	9.1 E-03
D	306.8	184.1	8.5 E-03

*Table 6-26: Plastic threshold stress state and plastic proppant embedment depth associated with it for all four samples.*

Failure envelopes presented above are subjected to uncertainties in terms of mechanical strength. Samples are initially saturated with water and fracture conductivity is measured by flowing water through the fracture. Water saturation has a great impact on reducing mechanical strength of shale as it was shown earlier (e.g. Zhang et al., 2017; Corapcioglu et al., 2014). To investigate the effect of water saturation, preconsolidation pressure was reduced by 50% and 75%, which will reduce rock strength as it is shown in Figure 6-37 and Figure 6-38. As can be seen for the soft sample, WS, reducing preconsolidation pressure by 50% and 75% will result in plastic deformations on fracture walls. These deformations contributed in the large strains associated with fracture closure. On the other hand, stiff samples did not show any possibility of undergoing plastic deformation even when preconsolidation pressure was reduced by 75%. This suggests that deformations associated with fracture closure are elastic. The plastic threshold was estimated for all failure envelopes with reduced preconsolidation pressure. The corresponding embedment depths are shown in Table 6-27 and Table 6-28 for 50% and 75% reduced preconsolidation pressure respectively. The estimated depth is still quite low which agrees the previous findings.

Sample	$p$ (MPa)	$q$ (MPa)	$d_p$ (mm)
WS	34.7	20.8	5.4 E-02
KC	127.3	76.4	1.5 E-02
OC	144.0	86.4	1.3 E-02
D	153.4	92.0	1.2 E-02

*Table 6-27: Plastic threshold stress state and plastic proppant embedment depth associated with it for all four samples at a reduced preconsolidation pressure by 50%.*

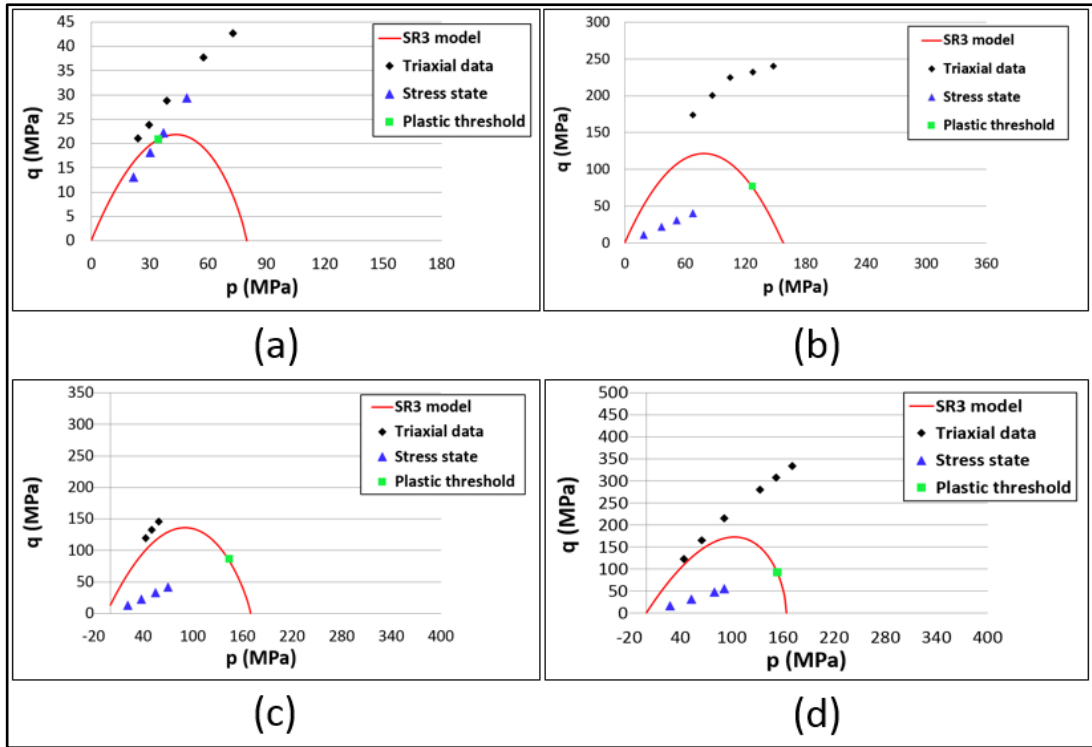


Figure 6-37: Failure envelope of (a) WS, (b) KC, (c) OC and (d) D samples with stress state (blue point) for all four confining pressure stages. Preconsolidation pressure was reduced by 50% for all samples.

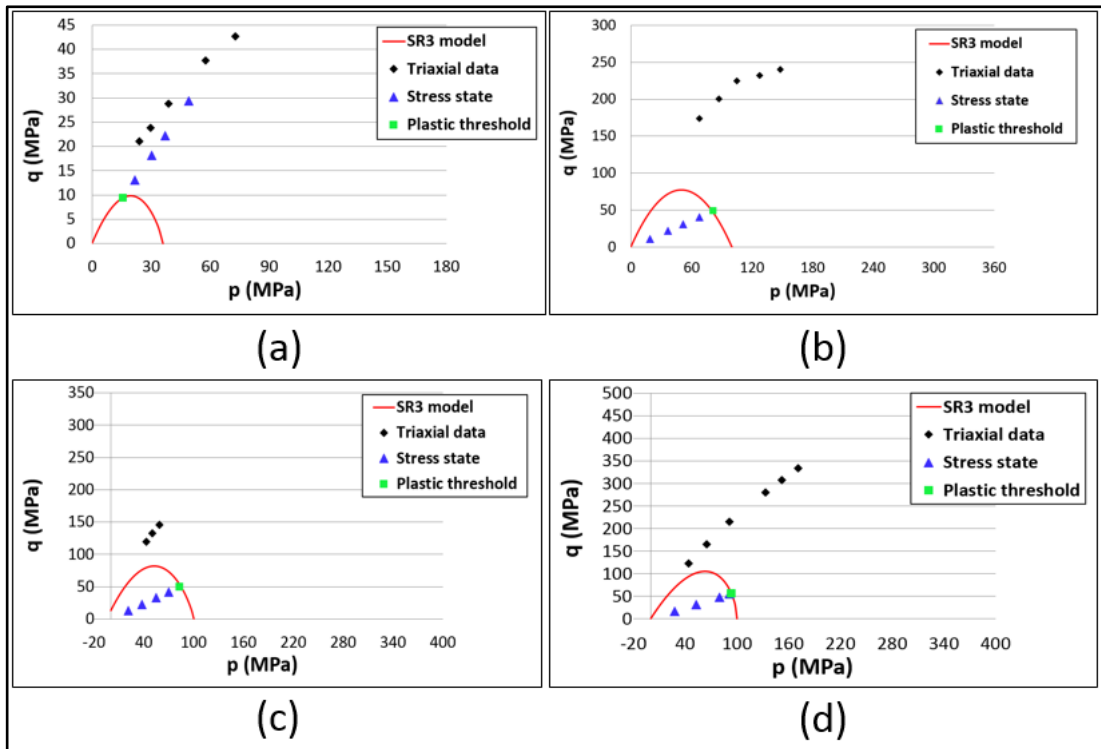


Figure 6-38: Failure envelope of (a) WS, (b) KC, (c) OC and (d) D samples with stress state (blue point) for all four confining pressure stages. Preconsolidation pressure was reduced by 75% for all samples.

Sample	$p$ (MPa)	$q$ (MPa)	$d_p$ (mm)
WS	15.6	9.4	1.20E-01
KC	81.4	48.8	2.3 E-02
OC	83.2	49.9	2.3 E-02
D	93.6	56.1	2.0 E-02

*Table 6-28: Plastic threshold stress state and plastic proppant embedment depth associated with it for all four samples at a reduced preconsolidation pressure by 75%.*

Fracture closure results were compared against fracture closure models that takes into account the three factors; Stress, fracture morphology and elastic properties. Figure 6-39 presents a comparison plot between experimental results and fracture closure model introduced by Duan et al. (2000). The parameters used in the model for all samples are listed in Table 6-29. Young's modulus values used are the ones obtained by microindentation and Poisson's ratio for all samples is assumed to be 0.25 as the model is not sensitive to change in Poisson's ratio. There is a variation between model results and experimental results. The comparison between results suggests that samples underwent larger closure at lower confining pressures than the one predicted by the model. Error in experimental results of embedment could be the reason of this variation.

Duan et al. (2000) suggested that fracture morphology ratio ( $\zeta$ ) has a value in the order of ( $10^{-2}$ ). However, the values estimated for all samples are in the order of ( $10^{-3}$ ) because the variation in surface morphology is large due to the size of proppant (Table 6-29). In addition, the samples were prepared such that the proppant packed fractures have the same fracture morphology. However, results showed some variation in fracture morphology ratio. Again, the accuracy of the experimental embedment depth plays a role in this variation.

The fracture closure model proposed by Duan et al. (2000) does not take time dependent deformation into account. Regardless of the accuracy of proppant depth data, the behaviour of the model suggests that embedment increases with increasing confining pressure. This behaviour is observed in experimental results of soft samples while stiff samples behaved quite differently. For the stiff, most of the embedment occurred at low confining stress and then embedment was very less at higher stresses.



This suggests that the variation between model and experimental data might be caused by time –related plastic deformation.

Sample	E (GPa)	$\nu$	$\zeta$
WS	11.1	0.25	0.0020
ALP	11.6	0.25	0.0018
AM	24.0	0.25	0.0012
KC	29.3	0.25	0.0015
OC	29.7	0.25	0.0018
D	57.6	0.25	0.0017

Table 6-29: Summary of parameters for all samples used in (Duan et al., 2000) to estimate fracture closure.

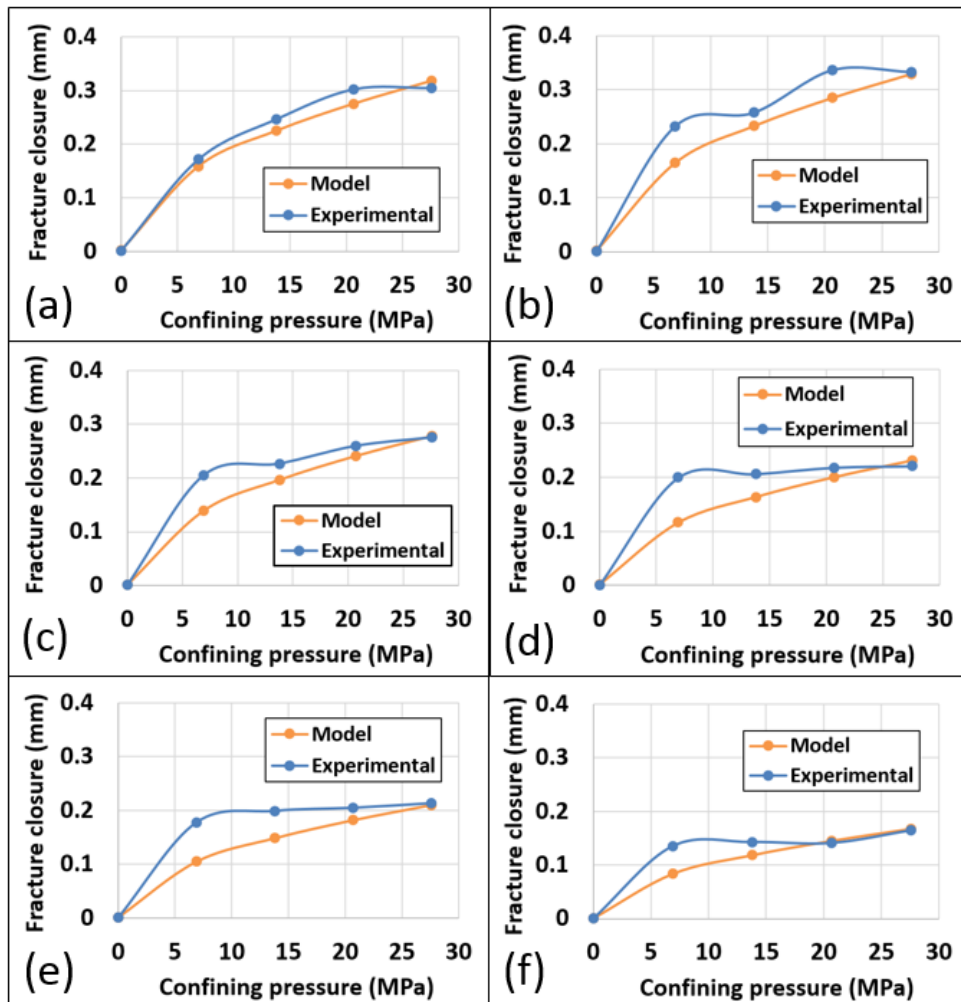


Figure 6-39: Fracture closure experimental results compared with fracture closure model suggested by (Duan et al., 2000) for (a) WS, (b) ALP, (c) AM, (d) KC, (e) OC and (f) D samples.

Time had a great impact as it was observed in fracture closure experiment results shown earlier. Creep deformation is a time-dependent deformation that could occur at stresses lower than the strength of the sample. Recalling the Burger body creep model (equation (2-64));

$$\varepsilon_1(t) = \frac{2\sigma_1}{9K} + \frac{\sigma_1}{3G_2} + \frac{\sigma_1}{3G_1} - \frac{\sigma_1}{3G_1} e^{-\left(\frac{G_1 t}{\eta_1}\right)} + \frac{\sigma_1}{3\eta_2} t \quad (6-8)$$

Where:  $\varepsilon$  is the strain  $\sigma$  is the maximum principle stress,  $G_1$  and  $G_2$  are shear moduli,  $\eta_1$  and  $\eta_2$  are viscosity parameters,  $t$  is time and  $K$  is bulk modulus such that:

$$K = E/3(1 - 2\nu) \quad (6-9)$$

$$G = E/2(1 + \nu) \quad (6-10)$$

Where  $E$  and  $\nu$  are Young's modulus and Poisson's ratio respectively.

It can be seen from Burger creep model that creep strain is directly proportional to stress. As bulk modulus and shear modulus are directly proportional to Young's modulus, creep strain is inversely proportional to Young's modulus. This means that creep strain increases with increasing stress and reduces with increasing Young's modulus. The logarithmic behaviour of creep is controlled by the exponential term in the model. The exponential term is a function of Young's modulus, viscosity parameter (which are basically the material properties of the rock) and time. This means that the logarithmic behaviour is independent of stress and is just a function of material properties of the rock.

The Burger creep model was simulated for various Young's modulus and stresses while fixing the other parameters, time, viscosity parameters and Poisson's ratio. It was found that increasing Young's modulus will decrease the magnitude of creep strain. In addition, increasing Young's modulus would reduce the time required for creep strain to plateau. To summarize, increasing Young's modulus will reduce creep strain in both magnitude and logarithmic behaviour as it is shown in Figure 6-40. On the other hand, increasing stress will increase creep strain magnitude but it will not have any effect on its logarithmic behaviour.

Time is the most important factor controlling creep process. Time appears in the Burger body model in two terms; the exponential term and direct proportionality

term. For a given material with known material properties subjected to a constant stress, creep strain initially behaves logarithmically under the effect of the exponential term (Figure 6-40). At early stages of the process, the proportional term is small and its effect is negligible. As time increases, exponential term becomes very small and proportional term increases. This explains the straight line behaviour observed on the other part of the curve shown in Figure 6-40.

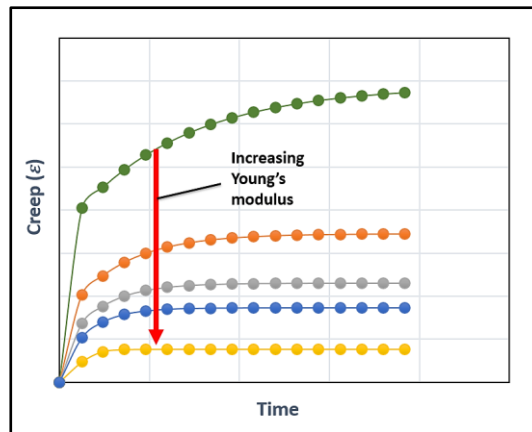


Figure 6-40: Plot of Burger body creep model for various Young's modulus. Red arrow indicates the direction of increasing Young's modulus.

The Burger body creep model was used to model creep deformation within fracture walls of the sample. To model creep deformation with time, a knowledge of daily fracture aperture change with time is required. However, fracture aperture was calculated using CT images, which were taken at the end of every stage. A relationship between final average conductivity at the end of every stage and fracture aperture was developed and presented in Figure 6-41. This relationship was then used to estimate daily aperture change using daily fracture conductivity measurements.

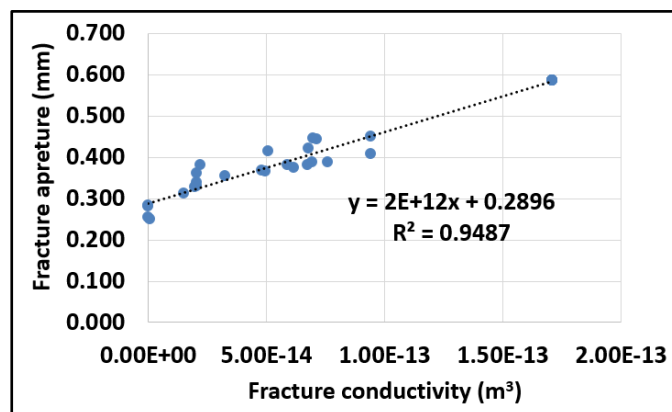


Figure 6-41: Fracture conductivity and fracture aperture relationship using experimental data.

Experimental fracture closure occurs under the influence of elastic and plastic deformations. To study the effect of creep, which is a plastic deformation, both deformations has to be decoupled. Elastic deformation will occur instantly as soon as the stress is applied. Fracture conductivity measurement was taken instantly after loading the sample to capture elastic deformation. The corresponding fracture closure to elastic deformation was then deducted from total fracture aperture reduction.

Creep parameters were estimated using elastic properties and approximations using published data. The  $K$  and  $G_2$  were estimated using equations (6-9) and (6-10) respectively using elastic properties. The stress used is the stress at the proppant-sample interface calculated earlier. Goodman (1980) suggested that for limestone,  $\eta_1$  and  $\eta_2$  are in the order of ( $10^7$  psi/min) and ( $10^9$  psi/min) respectively. At 1000 psi confining pressure, the values of  $\eta_1$  and  $\eta_2$  that provided a good fit with experimental data for all samples are (6 E+06 psi/min) and (5 E+09 psi/min) respectively. The parameter  $G_1$  showed dependency on stress for the limestone sample and the variation decreases with increasing stress (Goodman, 1980). The Burger body model parameters used to fit experimental data for all samples are shown in Table 6-30. The results for all samples are shown in Figure 6-42 to Figure 6-45.

Sample	$K$ (psi)	$G_2$ (psi)	$G_1$ (psi)
WS	1.07 E+06	6.44 E+05	6.80 E+03
KC	2.83 E+06	1.70 E+06	6.80 E+03
OC	2.87 E+06	1.72 E+06	6.50 E+03
D	5.57 E+06	3.34E+06	8.80 E+03

*Table 6-30: Parameters of the Burger body creep model used to fit experimental data at 1000 psi confining pressure.*

Considering all the errors in measuring fracture aperture using CT scanner and estimation of daily fracture closure using these data, the general behaviour of creep deformation agrees with above observations made from simulation. Regardless of the amount of fracture closure by creep, most of the creep deformations occurred at low stresses. The soft sample underwent creep in the first two confining pressure stages. The rest three stiff samples (KC, OC and D) underwent creep during the first stage.

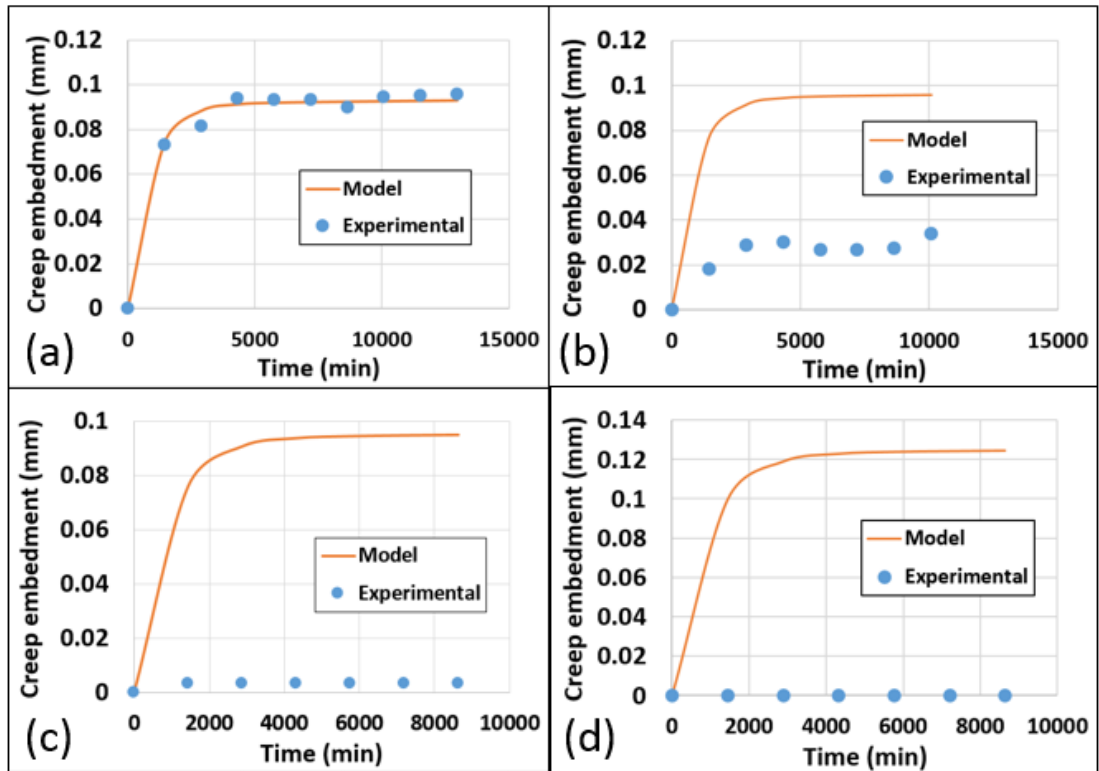


Figure 6-42: Creep model results against experimental plastic deformation data for WS sample at (a) 1000 psi, (b) 2000 psi, (c) 3000 psi and (d) 4000 psi confining pressure.

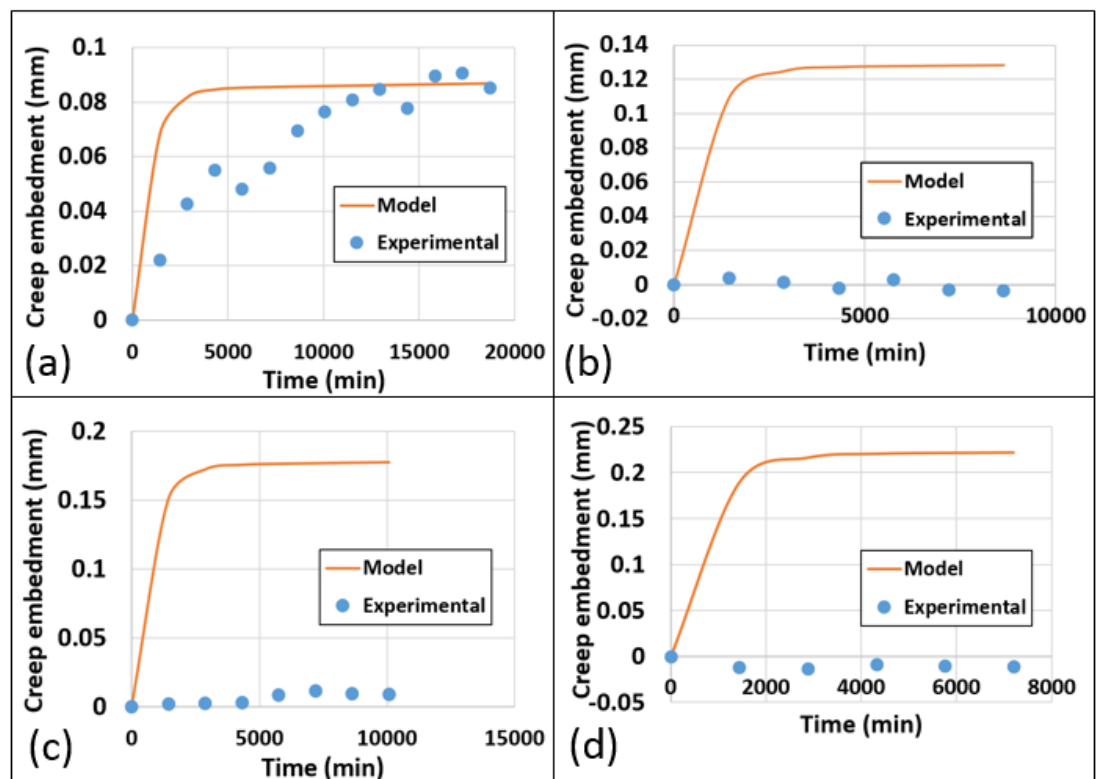


Figure 6-43: Creep model results against experimental plastic deformation data for KC sample at (a) 1000 psi, (b) 2000 psi, (c) 3000 psi and (d) 4000 psi confining pressure.

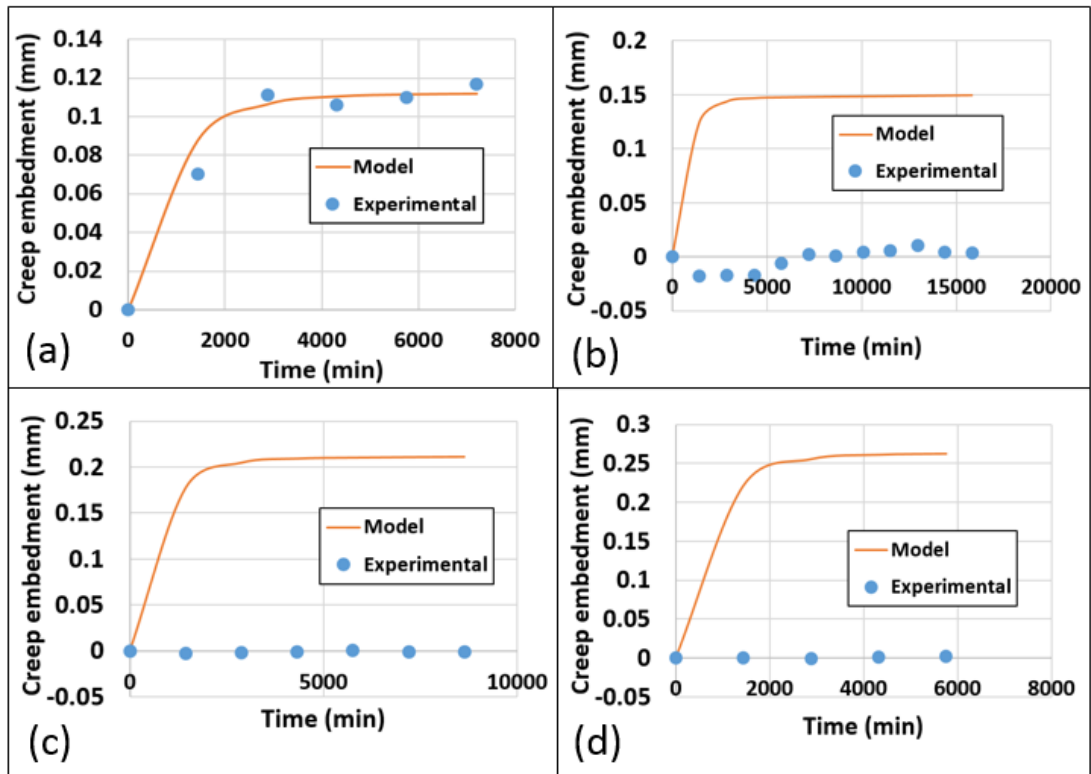


Figure 6-44: Creep model results against experimental plastic deformation data for OC sample at (a) 1000 psi, (b) 2000 psi, (c) 3000 psi and (d) 4000 psi confining pressure.

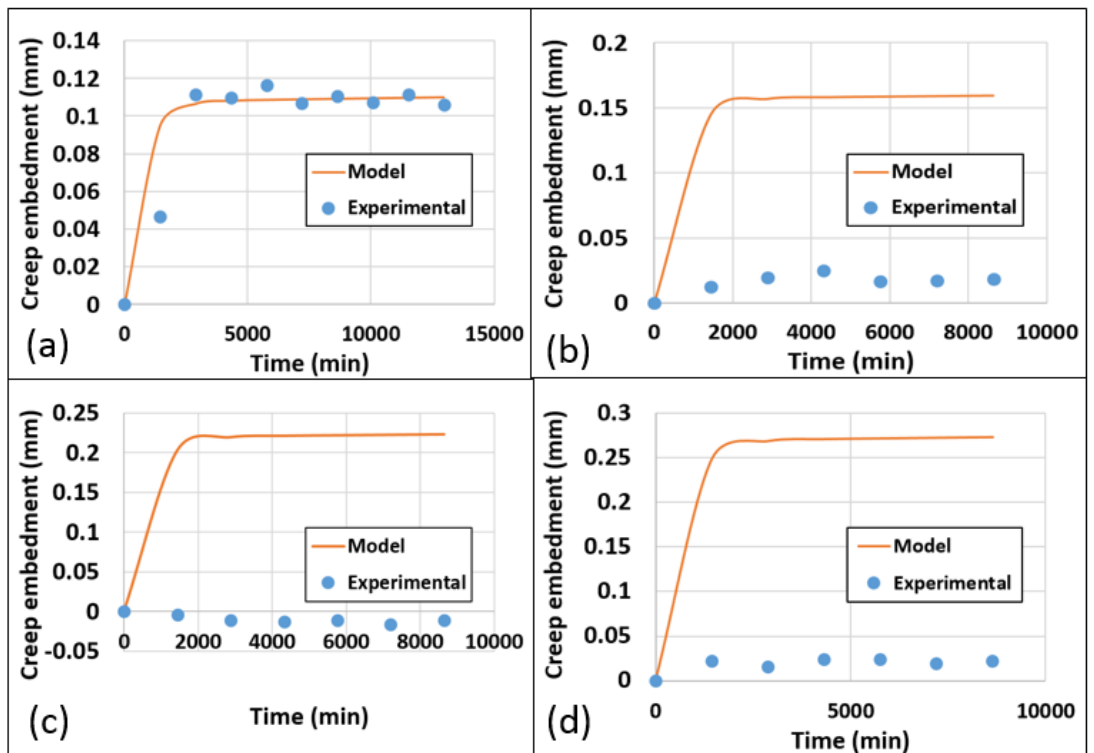


Figure 6-45: Creep model results against experimental plastic deformation data for D sample at (a) 1000 psi, (b) 2000 psi, (c) 3000 psi and (d) 4000 psi confining pressure.

The observations made from the simulations of the Burger creep model agrees with observation made from modelling and experimental results. The soft sample (WS) with high porosity and high clay content took about 5,000 minutes to stabilize at 1,000 psi confining pressure. On the other hand, the stiff samples (all except KC) took 50% less time to stabilize at same confining pressure. The magnitude of creep deformation at 1,000 psi for all sample was very similar cannot be used in the arguments due to error involved in calculating fracture aperture.

Decoupling elastic and plastic deformations suggests that for WS sample did not undergo any plastic deformations at confining pressures above 2,000 psi. However, conductivity measurement showed drastic reduction at stresses higher than 2,000 psi for the same sample. This suggests that WS sample underwent plastic failure above 2,000 psi confining pressure but not in a form of creep deformation. On the other hand, stiff samples showed no plastic above 1,000 psi which is similar to the fracture conductivity behaviour which showed very less changes in fracture properties above 2,000 psi.

From the above discussion, it can be suggested that deformations associated with fracture closure are elastic and plastic (in form of creep or ductile failure). Elastic and creep does contribute in fracture closure but their effect is relative small compared to ductile deformation. Fractures present in soft material are likely to close and self-seal under sufficient stress to cause ductile deformation. On the other hand, fractures in stiff materials are less likely to close and will remain open even when is subjected to very high stresses. The soft materials tend to have high porosity and clay content (which are directly related to Young's modulus) and the stiff materials tend to have low porosity and lower clay content. This suggests that porosity and clay content play a major role in controlling fracture closure in shale.

There are few fracture conductivity measurements available in the literature that allowed some time for the fracture to stabilize under the application of stress. Iriarte (2017) and Hejazy (2016) conducted fracture closure experiment on shale samples from Niobrara formation and Vaca Muerta formations respectively. Fractures in the studied samples were created using the Brazilian test and packed with a single layer of proppant similar to the samples tested in this thesis. The samples were kept under pressure for a period of 3 days at each confining pressure stage. Figure 6-46

presents the results of fracture conductivity normalized to the initial conductivity at each confining pressure stage. The behaviour was very similar to the samples tests in this thesis as most of fracture closure occurred at low stresses causing fracture conductivity to reach to a final value at low stresses. It can be seen that our samples settled to a final conductivity value at lower stress than Iriarte (2017) and Hejazy (2016) samples because the testing time per stage was higher, allowing fracture conductivity to stabilize at lower stress. This suggests that creep does actually occur during fracture closure process. The deformations will continue with time until it reaches equilibrium. The state of equilibrium is achieved when the contact area between proppant particles and fracture wall increases and reaches equilibrium.

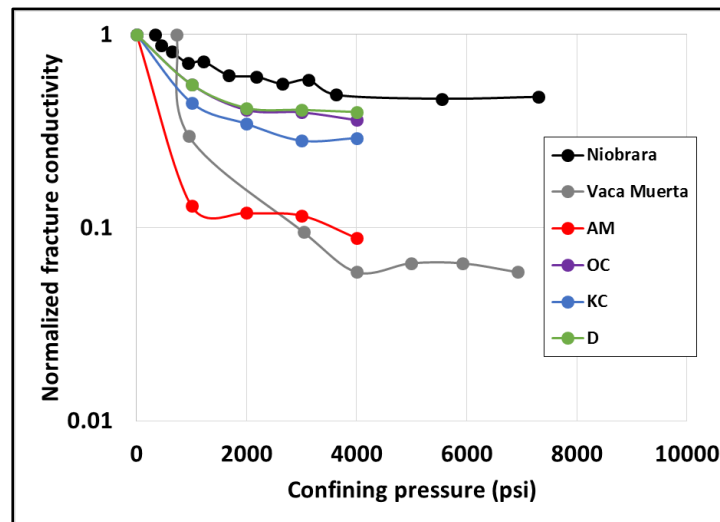


Figure 6-46: Normalized fracture conductivity at different confining pressure stages for Niobrara and Vaca Muerta samples (Iriarte, 2017; Hejazy, 2016) compared to samples tested in this thesis.

Alramahi and Sundberg (2012) conducted fracture conductivity test in proppant packed fracture. In this experiment, fracture conductivity continuously reduced throughout the stages as it is shown Figure 6-47. Looking at this data, the conclusion that could be made is that fracture conductivity will continuously reduce with stress. However, the samples were not kept for long enough time for creep deformation to take place and stabilize. Time effect was also observed when results were compared with data from Cho et al. (2013) who conducted fracture closure experiment on a shale samples from Bakken formation. The experiment was done on core sample with a natural fracture along the sample. Similar observation was made



and deformations during fracture closure was not given enough time to stabilize (Figure 6-48).

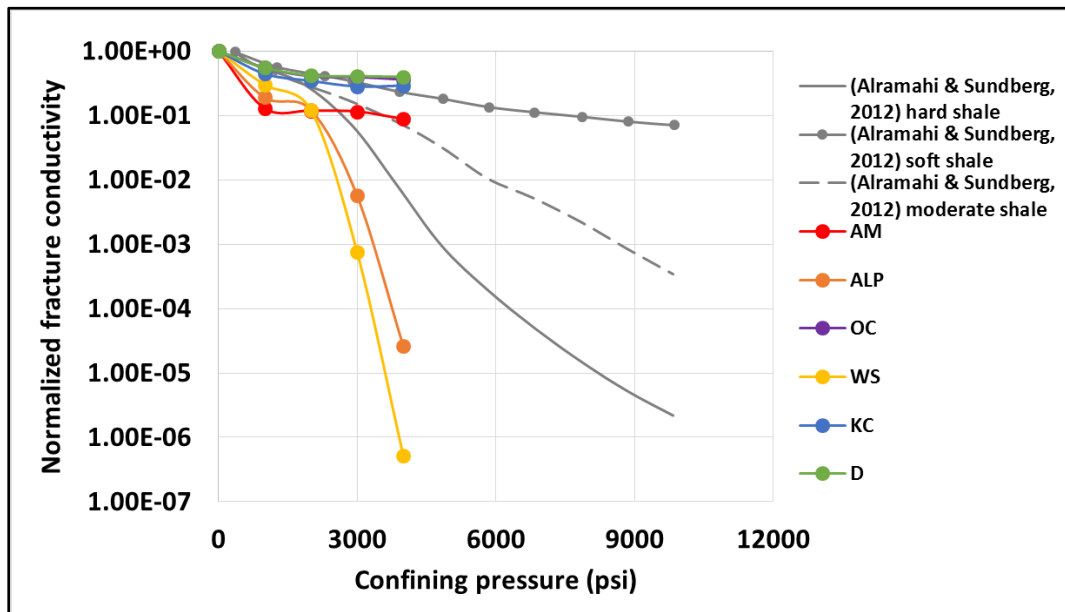


Figure 6-47: Normalized fracture conductivity at different confining pressure stages for different shale rocks (Alramahi and Sundberg, 2012) compared to samples tested in this thesis.

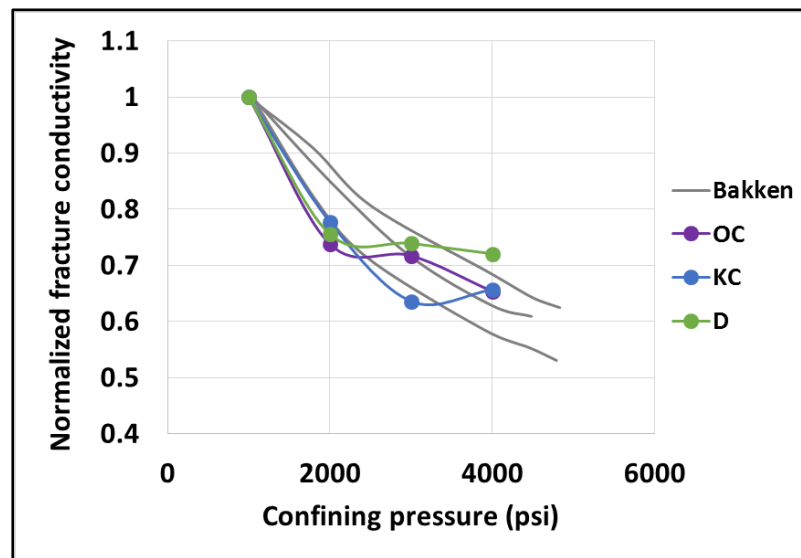


Figure 6-48: Normalized fracture conductivity at different confining pressure stages for different shale rocks (Cho et al., 2013) compared to samples tested in this thesis.

### 6.5.3 Fracture permeability estimation

Fracture conductivity of each sample was measured daily during fracture closure experiments. Fracture conductivity is relatively easy to measure using the setup adopted in this experiment because it does not require a knowledge of fracture aperture as was shown in Equation 6-1 earlier. Measuring the permeability of fracture is challenging as it requires knowledge of fracture aperture. Fracture permeability,  $k_f$ , can be calculated using fracture conductivity by:

$$k_f = \frac{C_f}{W_f} \quad (6-11)$$

Where  $C_f$  is fracture conductivity and  $W_f$  is fracture aperture. However, in this experiment, fracture aperture was estimated using Avizo image processing of the CT images taken at the end of each stage. Fracture permeability is then calculated using fracture aperture estimated by Avizo for all samples.

Knowledge of fracture permeability will lead to estimation of fracture aperture using commonly used fracture models in the industry. The most commonly used fracture model in oil and gas industry is a parallel plate model known as “cubic law” (Witherspoon et al., 1980). This model was developed based on the assumption that fracture walls are smooth parallel plates. The distance between these parallel plates is the fracture aperture as it is shown in Figure 6-49. This model provides a relationship between fracture permeability and fracture aperture. The model is given by:

$$k = \frac{h^2}{12} \quad (6-12)$$

Where  $k$  is permeability in  $m^2$  and  $h$  is fracture aperture in m. Permeability and cubic law calculations are shown in Table 6-31.

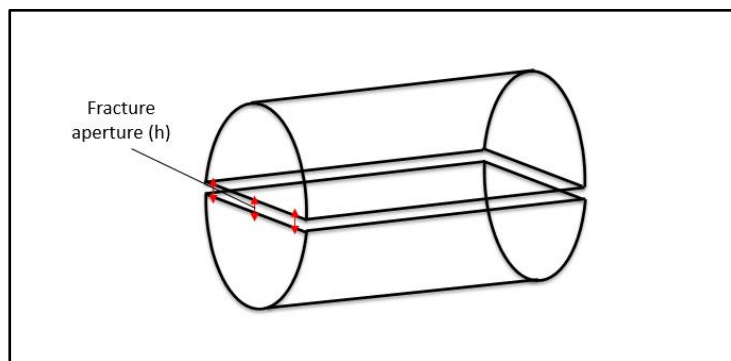


Figure 6-49: Diagram explaining cubic law.

Sample	Confining	Permeability (m2)	Permeability (D)	h (μm)
WS	0	2.91 E-10	295	59
	1000	1.23 E-10	124	39
	2000	6.09 E-11	62	27
	3000	4.55 E-13	0.46	2.35
	4000	3.10 E-16	3.14 E-04	6.14 E-02
ALP	0	2.91 E-10	295	59
	1000	9.16 E-11	93	33
	2000	6.28 E-11	64	28
	3000	3.84 E-12	3.89	6.83
	4000	1.74 E-14	1.76 E-02	4.60 E-01
AM	0	2.91 E-10	295	59
	1000	5.77 E-11	58	26
	2000	5.64 E-11	57	26
	3000	6.02 E-11	61	27
	4000	4.83 E-11	49	24
KC	0	2.91 E-10	295	59
	1000	1.95 E-10	198	49
	2000	1.54 E-10	157	43
	3000	1.31 E-10	132	40
	4000	1.36 E-10	138	41
OC	0	2.91 E-10	295	59
	1000	2.30 E-10	233	53
	2000	1.79 E-10	181	47
	3000	1.77 E-10	179	46
	4000	1.65 E-10	167	45
D	0	2.91 E-10	295	59
	1000	2.08 E-10	211	50
	2000	1.60 E-10	162	44
	3000	1.56 E-10	158	44
	4000	1.61 E-10	163	44

*Table 6-31: Fracture permeability calculated using fracture conductivity at each stage for all samples. Fracture aperture calculated using cubic law, h, is also presented table.*

Fracture conductivity normalized to initial conductivity correlates well with normalized permeability calculated using fracture conductivity and fracture aperture obtained from Avizo simulations (Figure 6-50). This suggests that for a measured fracture conductivity, permeability could be estimated using the relation provided in Figure 6-50.

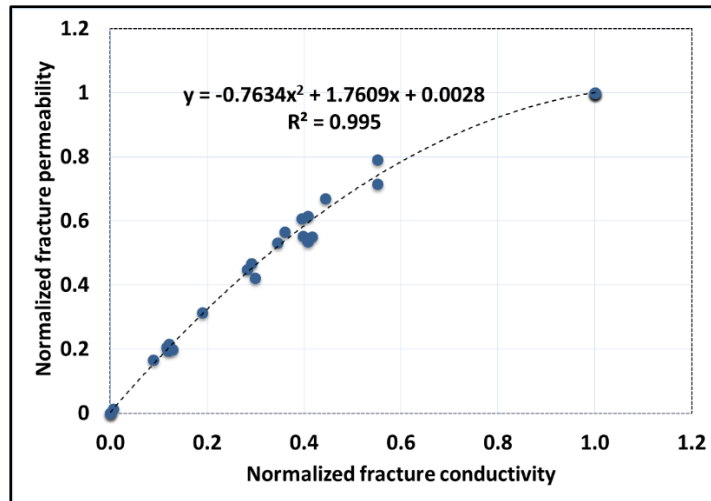


Figure 6-50: Correlation between normalized fracture conductivity with normalized fracture permeability of proppant packed fracture..

#### 6.5.4 Importance of geomechanical properties in controlling fracture closure

Geomechanical properties plays a big role in controlling fracture closure in shale rocks as they determine rock's strength. Soft rocks tend to have low Young's modulus whereas stiff rocks tend to have high Young's modulus. Samples with relatively low Young's modulus underwent large reduction in permeability during all confining pressure stages. These samples showed a potential of further closure if the confining stress was increased further as it was shown in (Figure 6-47). Soft samples could also experience ductile deformation in fracture walls, which will strongly contribute in fracture closure as it was shown earlier. On the other hand, samples with large Young's modulus had significantly less fracture closure and hence less reduction in fracture conductivity. Fracture closure in samples with high Young's modulus tended to plateau at a final value even if confining pressure is increased further.

Aramahi and Sundberg (2012) performed proppant embedment test on shale samples using a hydraulic ram. A power-law correlation between proppant embedment and Young's modulus was developed using embedment test results shown in Figure 6-51. In the thesis, proppant embedment will represent fracture closure, which also showed a correlation with Young's modulus using a power-law function and followed the same trend as Aramahi and Sundberg (2012) data. The same observation was made and samples with relatively low Young's modulus experience large proppant embedment whereas stiff samples experience very minimum

embedment. These results suggest that for a given reservoir fractured shale caprock, chances for complete fracture closure and re-seal under reservoir conditions for soft shale rocks ( $E < 20$  GPa) are higher under the effect of stress. On the other hand, fractures in soft shale rocks ( $E > 20$  GPa) will not close completely and will remain open and even if the stress increases and will only close by mechanisms other than stress.

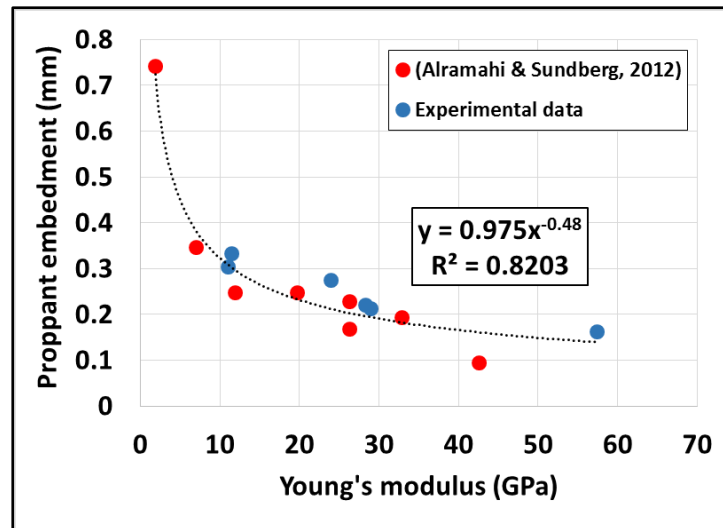


Figure 6-51: Correlation between measured proppant embedment at 5000 psi and static Young's Modulus measured from triaxial compression tests on vertical samples (Alramahi and Sundberg, 2012).

Mineralogy and porosity are strongly related to strength and elasticity of shale rock (Rybacki et al., 2014). Sone and Zoback (2013) presented a relationship between Clay and kerogen content and Young's modulus together with a relationship between clay content and porosity for different shale (Figure 6-52). Assessing the 20 GPa Young's modulus threshold presented earlier with Sone and Zoback (2013) results suggests that samples with porosity greater than 5% and clay and kerogen content (vol %) higher than 25% have high probability of fracture closure and re-seal at in situ condition. Similarly, samples with porosity less than 5% will have their fractures open unless it has large amount of clay and kerogen content (above 80%).

The correlation between and porosity presented in **Chapter 3** was also highlight the importance of porosity in controlling fracture closure. The unconfined compressive strength data was converted to Young's modulus values using the following relationship (Chang et al., 2006):

$$E = \left(\frac{UCS}{7.22}\right)^{1/0.712} \quad (6-13)$$

where  $E$  is in (GPa) and UCS in (MPa). The new correlation is presented in Figure 6-53 which agrees with observations made earlier. It can be clearly seen that samples with porosity higher than 5% will have Young's modulus lower than 20 GPa, which will make them more susceptible to fracture closure and self-seal.

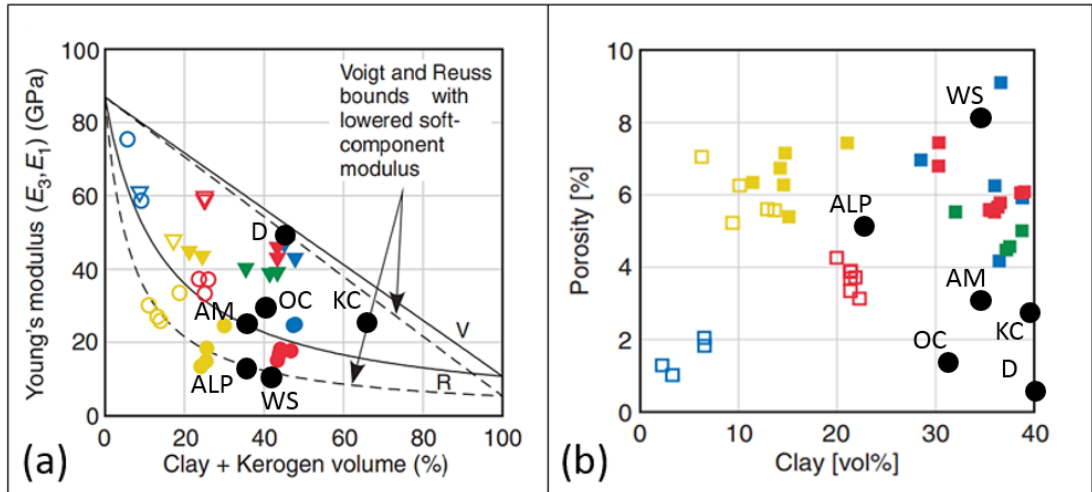


Figure 6-52: Relationship between (a) Clay plus kerogen content and Young's modulus; (b) Clay content and porosity for different shale samples (Sone and Zoback, 2013). The black points represent the samples used in this research.

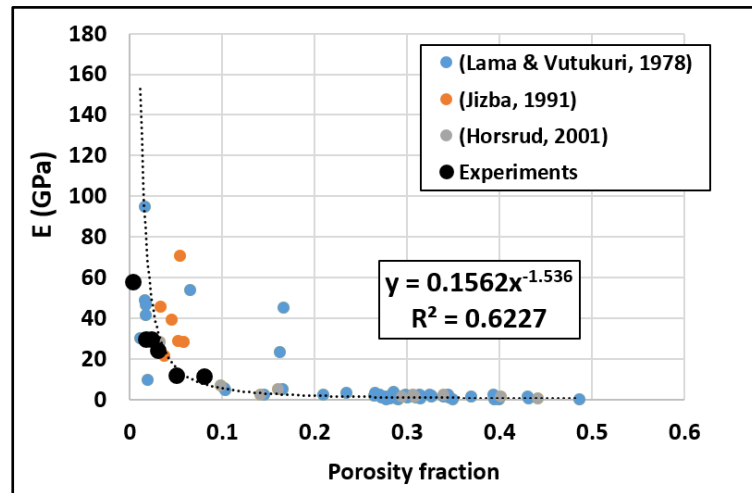


Figure 6-53: Correlation between Young's modulus and porosity after converting uniaxial compressive strength data presented by Chang et al. (2006) to Young's modulus values. Black points are for the samples tested in this thesis.

## 6.6 Conclusions

Understanding the controls on fracture closure is important as they may control fluid flow through tight rocks. An experimental investigation of fracture closure has been designed and conducted on a range of shale samples. Shale core plugs were cut into two halves longitudinally and packed with a single layer of proppant. The proppant in between the two fracture walls is assumed to represent fracture morphology. Samples with the artificial fracture were loaded into core holders and subjected to various stress conditions.

Stress was applied on the sample in stages from 1000 psi to 4000 psi in an increment of 1000 psi in each stage. Fracture conductivity was measured using the liquid steady-state method using water as the measurement fluid. At each confining pressure stage, the sample was kept under stress until fracture conductivity stabilized, which was in range of 4-13 days for all samples. Fracture conductivity measurement was done on a daily basis during all stages.

All shale samples underwent fracture closure throughout confining pressure stages. Soft samples, with relatively low Young's modulus, experienced larger fracture closure than stiff samples, with relatively high Young's modulus. In a single stage, fracture closure in soft samples took longer time to stabilize than stiff samples. This behaviour is due creep deformation experienced by the samples. Most of fracture conductivity reduction due to fracture closure occurred in the first two stages (1000 and 2000 psi). In the last two stages, soft samples continued to experience further fracture closure as fracture wall underwent ductile failure. The behaviour of stiff sample was completely different and fractures in them hardly experienced any closure in the last two stages. This observation suggested that fractures in soft shale rocks have a potential to close and re-seal under in situ conditions. On the other hand, once fractures in stiff shale rocks are formed, they will remain open and they will not re-seal again.

Fracture closure behaviour of soft and stiff samples described above was also observed when fracture closure results were compared with proppant embedment experiment results provided by Alramahi and Sundberg (2012). The results suggested that fractures in shale with a Young's modulus less than 20 GPa has the potential to close and re-seal unlike the ones in shale with Young's modulus higher than 20 GPa,

which will remain open and never re-seal. As strength of shale and its elasticity is related to the porosity and mineralogy of the rock, the corresponding porosity and clay content (Vol %) to 20 GPa elastic moduli is about 5% and 25% clay and kerogen content respectively. Fractures in shales with porosity higher than 5% and clay content higher than 25% have the potential to close and re-seal when the sufficient stress is present at in situ condition. On the other hand, fractures in shales with porosity lower than 5% will have their fracture open and never re-seal at in situ conditions unless large clay and kerogen content is present (80% and above).



## **7 Chapter VII: Finite element modelling of fracture closure in shale.**

### **7.1 Introduction**

Previous chapters have presented experimental work aimed at understanding key controls on fracture closure in shale. These experiments are extremely time-consuming and are limited to samples for which core plugs can be drilled; many shales are too weak to allow core plugs to be taken. Consequently, it is possible to only test the impact of a very limited range of material properties on fracture closure. Numerical modelling is therefore required to allow the results from these experiments to be extrapolated to shales with other material properties. To this end, the following chapter presents results from a series of finite-element based numerical models that were conducted with the aim of providing a more complete understanding of the key controls on the closure of fractures in the subsurface.

Most previous studies of fracture closure have concentrated on identifying empirical correlations that control fracture closure (e.g. joint roughness coefficient – Bandis et al., 1983) or conducting simple elastic models. It is, however, likely that shales also deform in a ductile manner by processes such as plastic deformation. The following chapter aims to take into account such deformation processes by using an elastoplastic constitutive relationship to model fracture closure in shale. The results are compared to both experimental data and the results of purely elastic models for fracture closure. All modelling was conducted using ELFEN, a general purpose finite-element code developed by Rockfield Global Solution Limited that contains a large library of material properties that are ideal for modelling shale deformation.

The proppant fracture closure samples presented in Chapter 6 can be modelled in 2D similar to the geometry shown in Figure 7-1-a. A series of 2D slices would form a 3D geometry shown in Figure 7-1-b. Since the 3D model is just series of repeated 2D slice, simulation result of 3D model would be the same as the 2D model. So for the sake of simplicity, a 2D geometry would be good enough to perform all the simulations planned. In this chapter, two modelling approaches were considered; the first was by considering only elastic deformation and allowing material to deform elastically while the second approach was to model the rock using elasto-plastic material definition which takes into account elastic and plastic deformations.

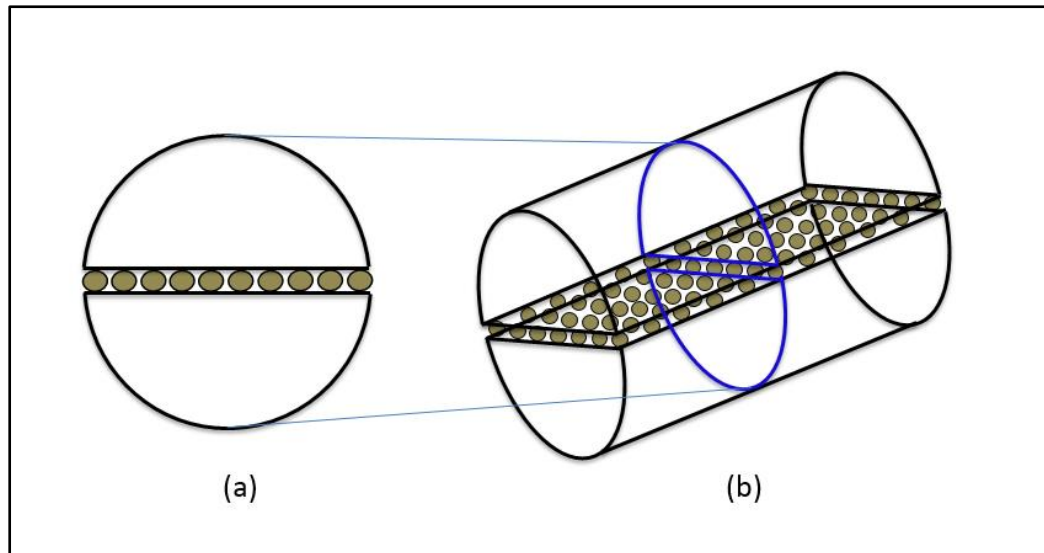


Figure 7-1: Exaggerated geometry of proppant fracture closure in (a) 2D (b) 3D.

## 7.2 Geometry description

The 2D geometry modelled for this simulation in ELFEN for FEM is shown in Figure 7-2. Proppant has spherical shape and thus proppant geometry was modelled as circular stiff objects. As the initial propped fracture had a width of 0.59 mm in Chapter 6, proppant was modelled as 0.59mm diameter circular geometries as it is shown in Figure 7-2. Face loading was applied around the sample to act as confining pressure at the outer surface of the core.

Movement constrains were applied to the geometry to ensure that deformation is similar to the actual experiment. The two pieces of the rock where constrained in x-direction movement and only allowed to move in y-direction. Proppant we fixed in plane in both x and y directions. All geometries were rotation constrains and not allowed to rotate around the z-axis. In addition, contact properties have to be defined properly to ensure that proppant contact with the rock is close to the real case. All contact properties were specified using the ELFEN user guide provided by Rockfield (Rockfield, 2014b).

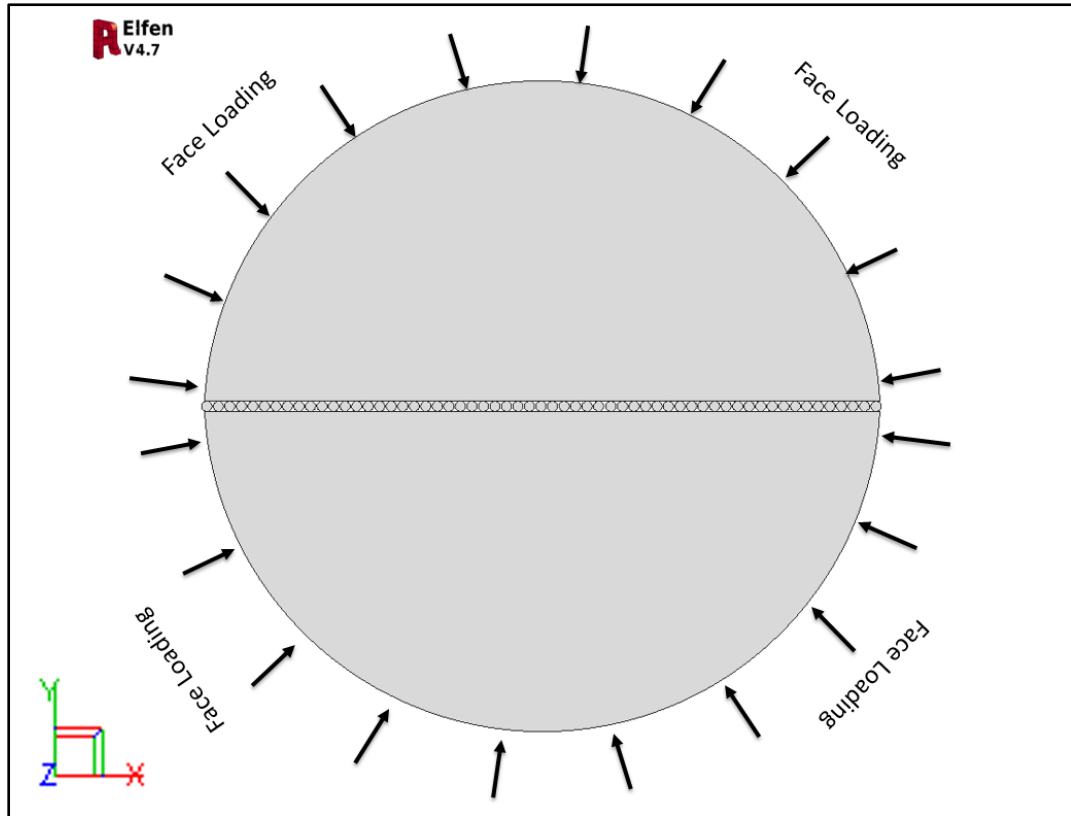


Figure 7-2: ELFEN 2D geometry of proppant fracture closure. The black arrows indicates the direction of the face loading applied.

### 7.3 Material Definition

ELFEN is capable of simulating elastic and elasto-plastic behaviour of rocks. For elastic simulation, the two basic elastic properties are required to define any material; Young's modulus ( $E$ ) and Poisson ratio ( $\nu$ ) together with material density ( $\rho$ ). In this thesis, Poisson's ratio and density will be held constant while Young's modulus will be varied to understand its importance in controlling elastic fracture closure.

ELFEN uses SR3 model explained earlier to define rock material for elasto-plastic simulation. The model is given by (Equation 2-39):

$$\Phi(\sigma, \varepsilon_v^p) = g(\theta, p) q + (p - p_t) \tan \beta \left( \frac{p - \sigma_c}{p_t - \sigma_c} \right)^{1/n}$$

ELFEN uses a material definition spreadsheet based on SR3 model called Geological Data Base (GEODB) to determine SR3 parameters and generate failure envelopes. This spread sheet is powerful and capable of determining SR3 parameters

and generating failure envelope using triaxial test. Triaxial data are analysed to produce  $(p, q)$  data that is used as reference to fit SR3 failure envelope. Fitting of SR3 failure envelope to triaxial  $(p, q)$  data is done by manipulating SR3 model parameters. When considering data from a conventional triaxial compression test (CTC), the constant  $\beta_0^\pi$  can be set to zero which will set the  $g(\theta, p)$  function to equal to 1.

For a given set of triaxial data, SR3 he parameters controlling the shape of the yield surface are listed in Table 7-1. All these parameters have to be manipulated realistically to fit the experimental data. Normally, when  $\sigma_c$  and  $p_t$  are not known (e.g. shale materials), four parameters have to be manipulated ( $\beta$ ,  $\sigma_c$ ,  $p_t$  and  $n$ ). This introduces a wide range of envelopes which can be far from reality as it was shown earlier.

Parameter	Comments
Tensile intercept ( $p_t$ )	It has less significance in defining failure envelope.
Preconsolidation pressure ( $\sigma_c$ )	Defines the size of the failure envelope.
Friction parameter ( $\beta$ )	Is a material constant that defines the shape and slightly the size of the failure envelope.
Exponent ( $n$ )	Is a material constant that defines the shape and slightly the size of the failure envelope.

Table 7-1: Inputs required to define a SR3 failure envelope based on a given tri-axial data.

As it is difficult to drill core cylinder of shale rocks, only four samples had tri-axial data (WS, KC, OC and D). Knowledge of  $\sigma_c$  will reduce the uncertainty in defining failure envelopes as it was shown in **Chapter 5**. Using the results of  $\sigma_c$  estimation provided in **Chapter 5**, the corresponding parameters that provide a good fit with triaxial data are shown in Table 7-2. All the failure envelopes generated for all samples using the parameters below are shown in Figure 7-3.

Sample	$\sigma_c$ (MPa)	$\beta$	$n$	$p_t$ (MPa)
WS	159.7	44.0	1.2	-0.1
OC	339.9	70.0	1.2	-5.0
KC	315.3	72.0	1.0	-0.1
D	327.6	71.5	1.7	-0.1

Table 7-2: Summary of SR3 model parameters for each samples.

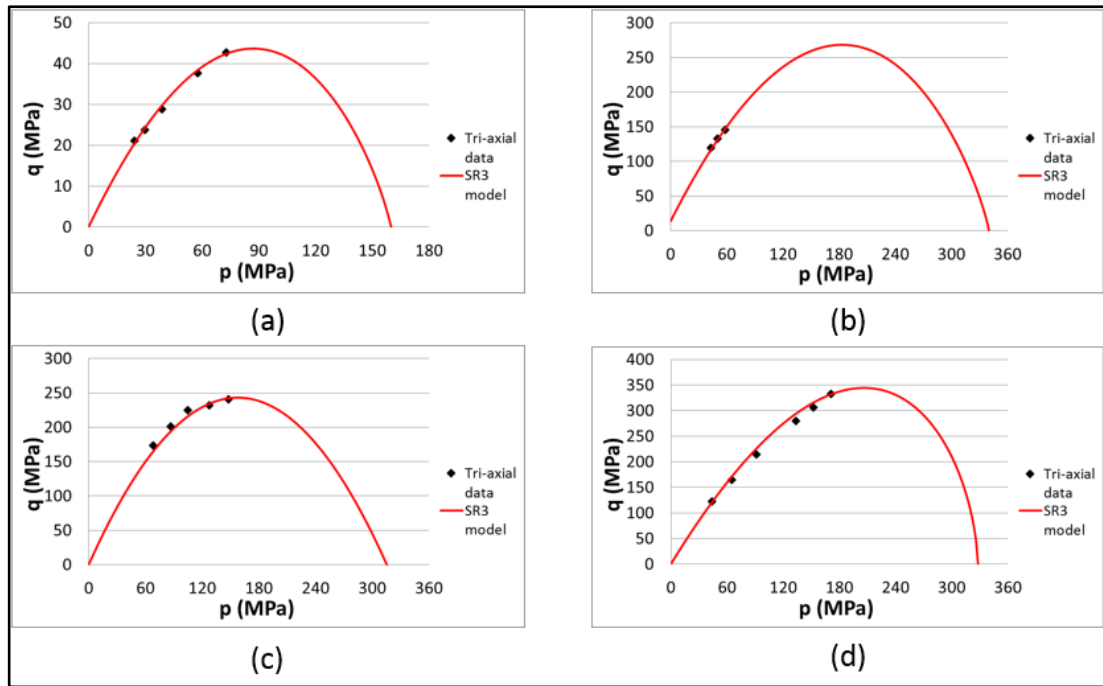


Figure 7-3: SR3 model failure envelope for (a) WS sample (b) OC sample (c) KC sample (d) D sample.

Conductivity measurement in fracture closure experiments presented in **Chapter 6** were done by flowing water through the fracture. Water saturation effects mechanical properties of shale dramatically as it was shown by several authors (e.g. Zhang et al., 2017; Corapcioglu et al., 2014). To understand this effect, several simulations runs were performed for the above described samples varying Young's modulus and preconsolidation pressure. Preconsolidation pressure was reduced by 70-80 % and Young's modulus was reduced by 25-50%. The mesh applied in this model is an unstructured mesh that divides the geometry into linear triangles elements. The mesh density used was 0.5 and shown in Figure 7-4.

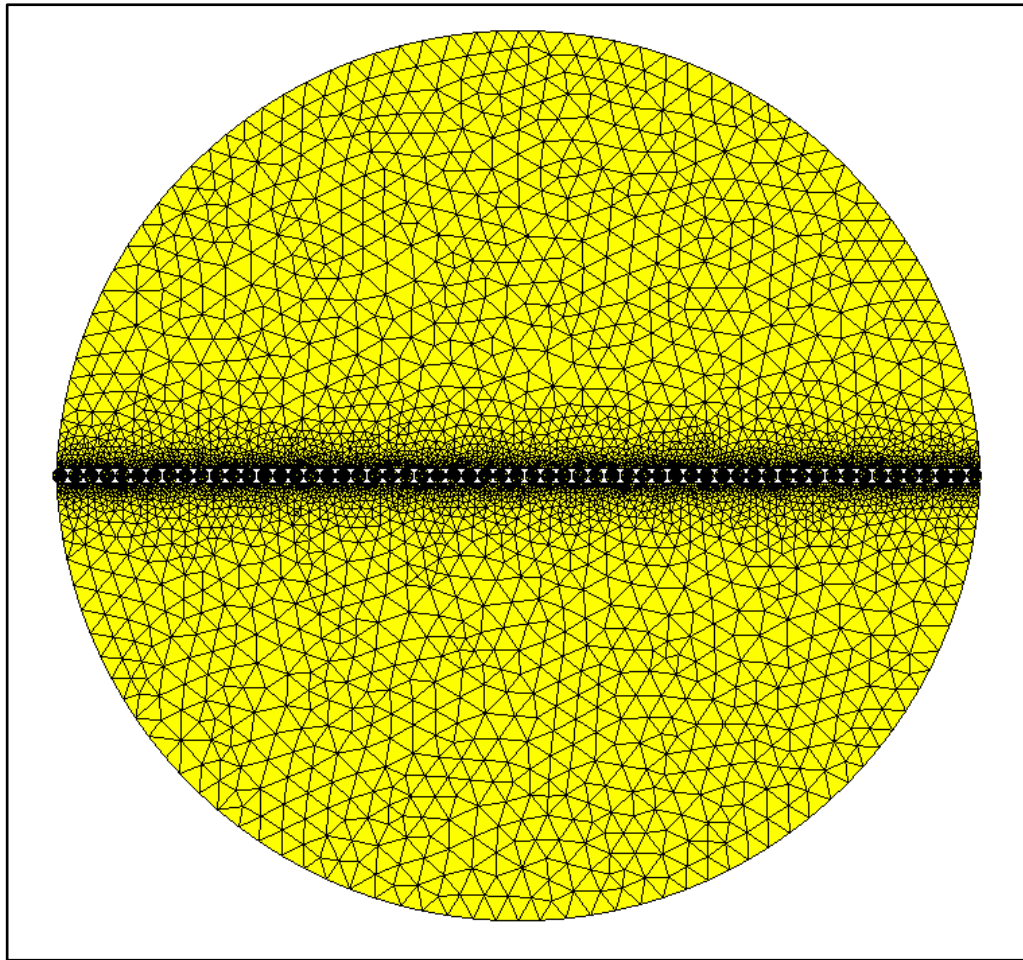


Figure 7-4: Model geometry with unstructured mesh applied to it.

## 7.4 Simulations results

### 7.4.1 Fracture closure modelling using elastic material definition

Elastic simulations were performed in the aim of investigating the type of deformations exists in the previous SR3 simulation (elastic/plastic). Elastic simulations were performed using the same algorithm as SR3 simulations. The elastic properties used in modelling are listed in Table 7-3.

Sample	$E$ (GPa)	$\nu$	$\rho$ (g/cm <sup>3</sup> )
WS	12.9	0.25	2.46
KC	25.5	0.299	2.51
OC	26.8	0.182	2.50
D	53.0	0.336	2.72

Table 7-3: Elastic properties of samples used in elastic simulations.

ELFEN results of elastic fracture closure simulation from 1,000 psi – 4,000 psi for all four sample are shown in Table 7-4- Table 7-7. Elastic simulations were also carried out further to 10,000 psi confining pressure using reduced values Young’s modulus similar to SR3 simulation. Fracture closure values at each confining pressure stage for all four samples up till 10,000 psi are shown in Table 7-8- Table 7-11.

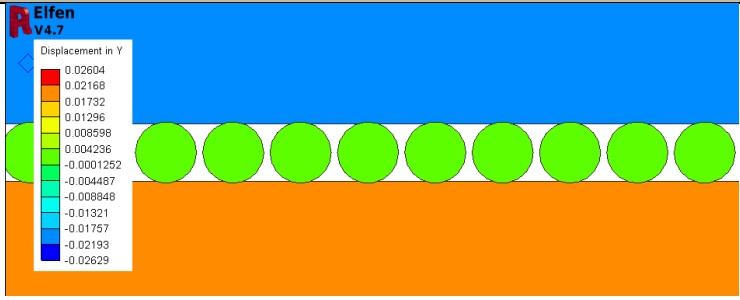
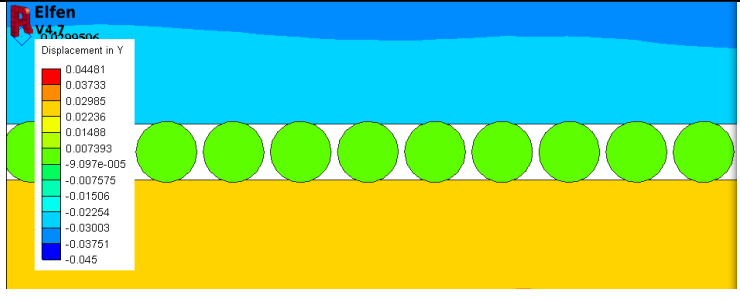
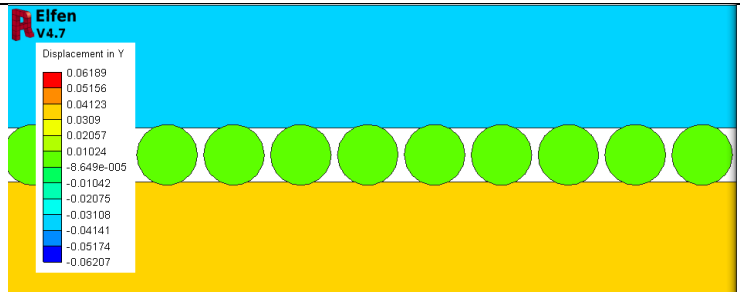
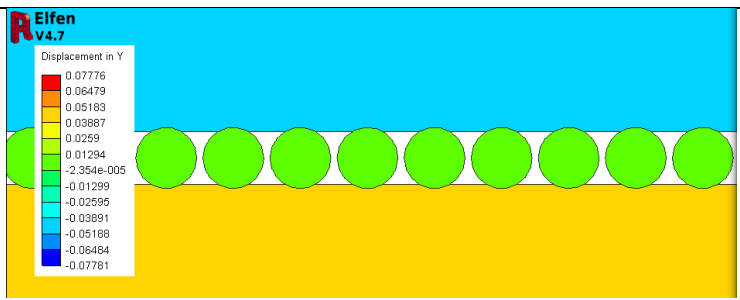
Confining Pressure (psi)	ELFEN fracture closure	Fracture closure (mm)
1,000		0.039
2,000		0.059
3,000		0.076
4,000		0.091

Table 7-4: Fracture closure elastic simulation results of WS sample from 1000 psi to 4000 psi.

Confining Pressure (psi)	ELFEN fracture closure	Fracture closure (mm)
1,000		0.036
2,000		0.042
3,000		0.052
4,000		0.062

Table 7-5: Fracture closure elastic simulation results of KC sample from 1000 psi to 4000 psi.



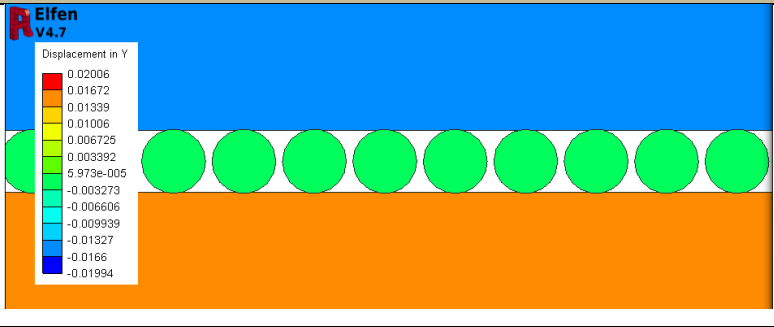
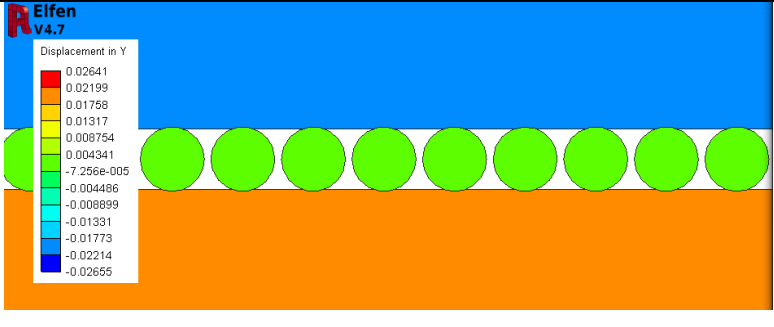
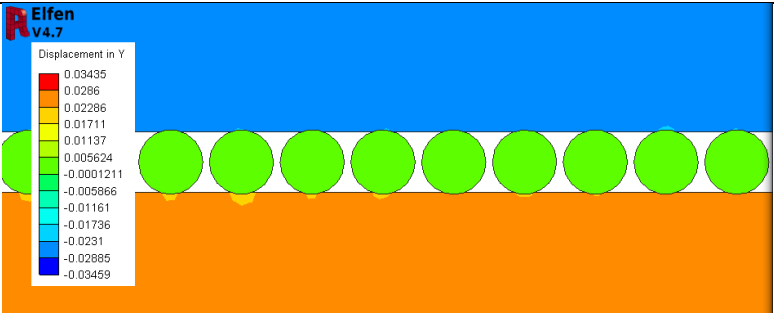
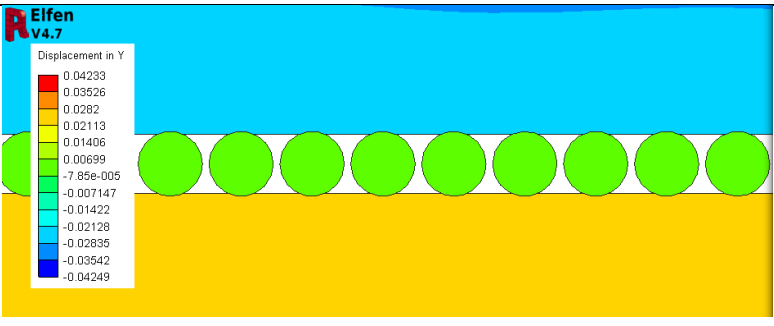
Confining Pressure (psi)	ELFEN fracture closure	Fracture closure (mm)
1,000		0.032
2,000		0.038
3,000		0.048
4,000		0.056

Table 7-6: Fracture closure elastic simulation results of OC sample from 1000 psi to 4000 psi.

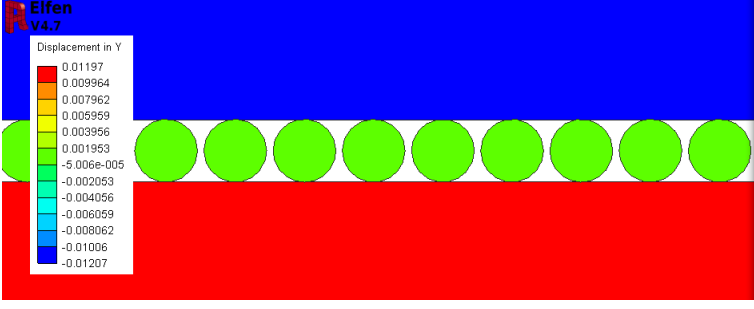
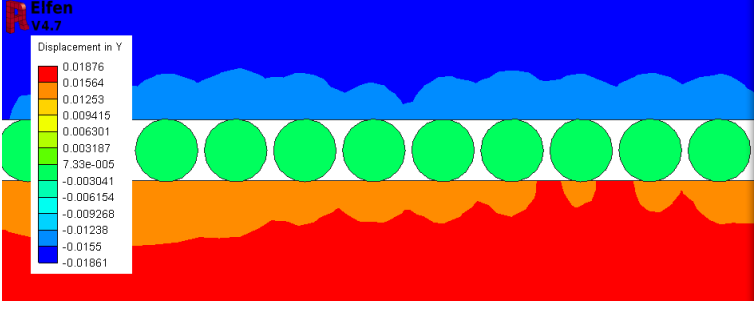
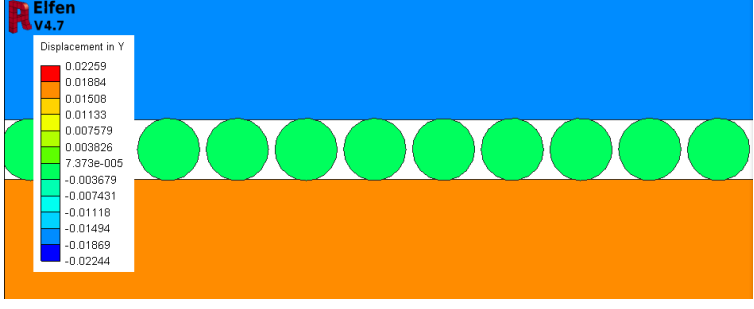
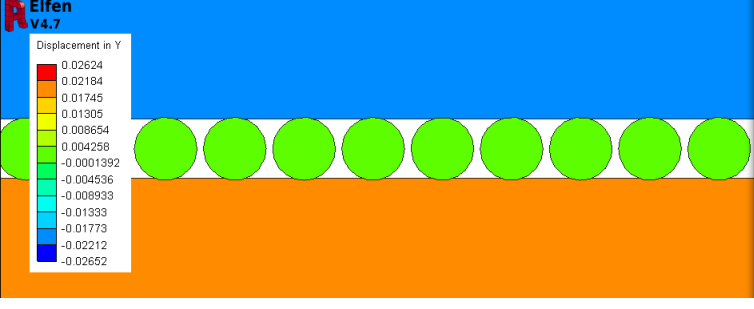
Confining Pressure (psi)	ELFEN fracture closure	Fracture closure (mm)
1,000		0.022
2,000		0.032
3,000		0.036
4,000		0.040

Table 7-7: Fracture closure elastic simulation results of D sample from 1000 psi to 4000 psi.

Confining pressure (psi)	Closure (mm)			
	Experimental	E=12.9	E=6.5	E=9.7
1,000	0.172	0.039	0.066	0.050
2,000	0.247	0.059	0.092	0.070
3,000	0.303	0.076	0.114	0.090
4,000	0.305	0.091	0.136	0.108
5,000	***	0.104	0.156	0.122
6,000	***	0.116	0.178	0.136
7,000	***	0.128	0.202	0.150
8,000	***	0.138	Closed	0.164
9,000	***	0.148	Closed	0.180
10,000	***	0.160	Closed	0.200

*Table 7-8: Fracture closure simulation results of WS sample from 1000 psi to 10,000 psi. Material definition was done based on the elastic properties with varying Young's modulus.*

Confining pressure (psi)	Closure (mm)			
	Experimental	E=24.5	E=12.3	E=18.4
1,000	0.199	0.036	0.040	0.036
2,000	0.206	0.042	0.062	0.050
3,000	0.218	0.052	0.080	0.064
4,000	0.221	0.062	0.094	0.074
5,000	***	0.070	0.108	0.084
6,000	***	0.080	0.120	0.094
7,000	***	0.088	0.130	0.102
8,000	***	0.094	0.142	0.112
9,000	***	0.102	0.152	0.120
10,000	***	0.108	0.164	0.126

*Table 7-9: Fracture closure simulation results of KC sample from 1000 psi to 10,000 psi. Material definition was done based on the elastic properties with varying Young's modulus.*

Confining pressure (psi)	Closure (mm)			
	Experimental	E=26.8	E=13.3	E=20.1
1,000	0.178	0.032	0.038	0.034
2,000	0.199	0.038	0.058	0.048
3,000	0.205	0.048	0.074	0.060
4,000	0.213	0.056	0.090	0.072
5,000	***	0.064	0.102	0.080
6,000	***	0.070	0.114	0.090
7,000	***	0.078	0.124	0.098
8,000	***	0.084	0.134	0.106
9,000	***	0.090	0.144	0.114
10,000	***	0.096	0.156	0.120

*Table 7-10: Fracture closure simulation results of OC sample from 1000 psi to 10,000 psi. Material definition was done based on the elastic properties with varying Young's modulus.*

Confining pressure (psi)	Closure (mm)			
	Experimental	E=53.0	E=26.5	E=39.8
1,000	0.135	0.022	0.022	0.026
2,000	0.143	0.032	0.042	0.034
3,000	0.141	0.036	0.050	0.042
4,000	0.164	0.040	0.058	0.048
5,000	***	0.046	0.068	0.054
6,000	***	0.050	0.076	0.060
7,000	***	0.054	0.082	0.066
8,000	***	0.060	0.090	0.070
9,000	***	0.064	0.096	0.076
10,000	***	0.068	0.102	0.080

*Table 7-11: Fracture closure simulation results of D sample from 1000 psi to 10,000 psi. Material definition was done based on the elastic properties with varying Young's modulus.*

#### 7.4.2 Fracture closure modelling using SR3 model material definition

Simulations using the SR3 model were conducted for the four samples with triaxial data; WS, KC, OC and D samples. The simulation was done using four stages compression algorithm. The first stage is compression of the sample with 1,000 psi confining pressure for a period of 0.1 seconds. Confining pressure was then increased in an increment of 1,000 psi per stage to a maximum confining pressure of 10,000 psi. Total simulation time is 1 second for all stages. In the actual fracture closure experiment conducted and explained in **Chapter 6**, each confining pressure stage is applied for a period of 4-7 days until fracture conductivity reaches stable steady state value. The reason for setting simulation time to be way less than the actual experiment time is that time related deformations (i.e. creep) is not included in these simulations.

The first simulation performed using SR3 model parameters obtained earlier. The first sample modelled was WS sample and had the maximum fracture closure at the end of the 4,000 psi stage. The simulation results show that WS sample experienced a closure of 0.482 mm at the end of the 4th stage. Table 7-12 shows fracture closure simulation results of WS sample for all four stages. The second set of simulations were performed for a reduced preconsolidation pressure ( $\sigma_c$ ) and Young's modulus ( $E$ ). Preconsolidation pressure was reduced to 36 MPa and Young's modulus was reduced 9.7 GPa and 6.5 GPa. Simulation results for different combinations of  $\sigma_c$  and  $E$  are shown in Table 7-13. At the reduced conditions, fracture underwent complete closure between 6,000-9,000 psi.

Confining Pressure (psi)	ELFEN fracture closure	Fracture closure (mm)
1,000		0.458
2,000		0.462
3,000		0.472
4,000		0.482

Table 7-12: Fracture closure simulation results of WS sample from 1000 psi to 4000 psi. Material definition was done based on the SR3 parameters obtained earlier.

Confining pressure (psi)	Experimental closure (mm)	Closure results from simulations (mm)				
		$\sigma_c = 158$	$\sigma_c = 36$		$\sigma_c = 158$	
		E=12.9	E=6.5	E=9.7	E=6.5	E=9.7
1,000	0.172	0.458	0.484	0.472	0.474	0.472
2,000	0.247	0.462	0.494	0.486	0.496	0.484
3,000	0.303	0.472	0.506	0.494	0.514	0.498
4,000	0.305	0.482	0.518	0.500	0.532	0.510
5,000	***	0.490	0.534	0.512	0.546	0.520
6,000	***	0.500	closed	0.522	closed	0.534
7,000	***	0.508	closed	0.532	closed	0.542
8,000	***	0.516	closed	closed	closed	0.552
9,000	***	0.526	closed	closed	closed	closed
10,000	***	0.534	closed	closed	closed	closed

*Table 7-13: Fracture closure simulation results of WS sample from 1000 psi to 10,000 psi. Material definition was done based on the SR3 parameters obtained earlier with varying  $\sigma_c$  and E.*

The second sample simulated was the KC sample, which was also simulated to 10,000 psi confining pressure. Simulation results of fracture closure using SR3 model parameters from 1,000-4,000 psi are shown in Table 7-14. Total simulation fracture closure at 4000 psi was about 0.062 mm, which is quite low compared to actual closure, which was about 0.22 mm. However, reducing Young's modulus to 12.3 GPa resulted in an increase in fracture closure by at least 52%. Results of reducing preconsolidation pressure to 100 MPa and reducing Young's modulus to 12.3 MPa and 18.4 MPa are shown in Table 7-15. The sample did not undergo complete closure even when Young's modulus and preconsolidation were reduced.

Confining Pressure (psi)	ELFEN fracture closure	Fracture closure (mm)
1,000		0.034
2,000		0.042
3,000		0.052
4,000		0.062

Table 7-14: Fracture closure simulation results of KC sample from 1000 psi to 4000 psi. Material definition was done based on the SR3 parameters obtained earlier.



Confining pressure (psi)	Experimental closure (mm)	Closure results from simulations (mm)				
		$\sigma_c = 315$	$\sigma_c = 100$		$\sigma_c = 315$	
		E=24.5	E=12.3	E=18.4	E=12.3	E=18.4
1,000	0.199	0.034	0.04	0.036	0.040	0.036
2,000	0.206	0.042	0.062	0.050	0.062	0.050
3,000	0.218	0.052	0.080	0.064	0.08	0.064
4,000	0.221	0.062	0.094	0.074	0.094	0.074
5,000	***	0.070	0.108	0.086	0.108	0.086
6,000	***	0.080	0.120	0.096	0.120	0.094
7,000	***	0.088	0.132	0.104	0.132	0.102
8,000	***	0.094	0.144	0.114	0.142	0.112
9,000	***	0.102	0.154	0.122	0.154	0.120
10,000	***	0.108	0.168	0.132	0.164	0.128

*Table 7-15: Fracture closure simulation results of KC sample from 1000 psi to 10,000 psi. Material definition was done based on the SR3 parameters obtained earlier with varying  $\sigma_c$  and E.*

OC sample has Young's modulus similar to KC sample and fracture closure results were expected to be similar. Simulation results met the expectations and maximum simulated fracture closure of OC sample above described SR3 model parameters at the end of 4,000 psi stage was about 0.058 mm (Table 7-16). KC experienced higher fracture closure at the same stress (0.062 mm). However, OC sample did not undergo complete fracture closure even when Young's modulus and preconsolidation pressure were reduced to 13.3 GPa and 100 MPa respectively. All results of simulation run at different combinations of Young's modulus and preconsolidation pressures are presented in Table 7-17.

Confining Pressure (psi)	ELFEN fracture closure	Fracture closure (mm)
1,000		0.034
2,000		0.042
3,000		0.050
4,000		0.058

Table 7-16: Fracture closure simulation results of OC sample from 1000 psi to 4000 psi. Material definition was done based on the SR3 parameters obtained earlier.

Confining pressure (psi)	Experimental closure (mm)	Closure results from simulations (mm)				
		$\sigma_c = 340$	$\sigma_c = 100$		$\sigma_c = 340$	
		E=26.8	E=13.3	E=20.1	E=13.3	E=20.1
1,000	0.178	0.034	0.038	0.034	0.038	0.034
2,000	0.199	0.042	0.058	0.048	0.058	0.048
3,000	0.205	0.050	0.076	0.060	0.076	0.060
4,000	0.213	0.058	0.090	0.070	0.090	0.070
5,000	***	0.066	0.104	0.080	0.102	0.080
6,000	***	0.074	0.114	0.090	0.114	0.090
7,000	***	0.082	0.126	0.100	0.126	0.098
8,000	***	0.090	0.138	0.108	0.014	0.106
9,000	***	0.096	0.148	0.116	0.146	0.114
10,000	***	0.102	0.160	0.124	0.156	0.120

*Table 7-17: Fracture closure simulation results of OC sample from 1000 psi to 10,000 psi. Material definition was done based on the SR3 parameters obtained earlier with varying  $\sigma_c$  and E.*

The last simulated sample was the D sample, which had the highest Young's modulus and the least fracture closure in fracture closure experiment in **Chapter 6**. At 4000 psi, simulated fracture closure was 0.042 mm, which was indeed the lowest. Screen shots of simulation results up till 4,000 psi are found in Table 7-18. These results are for the SR3 model parameters described earlier. Stressing the sample further to 10,000 psi did not result in complete closure even when Young's modulus and preconsolidation were reduced. Young's modulus was reduced to 39.8 GPa and 26.5 GPa and preconsolidation pressure was reduced to 100 MPa. All results of the simulation runs of different combination of  $E$  and  $\sigma_c$  are presented in Table 7-19.

Confining Pressure (psi)	ELFEN fracture closure	Fracture closure (mm)
1,000		0.022
2,000		0.032
3,000		0.036
4,000		0.042

Table 7-18: Fracture closure simulation results of D sample from 1000 psi to 4000 psi.  
Material definition was done based on the SR3 parameters obtained earlier

Confining pressure (psi)	Experimental closure (mm)	Closure results from simulations (mm)				
		$\sigma_c = 328$	$\sigma_c = 100$		$\sigma_c = 328$	
		E=53.0	E=26.5	E=39.8	E=26.5	E=39.8
1,000	0.135	0.022	0.032	0.026	0.034	0.026
2,000	0.143	0.032	0.042	0.034	0.042	0.034
3,000	0.141	0.036	0.050	0.042	0.050	0.042
4,000	0.164	0.042	0.060	0.048	0.058	0.048
5,000	***	0.046	0.068	0.054	0.068	0.054
6,000	***	0.050	0.076	0.060	0.076	0.060
7,000	***	0.056	0.084	0.066	0.082	0.066
8,000	***	0.060	0.092	0.074	0.090	0.072
9,000	***	0.064	0.098	0.078	0.096	0.076
10,000	***	0.068	0.106	0.084	0.102	0.080

Table 7-19: Fracture closure simulation results of D sample from 1000 psi to 10,000 psi. Material definition was done based on the SR3 parameters obtained earlier with varying  $\sigma_c$  and E.

### 7.4.3 Complete fracture closure simulation

Simulation were carried out further to find out the confining stress at which fracture would close completely. Elastic simulations were performed for a range of model with different Young's modulus. Density was assumed to be 2.5 g/cm<sup>3</sup> and Poisson's ratio of 0.25. Confining pressure was increased gradually until the fracture closes completely as it is shown in Figure 7-5. Young's modulus and corresponding confining pressure at which the fracture closes completely are shown in Table 7-20. The relation between complete closure pressure and Young's modulus is linear as it shown in Figure 7-6.

Young's modulus (GPa)	Closure pressure (MPa)
2	23
4	35
8	58
10	78
14	108
18	135
26	190
34	250
42	310
60	435

*Table 7-20: Confining pressures at which fracture closes completely found by elastic simulations.*

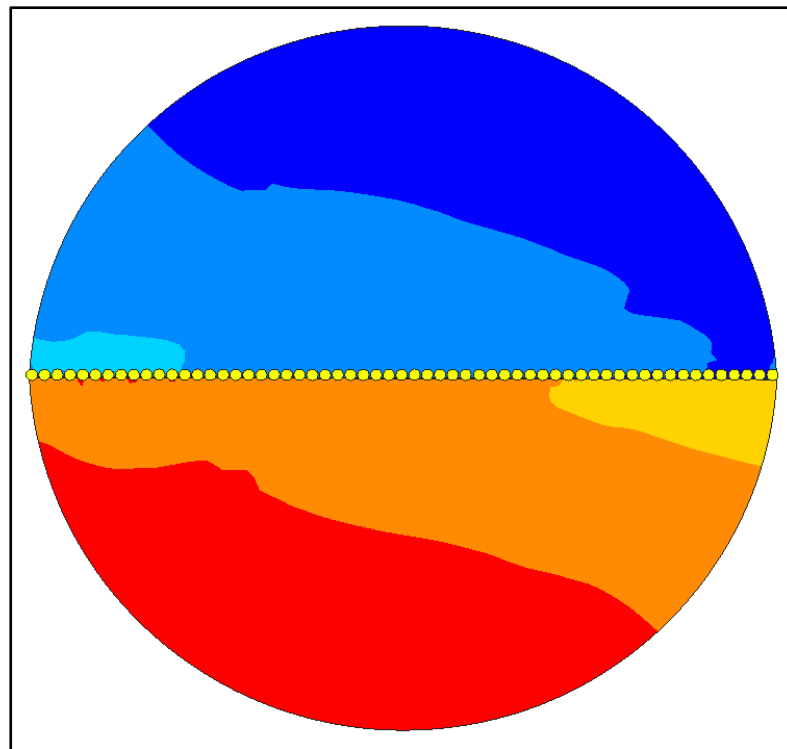


*Figure 7-5: Complete fracture closure ELFEN model.*

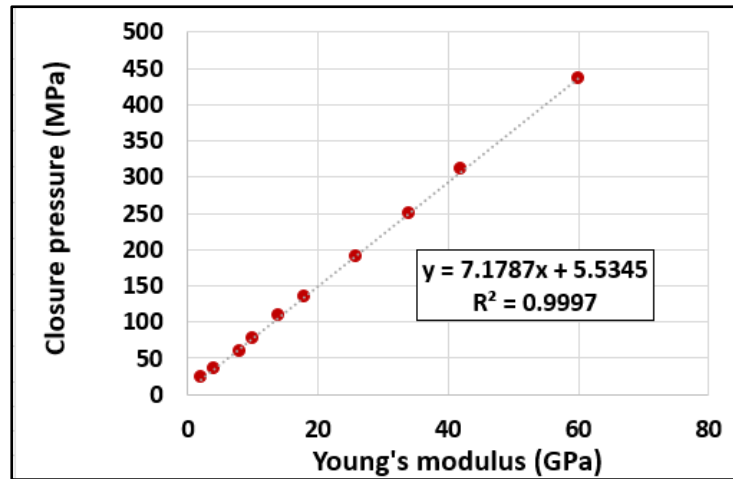


Figure 7-6: Elastic complete closure pressure vs. Young's modulus.

Simulations are carried out further even for SR3 model presented earlier. Samples were stressed until fracture is closed completely. The closure pressures for each sample comparison are presented in Table 7-21. Figure 7-7 presents relationship between Young's modulus and closure pressure for both elastic simulation and SR3 model simulation. Closure pressures using both models have similar linear trend and SR3 closure pressure values are very similar to the elastic ones.

Sample	$\sigma_c$ (MPa)	E (GPa)	Closure (MPa)
D	328	53.0	405
		39.8	310
		26.5	210
	100	26.5	210
		39.8	350
OC	340	26.8	210
		20.1	155
		13.3	95
	100	20.1	165
		13.3	105
KC	315	24.5	190
		12.3	95
		18.4	135
	100	12.3	100
		18.4	145
WS	158	12.89	75
		6.5	42
		9.7	62
	36	6.5	42
		9.7	55

Table 7-21: Confining pressures at complete fracture closure found by SR3 simulations.

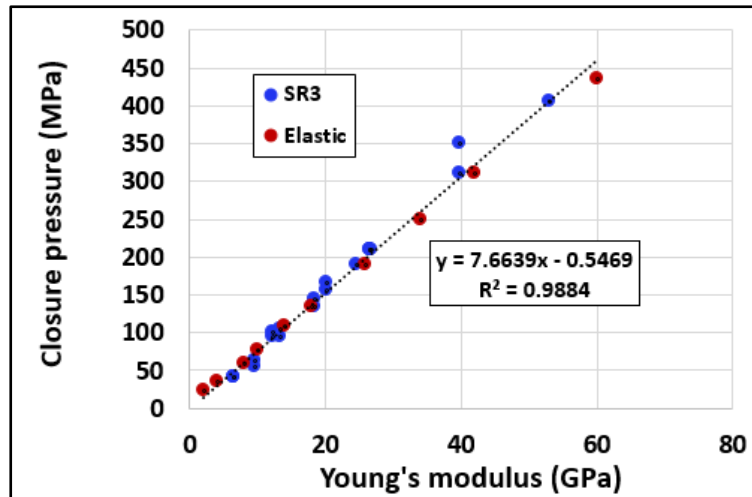


Figure 7-7: Young's modulus against closure pressure for both elastic simulation and SR3 model simulation.

## 7.5 Discussion

### 7.5.1 Matching SR3 models simulation results with experimental results

Simulation results using SR3 model parameters described earlier showed that simulated fracture closure is significantly less than experimental fracture closure. The two possible reasons behind this difference is either that the experimental results accuracy is questionable or the properties used in material modelling are wrong. As it was discussed in **Chapter 6**, error in fracture aperture estimation due to CT resolution could be about  $\pm 200 \mu\text{m}$ .

Water saturation has a great impact on mechanical properties of shale as it was shown earlier (e.g. Zhang et al., 2017; Corapcioglu et al., 2014). WS sample simulation results showed large deformations and closure on the first stage and then closure becomes minimal in the following stages which suggests that WS sample underwent plastic deformations during the first stage. This is due to the error introduced by the resolution of the CT. Simulation results were almost at the edge of the error bar as it is shown in Figure 7-8. For the hard samples (KC, OC and D), simulation results were less than the experimental results but within the error for both reduced and unreduced strength cases. However, the error is still too large compared to the small fracture closure figures, which makes matching experimental data with simulation results impossible.



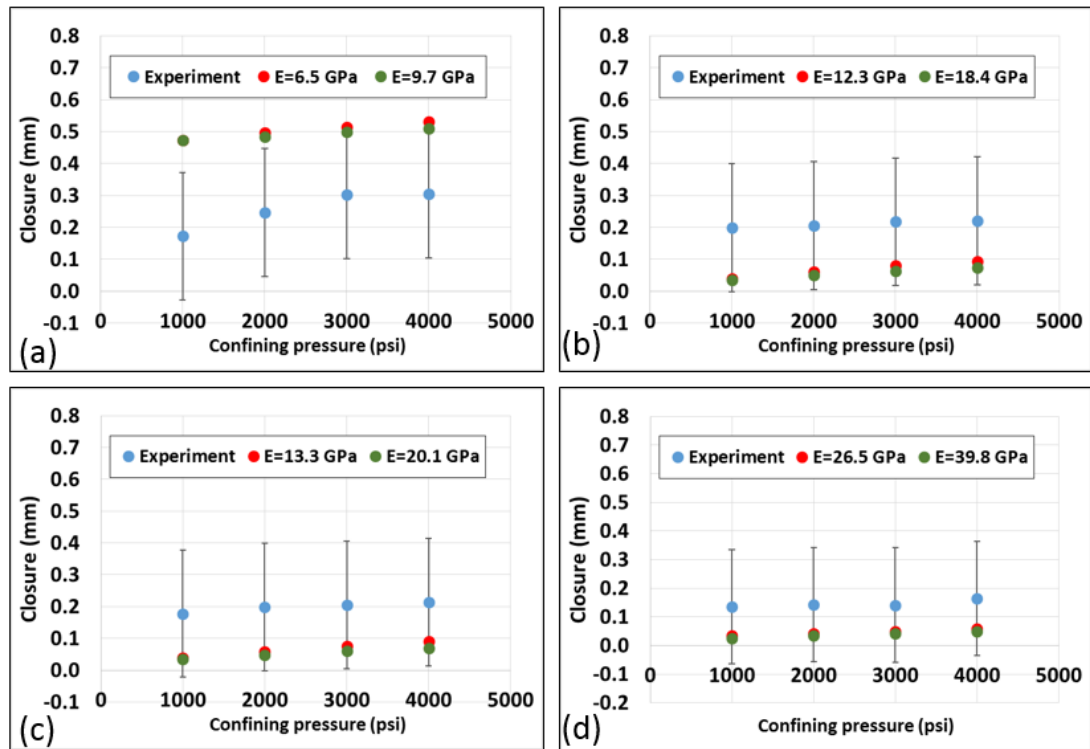


Figure 7-8: fracture closure obtained by experiments and simulations at different elastic modulus against confining pressure for samples (a) WS, (b) KC, (c) OC and (d) D. The error bars represents CT images resolution error.

According to the cubic law presented in **Chapter 6**, fracture conductivity is proportional to the square of fracture aperture. The fracture conductivity relationships with the square of fracture aperture for all four samples are shown in Figure 7-9. Data was plotted for experimental and simulation results. It can be clearly seen that simulation results followed the same trend as the experimental results but with a difference in magnitude. This suggests that fracture closure behaviour of the simulation is similar to the fracture closure behaviour in the experiment. The error between them is caused by the resolution of CT images used to estimate experimental fracture aperture.

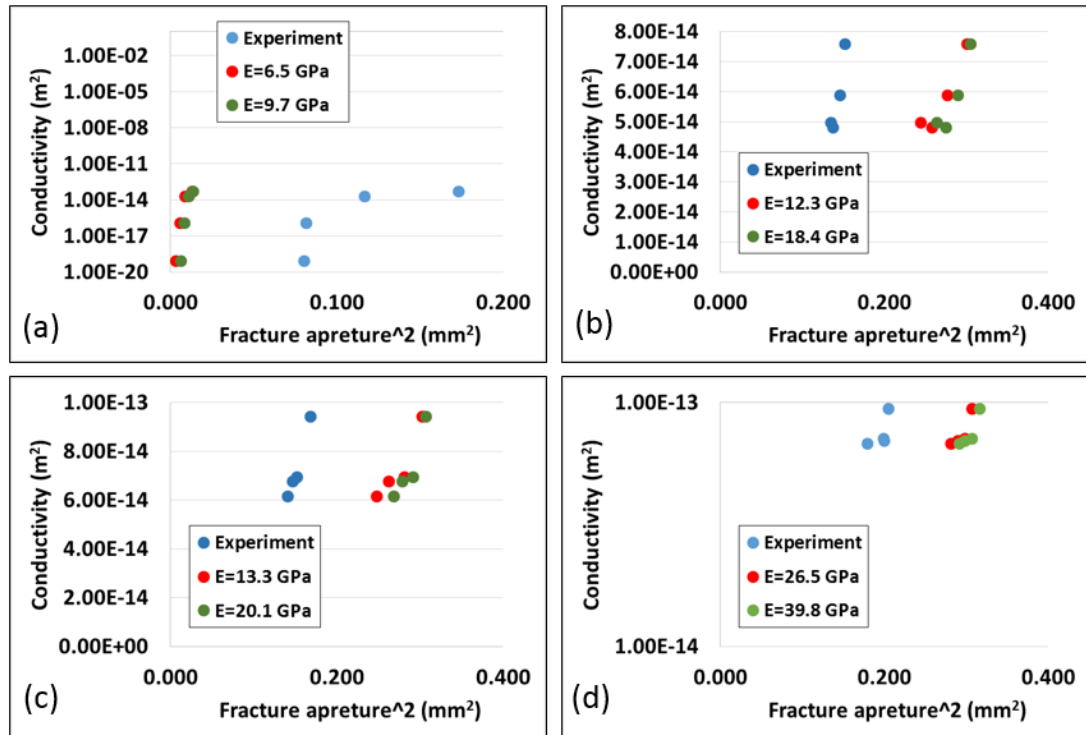


Figure 7-9: Fracture conductivity against fracture aperture for samples (a) WS, (b) KC, (c) OC and (d) D. Data is for experimental results and simulation results at different Young's modulus.

### 7.5.2 Comparison between elastic simulation and SR3 model simulation

Elastic simulations were performed for the same four samples using elastic properties only. Several runs were made for each sample with reduced Young's modulus similar to SR3 model simulation set. Using SR3 material definition, WS experienced large fracture closure at the first confining pressure stage without reducing the strength of the rock. This suggests that the sample probably underwent plastic deformations during closure process. This was confirmed when fracture closure results were compared for both sets of simulations. The difference between the SR3 model closure and elastic closure would be the plastic deformations. Figure 7-10 presents WS sample fracture closure during confining pressure stages for both elastic and SR3 simulation at preconsolidation pressure of 158 MPa. The trend of both simulations is similar, which suggests WS sample experienced most of the deformations at the initial stage, and then deformations were elastic for the rest of the stages. This behaviour is related to ductile failure experienced by sample before closure which is associated with large strain being accommodated by the sample.

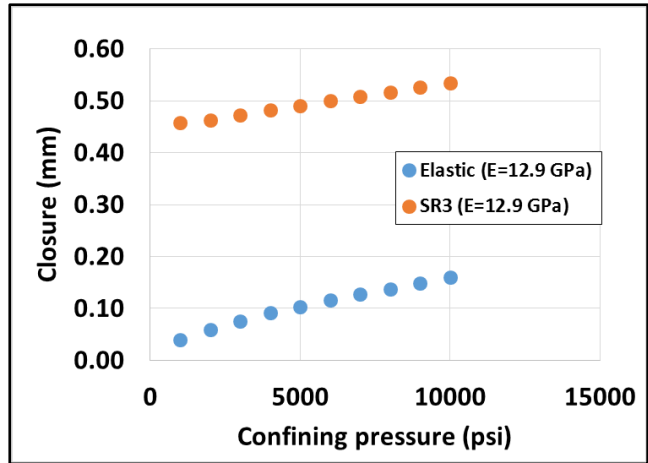


Figure 7-10: Comparison between fracture closure simulation results for both elastic and SR3 model simulations for WS sample. The results are at  $\sigma_c=158$  MPa for E value of 12.9 GPa .

The other samples which are considered hard (KC, OC and D) behaved quite different from the soft sample (WS). As it was discussed earlier, hard samples experienced similar fracture closure even when preconsolidation pressure was reduced by 70-80%. Considering initial preconsolidation pressure assumed earlier, all three samples had very similar results for both elastic and SR3 model simulations even when confining pressure was increased to 10,000 psi. These hard samples did not experience complete fracture closure even after reducing Young’s modulus by 50%. Comparisons between elastic and SR3 simulation for hard samples (KC, OC and D) are shown in Figure 7-11, Figure 7-12 and Figure 7-13 respectively.

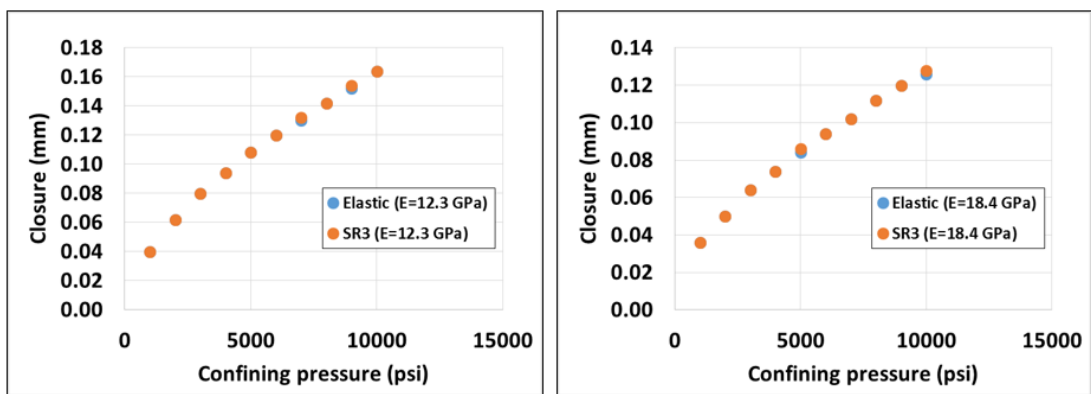


Figure 7-11: Comparison between fracture closure simulation results for both elastic and SR3 model simulations for KC sample. The results are at  $\sigma_c=315$  MPa for E values of 12.3 GPa and 18.4 GPa.

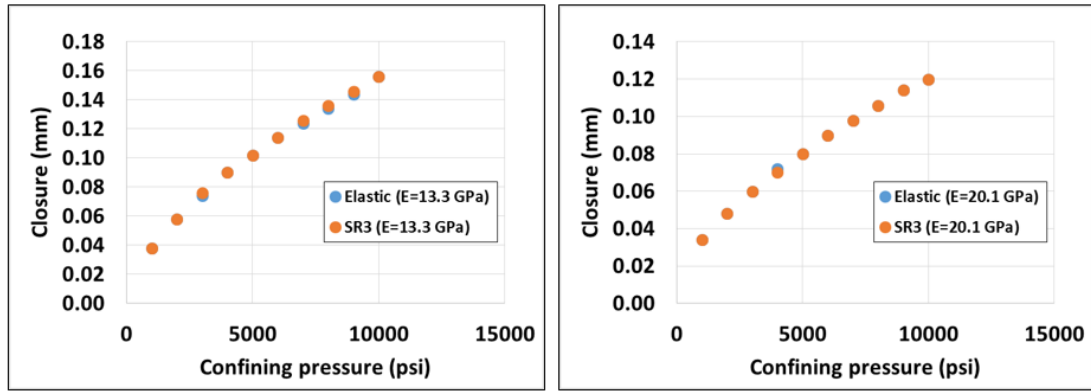


Figure 7-12: Comparison between fracture closure simulation results for both elastic and SR3 model simulations for OC sample. The results are at  $\sigma_c=340$  MPa for E values of 13.3 GPa and 20.1 GPa.

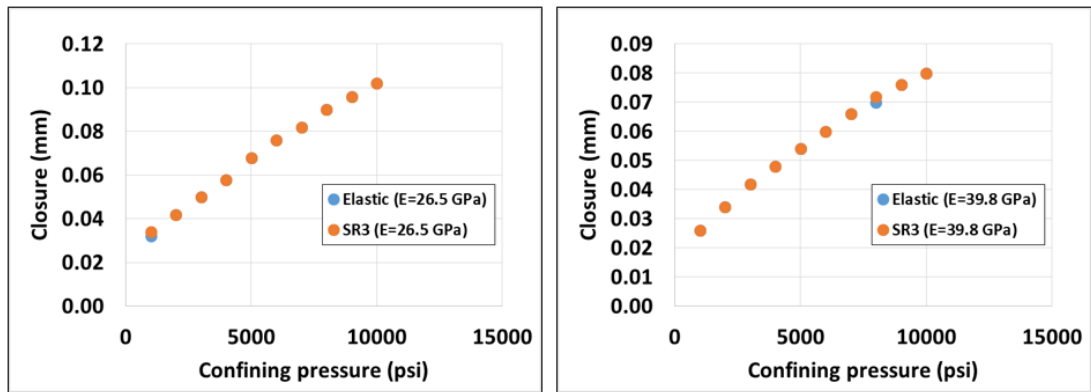


Figure 7-13: Comparison between fracture closure simulation results for both elastic and SR3 model simulations for D sample. The results are at  $\sigma_c=328$  MPa for E values of 26.5 GPa and 39.8 GPa.

The findings of these simulations suggest that fractures in shale could close or remain open depending on the strength of the rock. Fractures in weak shale with low preconsolidation pressure (<158MPa) have the potential close by ductile deformation as effective stress is increased. On the other hand, shales with preconsolidation pressure (>158 MPa) require high effective stress to push fracture wall toward ductile deformation regime even if the burial depth reaches 20,000 feet (6.1 km). It was shown as well that fractures in soft shale could close elastically. Soft rocks with low Young’s modulus have the potential to close elastically when sufficient effective stress is present. It was proved that fractures in samples with Young’s modulus (<7 GPa) have the potential to close elastically at effective stress less than 8,000 psi which corresponds to burial depth of approximately 16,000 feet (4.9 km). On the other hand,

samples with high Young's modulus (>12 GPa) will not close elastically even if they were buried as deep as 20,000 feet (6.1 km).

### 7.5.3 Estimation of the potential of fracture complete closure during burial

Simulation results for both SR3 and elastic models showed that there is a linear relationship between complete fracture closures and Young's modulus. This relationship was used to investigate the potential of complete fracture closure in shales buried at different depth using porosity-depth data collected by (Mondol et al., 2007). Porosity ( $\phi$ ) values were converted to unconfined compressive strength (UCS) using the following relationships (Lashkaripour & Dussealut, 1993; Chang et al., 2006):

$$UCS = 1.001 \phi^{-1.143} \quad \phi < 0.1 \quad (7-1)$$

$$USC = 0.286 \phi^{-1.762} \quad \phi > 0.27 \quad (7-2)$$

Where  $\phi$  is porosity fraction and UCS is in (MPa). UCS values are then estimated and were then used to estimate Young's modulus using the following relationship (Chang et al., 2006):

$$E = \left( \frac{UCS}{7.22} \right)^{1/0.712} \quad (7-3)$$

Where  $E$  is in (GPa). The relationship found earlier by simulations was then used to find fracture complete closure stress (CCS), which was then plotted against depth. The equation found is given by:

$$CCS = 1111.6 * E + 79.3 \quad (7-4)$$

Where CCS is in (psi). CCS is then plotted against depth and the resulting relationship is presented in Figure 7-14. Lithostatic gradient, hydrostatic gradient and effective pressure are also plotted in the same figure. Effective pressure slope will be changing depending on pore pressure.

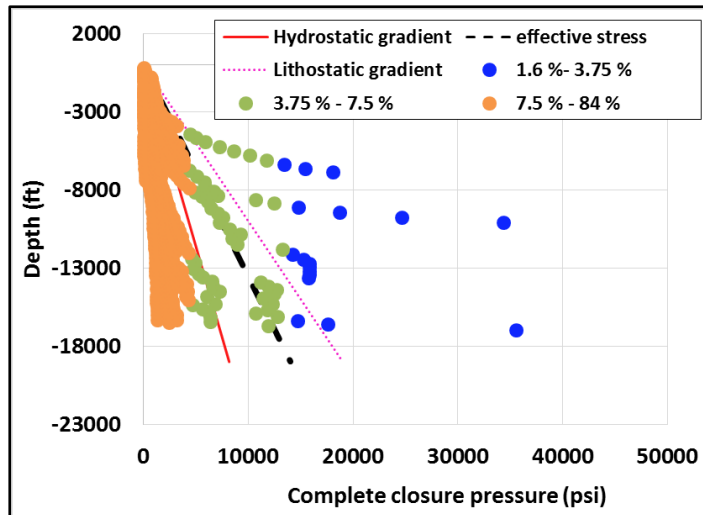


Figure 7-14: Generated complete fracture closure pressure against depth using porosity-depth curve provided by (Mondol et al., 2005). Data was divided into three porosity ranges; 1.6 % -3.2 %, 3.2%-7.5% and 7.5% -84%.

Data was divided into three porosity ranges; 1.6 % -3.75 %, 3.75% -7.5% and 7.5% -84%. The results suggest that fracture in shales with porosity lower than 3.75% will never close mechanically in the diagenetic regime due to insufficient stress even if it was buried up to 17,000 feet. The corresponding Young's modulus for this porosity range is about 16.3- 47.0 GPa. This agrees with observations made from fracture closure experiments presented in **Chapter 6**. It also agrees with observations made from simulation results presented earlier.

In the second group, fractures in shale with porosity range 3.75%- 7.5% will only close if effective stress is higher than closure pressure. It was proved by experimental and simulation work that shale sample within this porosity range could potentially close at stress between 6,000-8,000 psi, which agrees with complete closure data. Figure 7-14 also shows that fractures in some shales within this porosity range will never close and some will close regardless of the effective stress.

The high porosity shales (7.5 % and above) are soft and the data in Figure 7-14 suggested that fracture in these shales will definitely close as long as no tensile stresses generated across the fracture due to change in effective stress. The corresponding Young's modulus to this porosity range is about 0.02-4.0 GPa. This was proven earlier by simulations and fractures in such shale samples have potential to close elastically or plastically. Rocks within this porosity range are generally weak and have low preconsolidation pressure.

## 7.6 Conclusions

Finite element simulations were carried out for fracture closure in shale to arrive to a better understanding of fracture closure experiment. ELFEN FEM code provided by Rockfield was used to perform these simulations due to its capability to analyse geomechanical models. The geometry built for these simulations is a 2D geometry, which is representative to the 3D situation. Two material definition models were adopted; SR3 model derived from soil mechanics and elastic model using basic elastic properties. Both models do not take into account creep deformations.

Confining pressure was applied in four steps; 1000 psi, 2000 psi, 3000 psi and 4000 psi similar to the fracture closure experiments. Then simulations were carried out further to 10,000 psi confining pressure to investigate the effect of stress and the potential of complete fracture closure. Deformations in a form of fracture closure were recorded for each confining pressure stage. It was found that weak shales with low preconsolidation pressure will experience large fracture closure due to rock undergoing a ductile failure. On the other hand, shales with large preconsolidation pressure will deform elastically even if they were buried as deep as 20,000 feet. Another finding was that fractures in shales with low Young's modulus (<12 GPa) have a potential to close elastically at burial depth below 20,000 feet. On the other hand, shales with large Young's modulus (>12 GPa) will have their fracture open even if they were buried to 20,000 feet unless its preconsolidation pressure is low.

Simulation was carried out further until fracture closes completely for both material models. The results showed that for both model, closure pressure followed similar trend in closure pressure-Young's modulus relationship. This relationship together with porosity-depth curve of shale were used to determine closure pressure-depth curve of shale. The resulted relationship matches the observations from experimental and simulation work. Shales with porosities 1.6% - 3.75% (16.3-47.0 GPa) will have their fracture open regardless of the effective stress the rock is subjected to. Mid-range porosity shale samples (3.75% - 7.5%) will have their fracture closed if the effective stress is higher than complete closure pressure. During burial, fractures in shales with high porosities (7.5% and above) will close either elastically or by ductile failure. Fractures in high porosity shales will only stay open if tensile stresses are generated across the fracture due to change in effective stress. High porosity shales are normally weak and have low preconsolidation pressure.

## 8 Chapter VIII: Conclusion and Future work

### 8.1 Conclusions

Mechanisms of fluid flow through shale were reviewed in detail in this thesis. Fluid flow in shale could occur in three main flow regimes; non-deforming matrix flow in a form of single phase or multiphase flow, fluid pressure related flow in a form of pathway dilation or stress-related deformation flow in a form of fluid flow through fractures and fault caused by stress. Single phase flow is controlled by the permeability of the rock, which is very low for shale. Diagenetic processes and presence of high amount of clay within shale decrease permeability of shale. However, the presence of two or more phases will change flow regime from single phase to multiphase flow. Multiphase flow will only occur if the pressure of the non-wetting phase (oil/gas) is higher than the pressure of the wetting phase by the amount known as capillary entry pressure, which inversely proportional to pore throat. Shales normally have small pore throat, which makes capillary pressure higher. In addition, shales are stress sensitive and capillary entry pressure at in situ condition might be higher than the one measured in the lab using MIP instrument.

Faults and fractures are formed when the stress on the rock exceeds its strength causing failure. Failure could be brittle or ductile, which can be determined used rock properties and stress state of the rock. Shale forms discrete slip planes when it fails in a brittle manner while failure in a ductile manner would be by shear-enhanced compaction where most of the strain is accommodated by distributed deformation. Shale elasto-plastic behaviour is modelled in  $p$ - $q$  space to include both brittle and ductile behaviours, which are based on critical state theory. Several models are available in the literature, which include; Cam-Clay, Modified Cam-Clay and Soft Rock 3. Construction of these models requires knowledge of plastic properties of rocks, which is obtained from laboratory tests such as multistage triaxial experiments. This test provides data that describes brittle behaviour of the rock. However, there are plastic properties that are essential to describe ductile behaviour of the rock such as preconsolidation pressure. For the case of shale, this property is not easy to measure in drained conditions and laboratory tests take relatively long time. While modelling shale strength, preconsolidation pressure is normally assumed, which might lead to error in determination of the failure mode.



Fractures and faults may act as conduit or barriers to fluid flow. However, conductive fracture may also close if the sufficient closure conditions are present. Many theoreticians have attempted to model and study fracture closure of shale. Fracture closure is controlled by three factors; the stress the rock is subjected to, fracture roughness and geomechanical properties of the rock. In addition, fracture closure could also occur by time-dependent plastic deformations of the fracture walls (creep). Models and experimental work presented by theoreticians showed the dependency of fracture closure on the three factors presented earlier. However, exact controls of fracture closure in shale are still not well documented.

Preferential pathways are formed and propagated through rocks under the effect of high pressure fluid. This processes is known as pathway dilation in the management of radioactive waste. Pathway dilation exists in the environment in large scale in a form of mud-volcanos and in small scale in a form of bubble movement. Extensive research has been conducted to investigate the existence of pathways dilation process in bentonite buffers. Formation of these pathway was experimentally observed in clay-rich formations. However, all evidences of existence of pathway dilation presented are based on visual observations, seismic analysis, injection pressure and strain monitoring. There are no solid microstructural models to describe the nature of these pathways, their formation mechanisms and how they propagate through clay-rich sediments.

Experimental and simulation methods were developed to tackle the gaps identified from literature review conducted. Initially, sample characterization was done to have a full understanding of properties of the samples tested. Experimental and simulation work was then conducted to address the following gaps:

- Lack of understanding of stress sensitivity of capillary properties of shale.
- Difficulty in determining elastic and plastic properties of shale.
- Lack of understanding of controls of fracture closure and the potential of self-sealing of shale.
- Absence of microstructural description and controls of formation preferential pathways through shale matrix.

Experimental and simulation work done provided a number of suggestions that helped in explaining these mechanisms and their controls. Initially, sealing capacity of shale was measured under stress using MPUCS instrument to investigate shale

sealing capacity sensitivity to stress. The results suggested that for water-wet shale, buried shale at in situ stress will act as an effective seal and will never allow hydrocarbon to leak by multiphase flow through the matrix. Sealing capacity measured under stress using MPUCS was at least two times higher than the one estimated using MIP at a net stress of only 1,000 psi. At a net stress of 7,000 psi, shale will act as an effective seal to at least a 9.9 km column of gas oil or 9.1 km column of gas. The work suggests that shale will allow hydrocarbons to leak either by pathways dilation or through conductive faults and fractures.

Pathway dilation was investigated experimentally by injecting melted Field's metal into synthetic shale samples and visualize the pathways generated using SEM imaging. It was found that formation and propagation of preferential pathways is controlled mainly by compaction. Arching of sand grains leads to poor compaction in between the grains, which acts as the least resistance path for fluid flow. However, chemical diagenesis can improve compaction quality and hence prevents formation of these pathways. Pathway dilation observed in opalinus clay by nuclear waste management could be due to absence chemical diagenesis. Burial depth of this opalinus clay is not high enough for significant chemical diagenesis to occur.

The difficulty in measuring elastic and plastic properties of shale was tackled by using alternative method to measure elastic properties and developing a new technique to measure plastic properties particularly preconsolidation pressure. Micro-indentation technique was proposed and used to measure elastic properties, particularly Young's modulus, which can be used in determining elastic behaviour of shale. The results suggested that Young's modulus of shale measured using micro-indentation is close to the static Young's modulus obtained from tri-axial tests. In addition, it provides a good measurement of hardness and fracture toughness, which are essential inputs in hydraulic fracturing design. The effect of shale exposure to acid (HCL) was also studied using micro-indentation and it was found that acid reduces Young's modulus significantly even if there is no carbonate content within the shale.

A new technique using standard MIP instrument was developed to measure  $p^*$ , which is preconsolidation pressure under hydrostatic conditions. The method proposed was simple and quick and provided good estimation of  $p^*$  for all samples. Cylindrical small samples were sealed using epoxy and the stressed to 60,000 psi. The volume of the mercury pumped in was transformed into volumetric strains, which was

used as an indication of compaction. The point at which volumetric strain changes represents the  $p^*$  of the sample. All  $p^*$  measurement of shale provided a good fit with  $p^*$  of chalk samples, which was expected because both rocks are fine grained and they will have similar plastic behaviour. Measured  $p^*$  was used later to model elasto-plastic behaviour of shale using FEA techniques.

In deep buried shale, the chemical diagenesis plays a significant role in reducing porosity. At these depths, shale will only allow flow through conductive faults and fractures. As it was mentioned earlier, evidences from the literature and the industry suggest that fractures could remain open or close and re-seal. Fracture closure experiments were conducted for six shale samples under various closure stresses to investigate the controls of fracture closure and re-sealing mechanism. A parallel plates of artificial fracture were induced in the samples and packed with proppants to control fracture morphology. Deformations were allowed to settle for a sufficient time at each closure stress stage to capture time effect on fracture closure. It was found that fractures have a potential to close and re-seal by ductile deformation, which requires knowledge of geomechanical properties of shale to anticipate such deformations. The results suggested that the main parameters that control fracture closure in shale are porosity and clay content together with effective stress. Soft shale with porosity more than 5% and high clay can seal in the presence of sufficient effective stress. Stiff shale with porosity lower than 5% and relative low clay content will have their fracture open regardless of the stress applied.

Finite element simulations were also conducted to simulate fracture closure experiments. Same observations were made and soft samples with high porosity and clay content are more prone to fracture closure by ductile deformations in the fracture walls. A complete closure and re-seal simulation was conducted and it was found that fractures in shale with high porosity (above 7.5%) will always close and re-seal during burial either elastically or by ductile failure. On the other hand, fractures in shale with porosity lower than 3.75% will remain open regardless of the normal stress present across the fracture. Fractures in shale with porosity (3.75 %-7.5%) have a potential to close and re-seal if sufficient normal effective stress is present. Results of fracture closure experiments and finite element demonstrated the importance of porosity and clay content in controlling the re-sealing mechanism.

## 8.2 Future work

Experimental and simulation work done in this thesis attempted to answer research questions and close the gaps identified in the literature. The findings presented were promising, which opens a scope of further work in the future to make the findings more solid and mature. Further work proposed can be summarized as:

- Include more samples in the studies.

Sample availability was a key challenge faced in this research work. A wide range of shale samples with wide variation in mineralogy, mechanical and petrophysical properties will make the results and relationships established more solid.

- Use silt together with clay and sand in preparation of synthetic sample for Field's metal injection experiment.

Presence of slit within the clay-sand mixture will reduce porosity of the sample and hence improves compaction. Slit was not included in this research due to unavailability of the material in the laboratory.

- Use equipment with high pressure rating for Field's metal injection experiment.

The core holder available in the laboratory to conduct this experiment has a limitation in the confining pressure applied (maximum 3000 psi). Using high pressure rating equipment will allow injection into tight samples.

- Use high resolution CT scanner (e.g. micro or nano-CT).

Use of a high resolution CT will enhance the resolution of the images taken during the experiments. Regarding fracture closure experiments, the error in estimating fracture aperture was relatively large due to the resolution of the CT. Using a high resolution CT will significantly improve fracture aperture estimation. In addition, micro or nano-CT will enhance visualization of the pathways generated by Field's metal within the synthetic shale sample.

## 9 References

- Abaci, S., Edwards, J.S. & Whittaker, B.N. (1992). Relative permeability measurements for two phase flow in unconsolidated sands. *Mine Water and the Environment*, 11(2), pp.11-26.
- Al Zadjali, R.J.M. (2011). The impact of steam injection on fracture permeability in carbonate reservoir, PhD thesis. *University of Leeds*, 279
- Alfa Aesar. (2006). Safety data sheet of Bismuth Indium Tin ingot (Field's metal).
- Almon, W. R., Dawson, Wm. C., Ethridge, F. G. Rietsch, E., Sutton, S. J. & Castelblanco -Torres, B. (2005). Sedimentology and petrophysical character of Cretaceous marine shale sequences in foreland basins—Potential seismic response issues, in P. Boulton and J. Kaldi, eds., Evaluating fault and cap rock seals. *AAPG Hedberg Series*, no. 2, p. 215 – 235.
- Alramahi, B. & Sundberg, M.I. (2012). Proppant embedment and conductivity of hydraulic fractures in shales. *American Rock Mechanics Association*, ARMA 12-291.
- Andra. (2005). Dossier 2005 Argile: Phenomenological evolution of a geological repository. *Andra, France*, 114.
- Anstis, G., Chantikul, P., Lawn, B. & Marshall, D. (1981). A critical evaluation of indentation techniques for measuring fracture toughness: I, direct crack measurements. *Journal of the American Ceramic Society*, 64(9), 533-538.
- API RP-19D. (2008). Measuring the long-term conductivity of proppants.
- Aplin A. C., & Larter, S. R. (2005). Fluid flow, pore pressure, wettability, and leakage in mudstone cap rocks. *American Association of Petroleum Geologists, Hedberg Series*, 2, 1-12.
- Aydin, A. (2000). Fractures, faults and hydrocarbon entrapment, migration and flow. *Marine and Petroleum Geology*, 17, 797– 814.
- Babadagli, T., Ren, X. & Develi, K. (2015). Effects of fractal surface roughness and lithology on single and multiphase flow in a single fracture: An experimental investigation. *International Journal of Multiphase Flow*, 68, pp.40-58.
- Bachu, S. (2008). CO<sub>2</sub> storage in geological media: Role, means, status and barriers to deployment. *Progress in Energy and Combustion Science*, 34(2), 254-273.
- Bandis, S.C., Lumsden, A.C., & Barton, N.R. (1983). Fundamentals of rock joint deformation. *International Journal of Rock Mechanics Mineral Science & Geomechanics Abstracts*, 20, 249-268.

Barrington, J., & Kerr, P. F. (1961). Breccia pipe near Cameron, Arizona. *Geological Society of America Bulletin*, 72, 1661–1674.

Bear, J. (1972). Dynamics of fluids in porous media. *New York: American Elsevier Pub. Co.*

Belmokhtar, M., Delage, P., Ghabezloo, S. & Conil, N. (2018). Drained triaxial tests in Low-permeability shales: Application to the Callovo-Oxfordian claystone. *Rock Mechanics and Rock Engineering*.

Berg, R. R. (1975). Capillary pressure in stratigraphic traps. *American Association of Petroleum Geologists Bulletin*, 59, 939-956.

Berndt, C., Bunz, S., & Mienert, J. (2003). Fluid expulsion from polygonally faulted clays, Norwegian margin. *Geological Society (London) Special Publication*, 216, 223–243.

Berner., R. A. (1980). Early diagenesis: A theoretical approach. *Princeton University Press*, Princeton NJ, USA.

Bjørkum, P. A., Oelkers, E.H., Nadeau, P.H., Walderhaug, O., & Murphy, W.M. (1998). Porosity prediction in quartzose sandstones as a function of time, temperature, depth, stylolite frequency, and hydrocarbon saturation. *Bulletin of the American Association of Petroleum Geologists*, 82, 637-648.

Bock, H., Dehandschutter, B., Martin, C. D., Mazurek, M., De Haller, A., Skoczylas, F., & Davy, C. (2010). Self-sealing of fractures in argillaceous formations in the context of geological disposal of radioactive waste. *NEA No. 6184*.

Boles, J.R. & Franks, S.G. (1979). Clay diagenesis in Wilcox sandstones of Southwest Texas; implications of smectite diagenesis on sandstone cementation. *Journal of Sedimentary Petrology*, 49 (1), 55–70.

Borysenko, A., Clennell, B., Sedev, R. Burgar, I., Ralston, J., Raven, M., Dewhurst, D., & Liu K. (2009). Experimental investigations of the wettability of clays and shales. *Journal of Geophysical Research*, 114, B07202.

Boudreau, B. P., Algar, C., Johnson, B. D., Croudace, I. , Reed, A., Furukawa, Y., Dorgan, K. M. , Jumars, P. A. , Grader, A. S., & Gardiner, B. S. (2005). Bubble growth and rise in soft sediments. *Geology*, 33, 517-520.

Brace, W. F. (1964). Brittle fracture of rock, in state of stress in the earth's crust. *Elsevier*, 111-178.

Brace, W.F. (1960). An extension of Griffith theory of fracture to rocks. *Journal of Geophysical Research*, 65, 3477–3480.

- Brace, W.F., & Bombolakis, E.G. (1963). A note on brittle crack growth in compression. *Journal of Geophysical Research*, 68, 3709-3713.
- Brace, W.F., Walsh, J.B., Frangos, W.T. (1968). Permeability of granite under high pressure. *Journal of Geophysical Research*, 73, 2225-236
- Brady, B. (1969a). The nonlinear mechanical behaviour of brittle rock Part I—Stress-strain behaviour during regions I and II. *International Journal of Rock Mechanics and Mining Sciences & Geomechanics Abstracts*, 6(2), 211-225.
- Brady, B. (1969b). The nonlinear mechanical behaviour of brittle rock Part II — Stress-strain behaviour during regions III and IV. *International Journal of Rock Mechanics and Mining Sciences & Geomechanics Abstracts*, 6(3), 301-310.
- Brady, B. H. G., & Brown, E. T. (2005). Rock mechanics for underground mining. *Dordrecht: Springer*, 105-107, 173-176.
- Bragg, W.H. & Bragg, W.L. (1913). The reflection of X-Rays by crystals. *Proc. R. Soc. London*, A88, 428-438
- Brown, A.A. (2015). Interpreting permeability from mercury injection capillary pressure data. *AAPG Annual Convention and Exhibition*, Denver, Colorado, 41660.
- Brown, S. & Scholz, C. (1986). Closure of rock joints. *Journal of Geophysical Research*, 91(B5), 4939.
- Carey, J. W., Pini, R., Prasad, M., Frash, L. P. & Kumar, S. (2017). Leakage Processes in Damaged Shale: In Situ Measurements of Permeability, CO<sub>2</sub>-Sorptions Behaviour and Acoustic Properties. *Geophysics*, 1711.03032v1.
- Cartwright, J., Huuse, M., & Aplin, A. (2007). Seal bypass systems. *American Association of Petroleum Geologists Bulletin*, 91, 1141-1166.
- Chandler, M., Meredith, P., Brantut, N. & Crawford, B. (2016). Fracture toughness anisotropy in shale. *Journal of Geophysical Research: Solid Earth*, 121(3), 1706-1729..
- Chang, C., Zoback, M. & Khaksar, A. (2006). Empirical relations between rock strength and physical properties in sedimentary rocks. *Journal of Petroleum Science and Engineering*, 51, 223-237.
- Chen, D., Ye, Z., Pan, Z., Zhou, Y. & Zhang, J. (2017). A permeability model for the hydraulic fracture filled with proppant packs under combined effect of compaction and embedment. *Journal of Petroleum Science and Engineering*, 149, pp.428-435.
- Chilingarian, G.V., Mazzullo, S.J. & Rieke, H.H. (1996). Carbonate reservoir characterization: a geological engineering analysis, part II. *Elsevier*, 183.

Chilton, T. and Colburn, A. (1931). II—Pressure Drop in Packed Tubes 1. *Ind. Eng. Chem.*, 23(8), pp.913-919.

Cho, Y., Ozkan, E. & Apaydin, O. G. (2013). Pressure-dependent natural-fracture permeability in shale and its effect on shale-gas well production. *Society of Petroleum Engineers*, 16, 216–228.

Corapcioglu, H. (2014). Fracturing fluid effects on Young's modulus and embedment in the Niobrara formation: Master's thesis. *Colorado School of Mines*.

Corapcioglu, H., Miskimins, J., & Prasad, M. (2014). Fracturing fluid effects on Young's modulus and embedment in the Niobrara formation. *Society of Petroleum Engineers*, SPE-170835-MS

Cranganu, C. and Soleymani, H. (2015). Carbon dioxide sealing capacity: Textural or compositional controls? A case study from the Oklahoma Panhandle. *Environmental Geosciences*, 22(2), pp.57-74.

Cranganu, C., & Villa, M. A. (2005). Capillary sealing as an overpressure mechanism in the Anadarko basin. AAPG Ann Conv Calgary, Alberta.

Crook, A.j.l., Willson, S.m., Yu, J.g., & Owen, D.r.j. (2006). Predictive modelling of structure evolution in sandbox experiments. *Journal of Structural Geology*, 28, 729-744.

Cuss, R., Harrington, J., Giot, R. & Auvray, C. (2014a). Experimental observations of mechanical dilation at the onset of gas flow in Callovo-Oxfordian claystone. *Geological Society, London, Special Publications*, 400(1), pp.507-519.

Cuss, R.J., Harrington, J., Noy, D., Graham, C., & Sellin, P. (2014b). Evidence of localised gas propagation pathways in a field-scale bentonite engineered barrier system; results from three gas injection tests in the large scale gas injection test (Lasgit). *Applied Clay Science*, 102, 81-92.

Daniel, R. F., & Kaldi, J. G. (2009). Evaluating seal capacity of cap rocks and intraformational barriers for CO<sub>2</sub> containment. *AAPG Studies in Geology*, 59, p. 335–345.

Darcy, H. (1856). Les fontaines publiques de la ville de Dijon. *Paris, Dalmont*.

Dawson W.C, Almon, W.R., Rietsch E., Ethridge F.G., Sutton S.J. & Castelblanco-Torres, B. (2003). Sedimentology and Petrophysical Character of Cretaceous Marine Shale Sequences, Foreland Basins: Seismic Response of Seals Horizons. *AAPG Salt Lake City*.



- Desai, C.S., & Salami, M.R. (1987). A constitutive model and associated testing for soft rock. *International Journal of Rock Mechanics and Mining Sciences & Geomechanics Abstracts*, 24, 299-307.
- Duan, Y., Jing, X., Meng, Y., & Luo, P. (2000). Closure behaviour of natural rock fractures. *Society of Petroleum Engineering, SPE* 62539.
- Erdman, N. & Bell, D. (2015). Chapter 7: Scanning electron and ion microscopy of nanostructures. *Nanoscience & Nanotechnology Series*, 37, pp.300-350.
- Evans, A. G. (1979). Fracture toughness: the role of indentation techniques. *In Fracture Mechanics Applied to Brittle Materials*, ASTM International, 112–135.
- Evans, A.G. & Charles, E.A. (1976). Fracture toughness determinations by indentation. *Journal of The American Ceramic Society*, 59(7-8), 371-372.
- Fabricius, I. L. (2003). How burial diagenesis of chalk sediments controls sonic velocity and porosity. *Bulletin of the American Association of Petroleum Geologists*, 87, 1755-1778.
- Fancher, G. and Lewis, J. (1933). Flow of Simple Fluids through Porous Materials. *Ind. Eng. Chem.*, 25(10), pp.1139-1147.
- FEI. (2010). An introduction to electron microscopy. *Field Electron Ion Company*, 20, ISBN 978-0-578-06276-1.
- Fisher, Q. J. & Wignall P. B. (2001). Palaeoenvironmental controls on the uranium distribution in an Upper Carboniferous black shale (*Gastrioceras listeri* Marine Band) and associated strata; England. *Chemical Geology*, 175(3), 605–621.
- Fisher, Q. J., Harris, S. D., Casey, M. , & Knipe, R. J. (2007). Influence of grain size and geothermal gradient on the ductile-to-brittle transition in arenaceous sedimentary rocks: implications for fault structure and fluid flow. *Geological Society London Special Publications*, 289, 105-121.
- Fisher, Q.J., Kets, F. & Crook, A. (2013). Self-sealing of faults and fractures in argillaceous formations: Evidence from the petroleum industry. *Nagra*, NAB 13-06.
- Fjaer, E., Holt, R.M., Horsrud, P., Raaen, A.M., & Risens, R. (2008). Petroleum related rock mechanics. *Elsevier*.
- Freed, R. L., & Peacor, D.R. (1989). Geopressured shale and sealing effect of smectite to illite transition. *Bulletin of the American Association of Petroleum Geologists*, 73, 1223-1232.

- Gale, J. F. W., Reed, R. M. & Holder, J. (2007). Natural fractures in the Barnett shale and their importance for hydraulic fracture treatments. *Bulletin of the American Association of Petroleum Geologists*, 91, 603-622.
- Geochemistry lab (2016). Total carbon using LECO. Unpublished standard operating procedure. *School of Earth and Environment, University of Leeds*.
- Giles, M. R. (1997). In diagenesis and its impact on rock properties: A quantitative perspective, (p. 520). *Kluwer*.
- Goodman, R. (1980). Introduction to rock mechanics. *Wiley*, 182,202-210.
- Goodman, R.E. (1974). The mechanical properties of joints. *Proc. 3rd Congr. ISRM, Denver, 1*,127-140.
- Griffith, A.A. (1921). The phenomena of rupture and flow in solids. *Philosophical Transactions of the Royal Society of London, A* 221, 163–198.
- Griffith, A.A. (1924). The theory of rupture. *In: Proceedings of the First International Congress for Applied Mechanics, Delft*, 55-63.
- Griggs, D & Handin, J. (1960). Observations on fracture and a hypothesis of earthquakes in rock deformation. *Geological Society of America Memoir*, 79, 347-364.
- Grunau, H.R. (1987). A worldwide look at the cap-rock problem. *Journal of Petroleum Geology*, 10 (3), 243-266.
- Guder, H.S., Sahin, E., Sahin, O., Gocmez, H., Duran, C. & Ali Cetinkara, H. (2011). Vickers and Knoop Indentation microhardness Study of  $\beta$ -SiAlON Ceramic. *Acta Physica Polonica A*, 120, 1026-1033.
- Guise, P., Grattoni, C., Allshorn, S., Fisher, Q.J. & Schifer, A. (2017), Stress sensitivity of mercury injection instrument. *International Symposium of the Society of Core Analysts*. Vienna, Austria, SCA2017-011.
- Gutierrez, M., Nygård, R., Høeg, K. & Berre, T. (2008). Normalized undrained shear strength of clay shales. *Engineering Geology*, 99, 31-39.
- Gutierrez, M., Øino, L. E., & Nygård, R. (2000). Stress-dependent permeability of a de-mineralised fracture in shale. *Marine and Petroleum Geology*, 17, 895-907.
- Harrington, J., Graham, C., Cuss, R. & Norris, S. (2017). Gas network development in a precompacted bentonite experiment: Evidence of generation and evolution. *Applied Clay Science*, 147, 80-89.
- Harris, B. (1999). Engineering composite materials. London: IOM, 33-34.

- Hay, J. (2009). Introduction to instrumented indentation testing. *Experimental Techniques*, 33(6), 66-72.
- Heald, M. T. (1956). Cementation of Simpson and St Peter sand-stones in parts of Oklahoma, Arkansas, and Missouri. *Journal of Geology*, 64, 16-30.
- Hegazy, D. A. (2016). An experimental study to investigate the effects of in situ stress state and rock-fluid interactions on propped fracture conductivity in the Vaca Muerta formation. *MS Thesis, Colorado School of Mines*.
- Hermanrud, C., Nordgård Bolås, H. M., & Teige, G. M.G. (2005). Seal failure related to basin-scale processes. *American Association of Petroleum Geologists, Hedberg Series*, 2, 13– 22.
- Hettema, M.H.H., Schutjens, P.M.T.M., Verbroom, B.J.M. & Gussinklo, H.J. (2000). Production induced compaction of a sandstone reservoir: The strong influence of stress path. *Society of Petroleum Engineers, Reservoir Evaluation and Engineering*, 3, 342-347.
- Hildenbrand, A, & Urai, J.L. (2003). Investigation of the morphology of pore space in mudstones—First results. *Marine and Petroleum Geology* 20, 10, 1185-1200.
- Hillis, R.R. (2001). Coupled changes in pore pressures and stress in oil fields and sedimentary basins. *Petroleum Geoscience*, 7, 419-425.
- Hoek, E., & Bieniawski, Z.T. (1965). Brittle fracture propagation in rock under compression. *International Journal Fracture Mechanics*, 1, 137-155.
- Hoek, E., & Martin, C.D. (2014). Fracture initiation and propagation in intact rock – a review. *Journal of Rock Mechanics and Geotechnical Engineering*, 6, 287-300.
- Holland, M., Urai, J. L., Wouter, v. d. Z., Stanjek, H. & Konstanty, J. (2006). Fault Gouge Evolution in highly overconsolidated claystones. *Journal of Structural Geology*, 28, 323–332
- Horiba Ltd. (2012). Measurement of size and shape for frac sand and other proppants using the CAMSIZER: Application note. *Horiba ltd., USA*, AN205.
- Horseman, S., Harrington, J. & Sellin, P. (1999). Gas migration in clay barriers. *Engineering Geology*, 54(1-2), 139-149.
- Horseman, S.T., Cuss, R.J., Reeves, H.J. & Noy, D. (2005). Potential for self-healing of fractures in plastic clays and argillaceous rocks under repository conditions: Mechanical foundations. *Interim Report NEA-CC-3*.
- Horsrud, P. (2001). Estimating mechanical properties of shale from empirical correlations. *SPE Drilling & Completion*, 16(02), 68-73.

- Hough, E.W., Rzasa, M.J., Wood, B.B. (1951). Interfacial tensions of reservoir pressures and temperature, apparatus and the water-methane system. *AIME Petroleum Trans.*, 192, 57-60.
- Hubbert, M. K. & Rubey, W.W. (1959a). Mechanics of fluid filled porous solids and its application in overthrust faulting. I. Role of fluid pressure in mechanics of overthrust faulting. *Geological Society of America Bulletin*. 70, 115-166.
- Hubbert, M. K. & Rubey, W.W. (1959b). Mechanics of fluid filled porous solids and its application in overthrust faulting. II. Overthrust belt in geosynclinal area of Western Wyoming in light of fluid pressure hypothesis. *Geological Society of America Bulletin*, 70, 167-206.
- Hubbert, M. K. (1953). Entrapment of petroleum under hydro-dynamic conditions. *AAPG Bulletin*, 37, 1954-2026.
- Hubbert, M.K. & Willis, D.G. (1957). Mechanics of hydraulic fracturing. *Petroleum Transactions of the American Institute of Mining and Metallurgical Engineers*, 210, 153-168.
- Hubbert, M.K. (1953). Entrapment of petroleum under hydrodynamic conditions. *Bulletin of the American Association of Petroleum Geologists*, 37, 1954-2026.
- Huntsman (2013). Advanced materials Araldite 2000+ adhesive selector guide. *Huntsman Corp.*
- Ingram, G. & Urai, J. (1999). Top-seal leakage through faults and fractures: the role of mudrock properties. *Geological Society, London, Special Publications*, 158(1), 125-135.
- Instron. (2005). Series 5500 load frames reference manual – Equipment. Including series 5540, 5560 & 5580. *Instron Corp.*
- Iriarte, J. (2017). Fluid-shale-proppant interactions and the degradation of hydraulic fracture conductivity in the Niobrara formation. *MS Thesis, Colorado School of Mines.*
- ISRM. (1983). Suggested methods for determining the strength of rock materials in triaxial compression: Revised version. *International Journal of Rock Mechanics and Mining Sciences & Geomechanics Abstracts*, 20, No.6, 285-290.
- Japanese Industrial Standard (1990). Testing method for fracture toughness of high performance ceramics. *Japanese Standards Association*, J IS R-1607.
- Japsen, P., Dysthe, D. K. , Hartz, E. H. , Stipp, S. L. S. , Yarushina, V. M. , & Jamtveit, B. (2011). A compaction front in North Sea chalk. *Journal of Geophysical Research*, 116, B11208.

- Jennings, H. (1967). The effect of temperature and pressure on the interfacial tension of benzene-water and normal decane-water. *Journal of Colloid and Interface Science*, 24(3), 323-329.
- Jizba, D. (1991). Mechanical and acoustical properties of sandstones and shales, *PhD thesis, Stanford University*.
- Johnson, B.D., Boudreau, B.P., Gardiner, B.S., & Maass, R. (2002). Mechanical response of sediments to bubble growth. *Marine Geology*, 187, 347–363.
- Johnson, K. L. (1985). Contact mechanics. *Cambridge University Press, Cambridge*, 8-5
- Jones, L. & Wang, H. (1981). Ultrasonic velocities in Cretaceous shales from the Williston basin. *Geophysics*, 46(3), 288-297.
- Kalani, M., Koochak Zadeh, M., Jahren, J., Mondol, N.H. & Faleide, J.I. (2015). Effect of diagenesis on pore pressures in fine-grained rocks in the Egersund Basin, Central North Sea. *Norwegian Journal of Geology* 95, 171–189
- Kang, S., Kim, J., Park, C., Kim, H. & Kwon, D. (2009). Conventional Vickers and true instrumented indentation hardness determined by instrumented indentation tests. *Journal of Materials Research*, 25(02), 337-343.
- Karakin, A. V., Karakin, S. A., & Kambarova, G. N. (2001). Movement of a mud mixture through a mud volcano channel. *Izvestiya, Physics of the Solid Earth*, 37, 817–824.
- Karmakar, S., Sharma, J., & Kushwaha, R.L. (2004). Critical state elasto-plastic constitutive models for soil failure in tillage – A review. *Canadian Biosystems Engineering*, 46.
- Katz, A. J., & Thompson, A. H. (1986). Quantitative prediction of permeability in porous rock. *Physical Reviews*, 34, 8179-8181.
- Katz, A. J., & Thompson, A. H. (1987). Prediction of rock electrical conductivity from mercury injection measurements. *Journal of Geophysical Research*, 92, 599-607.
- Kim, MM. & Ko, HY. (1979). Multistage triaxial testing of rocks. *Geotech. Test J.*, 2, 98–105.
- Kirkham, C.B. (2015). A 3D seismic interpretation of mud volcanoes within the western slope of the Nile Cone. *PhD thesis, Cardiff University*.
- Klinkenberg, L. J. (1941). The permeability of porous media to liquids and gases. *Drilling and Production Practice*, 200-213

- Knudsen, M. (1934). The kinetic theory of gases. *London*
- Kouraytem, N., Li, E. & Thoroddsen, S. (2016). Formation of microbeads during vapour explosions of Field's metal in water. *Physical Review E*, 6, 93.
- Kouraytem, N., Li, E. & Thoroddsen, S. (2016). Formation of microbeads during vapour explosions of Field's metal in water. *Physical Review E*, 93(6).
- Kovari, K. & Tisa, A. (1975). Multiple failure state and strain controlled triaxial tests. *Rock mechanics* 7, 17-33
- Krumbein, W. C. & Sloss, L. L. (1963). Stratigraphy and sedimentation (2nd edition.). *San Francisco: W.H. Freeman and Company.*
- Kumar, V., Curtis, M. E., Gupta, N., Sondergeld, C. H., & Rai, C. S. (2012). Estimation of elastic properties of organic matter in Woodford shale through nanoindentation measurements. *Society of Petroleum Engineers*, SPE 162778
- Lama, R.D., Vutukuri, V.S. (1978). Handbook on mechanical properties of rocks, Vol. II. *Trans Tech Publications*, Clausthal, Germany.
- Lander, R. H., & Walderhaug, O. (1999). Predicting porosity through simulating sandstone compaction and quartz cementation. *Bulletin of the American Association of Petroleum Geologists*, 83, 433-449.
- Laplace, P.S. (1806). *Traité de Mécanique Céleste; Supplement au Dixième Livre, Sur l'Action Capillaire. Paris.*
- Lashkaripour, G.R. & Dusseault, M.B. (1993). A statistical study on shale properties; relationship among principal shale properties. *Proc. Conference on Probabilistic Methods in Geotechnical Engineering*, Canberra, Australia, 195–200.
- Lawn, B. & Fuller, E. (1975). Equilibrium penny-like cracks in indentation fracture. *Journal of Materials Science*, 10, 2016-2024.
- Lawn, B.R., Evans, A.G. & Marshall, D.B. (1980). Elastic/plastic indentation damage in ceramics: the median/radial crack system. *Journal of The American Ceramic Society*, 63, 574-581.
- Listiyowati, L. (2018). Laboratory characterization of shale pores. *IOP Conference Series: Earth and Environmental Science*, 118, 012067.
- Liu, Y. (2015). Fracture toughness assessment of shales by nanoindentation. *Master's thesis, University of Massachusetts Amherst, USA.*

- Løseth, H., Wensaas, L., Arntsen, B. , Hanken, N. , Basire, C., & Graue, K. (2001). 1000 m long gas blow-out pipes. *63rd European Association of Geoscientists and Engineers Conference and Exhibition, Amsterdam, Extended Abstracts*, 524.
- Løseth, H., Wensaas, L., Arntsen, B., & Hovland, M. (2003). Gas and fluid injection triggering shallow mud mobilization in the Hordaland Group, North Sea. *Geological Society (London) Special Publication*, 216, 139–157.
- Lundegard, P. D. (1991). Sandstone porosity loss -A big picture view of the importance of compaction. *Journal of Sedimentary Petrology* 62, 250-260.
- Mandl, G. (2005) Rock joints: The mechanical genesis. *Springer, Netherlands*, 4-8.
- Mazurek, M., Gautschi, A., Marschall, P., Vigneron, G., Lebon, P. & Delay, J. (2008). Transferability of geoscientific information from various sources (study sites, underground rock laboratories, natural analogues) to support safety cases for radioactive waste repositories in argillaceous formations. *Physics and Chemistry of the Earth*, 33, S95-S105.
- McClintock, F.A., Walsh, J.B. (1962). Friction on Griffith cracks under pressure. *In: Proc. Fourth U.S. Nat. Congress of Appl. Mech., ASME*, pp. 1015–1021.
- Milkov, A. V. (2000). Worldwide distribution of submarine mud volcanoes and associated gas hydrates. *Marine Geology*, 167(1), 29-42.
- Mitchell, P., Sincock, K., and Williams, J. (2003). On the effect of reservoir confining stress on mercury intrusion-derived pore frequency distribution. *Proc. International Symposium of Society of Core Analysts*, SCA2003-23.
- Mondol, N., Bjørlykke, K., Jahren, J. & Høeg, K. (2007). Experimental mechanical compaction of clay mineral aggregates—Changes in physical properties of mudstones during burial. *Marine and Petroleum Geology*, 24(5), pp.289-311.
- Moradkhani, A., Baharvandi, H., Tajdari, M., Latifi, H. & Martikainen, J. (2013). Determination of fracture toughness using the area of micro-crack tracks left in brittle materials by Vickers indentation test. *Journal of Advanced Ceramics*, 2(1), 87-102.
- Muskat, M. (1937) The Flow of homogeneous fluids through porous media. *McGraw-Hill Book Company*, New York.
- Nadeau, P. H., Peacor, D.R., Yan, J., & Hillier, S. (2002). I-S precipitation in pore space as the cause of geopressuring in Mesozoic mudstones, Egersund Basin, Norwegian continental shelf. *American Mineralogist*, 87, 1580 - 1589.
- Navarro, M. (2009). Simulating the migration of repository gases through argillaceous rock by implementing the mechanism of pathway dilation into the code TOUGH2

(TOUGH2-PD). PAMINA project, public milestone 3.2.14. *Gesellschaft für Anlagen- und Reaktorsicherheit (GRS) mbH, Cologne.*

Neuzil, C. E. (1994). How permeable are clays and shales?. *Water Resources Research*, 30, 145-150.

Newhouse, W. H. (1942). Ore deposits as related to structural features. *Princeton University Press, Princeton, USA*, p.240.

Niihara, K., Morena, R. & Hasselman, D. (1982). Evaluation of  $K_{IC}$  of brittle solids by the indentation method with low crack-to-indent ratios. *Journal of Materials Science Letters*, 1(1), 13-16.

Novikov, L. A., & Slobodskoy, R. M. (1978). Mechanism of formation of diatremes. *International Geology Review*, 21, 1131– 1139.

Nygård, R., Gutierrez, M., Bratli, R.K. & Høeg, K. (2006). Brittle-ductile transition, shear failure and leakages in shales and mudrocks. *Marine and Petroleum Geology*, 23, 201-212.

Nygård, R., Gutierrez, M., Bratli, R.K., & Høeg, K. (2006). Brittle-ductile transition, shear failure and leakages in shales and mudrocks. *Marine and Petroleum Geology*, 23, 201-212.

Oliver, W. & Pharr, G. (2003). Measurement of hardness and elastic modulus by instrumented indentation: Advances in understanding and refinements to methodology. *Journal of Materials Research*, 19(1), pp.3-20.

Oliver, W. & Pharr, G.M. (1992). An improved technique for determining hardness and elastic modulus using load and displacement sensing indentation experiments. *Journal of Materials Research*, 7(06), pp.1564-1583.

Ostensen, R. W. (1983) Microcrack permeability in tight gas sandstone. *Society of Petroleum Engineers of AIME*, 23, 919-927.

Palciauskas, V.V., and Domenico, P.A. (1980). Microfracture development in compacting sediments: relations to hydrocarbon maturation kinetics. *American Association of Petroleum Geologists Bulletin*, 64, 927–937.

PANalytical. (2009). The world of X-ray diffraction is no longer flat. *PANalytical B.V*, 12.

Passey, Q. R., Bohacs, K., Esch, W. L., Klimentidis, R., & Sinha, S. (2010). From oil-prone source rock to gas-producing shale reservoir - geologic and petrophysical characterization of unconventional shale gas reservoirs. *Society of Petroleum Engineers*.



- Petley, D.N. (1999). Failure Envelopes of Mudrocks at High Confining Pressures. *Geological Society of London, Special Publications*, 158, 61-71.
- Pharr, G., Oliver, W. & Brotzen, F. (1992). On the generality of the relationship among contact stiffness, contact area, and elastic modulus during indentation. *Journal of Materials Research*, 7(03), pp.613-617.
- Polyanin, A.D. & Manzhirov, A.V. (2006). Handbook of mathematics for engineers and scientists, *CRC Press*, 69.
- Purcell, W. R. (1949). Capillary pressure-their measurements using mercury and the calculation of permeability therefrom. *AIME Petroleum Transactions*, 186, 39-48.
- Pusch, R. (1979). Highly compacted sodium bentonite for isolating rock-deposited radioactive waste products. *Nuclear Technology*, 45(2), 153-157.
- Ramm, M. (1992). Porosity depth trends in reservoir sandstones; Theoretical models related to Jurassic sandstones offshore Norway. *Marine and Petroleum Geology*, 9, 553-567.
- Ramm, M. (1994). Porosity/depth trends in reservoir sandstones: Assessing the quantitative effects of varying pore-pressure, temperature history and mineralogy. *Norwegian Shelf Data, Clay Minerals*, 29, 475-490
- Revil, A., Grauls, D., & Brévert, O. (2002). Mechanical compaction of sand/clay mixtures. *J. Geophys. Res.*, 107, 2293.
- Rickman, R., Mullen, M., Petre, E., Grieser, B. & Kundert, D. (2008). A practical use of shale petrophysics for stimulation design optimization: all shale plays are not clones of the Barnett shale. *SPE Annual Technical Conference and Exhibition*. Denver, CO, USA.
- Rockfield (2014a). Constitutive models for sands, sandstones and shales: Part2 - SR3 model, ELFEN training notes. *Rockfield Software limited*, Swansea, UK.
- Rockfield (2014b). Discrete element modelling, ELFEN training notes. *Rockfield Software limited*, Swansea, UK.
- Roscoe, K.H., & Burland, J.B. (1968). On the generalized stress strain behaviour of wet clay. *Engineering Plasticity*, 33, 535-609.
- Roscoe, K.H., Schofield, A.N., & Wroth, C.P. (1958). On the yielding of soils. *Géotechnique*, 8, 22-53.
- Rothfuchs, T., Jockwer, N., & Zhang, C. L. (2007). Self-sealing barriers of clay/mineral mixtures – The SB project at the Mont Terri rock laboratory. *Physics and Chemistry of the Earth*, 32, 108-115.

- Rozhko, A. (2016). Two-phase fluid-flow modelling in a dilatant crack-like pathway. *Journal of Petroleum Science and Engineering*, 146, 1158-1172.
- Rybacki, E., Reinicke, A., Meier, T., Makasi, M. & Dresen, G. (2014). What controls the strength and brittleness of shale rocks?. *Geophysical Research Abstracts. EGU General Assembly 2014*, 16, EGU2014-1877
- Salz, L.B. (1977). Relationship between fracture propagation pressure and pore pressure. *Society of Petroleum Engineers*, 6870.
- Schechter, R.S. (1992). Oil well stimulation. *Prentice Hall, Englewood Cliffs, New Jersey*, 396.
- Schowalter, T.T. (1979). Mechanics of secondary hydrocarbon migration and entrapment. *Bulletin of the American Association of Petroleum Geologists*, 63, 723-760.
- Schutjens, P., Hanssen, T., Hettema, M., Merour, J., de Bree, P., Coremans, J. and Helliesen, G. (2004). Compaction-induced porosity/permeability reduction in sandstone reservoirs: data and model for elasticity-dominated deformation. *SPE Reservoir Evaluation & Engineering*, 7(03), pp.202-216.
- Shanley, K.W., Cluff, R.M., & Robinson, J.W. (2004). Factors controlling prolific gas production from low-permeability sandstone reservoirs: Implications for resource assessment, prospect development, and risk analysis. *Bulletin of the American Association of Petroleum Geologists*, 88, 1083-1121.
- Shetty, D., Wright, I., Mincer, P. & Clauer, A. (1985). Indentation fracture of WC-Co cermets. *Journal of Materials Science*, 20, 1873-1882.
- Shibata, K., Tani, K. and Okada, T. (2007). Creep behaviour of tuffaceous rock at high temperature observed in unconfined compression test. *Soils and Foundations*, 47(1), 1-10.
- Shukla, P., Kumar, V., Curtis, M., Sondergeld, C. H., & Rai, C. S. (2013). Nanoindentation Studies on Shales. *American Rock Mechanics Association, ARMA-2013-578*
- Smits, R. M. M., De Waal, J. A., & Van Kooten, J. F. C. (1988). Prediction of abrupt reservoir compaction and subsurface subsidence by pore collapse in carbonates. *SPE Formation Evaluation*, 3, 340-346.
- Snow (1965). A parallel plate model of fractured permeable media. *PhD Thesis, University of California, Berkeley, USA*.

Sone H. & Zoback M. D. (2010). Strength, creep and frictional properties of gas shale reservoir rocks. *The 44th US Rock Mechanics Symposium and 5th US Canada Rock Mechanics Symposium, American Rock Mechanics Association*, ARMA 10-463.

Stanton, R. J. (1966). The solution brecciation process. *Geological Society of America Bulletin*, 77, 843–848.

Sutton, S. J., Ethridge, F. G., Almon, W. R., Dawson, W. C., & Edwards, K. K. (2004). Textural and sequence-stratigraphic controls on sealing capacity of Lower and Upper Cretaceous shales, Denver basin, Colorado. *AAPG bulletin*, 88(8), 1185-1206.

Tawara, Y., Hazart, A., Mori, K., Tada, K., Shimura, T., Sato, S., Yamamoto, S., Asano, H., & Namiki, K. (2014). Extended two-phase flow model with mechanical capability to simulate gas migration in bentonite. *Clays in Natural and Engineered Barriers for Radioactive Waste Confinement*, 400, 545-562.

Teige, G. M. G., Hermanrud, C., Thomas, W. L. H., Wilson, O. B., & Nordgård Bolås, H. M. (2005). Capillary resistance and trapping of hydrocarbons: a laboratory experiment. *Petroleum Geoscience*, 11, 125-129.

Teufel, L.W., Rhatt, W. & Farrell, H.E. (1991). Effect of reservoir depletion and pore pressure drawdown on in situ stress and deformation in the Ekofisk field, North Sea. *Rock Mechanics as a Multidisciplinary Science*, Balkema, Rotterdam.

Thompson, A. (1959). Pressure solution and porosity. *In Silica in sediments. Society of Economic Paleontologists and Mineralogists Special Publications*, 7, 92-110.

Thyberg, B., Jahren, J., Winje, T., Bjørlykke, K., Faleide, J. I., & Marcussen, Ø. (2010). Quartz cementation in late Cretaceous mudstones, northern North Sea: Changes in rock properties due to dissolution of smectite and precipitation of micro-quartz crystals. *Marine and Petroleum Geology*, 27, 1752-1764.

Valdiviezo-Mijangos, Oscar C. and Nicolás-Lopez, Rubén (2014). Dynamic characterization of shale Systems by dispersion and attenuation of P- and S-waves considering their mineral composition and rock maturity. *Journal of Petroleum Science and Engineering*, 122, 420-427.

Van Dam, D., Papanastasiou, P. & de Pater, C. (2000). Impact of rock plasticity on hydraulic fracture propagation and closure. *SPE Production & Facilities*, 17(03), 149-159.

Van Eekelen, H.A.M. (1980). Isotropic yield surfaces in three dimensions for use in soil mechanics. *International Journal for Numerical and Analytical Methods in Geomechanics*, 4, 89–101.

- Watts, N. L. (1987). Theoretical aspects of cap-rock and fault seals for single- and two phase hydrocarbon column. *Marine and Petroleum Geology*, 4, 274-307.
- Whitehead, W.S., Hunt, E.R. & Holditch, S.A. (1987). The effect of lithology and reservoir pressure on in situ stresses in the Waskom (Travis Peak) field. *Society of Petroleum Engineers*, 16403.
- Wiseall, A., Cuss, R., Graham, C. & Harrington, J. (2015). The visualization of flow paths in experimental studies of clay-rich materials. *Mineralogical Magazine*, 79(06), 1335-1342.
- Witherspoon, P.A., Wang, J.S.Y., Iwai, K. & Gale, J.E. (1980). Validity of cubic law for fluid flow in a deformable rock fracture. *Water Resource. Res.*, 16, 1016-1024.
- Wong, T.F., David, C., & Zhu, W.L. (1997). The transition from brittle faulting to cataclastic flow in porous sandstones: Mechanical deformation. *Journal of Geophysical Research*, 102, 3009-3025.
- Wong, T.F., David, C., & Zhu, W.L. (1997). The transition from brittle faulting to cataclastic flow in porous sandstones: Mechanical deformation. *Journal of Geophysical Research*, 102, 3009-3025.
- Wood, D.M. (1990). Soil behaviour and critical state soil mechanics. *Cambridge University Press, Cambridge*, 65,118-123,139- 144,226-253.
- Yang, Y. L., & Aplin, A.C. (1998). Influence of lithology and effective stress on the pore size distribution and modelled permeability of some mudstones from the Norwegian margin. *Marine and Petroleum Geology*, 15, 163-175.
- Yang, Y., & Aplin, A.C. (2004). Definition and practical application of mudstone porosity-effective stress relationships. *Petroleum Geoscience*, 10, 153-162.
- Yang, Y., & Aplin, A.C. (2010). A permeability-porosity relationship for mudstones. *Marine and Petroleum Geology*, 27, 1692-1697.
- Youn, H. & Tonon, F. (2010). Multi-stage triaxial test on brittle rock. *International Journal of Rock Mechanics and Mining Sciences*, 47, 678-684.
- Young, T. (1805). An essay on the cohesion of fluids. *Philosophical Transactions of the Royal society of London*, 95, 65-87.
- Zhang, C. (2011). Experimental evidence for self-sealing of fractures in claystone. *Physics and Chemistry of the Earth*, 36(17-18), 1972-1980.
- Zhu, W. & Wong, T. (1997). The transition from brittle faulting to cataclastic flow: Permeability evolution. *Journal of Geophysical Research: Solid Earth*, 102(B2), 3027-3041.

Zoback, Mark D. (2007). Reservoir geomechanics. *Cambridge University Press, Cambridge*, 118-120.

## 10 Appendix A

Description of joint roughness characterization used by Bandis et al. (1983) is shown in Figure (A-1a & 1b). Surface roughness was characterized by joint type, weathering state, joint wall strength and joint wall geometry. Table A-1 describes all the symbols used in Figure (A-1a & 1b).

Characterization group	Symbols	Description
Joint type.	IF	Joint induced along a natural incipient fracture.
	CP	Cleavage plane.
	VJ	Vertical joint.
	BP	Bedding plane.
	AF	Artificial extension fracture.
Joint Wall strength.	R	Mean rebound number from Schmidt hammer (L-type) tests on dry joint surfaces.
	$\gamma$	Mean unit weight of joint wall material.
	JCS	Mean joint compressive strength calculated from: $\log_{10} JCS = 0.00088 \cdot \gamma \cdot R + 1.01$ .
Weathering state.	F	Fresh. Weathering state is quantified using JCS and uniaxial compressive strength ( $\sigma_n$ ) estimated from Schmidt hammer test. Range of F: $\sigma_n / JCS \leq 1.2$ .
	SW	Slightly weathered. Range of SW: $\sigma_n / JCS \leq 1.2$ .
	MW	Moderately weathered. Range of MW: $1.2 < \sigma_n / JCS \leq 2$ .
	W	Weathered. Range of W: $\sigma_n / JCS > 2$
Joint wall geometry	JRC	Joint roughness coefficient obtained from direct shear tests under $JCS/\sigma_n \approx 2000$ .
	JRA	Joint roughness amplitude measured on the joint profile as the average vertical amplitude of the prominent surface protrusions.
	$a_j$	Average aperture values for each group of joints measured with feeler gauges.

Table A-1: description of symbols used in joint roughness characterization (Bandis et al., 1983).

Table 2. Summary of the physical characteristics of the various joint types

Joint types and (no.) of samples	Joint wall strength				Joint wall geometry				JRA (mm)
	Weathering state	R (kN/m <sup>2</sup> )	$\gamma$ (kN/m <sup>3</sup> )	JCS (MPa)	Typical range of roughness profiles	$a_j$ (mm)	JRC	JRA (mm)	
IF (3)	[F]	50.6	27.7	175					0.80 0.93
CP (1)	[MW]	42.5	27.82	122					1.20
CP (3)	[W]	36.8	27.05	77					6.0- 6.8
VJ (2)	[F]-[SW]	47.5- 49.0	29.0	167- 182					0.15- 0.20
VJ (3)	[W]	32.4- 36.9	26.75- 26.92	60- 76					0.50- 0.60
BP & VJ (11)	[F]-[SW]	49.1- 50.2	26.95- 27.27	152- 170					0.20- 0.25

Figure A-1a: joint roughness characterization by Bandis et al. (1983).





## 11 Appendix B

Formation of faults and fractures due to brittle failure was discussed in **Chapter 2**. Below is detailed description of the theory of formation of each fracture type.

### *Wing crack model:*

This mechanism is favoured by most theoreticians who attempt to derive a macroscopic deformation from micro-mechanical processes (Mandl, 2005). All wing crack propagation models were derived from Griffith's (1924) theory of fractures in brittle material. Griffith (1924) demonstrated that in presence of elliptical cracks within rock material, having a confining pressure around the sample will still allow tensile fractures to form. According to his theory, for a tensile fracture to form in a confining environment, the effective stresses should obey the following condition:

$$\sigma_v = -T, \sigma_c < 3T \quad (\text{B-1})$$

The stress required to cause failure in a biaxial environment is:

$$\sigma_v = \frac{-8T(1+\frac{\sigma_v}{\sigma_c})}{(1-\frac{\sigma_v}{\sigma_c})^2} \quad (\text{B-2})$$

Griffith's (1924) theory was enhanced by Brace and Bombolakis (1963) and Hoek and Bieniawski (1965) who demonstrated that cracks that are inclined with respect to maximum effective stress will not propagate as shear cracks in their current planes when the compressive stress is raised, but will have tensile wing crack initiating at the crack tip. Crack growth will be stable with increasing compressive stress ( $\sigma_v$ ) until it aligns itself parallel to  $\sigma_v$  as shown in Figure B-1.

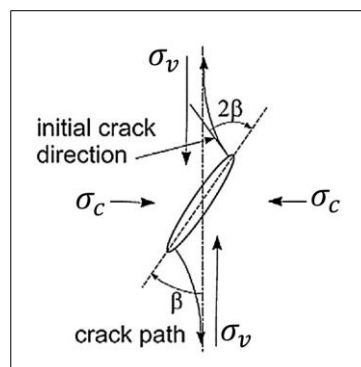


Figure B-1: Direction of wing crack propagation with respect to stresses (Hoek and Martin, 2014).

### ***Void model:***

This model is based on a material having spherical or elliptical holes within an elastic continuum. As the uniaxial compressive strength is applied, tangential components of the stress around the hole will induce a tensile stress at the top and bottom point of the hole. Cracks will open perpendicular to the compressive stress and propagate parallel to it. After the crack is initiated, cracks will extend more when the applied compressive stress is increased.

Stress components can be calculated using Kirsch equations (Brady and Brown, 2005). These equations are a set of closed form solutions derived from theory of elasticity used to calculate stresses and displacement around circular excavations (Figure B-2). The equations are:

$$\sigma_r = \frac{\sigma_v}{2} \left[ (1 + K) \left( 1 - \frac{a^2}{r^2} \right) - (1 - K) \left( 1 - 4 \frac{a^2}{r^2} + 3 \frac{a^4}{r^4} \right) \cos(2\theta) \right] \quad (\text{B-3})$$

$$\sigma_\theta = \frac{\sigma_v}{2} \left[ (1 + K) \left( 1 + \frac{a^2}{r^2} \right) + (1 - K) \left( 1 + 3 \frac{a^4}{r^4} \right) \cos(2\theta) \right] \quad (\text{B-4})$$

$$\tau_{r\theta} = \frac{\sigma_v}{2} \left[ (1 - K) \left( 1 + 2 \frac{a^2}{r^2} - 3 \frac{a^4}{r^4} \right) \sin(2\theta) \right] \quad (\text{B-5})$$

$$K = \frac{\sigma_h}{\sigma_c} \quad (\text{B-6})$$

Where:  $\sigma_r$ ,  $\sigma_\theta$  are radial and tangential components of the stress respectively,  $\sigma_v$ ,  $\sigma_c$  are vertical and horizontal stress applied respectively,  $K$  is the stress ratio,  $a$  is the radius of the circle,  $r$  is the distance from the centre of the circle to the element location and  $\theta$  is the angle between the positive x-axis and the location vector of the element. It is clear from the equations above that the element lying on the direction of the applied vertical stress will have no shear and tensile tangential components.

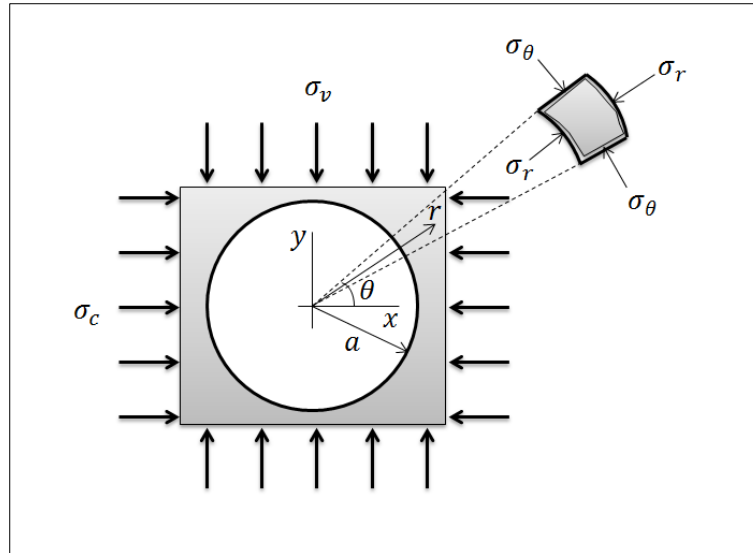


Figure B-2: Stresses on the elements around circular excavation (Brady and Brown, 2005).

**Grain contact model:**

This model is based on elastic contact theories, which assume two elastic spherical shapes in contact because of external stress application. Contact reaction stresses (normal and shear stresses) are developed at the contact area producing a tensile stress perpendicular to the external stress applied. In the case of rocks, when a compressive stress is applied, grains come into contact producing a tensile stress at the contact area. As compressive stress increases, the resulting reaction increases tensile stress until it exceeds the tensile strength and thus, fracture is initiated. This process can be clearly shown in Figure B-3.

This mechanism is well explained using Hertz theory for frictionless elastic contacts (Johnson, 1985). First of all, the effective radius of curvature ( $R^*$ ) of the two solids and effective young's modulus ( $E^*$ ) can be found using the following equations:

$$\frac{1}{R^*} + \frac{1}{R_1} + \frac{1}{R_2} \tag{B-7}$$

$$\frac{1}{E^*} + \frac{1-\nu_1^2}{E_1} + \frac{1-\nu_2^2}{E_2} \tag{B-8}$$

where  $F$  is the external force applied on the sphere, the radius of the contact area formed by the elastic deformation of the two solid sand particles ( $a$ ) is:

$$a = \left[ \frac{4FR^*}{\pi E^*} \right]^{1/2} \tag{B-9}$$

The maximum contact pressure ( $p_{max}$ ) due to the force is:

$$p_{max} = \frac{2F}{\pi a} \quad (\text{B-10})$$

The resultant stresses are:

$$\sigma_z = -p_{max} \frac{1}{\sqrt{1 + \left(\frac{z}{a}\right)^2}} \quad (\text{B-11})$$

$$\sigma_x = -2\nu p_{max} \left[ \sqrt{1 + \left(\frac{z}{a}\right)^2} - \left|\frac{z}{a}\right| \right] \quad (\text{B-12})$$

$$\sigma_y = -p_{max} \left[ \frac{1 + 2\left(\frac{z}{a}\right)^2}{\sqrt{1 + \left(\frac{z}{a}\right)^2}} - 2\left|\frac{z}{a}\right| \right] \quad (\text{B-13})$$

$$\tau_{xy} = \begin{cases} \frac{\sigma_z - \sigma_x}{2} & \text{for } 0 \leq z/a \leq 0.436 \\ \frac{\sigma_z - \sigma_y}{2} & \text{for } 0.436 \leq z/a \end{cases} \quad (\text{B-14})$$

Where:  $z$  is the location of stress calculated along the  $z$ -axis.

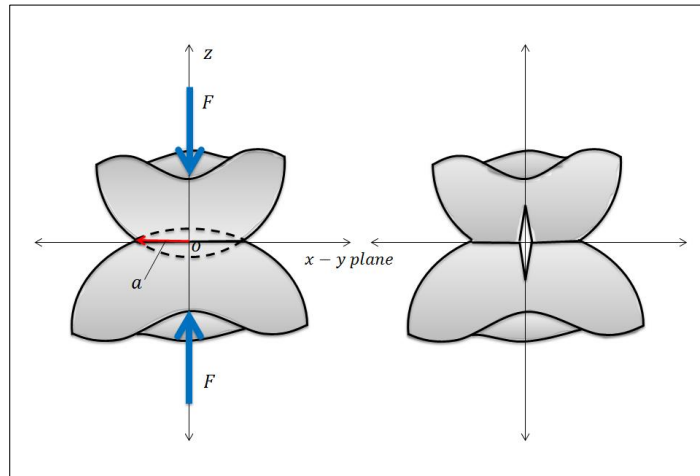


Figure B-3: Elastic contact area formation due to normal forces and fracture initiation.

### **Elastic mismatch model:**

Elastic mismatches occur when two layers are in contact along a common surface with different stiffness. The weaker layer tends to extend laterally during compression more than the stiffer layer. Friction around the contact surface will induce a tensile stress on the stiffer body which will form microscopic fractures. Stress at the contact can be calculated through numerical modelling (Bock et al., 2010).

## 12 Appendix C

The description of the yield surfaces presented in **Chapter 2** focussed on the yield surface projected in  $p$ - $q$  space. The third dimension of the model is the specific volume ( $v$ ), which represents the porosity reduction (and volume change) during compaction (Figure C-1) (Wood, 1990).

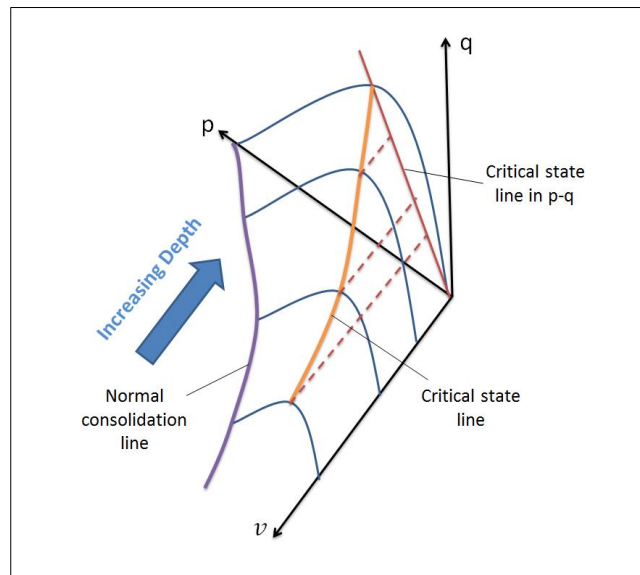


Figure C-1: Evolution of yield surface with depth as the specific volume decreases plotted in 3D ( $p$ - $q$ - $v$ ) space (Wood, 1990).

In  $v$ - $\ln p$  space, two important lines are present which control the shape of the yield surface presented in Figure C-2. The first line is the normal consolidation line, which appears to be a straight line in  $v$ - $\ln p$  space (Figure C-2). Soil states on this line will deform plastically with increasing effective stress ( $p$ ), which is represented by non-linear reduction in specific volume and hence reduction in porosity due to grain re-arrangement. The second line is the unloading curve, which represents loading and unloading of the soil at stresses below the maximum consolidation stress. Generally, the unloading line will have a different slope than the normal consolidation line due to the unrecoverable plastic volume change. The equations of the two lines in  $v$ - $\ln p$  space are (Wood, 1990):

Normal consolidation line:

$$v = N - \lambda \ln(p) \quad (\text{C-1})$$

Unloading line:

$$v = v_s - \kappa \ln(p) \quad (C-2)$$

Where:  $N$ ,  $\lambda$  and  $\kappa$  are material properties of a particular soil.

The CSL line shown in the  $p$ - $q$  space diagram is formed by a projection of all those intersections in  $v$ - $\ln p$  space (Figure C-1). It is very important to highlight that CSL line and normal consolidation line are parallel in  $v$ - $\ln p$  space but have different specific volume values at unit pressure (Figure C-2).  $N$  is the specific volume at unit pressure for the normal consolidation line and  $\Gamma$  is the specific volume at unit pressure for the CSL line. The two values,  $N$  and  $\Gamma$ , are related and only one of them is required as an input to the model. Specific volume at unit pressure of CSL line,  $\Gamma$ , is related to  $N$  by the following equations (Wood, 1990):

CC model:

$$\Gamma = N - (\lambda - \kappa) \quad (C-3)$$

MCC model:

$$\Gamma = N - (\lambda - \kappa) \ln 2 \quad (C-4)$$

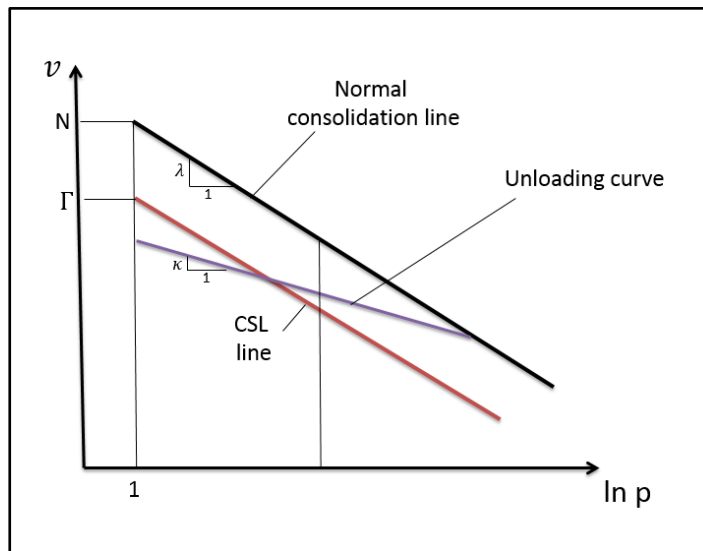


Figure C-2: Change in specific volume with pressure increase in  $v$ - $\ln p$  space for CSL, swelling and normal consolidation lines (Wood, 1990).